On the Development of Absorbed Dose Calorimeter Systems for Absolute Clinical Dosimetry

James Renaud

Department of Physics
McGill University, Montréal
October 2016

A thesis submitted to the Faculty of Graduate Studies and Research in partial fulfillment of the requirements of the degree of Doctor of Philosophy.

Dedicated in loving memory of my
grandmother, Clarabelle.

"Some are born to rule the world, to live their fantasies.
But most of us just dream about the things we'd like to be.
Sadder still to watch it die, than never to have known it.
For you, the blind who once could see, the bell tolls for thee."

Neil Peart

Abstract

The aim of this work is to develop and evaluate the feasibility of absolute dose to water measurements in clinical high-energy photon, electron, and proton beams using a probe-format graphite calorimeter (GPC; a.k.a. Aerrow), a sealed electron water calorimeter (ESWcal), and a short range water calorimeter (SHREWcal).

Measurements were performed using these calorimeters, all of which were designed and built in-house, and ionization chambers with calibrations traceable to national primary dose standards. A sealed glass vessel constructed at the National Research Council of Canada (NRC) was used as part of the water calorimeter experiments. Calorimeter-based dose results were validated in high-energy photon beams against established dose standards. A finite element analysis software package was used to numerically solve the heat transport equation in models of the calorimeters used throughout this project. Monte Carlo radiation transport codes were used to calculate the perturbation factors accounting for the presence of non-water (or graphite) detector materials in the path of the beam. For the GPC, absolute dose output measurements were performed using its two independent modes of operation for several clinical high-energy photon and electron beams, in addition to a relative characterization of the detector. For the ESWcal, electron beam quality conversion factors were directly measured for two types of ionization chambers. For the SHREWcal, dose measurements were performed for clinical short-range electron beams and cyclotron-based monoenergetic and modulated proton beams.

Absorbed doses measured using both GPC modes of operation were found to agree with chamber-derived doses to well within the combined uncertainty of about 1.5 %. Moreover, the detector was characterized as having a strong linear response in the range of 80 cGy to 470 cGy, and no dependence upon dose rate in the range of 0.5 Gy/min to 5.4 Gy/min. For

photon and electron beam qualities in the range of 58.4 % < $\%dd(10)_X$ < 86.8 % and 2.33 cm < R_{50} < 8.27 cm, respectively, no statistically significant energy response trend was exhibited and a maximum deviation of ± 1% from the average across all beam qualities was observed.

The ESWcal measured dose with a relative combined standard uncertainty of 0.5 % for electron beams with energies of 9 MeV and greater, and about 1.0 % for the 6 MeV beam. Validation measurements against the NRC water calorimeter in a high-energy photon beam were found to agree with the combined uncertainty of 0.43 %. Non-statistically significant differences of up to 0.7 % were found between the measured electron beam quality conversion factors and values listed in published protocols.

Absorbed doses to water were measured with the SHREWcal with an associated type A standard uncertainty of approximately 0.4 % and 0.2 % for the electron and proton beam experiments, respectively. In terms of thermal stability, drifts were on the order of a couple of hundred μK per minute, with a short-term variation of 5 – 10 μK. Relatively large heat transfer correction factors were calculated to be between 1.021 and 1.049. The overall combined standard uncertainty on the absorbed dose to water was estimated to be 0.6 % for the electron beams, as well as for the monoenergetic protons, and 0.7 % for the modulated proton beam.

In conclusion, this project establishes the foundations of several new calorimeter-based dose standards for use at the level of the clinic, as well as the national standards laboratory. The practical significance of these calorimeter devices is that they will allow for more accurate knowledge of the clinically delivered dose through reduced dosimetric uncertainties, thereby contributing to improved patient outcomes in terms of better tumour control and lower complication rates for those treated using photon, electron, and proton modalities.

Abrégé

Le but de ce travail est de développer et d'évaluer la faisabilité de mesurer la dose absolue dans des faisceaux à haute énergie de photon, d'électrons, et de protons en utilisant un calorimètre format sonde de graphite (GPC; alias Aerrow), un calorimètre d'eau d'électrons (ESWcal), et un calorimètre d'eau de courte portée (SHREWcal).

Les mesures ont été effectuées à l'aide de ces calorimètres, qui ont tous été conçus et construits en interne, et des chambres d'ionisation avec des étalonnages aux normes de dose primaires nationales. Un contenant en verre scellé construit au Conseil national de recherches du Canada (CNRC) a été utilisé dans le cadre des expériences de calorimètre d'eau. Les résultats de la dose mesuré avec les calorimètres ont été validés en faisceaux de photon à haute énergie photon par rapport aux normes de dose établies. Un logiciel d'analyse par éléments finis a été utilisé pour résoudre numériquement l'équation de transport de chaleur dans les modèles des calorimètres utilisés dans ce projet. Des codes de transport de rayonnement Monte Carlo ont été utilisés pour calculer les facteurs de perturbation qui représente la présence des matériaux de détection non-eau (ou graphite), dans le trajet du faisceau. Pour le GPC, les mesures de doses absolues ont été effectuées à l'aide de ses deux modes de fonctionnement indépendants pour plusieurs faisceaux à haute énergie de photon et d'électrons cliniques, en plus d'une caractérisation relative du détecteur. Pour le ESWcal, des facteurs de conversion de la qualité de faisceau d'électrons ont été mesurés directement pour deux types de chambres d'ionisation. Pour la SHREWcal, les mesures de dose ont été effectuées pour des faisceaux d'électrons et de protons monoénergétique et modulés de courte portée basé sur un cyclotron.

Les doses mesurées en utilisant les deux modes de fonctionnement GPC ont été trouvés d'accord avec des doses de chambre à bien au sein de l'incertitude combinée de 1,5%. Par ailleurs, le détecteur a été caractérisée comme ayant une forte réponse linéaire dans l'intervalle de 80 cGy à 470 cGy et aucune dépendance à l'égard du débit de dose dans

l'intervalle de 0,5 Gy/min à 5,4 Gy/min. Pour les qualités de photons et d'électrons dans la gamme de 58,4 % < %$dd(10)_X$ < 86,8 % et de 2,33 cm < R_{50} < 8,27 cm, respectivement, aucune tendance statistiquement significative de la réponse a été exposée et un déviation maximal de ±1 % de la moyenne de toutes les qualités de faisceau a été observée.

Les doses mesurées avec le ESWcal ont eu une incertitude de type A de 0,50 % pour les faisceaux d'électrons avec des énergies de 9 MeV et plus, et environ 1,00 % pour le faisceau de 6 MeV. Des mesures de validation contre le calorimètre d'eau du CNRC dans un faisceau de photons de haute énergie ont été trouvés d'accord avec l'incertitude combinée de 0,43 %. Des différences statistiquement non significatif allant jusqu'à 0,7 % ont été observées entre les facteurs de conversion de la qualité de faisceaux d'électrons mesurées et des valeurs mentionnés dans les protocoles publiés.

Des doses absorbées ont été mesurées avec le SHREWcal avec une incertitude standard de type A d'environ 0,4 % et 0,2 % pour les expériences de faisceaux d'électrons et de protons, respectivement. En termes de stabilité thermique, les déviation étaient de l'ordre de quelques centaines de μK par minute, avec une variation à court terme de 5-10 μK. Des facteurs de correction de transfert thermique entre 1,021 et 1,049 ont été calculés. L'incertitude standard combinée globale de la dose absorbée a été estimée à 0,6 % pour les faisceaux d'électrons, ainsi que pour les protons monoénergétiques, et 0,7 % pour le faisceau de protons modulé.

En conclusion, ce projet établit les fondations de plusieurs nouvelles normes de dose en fonction calorimètre-pour une utilisation au niveau de la clinique, ainsi que le laboratoire national. L'importance de ces calorimètres est qu'ils vont permettre une connaissance plus précise de la dose délivrée par les incertitudes dosimétriques réduits, contribuant ainsi à résultats pour les patients en termes de meilleur contrôle de la tumeur et les taux de complications plus bas pour ceux traités à l'aide de modalités de photons, d'électrons, et de protons.

Acknowledgements

First, I would like to express my gratitude to my supervisors, Dr. Arman Sarfehnia and Dr. Jan Seuntjens. Thank you for providing me with every opportunity to succeed scientifically and professionally. Your endless support has made this work possible, and your kindness has made it a pleasure.

I would like to acknowledge the help of all our collaborators at the National Research Council of Canada Ionizing Radiation Standards group, the National Physical Laboratory, the Université catholique de Louvain, the Sunnybrook Research Institute, The Clatterbridge Cancer Centre, the Allan Blair Cancer Centre, the Dutch Metrology Institute, and the University Medical Centre Utrecht. Special thanks goes out to Malcolm McEwen, Carl Ross, David Marchington, Mike Vandenhoff, Russell Thomas, Nigel Lee, Hugo Palmans, Séverine Rossomme, Stefaan Vynckier, Antoine Delor, Andrzej Kacperek, Tatsuaki Kanai, Kristin Marchant, Leon de Prez, Simon Woodings, Jan Kok, Bram van Asselen, Jochem Wolthaus, and Bas Raaymakers.

I thank the Canadian Institutes of Health Research (CIHR) for the doctoral fellowship award, the Natural Sciences and Engineering Research Council (NSERC) for the Medical Physics Collaborative Research and Training Experience Program funding, the McGill Faculties of Science and Medicine for the Reginald Fessenden Prize in Science Innovation, the Schulich graduate fellowship, and the numerous travel awards, the University of Toronto for the Terry Fox Foundation Strategic Training Initiative funding, and Sun Nuclear Corporation for the research and development grant.

Many thanks to the engineers of the Radiation Oncology Department of the McGill University Health Centre's Cedars Cancer Centre, Joe Larkin and Bhavan Siva, for helping us construct

pieces of equipment and for supplying several tools used in this work. I would also like to express my gratitude to Margery Knewstubb and Tatjana Nisic for all their assistance in dealing with administrative issues.

Finally, my sincere appreciation goes to all the staff, professors, and clinical physicists at the McGill Medical Physics Unit for their help and support, as well as many thanks to all my friends, colleagues and fellow students. Special thanks goes out to Daniel Markel, Julien Bancheri, Pavlos Papaconstadopoulos, Lalageh Mirzakhanian, Archd. James Coates, Marc-André Renaud, Pete Watson, Phil Savignac, and François Therriault-Proulx.

Table of Contents

List of Figures

List of Tables

Preface and Contribution of Authors

This thesis contains four manuscripts. All manuscripts have been written by me, although help from co-authors in reviewing the papers have been greatly appreciated. To the best of our knowledge, the methods, results and conclusions of the work presented in this thesis have not been previously published. The concept of absorbed dose calorimetry is not new, and it has been used for radiation dosimetry for many years. For this reason, a few chapters have been devoted to explaining the techniques and methodologies used in it.

However, to the best of the authors' knowledge, prior to our work on the subject, no one has published any work on a probe-format graphite calorimeter designed for application in the radiation therapy clinic. Small-scale graphite calorimeters have been built by dose standards laboratories in the past, however their reliance on vacuum systems limit their range of applicability. Similarly, the water calorimeters developed in this work represent wholly new designs used in unprecedented ways. While the use of water calorimetry for photon, electron and proton dosimetry is not new, we report on the first direct application of water calorimetry to low energy accelerator-based electrons (electron sealed water calorimeter; 6 MeV), and cyclotron-based protons (short-range water calorimeter; 60 MeV).

The initial proposal to develop a probe-format graphite calorimeter was made by my supervisors, Dr. Arman Sarfehnia and Dr. Jan Seuntjens. Similarly, the idea to apply water calorimetry to clinical electrons and short-range charged particle beams was also proposed by Dr. Seuntjens. They are both co-authors on all the manuscripts included in this thesis. My contributions to each body of work is listed below:

1) J Renaud, D Marchington, J Seuntjens, and A Sarfehnia, "Development of a graphite probe calorimeter for absolute clinical dosimetry," *Med. Phys.,* 2013;40(2): Medical Physics Letter, 020701-1, dx.doi.org/10.1118/1.4773870

I performed all the simulations, construction, measurements, and analysis in this work. David Marchington provided technical support and advice during the construction of the first probe calorimeter prototype.

2) J Renaud, A Sarfehnia, J Bancheri, and J Seuntjens, "Aerrow: a probe-format graphite calorimeter for use as a local absorbed dose standard for clinical high-energy photon and electron beams". *Med. Phys.*, 2016 [*Submitted*]

I performed the majority of simulations, and all construction, measurements, and analysis in this work. Julien Bancheri helped by performing the Monte Carlo modelling of the detector's energy dependence.

3) J Renaud, A Sarfehnia, K Marchant, M McEwen, C Ross, and J Seuntjens, "Direct measurement of electron beam quality conversion factors using water calorimetry," *Med. Phys.*, 2015;42(11):6357-6368. dx.doi.org/10.1118/1.4931970

I performed the majority of the simulations, and construction, and all of the measurements and analysis in this work. Dr. Kristin Marchant provided much of the foundation for this work during her PhD (2007), but due to unresolved discrepancies was unable to publish the work. Perturbation factors experimentally determined during her work were used in our analysis.

Dr. Malcolm McEwen and Dr. Carl Ross were involved at the time of Dr. Marchant's work on the project, and were heavily involved in the validation of the water calorimeter.

4) J Renaud, S Rossomme, A Sarfehnia, S Vynckier, H Palmans, A Kacperek, and J Seuntjens, "Development and application of a water calorimeter for the absolute dosimetry of short-range particle beams," *Phys. Med. Biol.*, 2016;61(18):6602-6619. doi:10.1088/0031-9155/61/18/6602

I performed the majority of the measurements and simulations, and all of the construction and analysis in this work. Dr. Séverine Rossomme helped with the finite element heat transfer simulations, and provided support during the experiments. Dr. Stefaan Vynckier and Dr. Hugo Palmans helped in the design of the experiments and interpretation of the results. Dr. Andrzej Kacperek helped support the work by operating the cyclotron and setting up experiments.

Chapter 1

INTRODUCTION

1.1 THE PREVALENCE AND MANAGEMENT OF CANCER

Cancer is currently the leading cause of premature death in Canada. Nearly 200,000 new cases of cancer and an average of 215 deaths per day from cancer were estimated to have occurred in 2015. Excluding non-melanoma skin cancers, lung, colorectal, breast (in women) and prostate (in men) remain the most common cancer types diagnosed, accounting for more than one half (51 %) of all new cases. Roughly 2 in 5 Canadians will develop cancer in their lifetimes and 1 in 4 will die of the disease. Approximately two thirds of Canadians with cancer will survive at least 5 years after their diagnosis.[1]

Improvements in the field of cancer detection and cancer therapy have resulted in significant advancements in diagnosis and treatment of cancer resulting in superior patient care and quality of life after treatment. According to the Canadian Cancer Society, the overall cancer mortality rate has been in steady decline since the mid 90's for both men and women, despite the slightly increasing incidence rate of cancer due to the growth and ageing of the population. A decrease in the mortality rate for a specific cancer can be attributed to either

a decrease in the incidence rate (*i.e.*, lung, oral and larynx due to reduced smoking rates) or an improvement in the survival rate (*i.e.*, earlier detection and the availability of better treatment options).[1]

Currently, there are four prevailing techniques of treating cancer: surgery, chemotherapy, hormonal therapy, and radiation therapy.[2] Surgery strives to resect the tumour, or in some cases, the affected organ in its entirety. In many instances, however, surgery is not possible due to the type, stage, or location of the tumour. Chemotherapy is a category of cancer treatment that uses one or more anti-cancer drugs to attempt to control the disease. Although it can be an effective therapy, chemotherapy drugs often result in some degree of toxicity in the patient due to a lack of cell specificity. Hormonal therapy involves the manipulation of the endocrine system through the administration of specific hormones, particularly steroid, or drugs which inhibit the production of activity of such hormones. The use of this treatment option is limited to a few types of cancers and is only effective for people with hormone receptor-positive tumours. Radiation therapy uses ionizing radiation to control or kill malignant cells through the damaging of the deoxyribonucleic acid (DNA). In North America, about two thirds of all cancer patients receive radiation therapy as part of their treatment (either as the sole mode of treatment or in combination with the other two modalities).[1,2]

Radiation therapy can use either directly ionizing radiation (charged particles including electrons, protons, and heavy ions) or indirectly ionizing radiation (almost exclusively photons) to target the cancer.[2] It can also be delivered either externally, often using high-energy medical linear accelerators, or internally by placing a radioactive source inside the patient in proximity to the tumour. High-energy external beam radiation therapy remains the most commonly used form of radiation treatment in cancer therapy.[2,3]

1.2 EXTERNAL BEAM RADIATION THERAPY

The goal of radiation therapy is to deliver the maximum possible radiation dose (energy per unit mass) to the malignant cancerous cells and to minimize the dose deposited in healthy or otherwise normal tissues. This is done in order to maximize the probability of controlling the tumour while concurrently minimizing the probability of normal tissue complications.[3] To this end, radiation therapy can involve the delivery of one or more beam types of varying energies, directed at the tumour from one or more directions, while potentially being modulated in intensity and/or gated in time. In this section, a few of the different external beam radiation therapy modalities are described.

1.2.1 High-energy photon beam therapy

The vast majority (~75 %) of all cancer patients around the world are treated with high-energy photon beams.[3] The invention of the cobalt-60 teletherapy unit by the Canadian, H.E. Johns, in the early 1950s gave a significant boost to the use of external beam radiotherapy in treatment of cancer. The concurrently-developed medical linear accelerator (linac), however, soon replaced many of the ^{60}Co teletherapy machines, especially in developed countries, and became the most widely used radiation source in modern radiation therapy. Linacs use microwave radiation in the frequency range of 10^3 - 10^4 MHz to accelerate electrons to energies ranging between 4 MeV and 30 MeV. Photons are then produced by directing the accelerated electrons onto a target material. Primarily as a result of Coulomb interactions between incident electrons with the nuclei of the target material, a bremsstrahlung photon spectrum is produced and is emanated towards the patient for treatment. The linac is normally mounted on a gantry (see Figure 1.1) that can rotate isocentrically around the patient and treat the target volume by irradiating it from any number of directions. On its path towards the patient, the photon field may undergo, filtering, flattening and/or collimation.[3]

1.2.2 High-energy electron beam therapy

In about 15 % of all cases, cancer patients are treated with high-energy electrons.[3] The majority of high-energy linacs, in addition to providing one or more photon energies, also provide electron beams with several nominal energies in the range of 6 MeV to 30 MeV. The acceleration mechanism of the high-energy electrons in the accelerating waveguide remains the same as that in the photon mode (albeit in the electron mode, an electron current three orders of magnitude lesser than when operating in photon beam mode is used). To operate in electron beam mode, the linac's target and flattening filter are removed from the beam line, and replaced by a thin high-Z scattering foil. As a result of interaction between the accelerated electron beam and the scattering foil, the electron beam is scattered over a relatively large area (*e.g.*, 25 × 25 cm^2) and is subsequently collimated to the desired field size used for radiation therapy.[3]

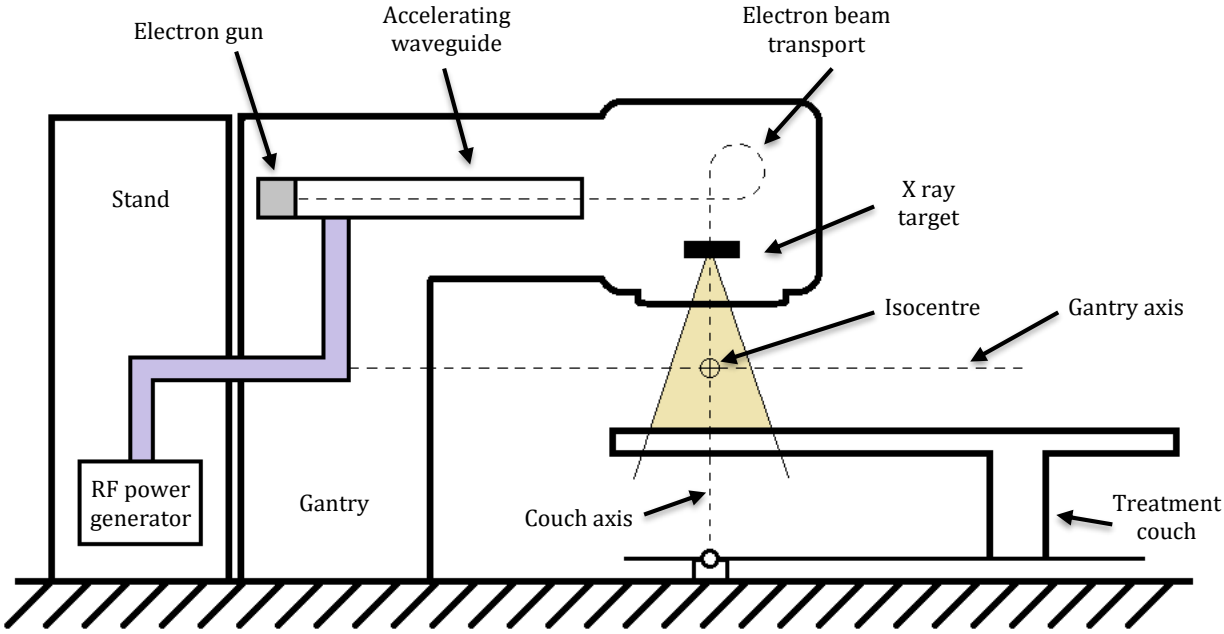

Figure 1.1: Design configuration for an isocentric medical linac.[3] The accelerating waveguide is in the gantry parallel to the isocentre axis. Electrons are brought to the movable target through a beam transport system. The RF power generator is located in the gantry stand. The unit can produce MV X rays as well as electrons.

1.2.3 Proton and heavy-ion beam therapy

Presently, hadron (protons and heavy-ions, collectively) therapy constitutes about 1 % of the total number of patients receiving treatment worldwide. In recent years, however, there has been a significant push to develop and promote this decades-old technology; proton therapy in particular.[4] The primary rationale for using hadrons is their potential to deliver a relatively conformal dose to the target volume at depth within the body while sparing critical structures and organs nearby. Figure 1.2 compares the relative depth dose distribution of various beam types used in radiation therapy. When normalized to 100 % at the depth of maximum dose, the relative depth dose distribution is referred to as percent depth dose (PDD; see *Chapter* 2 for further detail). The proton PDD is characterized by a relatively small dose deposition upon entrance, followed by a very slow rise in deposition with depth, and finally a relatively large deposition of dose in a well-defined and narrow depth range, referred to as the Bragg peak. The depth at which the Bragg peak occurs (referred to as the range of the beam) is strongly related to the incident energy of the proton beam.[3,4]

Since proton therapy is the most commonly used form of hadron therapy, and this work focuses solely on this modality, the discussion in this subsection will be focused on this form of treatment. With that said, much of this discussion applies equally to heavier ions, such as carbon-12. Normally accelerated by a cyclotron or a synchrotron, typical protons energies of up to 250 MeV are used to treat tumours at depth, and as low as 60 MeV for treatment of malignant diseases in the eye (ocular melanoma).[4,5] A mono-energetic proton beam's Bragg peak is normally insufficient to achieve a uniform dose coverage over the extent of the tumour volume, therefore a superposition of many proton beams of slightly varying ranges are delivered to produce a so-called spread-out Bragg peak (SOBP; see Figure 1.2). One method of achieving the tailoring of energies required to produce a SOBP is the passive double scattering technique. In this technique, the accelerated proton beam is scattered

laterally through multiple Coulomb scattering using two scattering foils, and attenuated with a range modulator wheel (also known as a variable degrader). The modulator wheel is a rotating attenuator of gradually varying thickness, which variably modulates the energy, and thus the range of the incident proton beam.[6]

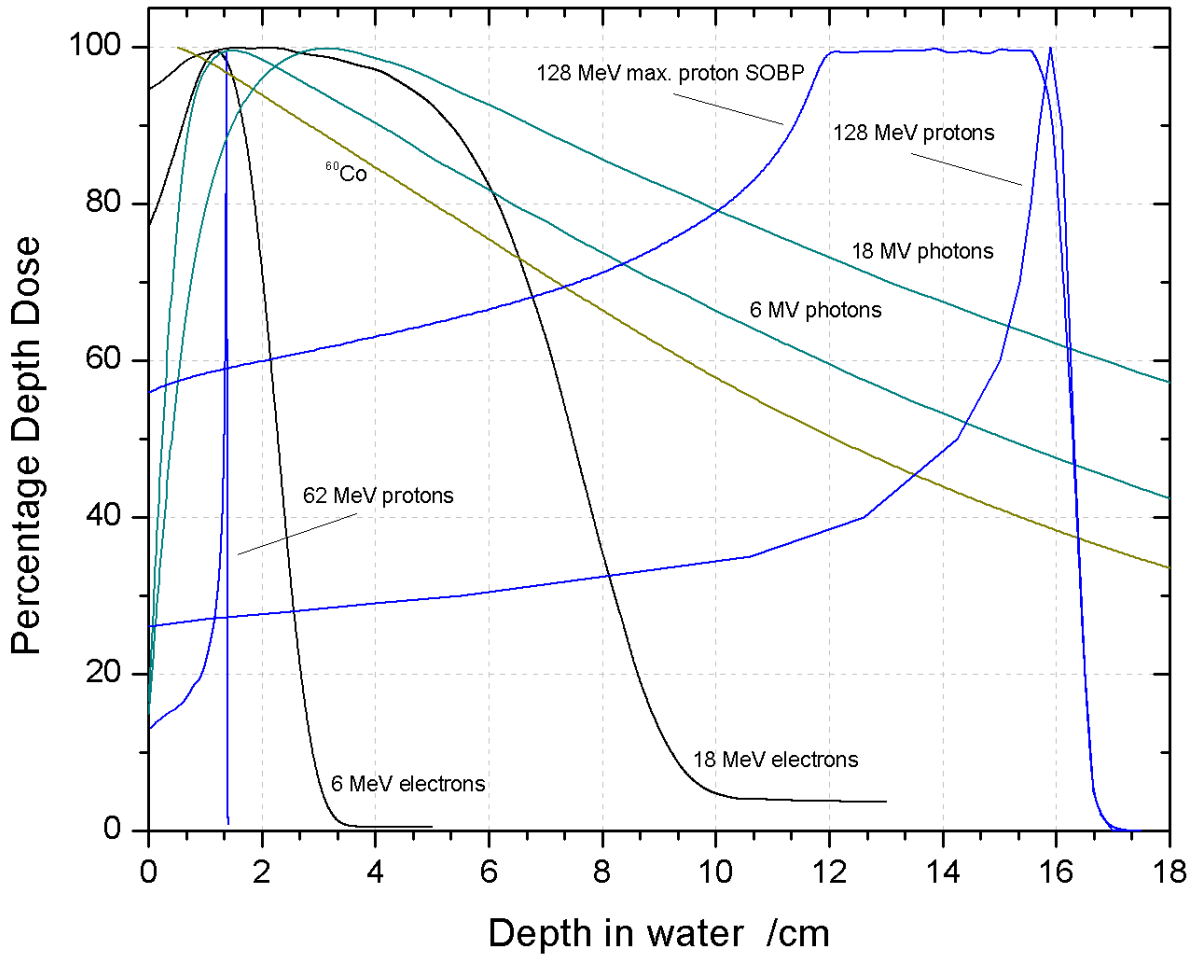

Figure 1.2: A comparison of the percentage depth dose distribution (PDD) curves of electrons, photons, and protons. The data reflects a source to surface distance (SSD) of 100 cm for photons and electrons, and 227 cm for protons. The PDDs shown are typical PDDs used for patient treatment. A proton spread-out Bragg peak (SOBP) obtained through range modulation is also displayed.

1.3 ACCURATE MEDICAL RADIATION DOSIMETRY

The success of any given radiation therapy delivery hinges on the accurate calculation and assessment of the radiation dose received by the patient, a practice known as dosimetry. The International Commission on Radiation Units and Measurements (ICRU) report 24 recommends an overall accuracy of ±5 % on the dose delivered based on a comprehensive analysis of dose response data and clinical outcomes due to errors in dose delivery.[7] Several examples have been reported in which a 7 % change in radiation dose was clinically detectable in terms of patient outcome (*e.g.*, survival or complication rate) and, based on radiation dose response curves for tumours and normal tissues, it is recognized that a 5 % change in dose can result in a 10 – 20 % change in tissue response.[8]

There are four major stages in the radiation therapy process, each one with its own uncertainty that contributes to the total uncertainty on the final dose delivered to the patient.[8]

1. The measurement of absorbed dose to water at a reference point under reference conditions;
2. Relative dose measurements at other depths and non-reference conditions;
3. Dose calculations for treatment planning;
4. Patient setup and beam delivery.

In order to achieve the recommended overall accuracy of 5 %, each stage would ideally contribute no more than 2.5 % uncertainty. Currently, the achievable accuracy of each stage ranges from 2 – 5 %, depending on the case. Research efforts to improve the accuracy of each stage in the radiation therapy process is underway. Through developing more conformal beam delivery techniques and combining these with more sophisticated imaging modalities, the accuracy attributable to patient setup and beam delivery is progressively improving.

Along the same lines, research into more accurate treatment planning algorithms, such as convolution/superposition, collapsed cone, and Monte Carlo show significant promise in reducing the uncertainty associated with the third stage of the radiation therapy process.[8] Improving the accuracy of the second stage relies primarily on the development of improved detector systems with better spatial resolution, ease of use, and less energy dependence. Finally, equivalent improvements to the first stage depend on advances in absorbed dose standards at the national and international levels, as well as on improvements in reference dosimetry protocols at the level of individual clinics. This work attempts to improve the radiation therapy process by reducing the uncertainties associated with the first stage, that is, the measurement of absorbed dose to water under reference conditions.

1.4 THESIS HYPOTHESES

The focus of this work is on the improvement of the accuracy of radiation therapy treatment delivery through improvements to the first stage: the determination of absorbed dose to the target volume (*i.e.*, reference dosimetry). We hypothesize that the development and application of new calorimetry-based instruments for radiation dose measurement will improve the accuracy of absorbed dose determination at the clinical level. In this thesis, three hypotheses are investigated:

1. Medical radiation calorimetry technology can be successfully translated from the primary standards laboratory setting to the radiation therapy clinic through the development of a probe-format graphite calorimeter (GPC; also referred to as Aerrow).

To date, calorimeter designs have primarily been driven by national metrology institutes, whose principle motivation is to achieve the lowest possible measurement uncertainty. Utility and usability of the devices are secondary considerations, and as a result, most calorimeters today are generally both bulky and fragile, and are operated by only handful of individuals possessing the required specialized equipment and tacit knowledge. Since calorimetry is considered the most direct and absolute method of measuring absorbed

radiation, its introduction as a mainstream device into the clinic is potentially significant, as it could play an important role in solving some of the major challenges of contemporary dosimetry (*e.g.*, small and non-standard field dosimetry, dosimetry of MR-guided therapy units, etc.) by providing a direct and absolute measure of absolute dose under almost any conditions. This aim can be achieved through an appropriate redesigning of current graphite calorimeter technology to conform to usability and utility aspects familiar to clinical staff (*i.e.*, small-scale and probe-format).

2. Accurate dosimetry of clinical high-energy electron beams in the range of 6 MeV – 20 MeV can be performed using an electron sealed water calorimeter (ESWcal).

There are currently large uncertainties on the determination of absorbed dose to water under reference conditions for electron beams. There are two reasons for this, the first of which is that most current absorbed dose standards are specifically designed for ^{60}Co or high-energy photon beams. There are calorimeters and ferrous-sulphate (Fricke) systems which determine absorbed dose to water for electron beams, but these systems either require procedures to convert the absorbed dose in the detector medium (graphite or ferrous-sulphate) to absorbed dose to water, or are unable to operate in the lowest electron energies (4 MeV – 6 MeV). In principle, water calorimetry would be the ideal system for measuring absorbed dose to water since no conversion procedure is required, however, the shallow measurement depths and steep dose gradients at lower energies require particular consideration.

The second issue relates to the protocols for clinical reference dosimetry. These currently rely on calibration of ionization chambers in terms of absorbed dose to water in a ^{60}Co beam. In order to determine the absorbed dose in other beams, an absorbed dose beam quality conversion factor is necessary. For photon beams, the factors given for various chamber types have been experimentally verified using water calorimetry. This is not the case for electron beams, and recent measurements and Monte Carlo simulations have indicated that there may be significant discrepancies between values given in protocols and actual values for certain chamber types. A specially-designed water calorimeter could be used to directly

measure these conversion factors in clinical electron beams, thus providing more accurate data for future clinical reference dosimetry protocols.

3. A suitably-designed transportable water calorimeter (SHREWcal) can serve as the basis of an absorbed dose standard for small field clinical high-energy electrons and protons with reference depths in the range of 6 – 20 mm.

Current dosimetry protocols are based on an indirect measurement of the dose using detectors that have been calibrated in a ^{60}Co beam. By using detector-specific, beam quality dependent conversion factors, the ^{60}Co-based detector calibration coefficient is converted from its reference conditions to the new measurement conditions (*e.g.*, in protons). In this work, we attempt to eliminate the need for such conversion factors in proton dosimetry, thereby improving the accuracy of dose measurements through the direct and absolute measurements of absorbed dose to water.

1.5 THESIS OBJECTIVES

There are three main objectives in this work, all of which fall within our aim to improve the accuracy of radiation dose reference measurements.

1. Develop the GPC (a.k.a. Aerrow) system specifically for routine use as a local absorbed dose standard in the radiation therapy clinic. This involves the designing, iterative prototyping, and experimental benchmarking in the clinical environment. Development of the custom thermal control systems and instrumentation needed for signal readout will also be built in-house. Thermal modeling and radiation transport simulations will be needed to optimize the detector design as well as to determine the factors necessary to convert from dose to graphite to dose to water. To confirm the accuracy of the Aerrow system, comparisons will be made in high-energy photon beams against a reference-class ionization chamber with a calibration traceable to the national dose standard. Finally, the use of the Aerrow will be tested in multiple high-energy photon and electron beams, and will also be

characterized in relative terms (linearity, dose rate dependence, energy dependence, angular dependence, and field size dependence).

2. Develop the ESWcal system and use it for absolute determination of absorbed dose in clinical high-energy electron beams. This involves designing and constructing the ESWcal in-house and properly calibrating its components. Moreover, corrections for perturbations caused by non-water materials and conductive heat transfer must be accurately determined for each electron beam energy. To confirm the accuracy of the ESWcal system, comparisons will be made in high-energy photon beams against the current water calorimetry standard that is operated and maintained by the NRC (National Research Council, Ottawa). Finally, the ESWcal will be used to directly measure beam quality conversion factors for ionization chambers in high-energy clinical electron beams

3. Develop the SHREWcal system and establish the feasibility of operating this type of water calorimeter in relatively low-energy clinical electrons and in a low-energy proton beam (both monoenergetic and modulated). This involves designing and constructing the SHREWcal in-house and properly calibrating its components. Moreover, corrections to account for the conductive heat transfer must be accurately determined for each beam type. To evaluate the suitability of the SHREWcal's unique design, the thermal stability, the radiation-induced heat transfer, baseline signal variations, as well as the reproducibility will be studied.

1.6 ORGANIZATION OF THE THESIS

Chapter 2 reviews some of the relevant topics in medical radiation physics and dosimetry, and describes the current techniques and protocols used at the level of the primary dose

standard laboratory. *Chapter* 3 provides an overview of the principles and applications of medical radiation calorimeters. *Chapter* 4 is a thorough detailing of the design, construction and application of the probe-format calorimeter, followed by two published manuscripts (*Chapters* 5 and 6). Similarly, *Chapter* 7 discusses the specifics of the two unique water calorimeters built and tested in-house, while *Chapters* 8 and 9 are the publications resulting from this work. *Chapter* 10 summarizes the work presented in this thesis as well as our plans for future developments.

1.7 REFERENCES

[1]Canadian Cancer Society's Advisory Committee on Cancer Statistics. *Canadian Cancer Statistics 2015.* Toronto, ON: Canadian Cancer Society; 2015.

[2]National Cancer Institute, Radiation Therapy for Cancer: Question and Answers. 2010.

[3]E.B. Podgorsak, "Review of Radiation Oncology Physics: A Handbook for Teachers and Students," in *Chapter 5. Treatment Machines for External Beam Radiotherapy*, ed. E.B. Podgorsak (International Atomic Energy Agency, Vienna 2005).

[4]A.K. Rath, "Particle Radiotherapy: Emerging Technology for Treatment of Cancer," in *Particle Radiotherapy: And Introduction*, ed. A.K. Rath and N. Sahoo (Springer, India 2016).

[5]A.R. Smith, "Proton therapy," Phys. Med. Biol. **51,** R491-R504 (2006).

[6]W.T. Chu, B.A. Ludewigt, and T.R. Renner, "Instrumentation for treatment of cancer using proton and light-ion beams," Rev. Sci. Instrum. **64**, 2055-2122 (1993).

[7]International Commission on Radiation Units and Measurements, *Determination of Absorbed Dose in a Patient Irradiated by Beams of X or Gamma Rays in Radiotherapy Procedures*, (ICRU Report No. 24, 1976).

[8]J. Van Dyke, "*The Modern Technology of Radiation Oncology: A Compendium for Medical Physicists and Radiation Oncologists*," ed. J. Van Dyke (Medical Physics Publishing, Madison, Wisconsin, 1999).

Chapter 2

MEDICAL RADIATION DOSIMETRY

2.1 CONCEPTS AND NOMENCLATURE

This section begins by describing various radiation dosimetry definitions and concepts relevant to this body of work. The discussions will be brief as they are provided for reference purposes only[1].

2.1.1 Nomenclature

1) KERMA, or Kinetic Energy Released per unit MAss, K, is the average energy transferred by uncharged particles to electrons in a volume element without taking into account subsequent interactions of the electrons. Its SI unit is joule per kilogram (J Kg^{-1}), or more commonly, gray (Gy). Kerma is typically subdivided into a collision (K_{col}), and a radiation

(K_{rad}) component. The former is the portion of kerma arising from inelastic collisions with orbital electrons (includes soft and hard collisions resulting in atomic excitations and ionizations), while the latter is the component of kerma arising from inelastic radiation interactions of the ionizing particle with the nucleus[1].

2) MASS ENERGY TRANSFER COEFFICIENT, $\left(\frac{\mu_{\text{tr}}}{\rho}\right)$, is an attenuation coefficient weighed with the average fractional energy transferred by photons traversing the medium to the charged particles (electrons and positrons) of the medium[1]. For a mono-energetic beam, the multiplication of this coefficient by the photon energy fluence, Ψ, yields kerma. Energy fluence is the product of a beam's fluence, Φ, and photon energy, E, $\Psi(E) = \Phi(E) \cdot E$.

3) MASS ENERGY ABSORPTION COEFFICIENT, $\left(\frac{\mu_{\text{en}}}{\rho}\right)$, is proportional to the fraction of energy transferred to the medium that is actually absorbed in the medium[1]. The average fraction of the energy transferred to charged particles of the medium that is lost through radiative processes is represented by a factor referred to as radiation yield, $\bar{g}$; hence, the mass energy absorption coefficient and the mass energy transfer coefficient are related by:

$$\left(\frac{\mu_{\text{en}}}{\rho}\right) = \left(\frac{\mu_{\text{tr}}}{\rho}\right) \cdot (1 - \bar{g}) \tag{2.1}$$

Hence, for a mono-energetic beam, all components of kerma can be expressed by the following three relations:

$$K = K_{\text{col}} + K_{\text{rad}} = \Phi \cdot E \cdot \left(\frac{\mu_{\text{tr}}}{\rho}\right) = \Psi \cdot \left(\frac{\mu_{\text{tr}}}{\rho}\right) \tag{2.2}$$

$$K_{\text{col}} = K \cdot (1 - \bar{g}) = \Phi \cdot E \cdot \left(\frac{\mu_{\text{en}}}{\rho}\right) = \Psi \cdot \left(\frac{\mu_{\text{en}}}{\rho}\right) \tag{2.3}$$

$$K_{\text{rad}} = K \cdot \bar{g} = \Phi \cdot E \cdot \left(\frac{\mu_{\text{tr}}}{\rho}\right) \cdot \bar{g} = \Psi \cdot \left(\frac{\mu_{\text{tr}}}{\rho}\right) \cdot \bar{g} \tag{2.4}$$

4) ABSORBED DOSE, D, is defined as the energy deposited by ionizing radiation per unit mass of a given material. Although energy is transferred to charged particles (kerma), not all of it is absorbed in the medium, as some of it is lost in radiative processes and leaves the medium. Hence, absorbed dose is kerma less the energy transferred away through radiative losses (bremsstrahlung and annihilation in-flight). Absorbed dose is also measured in Gy and is often the quantity of interest in radiation therapy[1].

5) CHARGED PARTICLE EQUILIBRIUM (CPE): As photons travel through the medium, more and more electrons are set into motion, increasing the number of ionizations, while on the other hand, photon attenuation results in a reduction in the total number of photons available for energy transfer. These two opposing effects give rise to a point of equilibrium, where the number of electrons entering a given volume equals the number of electrons leaving it, thus producing a condition referred to as CPE. Past this point, photon attenuation becomes the dominant factor resulting in a gradual decrease in kerma and absorbed dose. Since the absorbed dose at any point beyond the peak is due to the kerma further upstream, the absorbed dose is always greater than the collision kerma at a given depth (Figure 2.1). The region past the depth of maximum dose is referred to as the region of transient CPE (TCPE). Figure 2.1 illustrates the relation between collision kerma and absorbed dose as a function of depth in the medium.[2] The ratio of dose and collision kerma is defined as, β:

$$D = K_{\text{col}} \cdot \beta \tag{2.5}$$

6) PERCENTAGE DEPTH DOSE (PDD), is defined as the ratio, expressed as a percentage, of absorbed dose at any depth, z, to the absorbed dose at a reference depth, z_{ref}, along the central axis of the beam. The reference depth is normally taken as the depth of the maximum dose, z_{max}. It is a function of beam energy, field size on the surface of the phantom, distance between radiation source and the surface of the phantom (SSD), and depth in material, z. Figure 2.1 shows a generic PDD curve for a high-energy photon beam, if the maximum dose was to be normalized to 100 %.

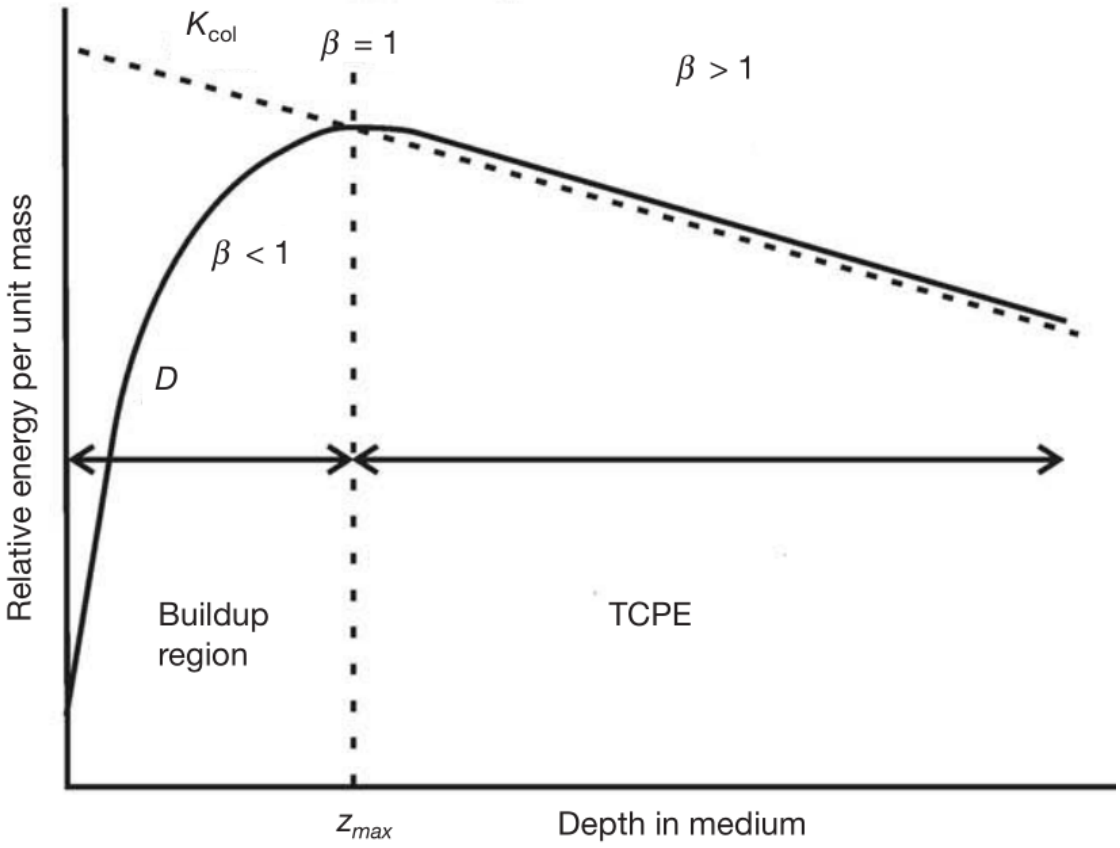

Figure 2.1: Collisional kerma and absorbed dose as a function of depth in a medium irradiated by a high-energy photon beam. If the dose curve was normalized to 100 % at z_{max}, it would then be a PDD curve.[2]

7) TOTAL MASS STOPPING POWER, $\left(\frac{S}{\rho}\right)$, describes the amount of energy loss by a particle per unit length along its track. Its unit is commonly taken to be (MeV cm^2 g^{-1}). Similar to kerma, the total mass stopping power consists of two components: the mass collision stopping power, which results from interactions of the ionizing particles with orbital electrons, and the mass radiative stopping power, which results from inelastic interactions of the ionizing particle with atomic nuclei. In radiation dosimetry, a closely related concept, the restricted stopping power, $\left(\frac{L_\Delta}{\rho}\right)$, is also often used. It is that fraction of collision stopping power that excludes hard collisions resulting in delta rays with energies greater than a defined cut-off value, Δ.

8) LINEAR ENERGY TRANSFER (LET), describes the rate at which a directly ionizing particle deposits energy along its track. LET is indeed equivalent to the restricted stopping power when attention is focused on the absorbing medium and the way energy is actually deposited along the particle's track. Typically expressed in units of (keV μm^{-1}), LET is often used to describe the quality of the radiation.

2.1.2 Cavity theory

In order to measure the absorbed dose in a medium, a radiation detector needs to be placed within the volume of the medium. Generally, the detector and its sensitive volume are not composed of the same material as the surrounding medium. The cavity theory is concerned with the conversion of measured dose in the detector (dosimeter) material into absorbed dose to surrounding medium.

Given a charged particle beam with a spectrum of energies traversing a particular medium, the dose delivered to the medium, D_{med}, can be described by:[2,3]

$$D_{\text{med}} = \int_0^{E_{\max}} \Phi_{\text{med}}(E) \cdot \left(\frac{S_{\text{col}}(E)}{\rho}\right)_{\text{med}} \cdot \mathrm{d}E \qquad (2.6)$$

where, $\Phi_{\text{med}}(E)$ is the particle fluence inside the medium and $\left(\frac{S_{\text{col}}(E)}{\rho}\right)$ is the unrestricted mass collisional stopping power of the particles in the medium, as previously defined in *Section 2.1.1*. The dose to the medium, as described in Eq. 2.6, is simply the sum of the deposited dose for every energy interval dE in the full range of electron energies up to the maximum electron energy, $E_{\max}$.

1) BRAGG-GRAY CAVITY THEORY: Many of the applications in radiotherapy involve the use of a detector whose sensitive volume is small relative to the range of the electrons that have been set in motion and are traversing the medium. In such cases, if it can be assumed that, to

first order, the detector only 'senses' the electrons without perturbing the charged particle fluence (both number and energy fluence), then the Bragg-Gray cavity theory can be applied.[3,4] Generally, a second assumption is made, which states that the dose in the detector material should come solely from the charged particles crossing the cavity. In such cases, given the primary charged particle's fluence map, $\Phi_{\text{med}}^{\text{prim}}(E)$ (which, according to Bragg-Gray cavity theory, is equivalent to the fluence in the detector's cavity), the dose to the detector material, D_{det}, can be converted to dose to the medium, D_{med}, by using Eq. 2.6 (where, $X_{\text{det}}^{\text{med}}$ is a shorthand notation for $\frac{X_{\text{med}}}{X_{\text{det}}}$).

$$\frac{D_{\text{med}}}{D_{\text{det}}} = \frac{\int_0^{E_{\max}} \Phi_{\text{med}}^{\text{prim}}(E) \cdot \left(\frac{S_{\text{col}}(E)}{\rho}\right)_{\text{med}} \cdot \mathrm{d}E}{\int_0^{E_{\max}} \Phi_{\text{det}}^{\text{prim}}(E) \cdot \left(\frac{S_{\text{col}}(E)}{\rho}\right)_{\text{det}} \cdot \mathrm{d}E} = \left(\frac{S_{\text{col}}(E)}{\rho}\right)_{det}^{med} \tag{2.7}$$

2) SPENCER-ATTIX CAVITY THEORY: The application of Eq. 2.7 and its accuracy in radiation therapy are limited. In reality, the primary radiation beam will continuously interact, both inside and outside the finite volume of the detector cavity), and the electrons produced inside the cavity may indeed lose a fraction of their energy as they leave the cavity. For the assumption of an unperturbed fluence to hold true, the electron spectra entering and leaving the cavity must be the same. This can only be true if either the secondary electrons produced by hard collisions (δ rays) are absorbed on the spot (Bragg-Gray's assumption) or that both the detector and its surrounding environment are composed on the same material.[5]

Spencer and Attix approached the problem without restricting themselves to zero-range δ rays. They accounted for the full slowing down spectrum and allowed for the higher generation electrons (secondary, tertiary, etc.) to travel a given distance. Spencer and Attix did not differentiate the various generations of electrons, and instead looked at the collective spectrum of all electrons set in motion.[5]

They divided the full spectrum of electrons into two categories based on their energies using an energy threshold parameter, Δ, which is calculated based on the size of the cavity. This threshold is taken to be the minimum energy of the electrons required to cross the length of the cavity. This approach assumes that all electrons with $E > \Delta$ cross the cavity, and as such, a state of CPE for these particles is assumed to exist. In this sense, the dose deposited in the medium, D_{med}, given a complete electron fluence spectrum (containing all electron generations), $\Phi_{\text{med}}^{\text{tot}}(E)$ can be calculated by:

$$D_{\text{med}} = \int_{\Delta}^{E_{\max}} \Phi_{\text{med}}^{\text{tot}}(E) \cdot \left(\frac{L_{\Delta}(E)}{\rho}\right)_{\text{det}} \cdot \mathrm{d}E \tag{2.8}$$

where, $\left(\frac{L_{\Delta}(E)}{\rho}\right)_{\text{det}}$ is the restricted stopping power, as defined in *Section 2.1.1*. Hence, to first order, Spencer and Attix only considered electrons with $E > \Delta$, while only the fraction of collisional stopping power resulting in energy losses less than Δ are taken into account.

If Eq. 2.8 was to be used on its own, all δ rays with energies below the threshold would be neglected. Although they deposit their energies locally, these low energy electrons may be produced inside the cavity as well, which means that Eq. 2.8 provides an underestimation of the absorbed dose. Nahum proposed an additional term accounting precisely for this 'end track' effect, which is given by:[6]

$$\Phi_{\text{med}}^{\text{tot}}(\Delta) \cdot \left(\frac{S_{\text{col}}(\Delta)}{\rho}\right)_{\text{det}} \cdot \Delta \tag{2.9}$$

He argued that the product of the total electron fluence at energy Δ and collisional stopping power calculated at Δ, approximated the number of electrons slowing down past Δ, which when multiplied by energy Δ, gives the total energy due to the track lengths. Thus, the full Spencer-Attix-Nahum cavity theory can be expressed as (combining Eq. 2.8 and 2.9):[3]

$$\frac{D_{\mathrm{med}}}{D_{\mathrm{det}}} = \frac{\int_{\Delta}^{E_{\max}} \Phi_{\mathrm{med}}^{\mathrm{tot}}(E) \cdot \left(\frac{L_{\Delta}(E)}{\rho}\right)_{\mathrm{med}} \cdot \mathrm{d}E + \Phi_{\mathrm{med}}^{\mathrm{tot}}(\Delta) \cdot \left(\frac{S_{\mathrm{col}}(\Delta)}{\rho}\right)_{\mathrm{med}} \cdot \Delta}{\int_{\Delta}^{E_{\max}} \Phi_{\mathrm{med}}^{\mathrm{tot}}(E) \cdot \left(\frac{L_{\Delta}(E)}{\rho}\right)_{\mathrm{det}} \cdot \mathrm{d}E + \Phi_{\mathrm{med}}^{\mathrm{tot}}(\Delta) \cdot \left(\frac{S_{\mathrm{col}}(\Delta)}{\rho}\right)_{\mathrm{det}} \cdot \Delta} = \left(\frac{\bar{L}_{\Delta}(E)}{\rho}\right)_{det}^{med} \quad (2.10)$$

The cavity theory as described for electrons, either by themselves or from photon beams, is also valid for any type of primary charged particles traversing the medium. Hence, similar formulations to the one presented above can be used for primary proton beams, provided the assumptions of the cavity theory hold true for the specific situation.[7]

2.1.3 Ionization chamber dosimetry

An ionization chamber is a type of gas-filled radiation detector and is one of the most widely used dosimeters used in radiation therapy. At its most basic, an ionization chamber consists of a gas-filled walled chamber (*i.e.*, cavity) and two electrodes. The cavity theory obtained above shall be applied to two special cases of ionization chamber cavities, and the procedures used to obtain the dose to medium will be explained[2].

1) THICK-WALLED CHAMBERS: As the name implies, a thick-walled chamber is one in which the wall is sufficiently thick to act as a medium for the air cavity of the ionization chamber (*i.e.*, all charged particles that pass through the cavity and contribute to the total signal are initiated inside the chamber wall).

Under conditions of CPE (or TCPE), Eq. 2.5 related dose to kerma. Furthermore, Eq. 2.3 described the relation between collisional kerma and the photon energy fluence. Combining these two relations, and generalizing Eq. 2.3 to take into account a spectrum of energies, the dose to medium can be obtained by:[2]

$$D_{med} = \beta \cdot (K_{\mathrm{col}})_{med} = \beta \cdot \int_0^{E_{\max}} \Psi(E) \cdot \left(\frac{\mu_{\mathrm{en}}(E)}{\rho}\right)_{\mathrm{med}} \cdot \mathrm{d}E$$
$$= \beta \cdot \Psi \cdot \left(\frac{\bar{\mu}_{\mathrm{en}}}{\rho}\right)_{\mathrm{med}} \tag{2.11}$$

where, $\left(\frac{\bar{\mu}_{\mathrm{en}}}{\rho}\right)_{\mathrm{med}}$ is defined as:

$$\left(\frac{\bar{\mu}_{\mathrm{en}}}{\rho}\right)_{\mathrm{med}} = \frac{\int_0^{E_{\max}} \Psi(E) \cdot \left(\frac{\mu_{\mathrm{en}}(E)}{\rho}\right)_{\mathrm{med}} \cdot \mathrm{d}E}{\int_0^{E_{\max}} \Psi(E) \cdot \mathrm{d}E} = \frac{(K_{\mathrm{col}})_{med}}{\Psi} \tag{2.12}$$

Ignoring the cavity altogether and taking the wall of the chamber to be a large photon detector, the dose contribution in the centre of the detector is dominated by the electrons produced by photons interacting within the detector. Hence, the ratio of the dose at the centre of the detector can be related to the dose at the same point in an otherwise uniform medium by taking the ratio of two collisional kermas. Using Eq. 2.11:

$$D_{\mathrm{med}}^{\mathrm{det}} = (K_{\mathrm{col}})_{\mathrm{med}}^{\mathrm{det}} = \left(\frac{\bar{\mu}_{\mathrm{en}}}{\rho}\right)_{\mathrm{med}}^{\mathrm{det}} \tag{2.13}$$

Eq. 2.13 assumes that the detector provides sufficient buildup without disturbing the photon energy fluence. The ratio of the total energy fluences is thus taken to be unity (*i.e.*, $\Psi_{m_2}^{m_1} = 1$). Moreover, it is assumed that the range of electrons is similar in both materials, resulting in a factor β that is constant. For not too dissimilar materials, both assumptions are valid.

From Eq. 2.13, the dose to the medium, D_{med}, as measured using a thick-walled ionization chamber can be related to the dose to the chamber wall, D_{wall}, by:[2]

$$D_{\mathrm{med}} = D_{\mathrm{wall}} \cdot \left(\frac{\bar{\mu}_{\mathrm{en}}}{\rho}\right)_{\mathrm{wall}}^{\mathrm{med}} \tag{2.14}$$

Since the wall is assumed to be thick enough to act as the medium for the air cavity of the ionization chamber, one can argue that the dose measured inside the chamber's gas cavity, D_{gas}, is related to D_{wall} through Eq. 2.10, hence:

$$D_{\text{wall}} = D_{\text{gas}} \cdot \left(\frac{\bar{L}_{\Delta}}{\rho}\right)_{\text{gas}}^{\text{wall}} \tag{2.15}$$

As a final note, an ionization chamber does not directly measure dose, but rather as the name implies, it measures ionization (or ion pairs). Although the material filling the chamber cavity has been generally referred to as 'gas', the material is almost exclusively air in commonly used ionization chambers. The dose to the detector is calculated through $\left(\frac{\bar{W}_{\text{air}}}{e}\right)$, the energy required to produce an ion pair in air. Hence, a very good approximation for the total dose deposited in the medium as measured by a thick-walled ionization chamber is given by:[2]

$$D_{\text{med}} = \left(\frac{Q_{\text{air}}}{m_{\text{air}}}\right) \cdot \left(\frac{\bar{W}_{\text{air}}}{e}\right) \cdot \left(\frac{\bar{L}_{\Delta}}{\rho}\right)_{\text{air}}^{\text{wall}} \cdot \left(\frac{\bar{\mu}_{\text{en}}}{\rho}\right)_{\text{wall}}^{\text{med}} \tag{2.16}$$

where $\left(\frac{Q_{\text{air}}}{m_{\text{air}}}\right)$ is the charge per unit mass measured inside the air cavity of the chamber. The product of $\left(\frac{Q_{\text{air}}}{m_{\text{air}}}\right) \cdot \left(\frac{\bar{W}_{\text{air}}}{e}\right)$ is equivalent to the dose to the air cavity, D_{air}.

2) THIN-WALLED CHAMBERS: A much more realistic scenario in the radiotherapy clinic is one in which an ionization chamber with a thin wall is used to measure dose in water (or water-equivalent plastic, for convenience). In this case, the thin wall does not act as the medium for the cavity, and its presence is accounted for through a correction.[2] Applying Spencer-Attix cavity theory (Eq. 2.10) yields:[2]

$$D_{\text{med}} = \left(\frac{Q_{\text{air}}}{m_{\text{air}}}\right) \cdot \left(\frac{\bar{W}_{\text{air}}}{e}\right) \cdot \left(\frac{\bar{L}_{\Delta}}{\rho}\right)_{\text{gas}}^{\text{med}} \cdot \prod_{i} P_i \tag{2.17}$$

where $\prod_i P_i$ is the product of the correction factors accounting for various perturbative effects, including but not limited to those due to the presence of the chamber wall, central electrode (if applicable), and the electron fluence perturbation.

2.2 OVERVIEW OF RADIATION DETECTORS AND MEASUREMENTS

In this section, detector-related terminology such as *response* are introduced, along with definitions of the frequently-employed terms *absolute*, *reference* and *relative* dosimetry. A brief overview of detectors employed as dosimeters in radiation therapy is also provided with emphasis on their strengths and limitations.

2.2.1 Detector response and calibration coefficient

Consider the situation in which a detector, 'det', is placed in a medium, 'med', irradiated by a beam of ionizing radiation of quality, Q. The generic quantity to be determined, usually air kerma or absorbed dose to the medium, is denoted by $\varsigma_{\mathrm{med},Q}(z)$, at a position, z, in the medium. The signal from a readout device associated with the detector as a result of a given radiation exposure will be denoted by $M_{\mathrm{det},Q}$. The detector response (sometimes referred to as the sensitivity), $R_{\varsigma,\mathrm{det},Q}$, is defined as:[8]

$$R_{\varsigma,\mathrm{det},Q} = \frac{M_{\mathrm{det},Q}}{\varsigma_{\mathrm{det},Q}} \tag{2.18}$$

and the detector calibration coefficient, $N_{\varsigma,\mathrm{det},Q}$, a key parameter normally determined at primary standards dosimetry laboratories (PSDLs), becomes:

$$N_{\varsigma,\mathrm{det},Q} = \frac{1}{R_{\varsigma,\mathrm{det},Q}} = \frac{\varsigma_{\mathrm{det},Q}}{M_{\mathrm{det},Q}} \tag{2.19}$$

The final dosimetry step is to relate $\varsigma_{\mathrm{det},Q}$ to the desired quantity in the medium, $\varsigma_{\mathrm{med},Q}(z)$ at the specified point, z, in the absence of the detector. This can be expressed generally as:

$$\varsigma_{\mathrm{med},Q}(z) = \varsigma_{\mathrm{det},Q} \cdot f_{\mathrm{med,det},Q}^{\varsigma_{\mathrm{det}} \to \varsigma_{\mathrm{med}}} \tag{2.20}$$

where the subscripts of the factor $f_{\mathrm{med,det},Q}^{\varsigma_{\mathrm{det}} \to \varsigma_{\mathrm{med}}}$ emphasize its dependence upon the medium, the detector, as well as the radiation quality. The superscript indicates that in this case the conversion is between the quantity of interest in the detector and the corresponding

quantity in the medium. The conversion of dose to a detector to dose to the medium is subject to cavity theory, as detailed in *Section 2.1.2*.

2.2.2 Absolute, reference, and relative dosimetry

Traditionally, in the clinical environment, the term 'absolute dosimetry' has been used for measurements made under certain defined conditions with a calibrated ionization chamber. The rationale is that the dosimeter yields a reading in terms of a physical quantity per unit of the signal reading (*e.g.*, cGy nC^{-1}). Measurements under other conditions for which the calibration coefficient is not applicable are related to the physical quantity determined above by using relevant ratios and/or appropriate corrections; hence, these are relative measurements. When considering the various steps in the dosimetry chain (*i.e.*, from the PSDL to the end user), it becomes clear that 'clinical absolute dosimetry' is not absolute in any true sense, but rather is related to the determination of the quantity in absolute terms through the detector calibration coefficient.[8]

1) ABSOLUTE DOSIMETRY: The dose is determined from fundamental principles consistent with the definition of the quantity and realized with a primary dose measurement standard (*i.e.*, ionometry, absorbed-dose calorimeters, or Fricke chemical dosimeters). Primary radiation dose standards are described in *Section 2.3*.

2) REFERENCE DOSIMETRY: The dose is determined at the user's facility using a detector, typically an ionization chamber, with a calibration coefficient traceable to a primary standard and following an accepted measurement dosimetry protocol (*e.g.*, AAPM TG-51)[23]. The calibration is only applicable under well-established reference measurement conditions matching those used to establish it at the laboratory. In such a case, the user's dosimeter is

considered a 'reference detector'. Reference dosimetry for external beam radiation therapy is covered in *Section 2.4*.

3) RELATIVE DOSIMETRY: When measurements in the user's beam are made under non-reference conditions (*i.e.,* different from those for which the calibration coefficient is strictly applicable), the dose is determined using relevant ratios and/or appropriate corrections.

2.2.3 General characteristics and desirable properties of detectors

Any device which can be used to measure a quantity, or the rate of a quantity, related to absorbed dose, such as kerma, exposure (related to the ability of radiation to ionize air), or even temperature, can be classified as a radiation dosimeter. A dosimeter must have some physical property that is dependent upon the dosimetric quantity to be measured, which when properly calibrated, can be directly related to a corresponding dose.[9]

There are several characteristics of dosimeters to consider when evaluating the suitability of employing a detector to measure dose under a particular set of experimental conditions. These include the linearity of the device, the dose-rate dependence, energy response, directional dependence, spatial resolution, as well as environmental (*i.e.*, temperature, *T*, pressure, *P*, and humidity, *H*) dependencies. No single radiation dosimeter is perfectly suited for all situations, and in fact, in many cases multiple dosimeters can be used as independent verifications of one another. For instance, an ionization chamber is recommended for accurate dose-at-a-point measurements in clinical reference dosimetry of linacs, while for IMRT patient plan quality assurance film dosimetry recommended for evaluation of the relative 2D dose distribution.

A dosimeter's characteristics are based on physical effects which are not necessarily mutually independent, although they are often assumed to be while under evaluation.[9,10] While functional behavior of a dosimeter is usually the main focus of study, utility (*i.e.*, applicability or appropriateness) and usability (*i.e.*, ease-of-use) are also require careful consideration if the detector is to be utilized in any practical way.

1) REPRODUCIBILITY: Also referred to as the *precision* of dosimeter measurements, this concept concerns random errors due to fluctuations in instrument characteristics, ambient conditions, etc., as well as the stochastic nature of radiation fields. The degree of reproducibility can be estimated from the data obtained in repeated measurements, and is usually stated in terms of the sample standard deviation.[9,10] Measurements may be highly reproducible but inaccurate, or vice versa, or may possess both or neither of these attributes.

2) LINEARITY: The relation between the reading of a dosimeter and the dosimetric quantity measured is ideally linearly proportional, ($M_{\mathrm{det},Q} \propto \overline{D}_{\mathrm{det},Q}$) (*i.e.*, if the dose is tripled in the detector, the reading should also triple). Often, a non-linear behavior arises when a sufficiently large dose causes the dosimeter signal to either exhibit a supra-linear behavior, or more commonly, saturation. A linear response is desirable for ease of calibration and interpretation.[9,10]

3) DOSE RANGE: To be useful, a dosimeter must have adequate sensitivity $\left(\frac{\mathrm{d}M_{\mathrm{det},Q}}{\mathrm{d}\overline{D}_{\mathrm{det},Q}}\right)$ throughout the applicable dose range to enable reproducible measurements to be made. The lower limit of the useful dose range may be determined by the instrumental background, or zero-dose reading (*i.e.*, $M_{\mathrm{det},Q}(D_{\mathrm{det},Q} = 0)$). As a rule of thumb, the lower limit of the practical dose range of a dosimeter is usually estimated to be the dose necessary to double the instrumental background reading. The upper limit of the useful dose range may be due to

external instrumental limitations (*e.g.*, dynamic range), or in some cases can be attributed to competing reactions by radiation products, radiation damage to the dosimeter, or exhaustion of the supply of solid-state entities ('traps') being acted upon.[9,10]

4) DOSE-RATE DEPENDENCE: If a dosimeter is to be used for measuring the time-integrated dose (as opposed to the dose-rate), then the reading should not depend on the rate at which the dose is delivered, at least within the range of dose-rates encountered. In dose-rate measuring dosimeters, it is desirable that the reading be proportional to the dose-rate ($M_{\mathrm{det},Q} \propto \dot{D}_{\mathrm{det},Q}$), or at least be a single-valued function of it.[9,10]

5) STABILITY: The characteristics of a dosimeter should be stable with time until it is used, including 'shelf-life' and time spent *in situ* until irradiated (*e.g.*, worn by personnel for health and safety monitoring). After irradiation, the latent reading in some types of integrating dosimeters may be unstable to some extent, suffering 'fading' losses during the time interval between irradiation and readout.[9,10]

6) ENERGY DEPENDENCE: The quality (spectral distribution) of a beam will have one of the more important effects on the response of a dosimeter. Since dosimeters are normally calibrated in a reference beam quality, Q_0, a correction factor, $k_{Q_0,Q}$, accounting for this effect must be applied when measurements are made in any other beam quality, Q, under otherwise reference conditions. This correction is of particular importance since the conversion process from dose to the detector material to dose to water is, in general, energy-dependent. Overall energy dependence is broken into two components: Intrinsic energy dependence and the absorbed dose energy dependence of the detector. The former relates the detector reading to the dose to the detector ($M_{\mathrm{det},Q} \rightarrow D_{\mathrm{det},Q}$), and is ideally constant as a function of energy, while the latter relates dose to the medium of interest to the dose to the detector ($D_{\mathrm{det},Q} \rightarrow D_{\mathrm{med},Q}$).[10]

7) ENVIRONMENTAL DEPENDENCIES: Temperature, pressure, and humidity are environmental conditions which can affect the reading of some dosimeters (*e.g.*, affecting the stability of chemical dosimeters, or affecting the mass of air within an ionization chamber cavity). These effects are often accounted for by correcting the obtained reading to a set of reference conditions (T_0, P_0, H_0) such as standard ambient temperature and pressure (SATP) and 0 % relative humidity.[9,10]

8) DIRECTIONAL DEPENDENCE: Often due to physical features in the construction of a dosimeter, response can exhibit a directional (or orientation) dependence with respect to the direction of the incident radiation field. Many detectors, including cylindrical ionization chambers, are generally axially symmetric and have no dependence upon the azimuthal angle, φ, as defined in a spherical coordinate system. Other types of dosimeters possess a strong directional dependence and may not be suitable for use in all orientations.[,10]

9) SPATIAL RESOLUTION AND SIZE EFFECTS: In terms of physical size, the dimensions of a dosimeter's sensitive volume largely determine the spatial resolution of that device. For absolute and reference dosimetry, the measurement of absorbed dose-at-a-point is ideally sought; however, this can only ever be approximated. For detectors with a finite sensitive region, volume averaging effects are present, whereas for film or gel dosimeters, the readout systems limit the achievable spatial resolution. The ability of a dosimeter to spatially resolve small dose differences is especially crucial when the field size is small (<2 cm in radiation therapy) or when a measurement is being made in a relatively high dose gradient region.[9,10]

10) GENERAL CONVENIENCE: A rugged dosimeter with a long lifespan, with little to no changes in sensitivity over time, which produces an instant reading is generally more desirable to work with, especially in the demanding clinical environment, than a fragile,

batch-dependent (*e.g.*, film, gel dosimeters, etc.), non-reusable dosimeter that has to be processed before being readout.[9,10]

2.2.4 Brief description of common dosimeters in radiation therapy

Several types of detectors can be used for absolute, for reference and for relative dosimetry; a few types are common for all kinds of measurements, although their design varies depending on the application. They can be classified into one of four major groups: calorimeters (graphite and water), ionization chambers (gas-filled and liquid), chemical detectors (Fricke, alanine, film, and gel), or solid state detectors (TLD, OSLD, scintillator, diode, diamond, and MOSFET).

1) CALORIMETERS: Calorimeters determine the energy imparted to a medium through the measurement of the radiation-induced temperature rise. Because of its relatively direct determination of energy deposition, calorimetry has the potential to provide a more accurate determination of absorbed dose. Water and graphite calorimetry are methods of choice for PSDLs (see *Chapter 3*). Measurements yield a signal on the order of mK per Gy, and their reproducibility can pose a disadvantage. The heat defect, (*i.e.*, the fraction of energy deposited that is not liberated as heat) requires special consideration in water calorimeters, whereas the conversion of dose in graphite to dose in water is the main constraint of graphite calorimeters.[11]

2) GAS-FILLED IONIZATION CHAMBERS: Ionization chambers come in several different shapes and forms, but at their very basic they all consist of a gas-filled cavity, the sensitive volume, an encapsulating polarizing electrode, and a central collecting electrode. A high voltage power supply is used to create an electric potential across the cavity between the electrodes. When placed in an ionizing radiation field, anions and cations created in the

cavity are attracted to their respective oppositely-charged electrode, and are collected and measured by an attached electrometer. The two most common types of ionization chambers used in clinics are the cylindrical thimble chamber and the flat parallel plate chamber, though other variants exist (spherical, pencil-like, free-air, thick-walled, well-type, etc.). Their main advantage is their reproducibility, which is however dependent upon their volume. As for limitations, their response is dependent upon atmospheric conditions, as well as the need for a correction for ion recombination effects.[12]

3) LIQUID IONIZATION CHAMBERS: These chambers are filled with a dielectric liquid (*e.g.*, isooctane, tetramethylsilane, etc.).[8] Because of the higher density of liquid, the chamber signal per unit volume of the liquid is greater than that of a gas-filled ionization chamber. In addition, the close equivalence of the liquid to water minimizes the chamber perturbation effects. Their response is dose–rate dependent because of substantial ion recombination, they also lack stability, and their response is significantly temperature-dependent.

4) FERROUS SULPHATE (FRICKE) DOSIMETERS: The ferrous sulphate (Fricke) dosimeter is the most widely used and longest established chemical dosimetry system. Its use as a primary radiation standard is described in *Section 2.3.3*. Its use requires the knowledge of the *G*-value, a factor that relates the production of a Fe^{3+} to the energy absorbed. The variation of $G(Fe^{3+})$ with beam quality is small for high-energy photon beams. With care, Fricke dosimetry is capable of a 0.1% reproducibility. On the other hand, its low sensitivity requires a very high dose, and extreme care must be taken to ensure the purity of chemical solutions, not to mention a costly readout device (spectrophotometer).[8]

5) ALANINE: These pellet-format chemical dosimeters have a density and macroscopic interaction coefficients that are close to those of water. They can be made to be quite small, and are generally quite stable. A major restriction of alanine is its low sensitivity,

environmental dependences, and prohibitively expensive readout system (electron paramagnetic resonance spectrometer).[8]

6) RADIOGRAPHIC AND RADIOCHROMIC FILM: Radiographic film is composed of a thin transparent plastic film base coated on both sides with an emulsion of silver bromide crystals. Upon exposure to ionizing radiation or visible light, chemical reactions occur within the crystals. The effect of developing a film is transparency in unexposed areas, and darkening in exposed areas. The amount of silver deposited in a particular region affects the degree of film opacification, which is related to the amount of dose absorbed locally through the use of calibration curves.[8]

Radiochromic is a more recent type of film dosimeter of near tissue-equivalent composition, consisting of a radiation-sensitive dye and clear plastic outer layers. Upon exposure to ionizing radiation, the dye polymerizes, which has the effect of increasing the opaqueness of the film, since the polymers absorb visible light. Film calibration and analysis is similar to that of radiochromic film, except that no chemical developing is required. Additionally, since radiochromic film is relatively insensitive to visible light, the expense of having a darkroom is eliminated.

The advantage of using films is that they provide a high resolution 2D measurement of relative dose independent of dose-rate, and in the case of radiochromic film, a relatively linear dose response. Energy dependence is however, pronounced at low energies. Off-line analysis can be time consuming with complex evaluation protocols and inter-batch variability can also necessitate separate calibration for each new set of films used. Uncertainties also arise from the film readout technique: Most notably, densitometers and scanners can exhibit non-linear response to film opaqueness and a non-uniform sensitivity over the analyzed region of interest, respectively.[13]

7) GEL DOSIMETERS: Gel dosimeters, either Fricke or polymer-based, quantify the effects of radiation-induced chemical changes in a material.[8] The preparation of 3D gel dosimeters is a laborious and sensitive process; several readout techniques are used (magnetic resonance relaxometry, CT x-ray imaging). Gel dosimeter response is reasonably energy independent in the megavoltage region, but shows a marked energy dependence in the keV region. This type of dosimeter fails to respond in a predictable manner in heavy-charged particle beams due to their higher LET.

8) THERMOLUMINESCENT DOSIMETERS (TLDs): TLDs are usually composed of doped lithium fluoride or lithium borate, and can be in the form of powders, chips or rods, among others.[8] Upon irradiation, a TLD stores a fraction of the energy absorbed by the crystal, and hence related to the absorbed dose. Impurities act as traps or recombination centres and permit the thermoluminescence process. A read out is obtained by heating the TLD, capturing the thermoluminescence photon fluence using a photo-multiplier tube to produce a proportional electrical signal, and measuring the electric charge of the produced signal using an electrometer. Through proper calibration, the area under the appropriate portion of the glow (emission vs. time) curve can be related to an absorbed dose. Due to their potentially small size, TLDs can have high spatial resolution. Their disadvantages, aside from the need for off-line evaluation, are their non-linear energy (especially at low energies) and dose responses (exhibits supralinear behavior followed by saturation with increasing dose).

9) OPTICALLY-STIMULATED LUMINESCENCE DOSIMETERS (OSLDs): OSLDs operate in much the same way as do TLDs, except that laser light, rather than heat, is used to trigger the release of trapped electrons. For this, an aluminum oxide chip doped with carbon is coupled to an optical fiber, which carries luminescent photons to a photo-multiplier tube. While OSLDs exhibit an angular dependence, their advantages over TLDs are their relative linear dose response and energy independence.[8]

10) PLASTIC AND ORGANIC SCINTILLATORS: Scintillators are materials which produce luminescence with a certain characteristic spectrum as a result of the absorption of energy from ionizing radiation. A scintillator dosimetry system is usually composed of plastic scintillators, photo-multiplier tubes (or a charge-coupled device camera) and optical fiber waveguides. The plastics used have an electron density and composition very similar to water, making them nearly energy independent. They can be made very small and yet provide adequate sensitivity. The main complication in their use is the correction for the Čerenkov light generated in the optical fiber. The signal-to-noise ratio of plastic scintillators is generally low and their response degrades with accumulated dose.[14]

11) SILICON DIODES: The radiation-sensitive structure in the silicon diode is a p-n junction. During irradiation, electron-hole pairs are created in the diode; these charge carriers are swept across the junction by the natural built-in potential.[8] The radiation-induced current is proportional to the radiation dose rate, which is measured by an electrometer. They have a very small sensitive volume, but often show angular dependence due to their design, as well as some dependence on temperature. In order to compensate for their over-response to low energy photons, diodes can be energy-compensated using a high density shielding material. Diodes also have a limited lifetime and their sensitivity depends on the dose accumulated.

12) DIAMOND DETECTORS: Natural diamond crystals are inherently semiconductors; they contain impurities making them p- or n-type devices. Diamond detectors have a high sensitivity, which is almost independent of energy and show no orientation dependence. Their absorbed dose rate dependence is significant and must be corrected for, and they require a substantial pre-irradiation dose. Natural diamond detectors are no longer commercially available and have been replaced by artificial chemical vapour deposition (CVD) diamonds, which are used without bias voltage. These have proven to be highly

suitable for radiotherapy measurements, although under certain conditions correction factors are required due to the large density difference relative to that of water.[15]

13) METAL-OXIDE SEMICONDUCTORS FIELD-EFFECT TRANSISTOR (MOSFET): MOSFETs consist of transistors operating at different threshold voltages. The effect of ionizing radiation is to generate charges within the oxide, where they remain trapped. In turn, this causes a linearly proportional change in the threshold voltage. By measuring the difference in the threshold voltages for two transistors, either during or after irradiation, it is possible to recover the relative absorbed dose. Like silicon diodes, MOSFETs are very small, affording them excellent spatial resolution. They do also exhibit a temperature and significant angular dependence. Moreover, their linear response with dose is limited to specified lifespan.[16]

2.3 PRIMARY RADIATION STANDARDS

Human tissue is mostly composed of water, as such, absorbed dose to water has become the quantity of interest in radiotherapy. As a result, dose conversion coefficients are normally used to convert dose in the detector medium into dose to water. At present, three types of dosimetry systems are employed by PSDLs as primary dose standards: ionization chambers, calorimeters, and Fricke dosimeters.

As per *Section 2.1.2*, the general form describing the conversion of a detector measurement, M_{det}, into absorbed dose to water, D_{w}, can be expressed as:[11]

$$D_w = M_{\mathrm{det}} \cdot N_{D,\mathrm{det},Q} \cdot f_{\mathrm{med,det},Q}^{D_{\mathrm{det}} \to D_{\mathrm{w}}} \cdot \prod_i k_i \qquad (2.21)$$

where $N_{D,\mathrm{det},Q}$ is the detector calibration coefficient that converts the measured quantity into absorbed dose, while $f_{\mathrm{med,det},Q}^{D_{\mathrm{det}} \to D_{\mathrm{med}}}$ is the conversion parameter going from detected dose

to absorbed dose to water. Several correction factors, k_i, are usually applied to account for non-ideal measurement conditions.[11,17]

2.3.1 Ionometry

The International Bureau of Weights and Measures (BIPM) maintains a parallel-plate ionization chamber absorbed dose standard with thick graphite walls and a relatively large and accurately known sensitive volume (~6.8 cm^3), V_{air}, constructed to approximate a Bragg-Gray cavity.[18] Ionization measurements, which are made at a reference depth of 5 cm in water, are converted to absorbed dose to water using a procedure derived from cavity theory (*Section 2.1.2*):

$$D_{\mathrm{w}} = \left(\frac{Q_{\mathrm{air}}}{\rho_{\mathrm{air},} \cdot V_{\mathrm{air},}}\right) \cdot \left(\frac{\overline{W}_{\mathrm{air}}}{e}\right) \cdot \left(\frac{\bar{L}_{\Delta}}{\rho}\right)_{\mathrm{air}}^{\mathrm{wall}} \cdot \left(\frac{\bar{\mu}_{en}}{\rho}\right)_{\mathrm{wall}}^{w} \cdot (\Psi_{wall}^{w} \cdot \beta_{wall}^{w}) \cdot k_{\mathrm{cav}} \cdot k_h \cdot k_{pf} \cdot k_m \cdot k_{\mathrm{ion}} \cdot k_{\mathrm{other}} \tag{2.22}$$

where,

$$M_{\mathrm{det}} \rightarrow Q_{\mathrm{air}} \tag{2.22a}$$

$$N_{D,\mathrm{det},Q} \rightarrow \left(\frac{1}{\rho_{\mathrm{air},} \cdot V_{\mathrm{air},}}\right) \cdot \left(\frac{\overline{W}_{\mathrm{air}}}{e}\right) \tag{2.22b}$$

$$f_{\mathrm{med,det},Q}^{D_{\mathrm{det}} \rightarrow D_{\mathrm{w}}} \rightarrow \left(\frac{\bar{L}_{\Delta}}{\rho}\right)_{\mathrm{air}}^{\mathrm{wall}} \cdot \left(\frac{\bar{\mu}_{en}}{\rho}\right)_{\mathrm{wall}}^{w} \cdot (\Psi_{wall}^{w} \cdot \beta_{wall}^{w}) \cdot k_{\mathrm{cav}} \tag{2.22c}$$

Eq. 2.22c relates the dose to the detector to the dose to the absorbing medium by accounting for the fluence and energy spectrum perturbation in the cavity and chamber wall. The various correction factors account for deviations from a perfect Bragg-Gray cavity (k_{cav}), the effects of humidity on ion collection (k_h), the non-water-equivalence of the chamber front plate (k_{pf}), lateral field non-uniformity (k_m), ion recombination (k_{ion}) and other smaller effects (k_{other}). The uncertainty of this method has been estimated to be 0.43% (1σ), with the

main contributions coming from the mean restricted stopping power ratio, mean mass-energy absorption coefficient ratio and the consensus value of $\left(\frac{\bar{W}_{\text{air}}}{e}\right)$.[11,18]

2.3.2 Absorbed-dose calorimeters

The most fundamental effect of energy absorption by a medium is temperature rise. Absorbed dose in the medium, most commonly water or graphite, is determined by converting from measured temperature change using specific heat capacity of the medium, $c_{p,\text{med}}$. Absorbed dose to water determination in calorimetry can be summarized as:

$$D_{\text{w}} = \Delta T \cdot c_{p,\text{med}} \cdot f_{\text{w,det},Q}^{D_{\text{med}} \to D_{\text{w}}} \cdot \prod_i k_i \tag{2.23}$$

where,

$$M_{\text{det}} \quad \to \Delta T \tag{2.23a}$$

$$N_{D,\text{det},Q} \to c_{p,\text{med}} \tag{2.23b}$$

For water calorimetry, absorbed dose to water is measured at a point in water, and $f_{\text{w,det},Q}^{D_{\text{med}} \to D_{\text{w}}}$ is unity, while for graphite, a dose conversion process is required. In general, it is assumed that all the absorbed energy contributes to a temperature rise in the medium. If some fraction of the energy is in fact absorbed or released by radiation-induced physical or chemical reactions, then there is said to be a heat defect. The effects of water radiolysis and radiochemistry involving dissolved ions, gases and other impurities must be taken into account in water calorimeters. This is often done by measuring the dose inside a sealed water vessel containing pure water, saturated with a known gas system for which the heat defect has been studied and well documented. Furthermore, heat transfer must be well known and accounted for in calorimetry in order to perform accurate dose to water measurements.

Calorimetry is unique in that calibration can be achieved entirely in terms of traceable standards (electrical energy and temperature), independent of radiation. It is for this reason that calorimeters can be considered the most absolute dosimetry technique. In contrast, ionometry and Fricke solution standards (*Section* 2.3.1 and 2.3.3) require a characterized radiation field in order to accurately determine $\left(\frac{\overline{W}_{\text{air}}}{e}\right)$ and $(\varepsilon G)_{Fe^{3+}}$, respectively. The principles and operation of absorbed dose radiation calorimeters are the subject of *Chapter* 3.

2.3.3 Fricke chemical dosimeters

Absorbed dose to water standards based on measuring the radiation-induced chemical change produced in ferrous sulfate solution, otherwise known as Fricke dosimeters, have been developed for use in photon beams. The chemical change of interest is the oxidization of ferrous ions, Fe^{2+}, into ferric ions, Fe^{3+}. Similar to film dosimetry, the chemical reaction results in a measurable change in the optical density, *OD*. In particular, the ferric ions exhibit an absorption peak in the ultraviolet spectrum at a wavelength of 304 nm, a characteristic not shared by the ferrous ions. By applying spectrophotometry, the absorbance of a solution can be measured. Absorbed dose to water is thus determined by:

$$D_{\text{w}} = \left(\frac{\Delta OD}{\rho \cdot l}\right) \cdot \left(\frac{1}{(\varepsilon G)_{Fe^{3+}}}\right) \cdot f_{\text{w},F,Q}^{D_F \to D_{\text{w}}} \cdot k_{\text{vial}} \cdot k_{dd} \cdot k_E \cdot k_{\text{other}} \tag{2.24}$$

where,

$$M_{\text{det}} \quad \to \frac{\Delta OD}{\rho \cdot l} \tag{2.24a}$$

$$N_{D,\text{det},Q} \to \frac{1}{(\varepsilon G)_{Fe^{3+}}} \tag{2.24b}$$

In Eq. 2.24, ρ is the density of the solution, l is the optical path length, $(\varepsilon G)_{Fe^{3+}}$ is the product of the molar extinction coefficient and the radiation chemical yield. The correction factor,

k_{vial}, corrects for the perturbation of the container material, usually Pyrex or quartz, while k_{dd} corrects for non-uniform lateral fields, and k_E corrects for the energy dependence of $(\varepsilon G)_{Fe^{3+}}$. For this dosimetric technique, $(\varepsilon G)_{Fe^{3+}}$ is the detector dose calibration coefficient, and like $\left(\frac{\overline{W}_{\text{air}}}{e}\right)$, it cannot be directly measured. Rather, its value can be determined through calibration against calorimetry-based absorbed dose data. The uncertainty of this method has been estimated to be 0.51% (1σ).[19]

2.3.4 Traceability framework in radiation dosimetry

The mechanism by which primary measurements are transferred to the clinical community is by the calibration of secondary standards against the appropriate primary standard and the subsequent use of this secondary standard to calibrate tertiary and ultimately user instruments. This process renders user instruments traceable to a primary standard, which is usually a national standard that must itself be verified internationally. The international framework for traceability is centralized at the BIPM, where a system of primary standards to enable international comparisons and traceability to the SI for radiation standards is maintained. The principal test of the validity of a primary standard is comparison measurements with another national or international standard of the same quality.[20]

The BIPM works with the national metrology institutes (NMIs) that operate the PSDLs. These in turn provide calibrations to secondary standard dosimetry laboratories (SSDLs) designated nationally. To extend traceability worldwide, the BIPM provides calibrations to the International Atomic Energy Agency (IAEA), who along with the World Health Organization (WHO) have set up a network of SSDLs to bridge the gap between PSDLs and end users, particularly in countries that are not Member States of the BIPM. In the United States, additional agencies which have been granted the status of accredited dosimetry

calibration laboratories (ADCLs; conceptually similar to SSDLs), were formed to maintain traceable standards and disseminate the standard to users across the nation.[20-22]

The concept of traceability of a user's detector to a PSDL implies that a calibration coefficient was obtained from either: (i) PSDL (directly in terms of a primary standard); (ii) SSDL or ADCL (with secondary standards traceable to a PSDL); or (iii) another detector which satisfies either (i) or (ii) (cross calibration is often performed in clinics). In general, the shorter the calibration chain, the smaller the overall uncertainty on the measured results.

2.4 REFERENCE DOSIMETRY FOR EXTERNAL BEAM RADIATION THERAPY

Meaningful comparisons of the outcome of radiation therapy (RT) treatments require a degree of uniformity in the entire RT process, from treatment prescription to delivery, so that common criteria are applied throughout. A key step in the RT process is the requirement for harmonized reference dosimetry procedures. The term reference dosimetry is used to designate the determination of the absorbed dose produced by a radiation beam of quality, Q (*Section* 2.4.2), at a reference point within a medium (normally water) under specific irradiation conditions. The point is situated on the beam central axis, at a given reference depth, z, in the medium under otherwise reference conditions.

2.4.1 Reference Dosimetry Protocols

The implementation of dosimetry protocols (or codes of practice) are common procedures that enable reliable dosimetry comparisons. They are issued by national, regional or international organizations, and all such protocols to date are based on the use of an ionization chamber with a calibration traceable to a PSDL as the preferred reference

radiation detector. While reference dosimetry in protocols may be based on primary standards for air kerma or absorbed dose to water, this work will focus solely on the latter. Examples of absorbed dose reference dosimetry protocols include the American Association of Physicists in Medicine (AAPM) Task Group (TG) report 51, and the IAEA's Technical Report Series (TRS) 398.[23-25]

At the standards laboratory, the absorbed dose to water, D_{w,Q_0}, is determined at a reference depth in water using a suitable standard technique, and used to provide the user's ionization chamber with a calibration coefficient in terms of absorbed dose to water, $N_{D,w}$. The reference beam quality, Q_0, may be ^{60}Co γ-rays or high-energy photon or electron beams. The calibration coefficient of the ionization chamber enables the direct determination of the reference absorbed dose to water in a user's beam having the same quality as Q_0 using the expression:

$$D_{w,Q_0}(z_{\mathrm{ref}}) = M_{w,Q_0}(z_{\mathrm{ref}}) \cdot N_{D,w,Q_0} \tag{2.25}$$

If the chamber is used in a beam quality, Q, different from the quality, Q_0, used for the chamber calibration at the standards laboratory, the absorbed dose to water is given by:

$$D_{w,Q}(z_{\mathrm{ref}}) = M_{w,Q}(z_{\mathrm{ref}}) \cdot N_{D,w,Q_0} \cdot k_{Q,Q_0} \tag{2.26}$$

where k_{Q,Q_0} is a factor that corrects the calibration coefficient for the difference in beam quality (beam quality correction factor). It is defined as the ratio of an ionization chamber's absorbed dose to water calibration coefficients at beam qualities Q and Q_0. Experimental and theoretically calculated (*i.e.*, numerically simulated) values of k_{Q,Q_0} have been determined for many chambers. The following general (valid for all types of beams) expression is obtained:

$$k_{Q,Q_0} = \frac{(s_{w,air})_Q}{(s_{w,air})_{Q_0}} \cdot \left(\frac{P_{ch,Q}}{P_{ch,Q_0}}\right) \cdot \left(\frac{W_{air}}{e}\right)_{Q_0}^{Q} \tag{2.26}$$

where $s_{w,air}$ is shorthand for $\left(\frac{S}{\rho}\right)_{air}^{w}$, and $P_{ch,Q}$ is an ionization chamber specific overall perturbation correction factor for a beam of quality Q accounting for the presence of the detector in the medium. For high-energy photon and electron dosimetry, $\left(\frac{\bar{W}_{\text{air}}}{e}\right)$ is assumed to be constant, further simplifying Eq. 2.26.

2.4.2 High-energy photon, electron, and proton beam quality specification

Since most radiation fields are not mono-energetic, there needs to be a way to uniquely specify the dosimetric "effectiveness" of a beam, or alternatively, a figure of merit describing the spectrum of the beam. This specification is known as beam quality, and is commonly represented by the variable Q. For high-energy photon beams, two common beam quality specifiers are used: TPR_{10}^{20} and $\%dd(10)_x$. The former is used in the IAEA TRS-398 protocol and stands for tissue-phantom-ratio. TPR_{10}^{20} is the ratio of the dose at a depth of 20 cm to the dose at 10 cm for a constant source-detector distance (SAD) of 100 cm and a field size defined at the plane of the detector of 10 × 10 cm^2. On the other hand, the AAPM's TG-51 protocol uses $\%dd(10)_x$, or the PDD at a depth of 10 cm given an SSD of 100 cm and a field size of 10 × 10 cm^2 at the phantom surface.

For high-energy electron beams, the beam quality specifier used is, R_{50}, the depth along the central axis at which the dose is 50% of the maximum dose. There are two methods to determine R_{50}. Since the average electron energy varies with depth, one option is to use a detector with little energy dependence over the range of electron energies present, such as a silicon diode. Another option is to convert the ionization, measured using an ionization chamber, into dose. A commonly used empirical expression used to relate R_{50} to the electron beam reference depth (in units of cm):

$$z_{\text{ref}} = 0.6 \cdot R_{50} - 0.1 \tag{2.27}$$

Finally, for proton beams, the IAEA TRS-398 recommends the use of the residual range, R_{res}, as the beam quality index.[25] The residual range (in units of g cm^{-2}) at a measurement depth, z, is defined as:

$$R_{\text{res}} = R_p - z \tag{2.28}$$

where R_p is the practical range, or the depth at which the absorbed dose beyond the Bragg peak or spread-out Bragg peak (SOBP) falls to 10 % of its maximum value. Unlike photons and electrons, the proton beam quality is not unique to a particular beam, but is also specified by the reference depth, z_{ref}, chosen for measurement. For modulated beams, z_{ref} is chosen at the middle of the SOBP, while for monoenergetic beams, a depth of 3 cm in water is recommended.

2.5 REFERENCES

[1]International Commission on Radiation Units and Measurements, *Fundamental Quantities and Units for Ionizing Radiation*, (ICRU Report No. 85, 2011).

[2]J.P. Seuntjens, W. Strydom, and K.R. Shortt, "Dosimetric Principles, Quantities and Units," in *Review of Radiation Oncology Physics: A Handbook for Teachers and Students*, ed. E.B. Podgorsak (International Atomic Energy Agency, Vienna 2005).

[3]A.E. Nahum, "Cavity Theory, Stopping-Power Ratios, Correction Factors," in *Clinical dosimetry measurements in radiotherapy*, ed. D.W. Rogers and J.E. Cygler (Medical Physics Publishing, Madison, Wisconsin, 2009).

[4]L.H. Gray, "An ionization method for the absolute measurement of gamma-ray energy," Proc. R. Soc. A. **156,** 578-596 (1936).

[5]L.V. Spencer, and F.H. Attix, "A theory of cavity ionisation," Radiat. Res. **3,** 239-254 (1955).

[6]A.E. Nahum, "Water/air mass stopping-power ratios for megavoltage photon and electron beams," Phys. Med. Biol. **23**, 24-38 (1978).

[7]W. Wieszczycka, and W.H. Scharf, "Proton radiotherapy accelerators," (World Scientific Publishign Co. Pte. Ltd., Singapore, 2001).

[8]P. Andreo, D.T. Burns, A.E. Nahum, J. Seuntjens, and F.H. Attix, "Overview of Radiation Detectors and Measurement," in *Fundamentals of Ionizing Radiation Dosimetry (Introduction to Radiological Physics and Radiation Dosimetry, 2nd ed.)*, (Wiley, 2016, *in press*).

[9]J. Izewska, and G. Rajan, "Radiation Dosimeters," in *Review of Radiation Oncology Physics: A Handbook for Teachers and Students*, ed. E.B. Podgorsak (International Atomic Energy Agency, Vienna 2005).

[10]D.W. Rogers, "General Characteristics of Radiation Dosimeters and a Terminology to Describe Them," in *Clinical Dosimetry Measurements in Radiotherapy*, ed. D.W. Rogers and J.E. Cygler (Medical Physics Publishing, Madison, Wisconsin, 2009).

[11]J. Seuntjens, and S. Duane, "Photon absorbed dose standards," Metrologia **46**, S39-S58 (2009).

[12]J.W. Boag, "Ionization Chambers," in *Radiation Dosimetry Volume II*: *Instrumentation*, ed. F.H. Attix and W.C. Roesch (Academic Press, New York, 1966).

[13] A. Niroomand-Rad, C.R. Blackwell, B.M. Coursey, K.P. Gall, J.M. Galvin, W.L. McLaughlin, A.S. Meigooni, R. Nath, J.E. Rodgers, and C.G. Soares, "Radiochromic film dosimetry: Recommendations of AAPM Radiation Therapy Committee Task Group 55," Med. Phys. **25**(11), 2093-2115 (1998).

[14]A.S. Beddar, "Plastic scintillation dosimetry and its application to radiotherapy," Radiat. Meas. **41**, S124-S133 (2007).

[15]A.J. Whitehead, R. Airey, C.M. Buttar, J. Conway, G. Hill, S. Ramkumar, G.A. Scarsbrook, R.S. Sussmann, and S. Walker, "CVD diamond for medical dosimetry applications," Proc. 1st Int. Workshop on Radiation Imaging Detectors **460**, 20-26 (2001).

[16]M.J. Butson, A. Rozenfeld, J.N. Mathur, M. Carlon, T.P.Y. Wong, and P.E. Metcalfe, "A new radiotherapy surface dose detector: The MOSFET," Med. Phys. **23**, 655-658 (1996).

[17]M. McEwen, "Primary Standards of Air Kerma for ^{60}Co and X-Rays and Absorbed Dose in Photon and Electron Beams," in *Clinical Dosimetry Measurements in Radiotherapy*, ed. D.W. Rogers and J.E. Cygler (Medical Physics Publishing, Madison, Wisconsin, 2009).

[18]D.T. Burns, P.J. Allisy, and C. Kessler, "Re-evaluation of the BIPM international standard for air kerma in ^{60}Co gamma radiation," Metrologia **44**, L53-L56 (2007).

[19]H. Feist, "Determination of the absorbed dose to water for high-energy photons and electrons by total absorption of electrons in ferrous sulphate solution," Phys. Med. Biol. **27** (1982).

[20]J. Seuntjens, and M. McEwen, "The calibration chain: Role of BIPM, PSDLs and ADCLs," in *Clinical Dosimetry Measurements in Radiotherapy*, ed. D.W. Rogers and J.E. Cygler (Medical Physics Publishing, Madison, Wisconsin, 2009).

[21]P.J. Allisy, D.T. Burns, and P. Andreo, "International framework of traceability for radiation dosimetry quantities," Metrologia **46**, S1-S8 (2009).

[22]K.R. Shortt, C.K. Ross, and J.P. Seuntjens, "The role of comparisons in confirming the accuracy of dosimetric standards," in *Proc. International Proceedings Series 13)* ed. J.P. Seuntjens and P.N. Mobit (Medical Physics Publishing, Madison, Wisconsin, 2002).

[23]P.R. Almond, P.J. Biggs, B.M. Coursey, W.F. Hanson, M. Saiful Huq, R. Nath, and D.W.O. Rogers, "AAPM's TG-51 protocol for clinical reference dosimetry of high-energy photon and electron beams," Med. Phys. **26**, 1847-1870 (1999).

[24]M. McEwen, L. DeWerd, G. Ibbott, D. Followill, D.W. Rogers, S. Seltzer, and J. Seuntjens, "Addendum to the AAPM's TG-51 protocol for clinical reference dosimetry of high-energy photon beams," Med. Phys. **41**, 041501 (2014).

[25]IAEA (International Atomic Energy Agency), "Absorbed dose determination in external beam radiotherapy based on absorbed-dose-to-water standards: An international code of practice for dosimetry," Technical Report Series 398 (IAEA, Vienna, Austria, 2001).

Chapter 3

ABSORBED DOSE RADIATION CALORIMETRY

3.1 THEORY

Radiation calorimetry forms the basis of absorbed dose standards in many countries around the world, and relies on the underlying assumption that the energy imparted by ionizing radiation results in a measurable temperature rise, ΔT_m:[1]

$$D_m = c_{p,m} \cdot \Delta T_m \tag{3.1}$$

where D_m is the absorbed dose to the medium, and $c_{p,m}$ represents the specific heat capacity of the absorbing material.

This assumption isn't always necessarily true; a discrepancy referred to as the heat defect (*Section* 3.3.3) can manifest itself through endothermic or exothermic chemical reactions or energy absorption in the lattice.[2] In such instances, calorimetry can still be considered the most fundamental and absolute means of measuring absorbed dose, provided that any heat defect is well understood and taken into account. In the following section, the theory behind

the two most common types of absorbed dose calorimeters (water and graphite) is described.

3.1.1 Water calorimetry

The accurate measurement of temperature rises at a point is fundamentally possible in stagnant water calorimeters due to the relatively low thermal diffusivity of water.[1] In principle, water calorimetry is conceptually straight forward: the calorimeter is used to measure the temperature rise at a point, ΔT_w, which is then multiplied by the specific heat capacity of water, $c_{p,w}$, to immediately yield absorbed dose to water at a point. In practice, this process is complicated by fundamental effects that potentially disturb the energy balanced between absorbed dose and energy appearing as a temperature rise, and technical effects that complicate the accurate measurement of the temperature rise. Both fundamental and technical effects are handled as correction factors, as shown in the following expression:

$$D_w = c_{p,w} \cdot \Delta T_w \cdot k_{hd} \cdot k_{ht} \cdot k_p \cdot k_{dd} \cdot k_\rho \qquad (3.2)$$

where k_{hd} is the correction for the heat defect, h; k_{ht} is a general correction for heat transfer due to conduction and convection; k_p is the radiation field perturbation factor due to the presence of non-water materials in the beam; k_{dd} corrects for a non-uniform dose profile at the point of measurement; and k_ρ accounts for the difference in density between the calorimeter operating temperature and the temperature at which another detector is calibrated.[1] An expanded description of these corrections is provided in *Section* 3.3.

While the specific heat capacity of water is a function of temperature, the μK temperature variations experienced during water calorimetry are sufficiently small that it may be approximated as nominally constant. During this project, a constant $c_{p,w}$ of 4.2048×10^3 J kg^{-1} K^{-1} was used at the calorimeter operating temperature of 4 °C based on measurements made by Osborne *et al*. in 1939.[3]

3.1.2 Graphite calorimetry

Within the context of absorbed dose calorimetry, graphite differs from water in three important respects as an absorbing medium: (i) its specific heat is approximately six times smaller, (ii) its thermal diffusivity is about six hundred times larger, and (iii) it is a rigid elemental solid rather than a liquid chemical compound. As a technique, graphite calorimetry holds several advantages and disadvantages over water calorimetry. For one, its smaller specific heat capacity results in signal to noise ratio that is six times larger than water. For graphite, there are no radiation-induced chemical reactions to contribute to a heat defect, unlike water (radiation-induced heat defect due the lattice is generally thought to be negligible).[4] As a machinable solid with a high thermal diffusivity, the effective measurement becomes one of absorbed dose averaged over the entire absorbing graphite core (*i.e.*, the sensitive volume), rather than dose at a point in water. The major downside of using graphite is the need to convert the measured dose to absorbed dose to water. While the conversion itself is not strongly energy dependent, it does nevertheless introduce an uncertainty not present in water calorimetry.[1]

In graphite calorimetry, dose to graphite is commonly measured over the extent of the core, which is positioned at a specific point in a homogeneous graphite phantom, and is subsequently converted to realize absorbed dose to water (*Section* 3.3.5). The effects of heat transfer are minimized by nesting the core within one or more graphite layers (referred to as jackets), each separated by insulating gaps (often evacuated). The high thermal diffusivity of graphite permits the use of electrical heating as an integral part of the dose measurement.

From the definition of absorbed dose, the dose to graphite, D_{gr} is obtained from:[5]

$$D_{gr} = \frac{E_{\text{rad}}}{m_{\text{core}}} \cdot \prod_i k_i \tag{3.3}$$

where E_{rad} is the energy imparted to the core by radiation, m_{core} is the core mass, and k_i are the various correction factors, including those which take into account heat transfer, the presence of the gaps, etc. (see *Section* 3.3 for details).

The total change in thermal energy in the core, $\Delta E_{\text{tot,thermal}}$, can be expressed as the sum of contributing sources (*i.e.*, from radiation, electrical heating, and heat transfer), and also as the product of the core mass, m_{core}, specific heat capacity, $c_{p,\text{core}}$, and change in core temperature, ΔT_{core}:

$$\Delta E_{\text{tot,thermal}} = m_{\text{core}} \cdot c_{p,\text{core}} \cdot \Delta T_{\text{core}} = E_{\text{rad}} + \Delta E_{\text{elec}} + \Delta E_{\text{transfer}} \qquad (3.4)$$

Dividing Eq. 3.4 by the core mass yields the expression for the mean core dose. This is summarized in Table 3.1, along with the other graphite calorimetry modes of operation. A short description of each mode is presented below:

1. QUASI-ADIABATIC RADIATION MODE: The sensed core temperature is measured over time in the absence of electrical heating. Provided that the core temperature is adequately stable, the radiation is turned on for a period of time. Independent fits are made to the pre- and post-irradiation temperature curve, and the rise in temperature is obtained by extrapolating these fits to the mid-heating time. This assumes that the rate of heat transfer between the core and its environment is constant.

2. QUASI-ADIABATIC ELECTRICAL MODE: The temperature rise obtained in the quasi-adiabatic radiation mode may be multiplied by the specific heat capacity to determine the dose, or alternatively, the calorimeter response may be quantified by the quasi-adiabatic electrical mode. By dissipating a known amount of electrical energy into the core and measuring its response, an effective specific heat capacity can be experimentally measured and serve as a calibration factor.

3. ISOTHERMAL MODE: In this mode, electrical energy dissipation is controlled such that the temperature of the calorimeter components remains constant throughout operation. The quantity of interest is the electrical power deficit during the irradiation, which then by substitution, provides a measure of the rate of energy imparted by the radiation. The energy from electrical heating of the core is obtained by integrating the core electrical power with respect to time:

$$\Delta E_{\mathrm{elec}}(t) = \int^{t} P_{\mathrm{core}}(t') \cdot \mathrm{d}t' \tag{3.5}$$

Table 3.1. Summary of measurement equations for each graphite calorimeter operation mode. Heat transfer in the core is kept to zero in the quasi-adiabatic modes, which can either be realized during electrical calibration or during irradiation. For the isothermal mode, core temperature is kept constant (adapted from Seuntjens and Duane, 2009)

Operation mode	Measurand	Primary expression	Corrections
Quasi-adiabatic radiation	$\frac{E_{\mathrm{rad}}}{m_{\mathrm{core}}}$	$= c_{p,\mathrm{core}} \cdot \Delta T_{\mathrm{core}}$	$-\frac{\Delta E_{\mathrm{transfer}}}{m_{\mathrm{core}}}$
Quasi-adiabatic electrical	$c_{p,\mathrm{core}} \cdot \Delta T_{\mathrm{core}}$	$= \frac{\Delta E_{\mathrm{elec}}}{m_{\mathrm{core}}}$	$+\frac{\Delta E_{\mathrm{transfer}}}{m_{\mathrm{core}}}$
Isothermal	$\frac{E_{\mathrm{rad}}}{m_{\mathrm{core}}}$	$= -\frac{\Delta E_{\mathrm{elec}}}{m_{\mathrm{core}}}$	$c_{p,\mathrm{core}} \cdot \Delta T_{\mathrm{core}} - \frac{\Delta E_{\mathrm{transfer}}}{m_{\mathrm{core}}}$

3.2 TECHNICAL IMPLEMENTATION

In this section, a description of practical aspects common to many water and graphite calorimeters is presented. This includes design considerations for thermal management, temperature measurement, and signal analysis techniques. Figures 3.1 and 3.2 depict some examples of water and graphite calorimeter setups, respectively.

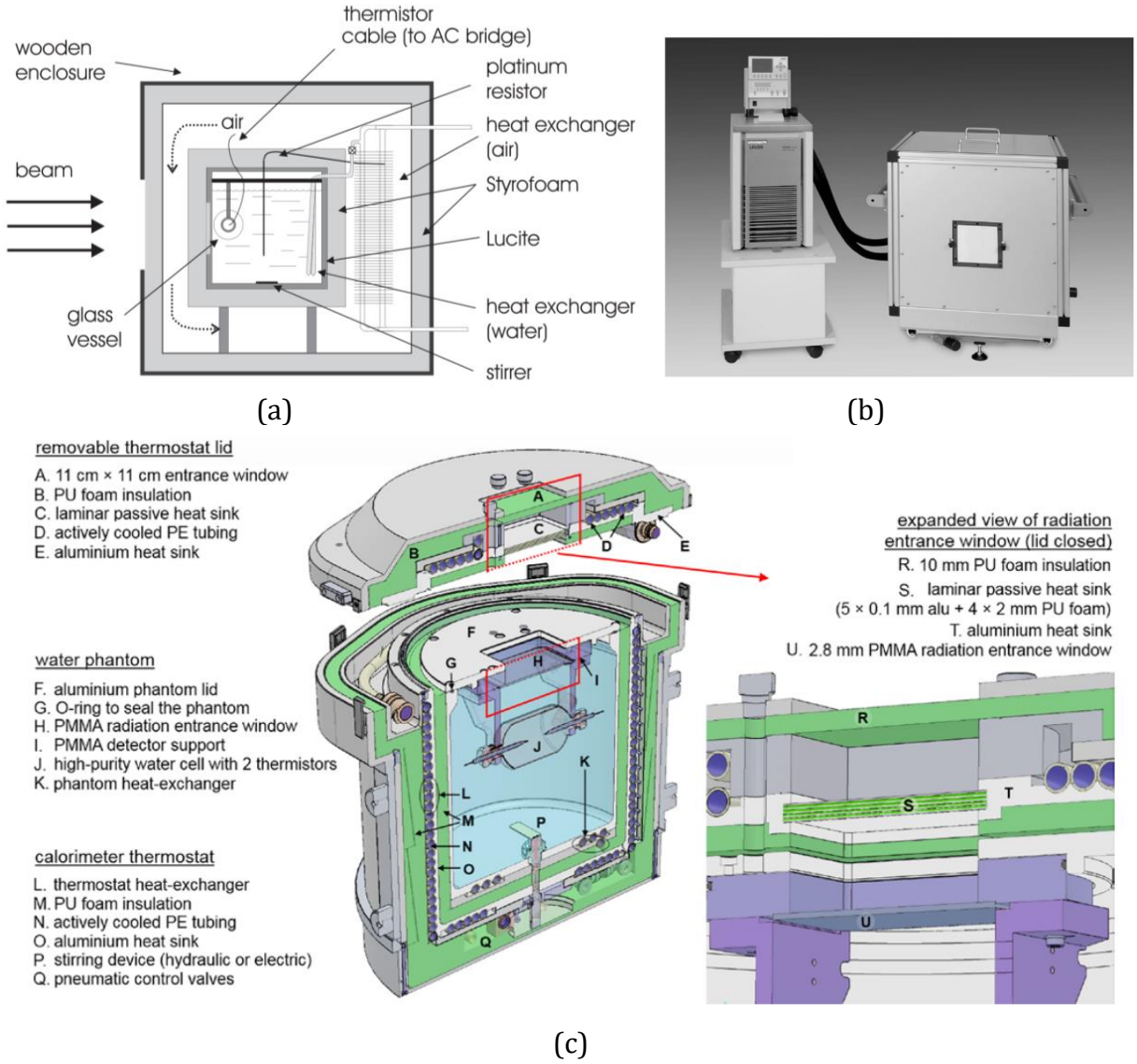

Figure 3.1: (a) Schematic drawing of the primary standard water calorimeter developed by the National Research Council of Canada (NRC) (reproduced from Seuntjens, 2003). Thermal isolation is achieved through the use the circulation of air through a radiator. (b) Transportable water calorimeter developed by Physikalisch-Technische Bundesanstalt (PTB) with associated cooling unit on the left side. The radiation entrance region of the calorimeter is indicated by the square in the middle of the calorimeter housing (Krauss, 2012; dx.doi.org/10.1088/0031-9155/57/19/6245). (c) Cross-section of the MR-compatible calorimeter developed by the Dutch Metrology Institute (VSL) containing the high-purity glass vessel at a depth of 10 cm, and an expanded view of the radiation entrance window (de Prez, 2016; dx.doi.org/10.1088/0031-9155/61/13/5051).

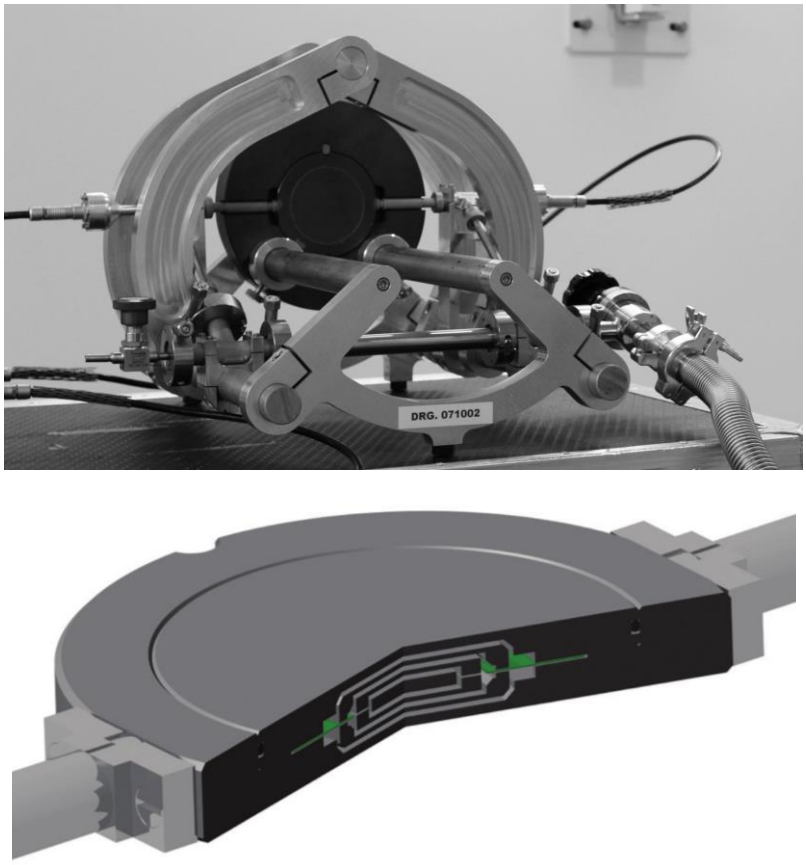

(a)

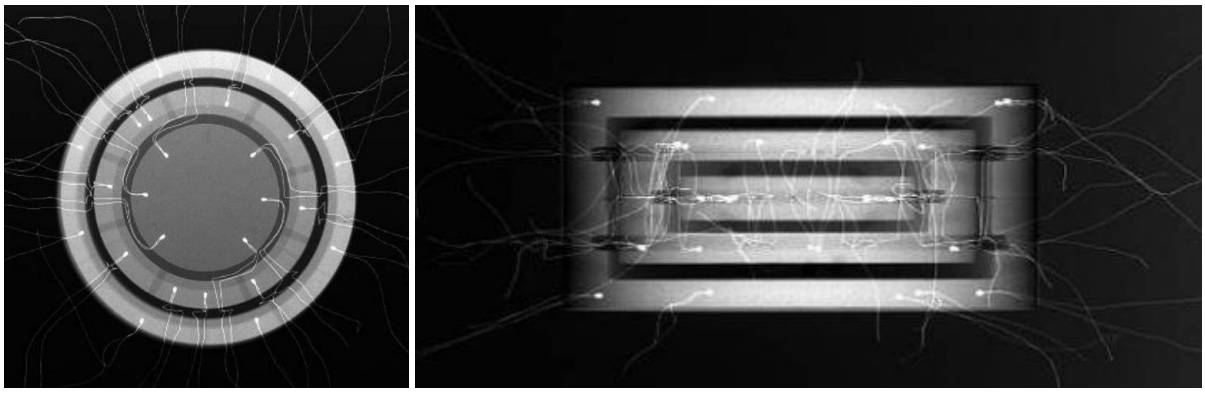

(b)

Figure 3.2: (a) General view of the assembled, and (b) cutaway schematic showing the internal structure and evacuated gaps of the proton/light ion therapy-level absorbed dose graphite calorimeter developed at the National Physical Laboratory (NPL).[8] (c) Radiographs of the GR9 graphite calorimeter developed at the Laboratoire National Henri Becquerel (LNE-LNHB) as seen from the top down and the side showing thermistor placement (reproduced from Ostrowsky, 2008).[9]

3.2.1 Thermal isolation

Water calorimeters are typically operated at 4 °C to minimize heat transfer due to convection, as this is the temperature at which, for water, the coefficient of volumetric expansion is zero and the driving force for convection is zero. Since radiative transfer is negligible, it is assumed that heat transfer in water calorimeters is primarily due to of radiation-induced conduction. Non-uniformities in the temperature distribution are caused by two sources of excess heat: (i) non-water materials (*e.g.*, glass vessel, thermistor probes) with specific heat capacities and radiation absorption characteristics significantly different than water, and (ii) electrical power dissipation in the thermistors. Furthermore, heat transfer is also a result of thermal gradients generated by the non-uniform absorbed dose distribution.

Thermal equilibrium within the calorimeter phantom is usually achieved through the circulation of a thermally controlled fluid. In some instances, a coolant flowing through a network of pipes in direct contact with a conductive layer (*e.g.*, copper plate) enclosing the water phantom on all sides may be used (Figure 3.3; also see *Chapter* 8). The conductive layer becomes a quasi-isothermal surface, which effectively isolates the calorimeter from thermal fluctuations in the surrounding environment. The isothermal surface is often sandwiched by additional insulating layers (*e.g.*, expanded polystyrene) to further dampen changes in ambient temperature. In other instances, thermal isolation is achieved by the fluid, which is circulated through a radiator inside the calorimeter (Figure 3.1a; also see *Chapter* 9). Attached fans force a large air mass through the radiator, which eventually thermally stabilizes the contents of the calorimeter. In both cases, the fluid is circulated by a temperature controlled chiller (Figure 3.1b and 3.3).

In the case of graphite calorimeters, heat transfer may occur via conduction, convection, or radiative processes. Conduction is mitigated through the use of evacuated gaps to separate

adjacent graphite bodies. Some conduction through the electrical leads and graphite supports is unavoidable, though the use of fine gauge wire and silk threads under tension, respectively, minimizes these effects to generally negligible levels. Radiative transfer is also reduced by coating the surfaces of the graphite jackets in aluminized Mylar. The effectiveness of thermal isolation can be ascertained by measuring the time constant for the core temperature to relax towards its equilibrium value, given a constant jacket temperature and constant core heating power.[1] This time constant is the ratio of the relevant heat capacity and heat transfer coefficient, and may range as short as ~30 s for older portable calorimeters using air gaps, or as long as ~1800 s for the LNE-LNHB primary standard, under vacuum, with aluminized Mylar and silk thread supports.[9]

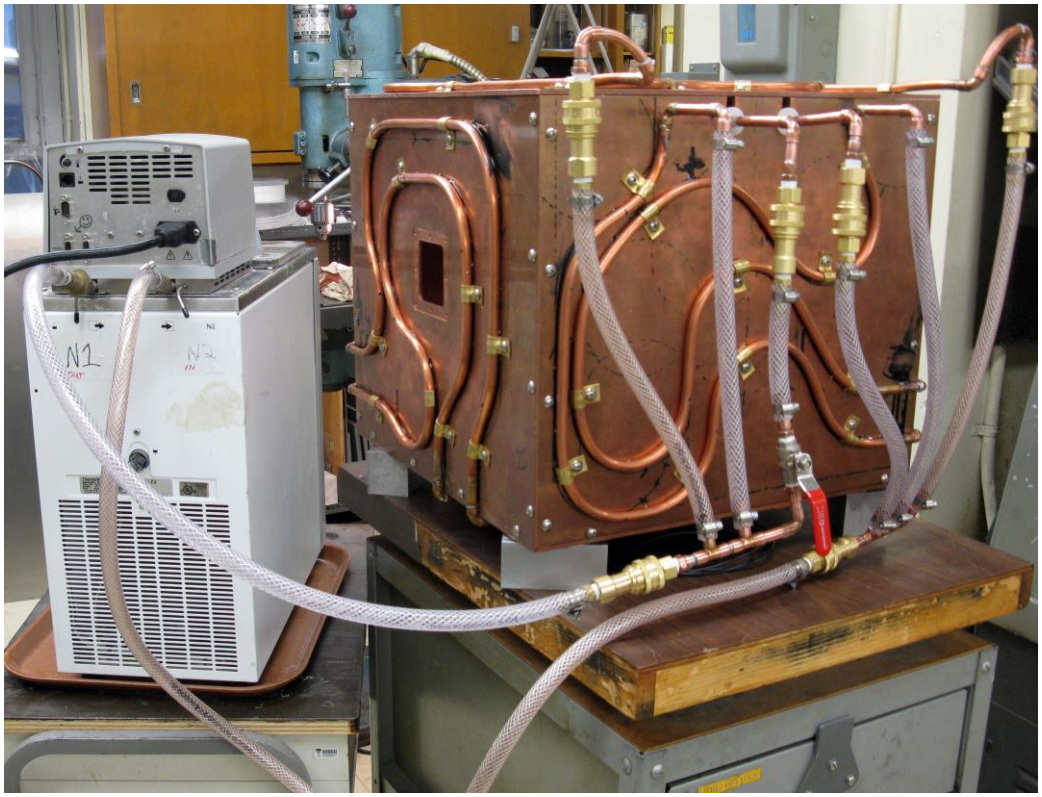

Figure 3.3: Water calorimeter construction at McGill University. The temperature controlled chiller circulates fluid through a network of copper pipes that are in direct thermal contact with a box made of copper plate. The calorimeter water phantom and vessel are enclosed by the copper box, which acts as a quasi-isothermal surface during operation.

Isolation of the core from variations in the environment temperature is achieved by introducing multiple nested jackets, often referred to as the shield and mantle. These extra layers may be temperature controlled at a set point above ambient through means of electrical dissipation. These graphite bodies may be made to be sufficiently massive to dampen the relatively rapid changes in room temperature. The downside to this strategy is that the introduction of insulating gaps perturbs the dose distribution in the calorimeter, compared to the dose distribution in homogenous graphite. As a result, a perturbation correction is needed to recover an accurate measure of dose (*Section* 3.3.2).

3.2.2 Temperature sensing

Currently, all calorimeters operated at laboratories as primary standards use negative temperature coefficient (NTC) thermistors to measure the temperature rise (see Figure 3.2b and 3.4). Thermistors are made of semiconductor material (generally ceramics) that have been sintered in order to display large changes in resistance in proportion to small changes in temperature. The resistance of NTC thermistors will decrease non-linearly as the temperature increases. The manner in which the resistance decreases is related to a material constant referred to as β; see Eq. 3.6. Their unrivaled sensitivity, small size, long term stability, and relatively low cost make NTC thermistors the temperature sensor of choice for absorbed dose calorimetry. Thermistors are calibrated relative to reference temperature standards (*e.g.*, mercury thermometer) over a relatively larger range centred about the calorimeter operating temperature. Based on the measured temperature-resistance relation for thermistors, the material constant, β, can be determined:

$$R(T) = R_0 \cdot e^{\beta \cdot (T^{-1} - T_0^{-1})} \tag{3.6}$$

where R_0 is the thermistor bead resistance at the reference temperature, T_0 (typically 25 °C). In reality, β is dependent upon T, however this can be neglected if the temperature range of

operation is kept sufficiently small. Once β has been determined, a temperature rise, ΔT, can related to a resistance change, ΔR, through the thermistor sensitivity, S:

$$\Delta T = S^{-1} \cdot \left(\frac{\Delta R}{R}\right) \tag{3.7}$$

$$S = \beta \cdot T^{-2} \tag{3.7a}$$

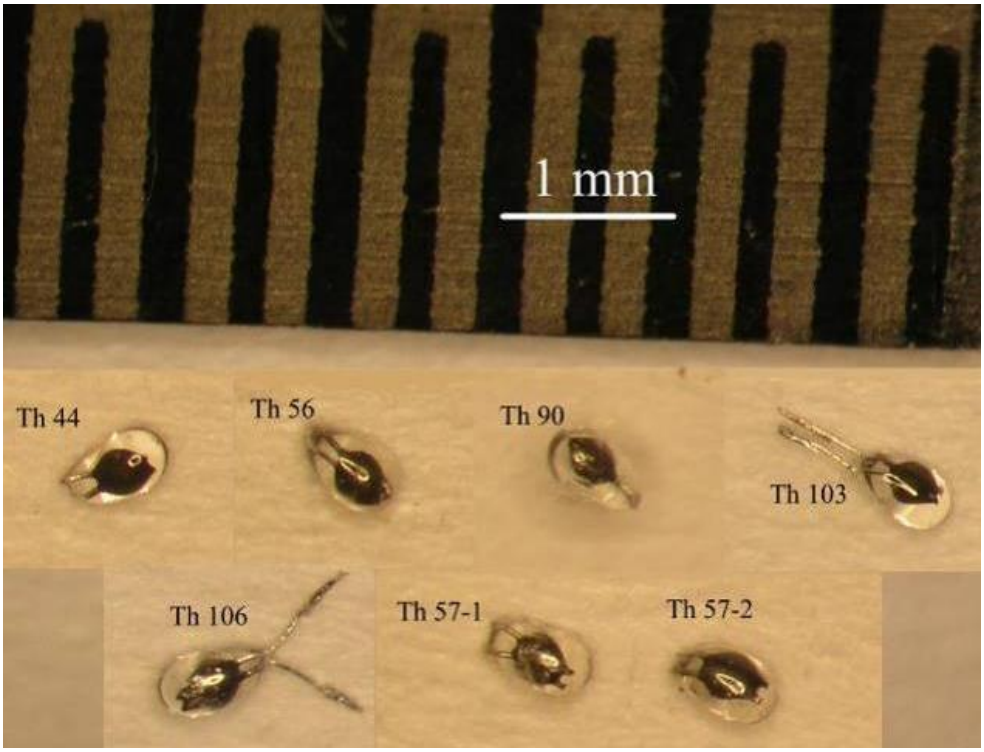

Figure 3.4: Several glass encapsulated negative temperature coefficient (NTC) thermistor beads used by the Laboratoire National Henri Becquerel (LNE-LNHB) in their GR9 graphite calorimeter (reproduced from Ostrowsky, 2008).[9]

The most common way to measure temperature using an NTC thermistor is through the use of a Wheatstone bridge; both DC and AC variants have been successfully used in the past (*Section* 4.3 and 7.6). While DC bridges have the advantage of being simple, AC bridges tend to be slightly less electrically noisy. In most cases, water calorimeters are operated using a pair of thermistors connected in serial, as it improves the signal to noise ratio by roughly

40 %. Bridge excitation voltage is usually no more than a few volts, as high current in the thermistors will result in a lower signal to noise ratio due to increased pink (1/f) noise.

3.2.3 Signal analysis

Figure 3.5 shows a typical water calorimeter measurement run, also referred to as a temperature drift curve. The contents of Figure 3.5 are also representative of a graphite calorimetry quasi-adiabatic radiation mode measurement. A bridge calibration run (see *Section* 7.9.3), representing the output of the bridge in response to a user-induced 1 Ω change in the decade resistor box setting, has been included for comparison sake. Although the ordinate is in units of voltage, it is for all practical purposes, proportional to temperature. A calorimetry run such as this is composed of three parts:

1) PRE-DRIFT: This is the temperature drift measured by the thermistors prior to the start of radiation. An ideal measurement is one with zero pre-drift, although, this is not a requirement for successful calorimetric measurements. As long as the time scale of the drift throughout is small compared to the timescale of the irradiation period, it can be approximated as being linear and can be accounted for in the analysis.

2) IRRADIATION: This is the temperature rise (due to radiation) as measured by the thermistor pair. Unlike other radiation detectors (*e.g.*, ionization chambers) that average the energy deposited over a volume, the thermistor beads in stagnant water calorimetry allow for the measurement of temperature rise at virtually a point.

3) POST-DRIFT: This is the temperature drift measurement proceeding the end of irradiation. In an ideal world in which heat transfer is absent, the post-drift would have exactly the same slope as the pre-drift. However, in reality, this is not the case due to the

presence of thermal gradients produced inside the calorimeter as a result of sources of excess heat and the non-uniform dose distribution (*Section* 3.2.1).

A radiation-induced temperature rise can be determined by measuring the difference between linear extrapolations of the pre- and post-drifts to the midpoint of the irradiation. In the absence of strong non-linear drifts, ΔT should be relatively insensitive to the pre- and post-drift intervals used for fitting. This procedure assumes that the heat transfer is constant throughout operation.

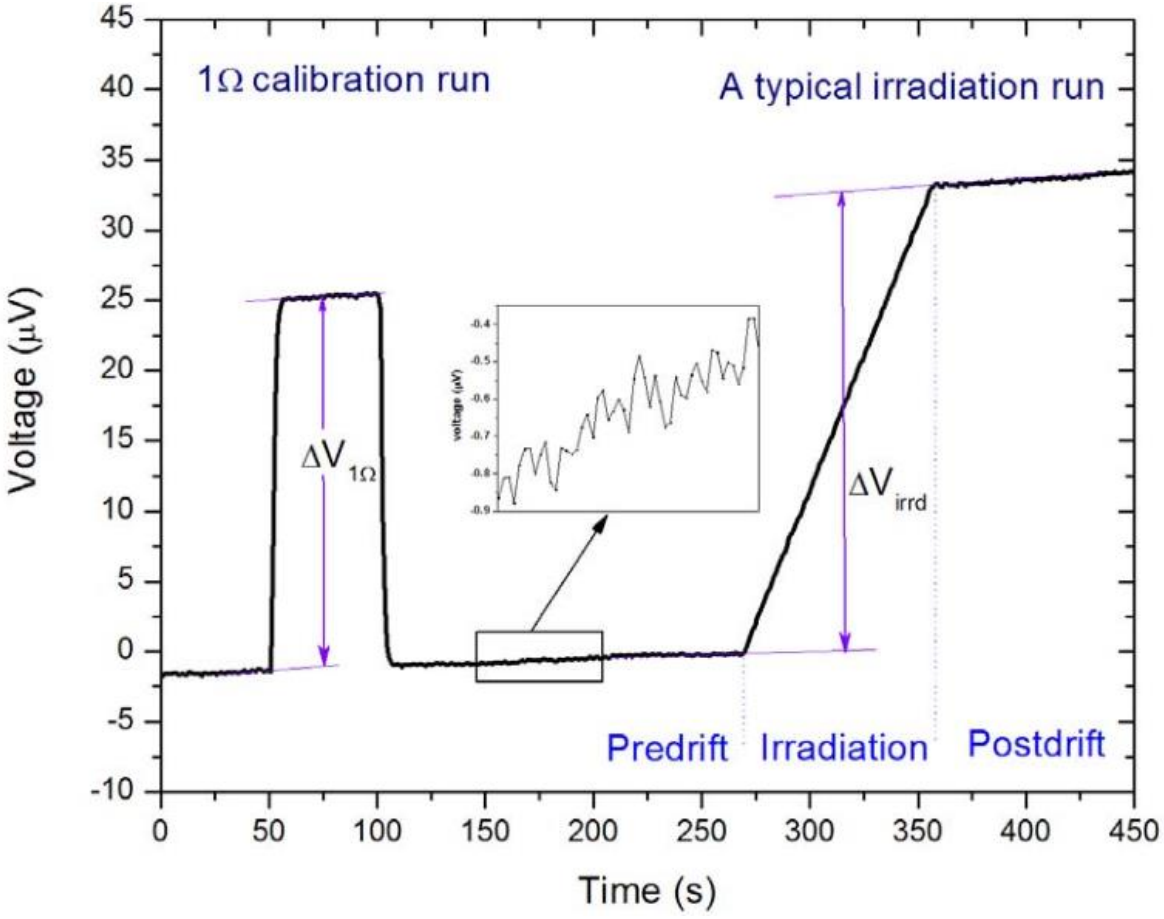

Figure 3.5: A water calorimeter run showing the three stages of an experimental run: pre-drift, irradiation, and post-drift. Note that the signal is in volts (bridge output) and not temperature, although the two are proportional. The contents of this figure could also represent a quasi-adiabatic radiation mode graphite calorimetry run (Sarfehnia, 2010).

Figure 3.6 shows a sample run of a graphite calorimeter being used to measure absorbed dose while being operated in the isothermal mode. In this mode, the quantity of interest is the electrical energy dissipated to maintain a constant core temperature throughout operation. During irradiation, the electrical energy contribution drops in an amount equal to the rate of energy imparted by the radiation. Thus, the absorbed dose is measured via substitution. As before, an isothermal calorimetry run is composed of three parts:

1) PRE-DRIFT: This is the electrical power drift as measured by two voltmeters (see *Section* 4.1) prior to the start of radiation. An ideal measurement is one with zero pre-drift, although, this is not a requirement for successful calorimetric measurements. As long as the time scale of the drift throughout is small compared to the timescale of the irradiation period, it can be approximated as being linear and can be accounted for in the analysis.

2) IRRADIATION: This is the electrical power drop (balancing the radiation energy) as measured by the sensing thermistors. Similar to other radiation detectors (*e.g.*, ionization chambers) that average the energy deposited over a volume, the thermistor beads sense and modulate the temperature of the entire core. During the irradiation period, overshoots may occur depending on the nature of the radiation 'impulse' and the tuning of the temperature controllers (denoted as 'A' and 'B' in Figure 3.6a).

3) POST-DRIFT: This is the power drift measurement proceeding the end of irradiation. In an ideal world in which heat transfer is absent, the post-drift would have exactly the same slope as the pre-drift. Since the temperature of each graphite component is actively controlled to be quasi-constant throughout the operation of the calorimeter, and the thermal diffusivity of graphite is relatively large, heat transfer is often assumed to be negligible.[1]

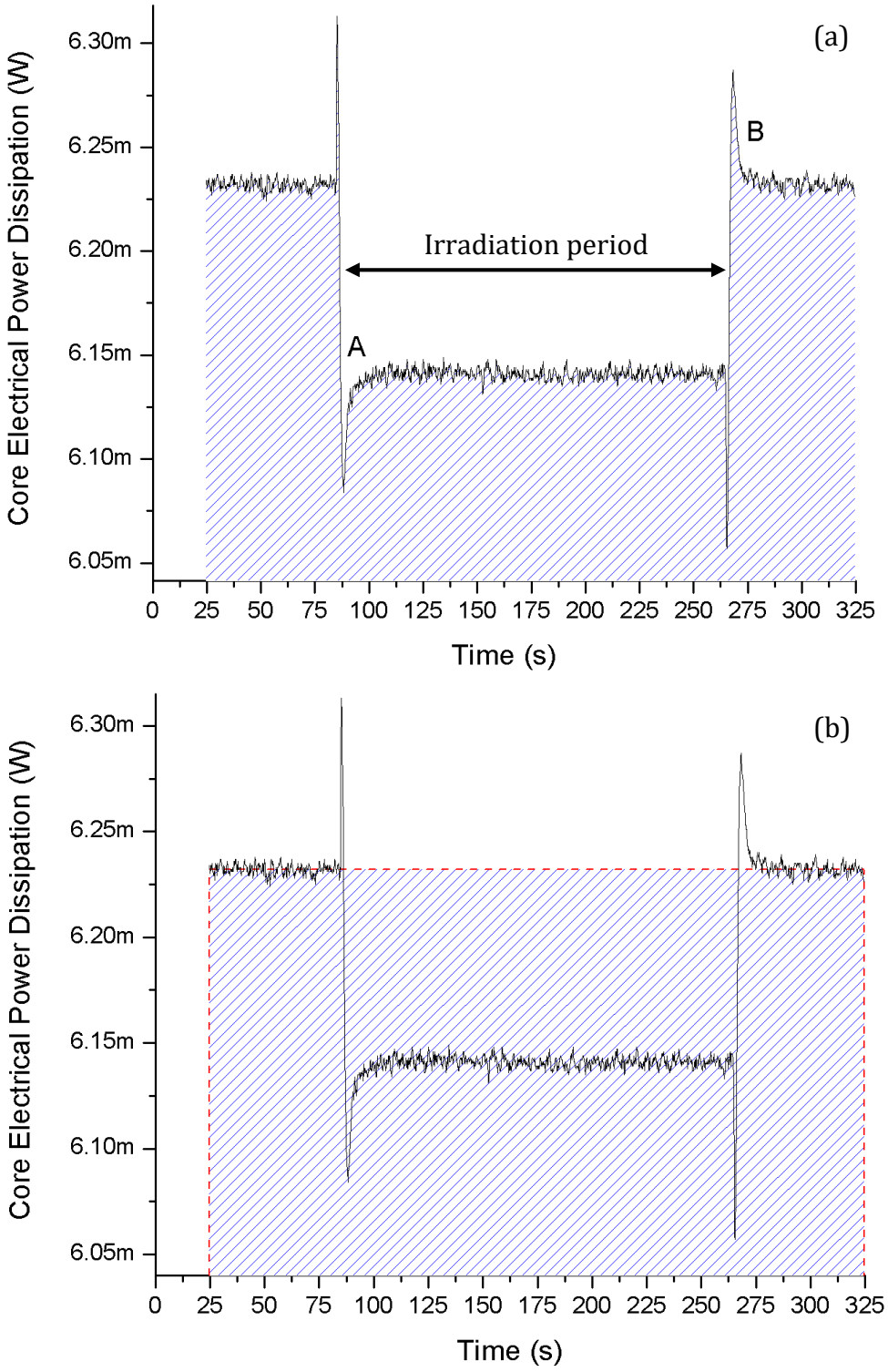

Figure 3.6: The isothermal response is measured by determining the absolute difference in the integrated powers illustrated by the areas covered in blue lines. The spikes exhibited at the points at which the beam is turned on and off are electrically-induced, as they are observed only during electrical simulation, and not during a radiation measurement.

Absorbed dose is derived from an isothermal run by integrating the power deficit occurring during the irradiation period (illustrated by the difference in the areas covered by blue lines in Figure 3.6). In Figure 3.6b, the pre- and post-drifts are linearly interpolated over the extent of the run and the resulting fit is integrated to calculate the area covered by the blue lines. To determine absorbed dose to graphite, the radiation energy calculated from the integrated power deficit is divided by the core mass.

3.2.4 Active thermal control

In graphite calorimetry, thermistors serve the purpose of electrical heating in addition to temperature sensing. While sensing thermistors have essentially a constant self-heating and do not contribute to changes in electrical heating power, the current supplied to the heating thermistor networks are driven by proportional-integral-derivative (PID) controllers (see *Section* 4.4.1).

Not all of the electrical energy supplied to the core heating network contributes to direct warming of the core however; an apportioning of the electrical heat occurs between the core in which the thermistor is embedded, and the surrounding jacket through which the thermistor leads pass. Lead losses are reduced by using thermistors with relatively large nominal resistances.

By using the sensed temperature as the process variable in a process controller, electrical heating powers can be used as active control parameters to maintain the calorimeter in a stable thermal state.[11] This is the basis for isothermal operation, in which each graphite body is maintained at constant and independent temperatures. In other instances, the difference between the core and jacket can be input into a temperature controller as a process variable in order to maintain a constant core-jacket temperature difference. The purpose of doing so is to eliminate the drift in the core temperature between measurements.[12]

3.3 CORRECTIONS AND CONVERSION

Corrections factors used in calorimetry are applied to account for both the fundamental and physical effects that perturb an accurate absorbed dose measurement. These corrections may be common to both water and graphite calorimetry (*e.g.*, heat transfer), or they may be exclusive to one of two techniques (*e.g.*, heat defect). It is important to note that, since calorimetry measurements require a time span on the order of minutes, the temporal dependence of the effects underlying the corrections and the details of the procedure used to analyze a run are important in assessing the values of the factors. In this section, the most important correction factors applied in water and graphite calorimetry are described.[1]

3.3.1 Heat transfer

The heat transfer correction factor, k_{ht}, accounts for the effects of heat transfer due to conduction, convection and radiative transfer on the temperature distribution inside the calorimeter (although radiative effects are often treated as negligible since the temperature differences are small). k_{ht} is defined as the ratio of the ideal temperature rise (a temperature rise solely due to locally deposited absorbed dose in the absence of heat transfer) to the actual temperature rise (with the effects of heat transfer taken into account) at a given point or over a given volume. Whereas it is possible to analytically calculate the ideal temperature rise with a knowledge of the depth dose curve, the actual temperature rise in the presence of heat transfer can generally only be solved using numerical techniques.

Throughout this work, COMSOL MULTIPHYSICS® software was used to calculate the heat transfer correction factor using an analysis based on the finite element method (FEM). FEM is a numerical technique used to solve partial differential equations (PDEs). FEM relies on discretizing the PDE-governed problem into one which has a finite number of unknown parameters (*i.e.*, degrees of freedom). The discretized problem is then solved over a

discretized version (composed of many "mesh" elements or volumes) of the geometrical model of interest (Figure 3.7). A major challenge in FEM is the selection of a numerically stable system of equations to approximate the initial PDE problem. Such calculations of k_{ht} using COMSOL was validated by Sarfehnia (2010) by comparing simulated results to both experiments and to othe independent FEM-based heat transport solvers.

COMSOL was found to be able to adequately handle k_{ht} calculations for all the various calorimeter designs and radiation therapy beams of interest over the course of this project. To solve a given problem, the system of PDE equations must first be defined. If necessary, the software also permits the coupling of PDEs describing common physical processes (*e.g.*, conduction and convection through the temperature and particle velocity fields). In general, a geometrical model of the experimental setup, the definition of all boundary conditions, as well as all heat sources and heat sinks is required by the user.

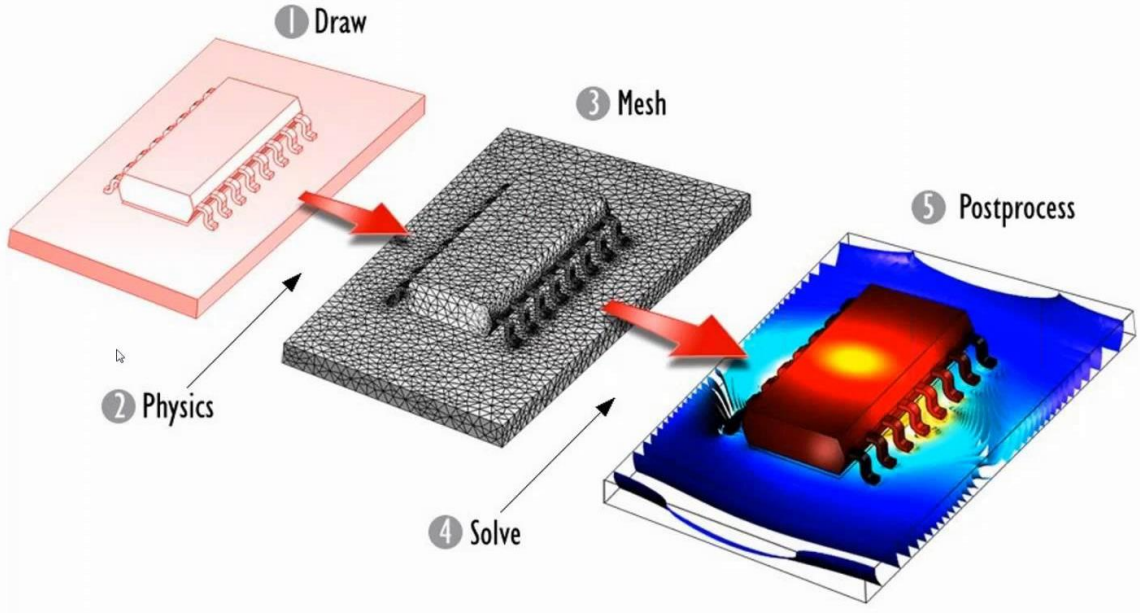

Figure 3.7: Illustrating the COMSOL Multiphysics® workflow: (1) material properties are assigned to a geometry; (2) a system of PDEs governing the physics of interest are defined; (3) meshing of the geometry in a number of degrees of freedom; (4) system of equations approximating the initial PDE problem is solved; (5) visualization of resulting solution.[13]

Although COMSOL is a general purpose FEM solver, this scope of this work was limited to conduction only. Neglecting convection is justified by the fact that for water calorimetry, the operating temperature is kept to within a few 10's of mK of the temperature at which the volumetric expansion of water is zero. While for graphite calorimetry, there is no fluid volume to drive convection. Radiative transfer is neglected due to the sufficiently small temperature differences induced by the radiation.

The heat transport problem based on conduction only (*i.e.*, the velocity field is zero) can be described by the following PDE:[14]

$$\rho \cdot c_p \cdot \frac{\partial T}{\partial t} + \nabla(-k \cdot \nabla T) = Q = \rho \cdot \dot{D} \tag{3.8}$$

where ρ, c_p, and k refer to the physical properties of a given material (density, specific heat capacity at constant pressure, and thermal conductivity, respectively). Q is the heat source of the system, which consists of the locally apparent absorbed dose rate, $\dot{D}$, which may include heat defect and thermistor self-heating. Eq. 3.8 described the conservation formulation of the heat flow due to conduction.

Important modeling considerations include the memory requirements and the time to reach a solution, both of which strongly depend on the number of degrees of freedom of the model. This parameter is proportional to the number of geometrical mesh elements and the number of dependent variables in the physics model. For instance, modelling both conduction and convection is significantly more resource intensive, as it requires five dependent variables (the three components of the velocity field, the pressure, and temperature), while conduction alone requires a single variable only (temperature). A common strategy to minimize the number of degrees of freedom is to take advantage of symmetries in the model (*i.e.*, simulate a 2D axially symmetric model rather than a full 3D model).

The traditional data analysis method used in water calorimetry is fitting and extrapolating the pre- and post-drift curves (*Section* 3.2.3). This procedure provides an approximate heat loss correction as the heat loss is proportional to the temperature difference between two bodies and the proportionality factor (sometimes referred to as the heat modulus), is approximately constant over the time frame of the measurement. k_{ht} are factors in addition to this standard extrapolation correction procedure.

k_{ht} factors are strongly dependent upon the excess heat, which is defined as the relative difference between the true and ideal temperature rises, for an irradiation of duration, Δt:

$$\frac{\Delta T_{\text{real}} - \Delta T_{\text{ideal}}}{\Delta T_{\text{ideal}}} = \frac{\int_0^{\Delta t} \left(\frac{\partial T}{\partial t} - \frac{1}{c} \cdot \frac{\mathrm{d}D}{\mathrm{d}t} \right) \cdot \mathrm{d}t'}{\int_0^{\Delta t} \frac{1}{c} \cdot \frac{\mathrm{d}D}{\mathrm{d}t} \cdot \mathrm{d}t'} = \frac{c}{D} \int_0^{\Delta t} \nabla \cdot (k \cdot \nabla T) \cdot dt' \qquad (3.9)$$

Eq. 3.9 reveals that the excess heat is independent of dose rate, $\dot{D}$, and only depends on the irradiation time, Δt, and the involved thermal conductivities. Furthermore, the solution to Eq. 3.8 does not depend on the absolute temperature, T (assuming constant specific heat capacities and thermal conductivities), but rather on the relative temperature difference between bodies.[1] Excess heat curves can be calculated to describe the post-drift thermal behavior of non-water (or graphite) materials in the calorimeter (see example in Figure 3.8).

For graphite calorimetry, each operating mode requires a correction for heat transfer in the core. Note that, in addition to the locally absorbed dose, the heat source, Q, in Eq. 3.8 now includes the electrical heating power, P, from the thermistors. Owing to the high thermal conductivity of graphite, the spatial variations in temperature within each graphite component are generally much smaller than the differences between components. This leads to a simplified model, in which each component is assigned a single temperature, and the full heat equation is replaced by coupled equations involving effective coefficients of heat transfer, h, between components. For instance, the core-jacket equation shown in Eq. 3.10:

$$m_{\text{core}} \cdot c_p \cdot \frac{\mathrm{d}T_{\text{core}}}{\mathrm{d}t} = P_{\text{core}} + h_{\text{core-jacket}} \cdot (T_{\text{jacket}} - T_{\text{core}}) \tag{3.10}$$

In reality, there are other bodies between which heat transfer may occur (*e.g.*, thermistor leads). Once calibrated, the simplified model may be used to estimate the energy of heat transfer by integrating its power with respect to time:

$$\Delta E_{\text{transfer}}(t) = h_{\text{core-jacket}} \int^{t} (T_{\text{jacket}}(t') - T_{\text{core}}(t')) \cdot \mathrm{d}t' \tag{3.11}$$

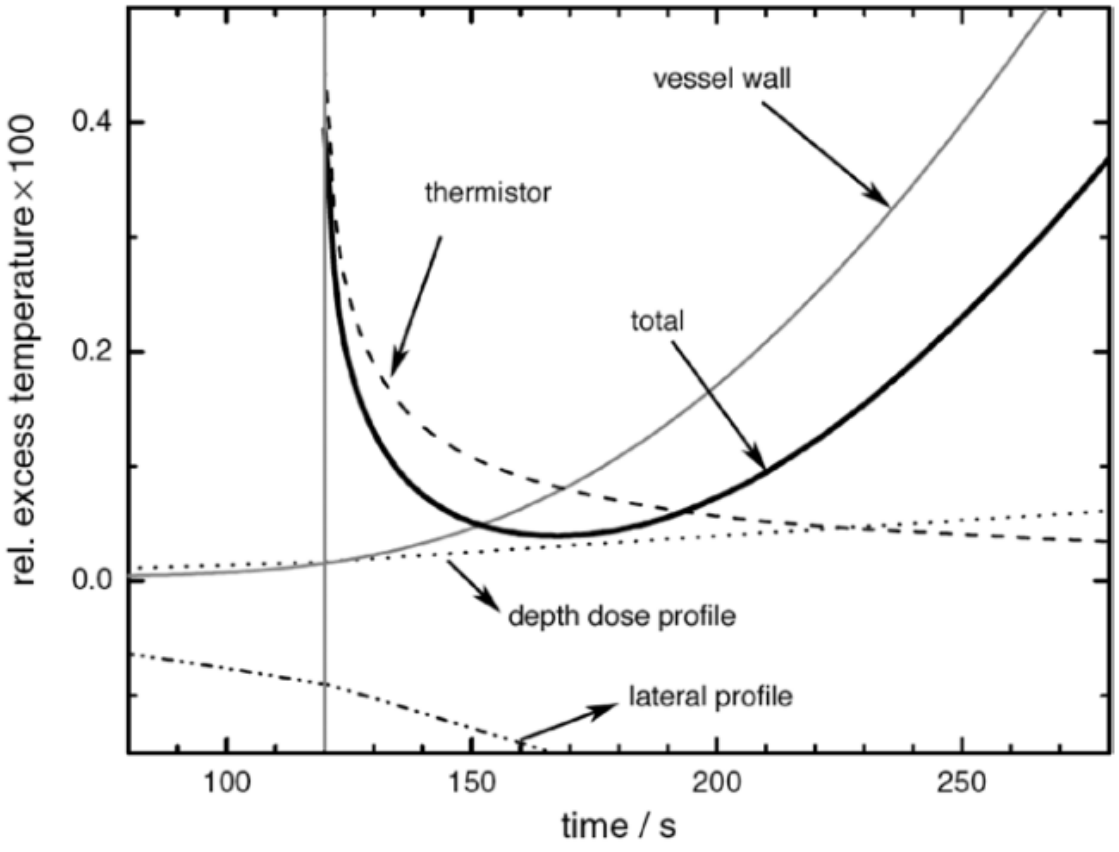

Figure 3.8: Calculated time evolution of a water calorimeter post-drift curve after the end of a 120 s irradiation (indicated by the vertical line). The total relative excess temperature and the heat conduction effect contributions from the parallel plate vessel wall, thermistor, lateral dose distribution, and depth dose distribution are shown (adapted from Krauss, 2006; dx.doi.org/10.1088/0026-1394/43/3/008).

3.3.2 Radiation field perturbation

In general, the radiation field perturbation factor, k_p, corrects for the scattering and absorption effects of non-water (or non-graphite) materials present in a water (or graphite) calorimeter on the dose distribution. For water calorimeters, the largest contributing factor to this correction is the glass vessel, which encompass the thermistor probes. Experimental determination of this factor, which depends on the vessel wall thickness, diameter, and beam energy, requires relative measurements with a small-volume dosimeter (*e.g.*, small ionization chamber or diode).[16]

For graphite calorimeters, the dominant source of perturbation is the low density gaps between the graphite bodies. The gaps lead to a decrease in the dose to the core, which is dependent upon the geometry of the structures, beam energy, and the depth of measurement. The so-called gap effect, can be defined as the ratio of the dose in the absence of the gaps to the dose in the presence of the gaps, while maintaining the core at a constant distance from the source and the actual thickness of graphite in front of the core being the same in both cases.[17]

k_p is most commonly calculated using a Monte Carlo (MC) beam transport simulation. In this work, EGSnrc MC user codes (DOSRZnrc, egs_chamber; National Research Council of Canada) were used.[18] For water calorimetry, the correction is evaluated as the ratio of the dose scored at the position of the thermistors for two MC simulations: one with non-water materials modeled (glass vessel included) and one with water only (*i.e.*, all non-water material properties are changed to water). For graphite calorimetry, a similar procedure is carried out which effectively combined k_p with the absorbed dose conversion.

3.3.3 Heat defect

Early water calorimeters exhibited anomalous behaviour resulting in dose measurement values that were different from results obtained by graphite calorimetry or ion chamber dosimetry by 2 % – 5 %.[19] These results were indeed too large to be accounted for by the uncertainty on the measurement. A closer look at Domen's first operational water calorimeter revealed that although the water inside the calorimeter was thermally isolated from surrounding environment, it was not protected against the exchange of gases or other impurities.[20] As such, a heat defect correction factor, k_{hd}, was introduced:[1]

$$k_{hd} = \frac{E_a}{E_h} \tag{3.12}$$

where E_a is the energy absorbed from radiation, and E_h is the energy which appears in the for form of heat. Ross *et al.* described four techniques which can result in heat defect, including two kinds of radiation-induced optical emission, acoustic energy generated by energetic charged particles, as well as radiation-induced chemical reactions. They showed that chemical reactions are most likely to be the only significant source of heat defect, with the first three abovementioned effects contributing less than 0.1 %.[21] k_{hd} is less than unity for exothermic reactions, which release heat, and greater than unity for endothermic processes, which absorb energy from the surrounding environment.

The effects of heat defect are minimized in current water calorimeters by encompassing the thermistor detectors inside a glass vessel. Although the purity of water and concentration of dissolved gases cannot easily be controlled in the entire volume of water inside the calorimeter, it can be controlled to a much greater extent in the relatively small volume of the vessel. By filling the vessel with very pure water and saturating it through bubbling with pure known gases (a procedure described in *Section* 7.10), the concentration of impurities and dissolved gases inside the vessel can be estimated. In this way, not only can heat defect be minimized, but it can also be numerically calculated. Chemically inert Pyrex glass is the

material of choice for vessel fabrication as it does not tend to leech impurities into the pure water over time.

As ionizing radiation traverses medium, it deposits energy through individual interactions in a discontinuous manner, depositing discrete amounts of energy in discrete volumes. The amount of energy deposited in a given interaction (event) can vary widely, and can be categorized as being either a 'spur' (6 – 100 eV/event), a 'blob' (100 – 500 eV/event), or a 'short track' (500 – 5000 eV/event).[22]

The concept of dose deposition along the path of the particle is closely related to that of linear energy transfer (LET), as defined in *Section* 2.1.1. Since high energy photons and electrons are the most widely studied radiation type in water calorimetry, data on low-LET radiation is relatively abundant.[23-28] For these types of radiation, about 70 % of the energy is deposited in spurs. A relatively smaller body of work exists for medium-LET radiation (pertinent to proton therapy).[29-31]

Radiation chemistry in water occurs over a relatively large time range (10^{-17} s to seconds). At the onset of irradiation, the earliest changes are the excitation and ionization of water molecules ($\sim 10^{-17}$ s). After about a picosecond ($\sim 10^{-12}$ s), the earliest chemical reactions begin to occur, producing large concentrations of free radicals and extremely reactive species in the vicinity of each other. These species in turn produce additional spurs during the time span of 10^{-12} s and 10^{-7} s. During this time, the concentration of species is so high that spur production is not affected by the relatively low concentrations (mM) of reactive solutes (*i.e.*, impurities) in the water. Only after about 10^{-7} s to 10^{-6} s do impurities begin to act as scavengers of reactive species.

In radiation chemistry, for a given LET, yield of a given species X, denoted as $G(X)$, is the number of molecules of that particular species produced per 100 eV of energy absorbed that do not react within the first 10^{-6} s. The study of G-values is important as these are used as input parameter in the numerical simulation of the heat defect. Figure 3.9a shows an example of $G(X)$ studied for various species in water over a wide range of LET.[32] The heat defect obtained from the simulation of various aqueous systems (water saturated with various gases) has been studied and corroborated by experiments involving small, sealed vessels filled with high purity water. Figure 3.9b shows a comparison of the measured and calculated heat defects for six aqueous systems and a low LET radiation. In this work, an H_2-saturated system is used.[33] As shown in Figure 3.8b, an H_2-saturated system reaches an equilibrium state of zero heat defect. This is true for concentrations of H_2 that are as low as 1 μmol L^{-1}. An additional benefit of an H_2 system is that once the system reaches a steady state, it no longer deviates from a zero heat defect. On the down side, H_2 systems are very sensitive to trace amounts of O_2. As the system is initially irradiated, O_2 in the system is used up, producing a characteristic, sharp exothermic peak. Upon O_2 depletion (beyond the peak) a zero heat defect equilibrium state is achieved. Since we irradiated the vessel to doses well beyond the minimum required dose to achieve zero heat defect, a k_{ht} of unity is assumed with a non-zero uncertainty (1.000 ± 0.15 %).[33]

3.3.4 Other corrections

The profile uniformity correction factor, k_{dd}, corrects for the effect of the difference in dose measured by the calorimeter versus the dose at the reference point. For water calorimetry, the measured dose is at the points of measurement of the thermistor probes, while for graphite calorimetry, this is taken as an average dose evaluated over the extent of the core volume. Both the correction and its uncertainty are often small radiation therapy, as uniform dose distributions can be achieved.

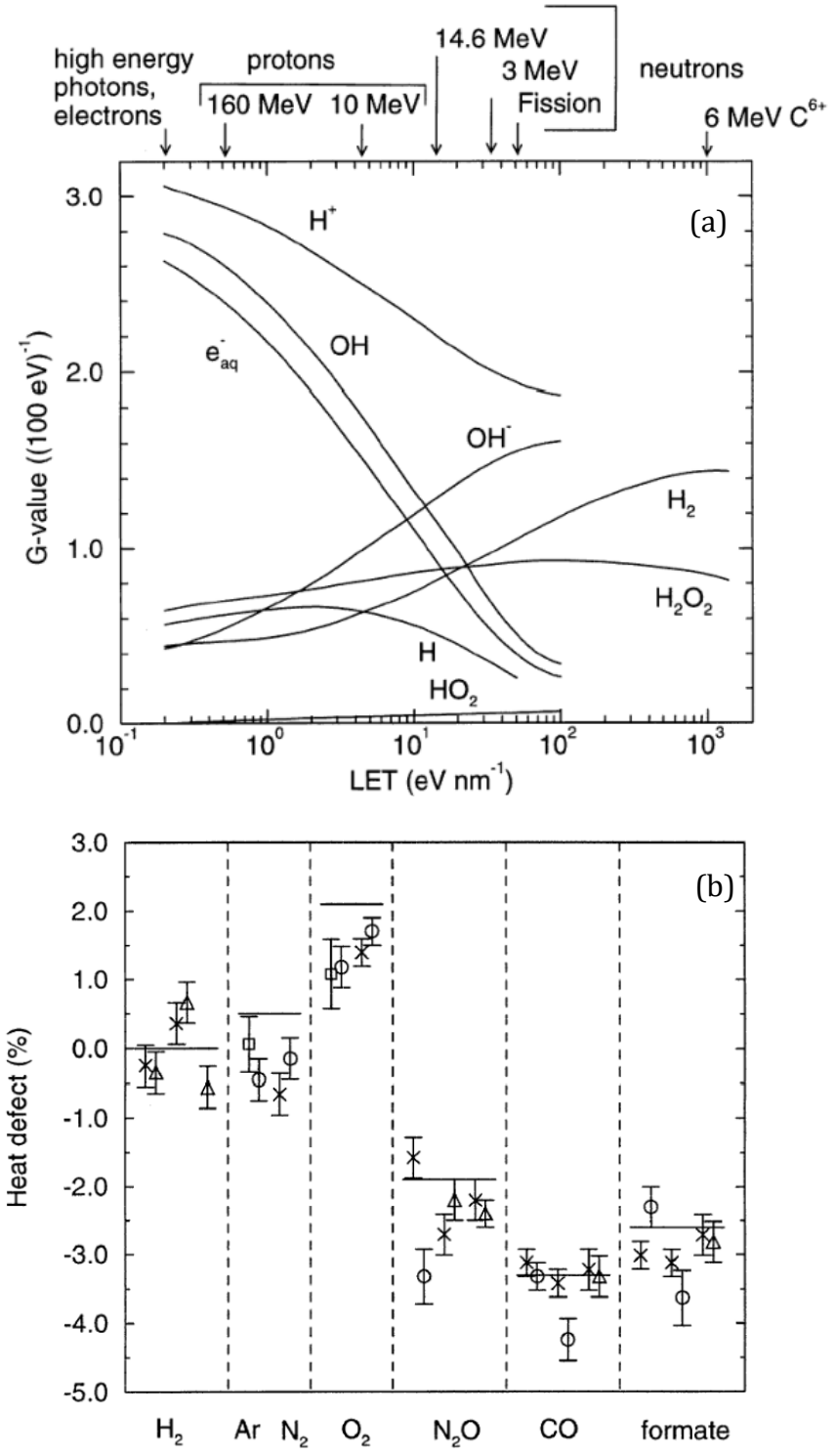

Figure 3.9: (a) *G*-values of several spur products as a function of LET. (b) Comparison of calculated (horizontal lines) and measured (symbols) heat defects for different aqueous systems (Ross and Klassen, 1996; doi.org/10.1088/0031-9155/41/1/002).

For water calorimeters operated at 4 °C, the difference in water density between the operation temperature and the temperature at which the dosimeter is calibrated (typically room temperature) gives rise to a minor, slightly depth-dependent correction factor. For instance, for a depth of measurement of 8 cm, the density effect amounts to about 0.2 mm when comparing water at 4 °C and 22 °C.

3.3.5 Dose conversion methods

For graphite calorimeters, the conversion of dose to graphite to dose to water is commonly accomplished in two ways. The first technique is the photon fluence scaling method, where the dose to graphite is simply converters to dose to water by calculating the water-graphite dose ratio, $\left(\frac{D_w}{D_g}\right)_{\text{calc}}$.[34,35] The relation between absorbed dose and collisional kerma is used to calculate this factor (see *Section* 2.1):

$$D_w = D_g \cdot \left(\frac{D_w}{D_g}\right)_{\text{calc}} = D_g \cdot \left(\frac{K_{\text{coll},w} \cdot \beta_w}{K_{\text{coll},g} \cdot \beta_g}\right)_{\text{calc}} = D_g \cdot \left[\left(\frac{\bar{\mu}_{en}}{\rho}\right)_g^w \cdot \Psi_g^w \cdot \beta_g^w\right]_{\text{calc}} \qquad (3.13)$$

Additional corrections are often necessary to account for differences in air attenuation and the finite source size, among other small effects.

The second technique to determine the dose conversion factor involves the use of a transfer instrument (often an ionization chamber).[12] The ionization chamber is first calibrated in a graphite phantom representation of the calorimeter and subsequently is used to measure absorbed dose at a reference point in a water phantom.[1] Depending on the ionization chamber wall thickness, either Eq. 2.16 or Eq. 2.17 is applied. For a thick wall ionization chamber (Eq. 2.16), the dose to water formulation becomes:

$$D_w = D_g \cdot \left(\frac{D_w}{D_g}\right)_{\text{meas}} = D_g \cdot M_g^w \cdot \beta_g^w \cdot \left(\frac{\left(\frac{\bar{L}_\Delta}{\rho}\right)_{\text{gas}}^{\text{wall}} \cdot \left(\frac{\bar{\mu}_{\text{en}}}{\rho}\right)_{\text{wall}}^{w} \cdot \prod_i P_{i,w}}{\left(\frac{\bar{L}_\Delta}{\rho}\right)_{\text{gas}}^{\text{wall}} \cdot \left(\frac{\bar{\mu}_{\text{en}}}{\rho}\right)_{\text{wall}}^{g} \cdot \prod_i P_{i,g}} \right) \tag{3.14}$$

$$= D_g \cdot M_g^w \cdot \beta_g^w \cdot \left(\frac{\bar{\mu}_{en}}{\rho}\right)_g^w \cdot P_g^w$$

where β_g^w is approximately unity, but has been included for completeness, while P_g^w is presented as shorthand for the ratio of the products of ionization chamber correction coefficients in water to graphite. The elimination of the stopping power ratios in Eq. 3.14 implies that the electron spectrum in the chamber wall is the same whether the device is in water or graphite.

Similarly, for a thin wall ionization chamber (Eq. 2.17), the conversion expression becomes:

$$D_w = D_g \cdot \left(\frac{D_w}{D_g}\right)_{\text{meas}} = D_g \cdot M_g^w \cdot \left(\frac{\bar{L}_\Delta}{\rho}\right)_{\text{g}}^{\text{w}} \cdot P_g^w \tag{3.15}$$

3.4 REFERENCES

[1]J. Seuntjens, and S. Duane, “Photon absorbed dose standards,” Metrologia **46**, S39-S58 (2009).

[2]N.V. Klassen, and C.K. Ross, “Water calorimetry: the heat defect,” J. Res. Natl. Stand. Technol. **102**, 63-71 (2002).

[3]N.S. Osborne, H.F. Stimson, and D.C. Grinnings, "Measurements of heat capacity and heat of vaporization of water in the range 0 to 100 C," J. Res. Natl. But. Stand. **23**, 197-259 (1939).

[4]S.R. Domen, and P.J. Lamperti, "A heat-loss compensated calorimeter: Theory, design and performance," J. Res. Natl. Bur. Stand. **78**, 595-610 (1974).

[5]J.P. Seuntjens, and A.R. DuSautoy, “Review of calorimeter-based absorbed dose to water standards,” in *Standards and Codes of Practice in Medical Radiation Dosimetry: Proc of an International Symposium* IAEA-CN-96-3 (International Atomic Energy Agency, Vienna, Austria, 2003).

[6]A. Krauss, L. Büermann, H.M. Kramer, and H-J Selbach, “Calorimetric determination of the absorbed dose to water for medium-energy x-rays with generating voltages from 70 to 280 kV,” Phys. Med. Biol. **57**, 6245-6268 (2012).

[7]L. de Prez, J. de Pooter, B. Jansen, and T. Aalbers, “A water calorimeter for on-site absorbed dose to water calibrations in ^{60}Co and MV-photon beams including MRI incorporated treatment equipment,” Phys. Med. Biol. **61**, 5051-5076 (2016).

[8]”Graphite calorimeters are the primary standards for absorbed dose at NPL”, National Physics Laboratory official website, updated 15 Aug 2013, npl.co.uk/science-technology/radiation-dosimetry/research/calorimetry.

[9]A. Ostrowsky, and J. Daures, “The construction of the graphite calorimeter GR9 at LNE-LNHB (geometrical and technical considerations),” LNE-LNHB Technical Report No. CEA-R-6184 (Laboratoire National Henri Becquerel, Paris, France, 2008).

[10]A. Sarfehnia, “Water calorimetry-based radiation dosimetry in iridium-192 brachytherapy and proton therapy,” *Ph.D. thesis* (Montreal: McGill University 2010).

[11]J. Witzani, K.E. Duftschmid, C. Strachotinky, and A Leitner, “A graphite absorbed-dose calorimeter in the quasi-isothermal mode of operation,” Metrologia **20**, 73-79 (1984).

[12]J. Daures, A. Ostrowsky, P. Gross, J.P. Jeannot, and J. Gouriou, “Calorimetry for absorbed-dose measurements at BNM-LNHB,” in *Proc. Workshop on Recent Advances in Calorimetric Absorbed Dose Standards*, CIRM 42 pp 15-21 (National Physical Laboratory, Teddington, UK, 2000).

[13]”Heat transfer module”, Comsol MULTIPHYSICS® official website, updated 2016, https://www.comsol.com/heat-transfer-module

[14]S.V. Patankar, "Numerical heat transfer and fluid flow," (Hemisphere Publishing Corporation, Washington, 1980).

[15]A. Krauss, “The PTB water calorimeter for the absolute determination of absorbed dose to water in ^{60}Co radiation,” Metrologia **43**, 259-272 (2006).

[16]K.J. Stewart, “The development of new devices for accurate radiation dose measurement: a guarded liquid ionization chamber and an electron sealed water calorimeter,” *Ph.D. thesis* (Montreal: McGill University 2007).

[17]B. Owen, and A.R. DuSautoy, “Correction for the effect of the gaps around the core of an absorbed dose graphite calorimeter in high energy photon radiation,” Phys. Med. Biol. **36**, 1699-1704 (1991).

[18]I. Kawrakow, and D.W.O. Rogers, “The EGSnrc code system: Monte Carlo simulation of electron and photon transport,” NRC Technical Report No. PIRS-701 v4-2-2-5 (National Research Council of Canada, Ottawa, Canada, 2007).

[19]S.R. Domen, "Absorbed dose water calorimeter," Med, Phys, **7**, 157-159 (1980).

[20]S.R. Domen, "An absorbed dose water calorimeter: Theory, design, and performance," J. Res. Natl. Bur. Stand. **87**, 211-235 (1982).

[21]C.K. Ross, N.V. Klassen, K.R. Shortt, and G.D. Smith, "A direct comparison of water calorimetry and Fricke dosimetry," Phys. Med. Biol. **34**, 23-42 (1989).

[22]A. Mozumder, and J. L. Magee, "Model of tracks of ionizing radiations for radical reaction mechanisms," Radiat. Res. **20**, 203-214 (1966).

[23]A.W. Boyd, M.B. Carver, and R.S. Dixon, "Computed and experimental product concentrations in the radiolysis of water," Radiat. Phys. Chem. **15**, 177-185 (1980).

[24]M.B. Carver, D.V. Hanley, and K.R. Chaplin, "MAKSIMA-CHEMIST: A program for mass action kinetics simulation by automatic chemical equation manipulation and integration using stiff techniques," AECL, Chalk River Nuclear Laboratories AECL-6413 (1979).

[25]A.J. Elliot, "Rate constants and G-values for the simulation of the radiolysis of light water over 0-300 C range," AECL, Chalk River Nuclear Laboratories AECL-11073 (1994).

[26]J.W. Fletcher, "Radiation chemistry of water at low dose rates-emphasis on the energy balance: a computer study " AECL, Chalk River Nuclear Laboratories AECL-7834 (1982).

[27]N.V. Klassen, and C.K. Ross, "Water Calorimetry: The Heat Defect," J. Res. Natl. Inst. Stand. Technol. **102**, 63-74 (1997).

[28]N.V. Klassen, and C.K. Ross, "Water calorimetry: A correction to the heat defect calculations," J. Res. Natl. Inst. Stan. **107**, 171-178 (2002).

[29]M. Sassowsky, and E. Pedroni, "On the feasibility of water calorimetry with scanned proton radiation," Phys. Med. Biol. **50**, 5381-5400 (2005).

[30]J. Seuntjens, “Comparative study of ion chamber dosimetry and water calorimetry in medium energy x-ray beams,” *Ph.D. thesis* (Gent: Gent University 1991).

[31]R.J. Schulz, L.J. Verhey, M.S. Huq, and N. Venkataramanan, "Water calorimeter dosimetry for 160 MeV protons," Phys. Med. Biol. **37**, 947-953 (1992).

[32]C.K. Ross, and N.V. Klassen, "Water calorimetry for radiation dosimetry," Phys. Med. Biol. **41**, 1-29 (1996).

[33]S. Picard, D.T. Burns, P. Roger, P.J. Allisy-Roberts, M.R. McEwen, C.D. Cojocaru, and C.K. Ross, “Comparison of the standards for absorbed dose to water of the NRC and the BIPM for accelerator photon beams,” Metrologia **47**, 06025 (2010).

[34]J.E. Burns, "Absorbed-dose calibrations in high-energy photon beams at the National Physical Laboratory: conversion procedure," Phys. Med. Biol. **39**, 1555-1575 (1994).

[35]R. Nutbrown, S. Duane, D.R. Shipley, and R.A. Thomas, "Evaluation of factors to convert absorbed dose calibrations from graphite to water for the NPL high-energy photon calibration service," Phys. Med. Biol. **47**, 441-454 (2002).

Chapter 4

THE MCGILL GRAPHITE CALORIMETRY SYSTEM

4.1 INSTRUMENTATION

This section provides an overview of the McGill graphite calorimetry system from a hardware point of view (equipment and circuitry). This section is meant to provide a high level perspective of our experimental setup and to compliment the theory provided in *Chapter* 3. Following this, a section is dedicated to the graphite calorimeter used during this project. The remainder of this Chapter focuses on the details of the methodologies employed throughout the experimental portion of this work.

Figure 4.1 shows a schematic diagram of the experimental setup, including the most important components and electrical connections. A graphite calorimeter is simply an assembly of thermally-insulated nested graphite volumes (typically cylinders) with a very precise thermal control system. The temperature of the graphite bodies are warmed to ~30 °C (well above ambient temperature) to reduce environmental influence, and actively maintained to provide an adequately stable environment to measure sub-mK

radiation-induced temperature rises and sub-mW electrical powers in the case of quasi-adiabatic and isothermal operation, respectively.

The graphite calorimetry system is controlled by various PXI modules (multimeters, power supplies, etc; National Instruments (NI)) which are housed in a 14-slot powered chassis (PXI-1044, NI). An open industry standard, PXI is a PC-based platform for measurement and automation systems combining PCI electrical-bus features with the modular, Eurocard packaging of CompactPCI and synchronization buses.

Similar to the McGill water calorimetry system (see *Chapter* 7), thermistors are used as the sensor of choice in graphite calorimetry. For a typical temperature rise of roughly 1.25 mK/Gy, a thermistor's resistance will decrease by roughly 600 mΩ. These small resistance changes are measured using a passive DC Wheatstone bridge. Thermistors also serve a second important function in the graphite calorimeter: by modulating the current output of a programmable power supply (PXI-4070, NI), embedded thermistors act as Joule heaters.

The resistances of sensing thermistors embedded in a given graphite component are measured as an out-of-balance Wheatstone bridge voltage (*Section* 4.3). A PXI-4070 power supply is used to provide a 1 V bridge excitation. Keithley 2182A nanovoltmeters are used to measure the output voltage from the bridge. The nanovoltmeters allow accurate measurements of the DC signal down to a few nV at a sampling rate of 6 Hz. The nanovoltmeter readouts are acquired by a computer through a General Purpose Interface Bus (GPIB, IEEE-488), which is converted to a USB 2.0 connection (GPIB-USB-HS, NI).

A Burster 1408 high-precision decade resistor box is used to balance the sensing thermistors resistance in the bridge circuit (*i.e.*, a null voltage is recorded as the output signal), and also

to perform bridge calibrations (see *Sections* 4.3 and 7.9.3, respectively). The unit consists of a series of high precision Zeranin® resistors with nominal accuracies of 0.01 % - 0.02 %. The case of the resistance decade box is grounded to earth, and is directly connected to the bridge via a well-shielded coax cable.

In the isothermal mode of operation, the quantity of interest is the electrical power required to dissipate in order to maintain a stable temperature in the graphite calorimeter. To measure the electrical power, two voltage measurements are made using PXI-4070 digital multimeters (NI): (i) the voltage across the heating thermistor network, and (ii) the voltage across a 10 kΩ ± 0.01 % precision shunt (1152 series, Burster) connected serially with the heating thermistors. The latter provides a measure of the current flowing through the resistive elements, while power is calculated as the product of the current and voltage measured in (i).

Due to radiation safety, the operator must be outside the treatment room during experiments. For this reason, sensing and heating thermistor leads are connected by a 15 m two-row DE-9 (serial cable) and three-row DE-15 (VGA cable), respectively, to the bridge in the control area. The bridge box also serves as an interface box for the power supplies (connected via coax) and multimeters (connected via BNC). Communication with the PXI components is achieved through an ExpressCard controller (PXI-8360, NI). To avoid ground loops, all devices and cables are grounded through a single power supply.

In order to simplify the shipping of the instrumentation, the PXI chassis, the nanovoltmeters, and decade resistor boxes are contained within a shock-mounted 19” wide rack case. Removable clamshells at the front and back sides permit access to the various connections.

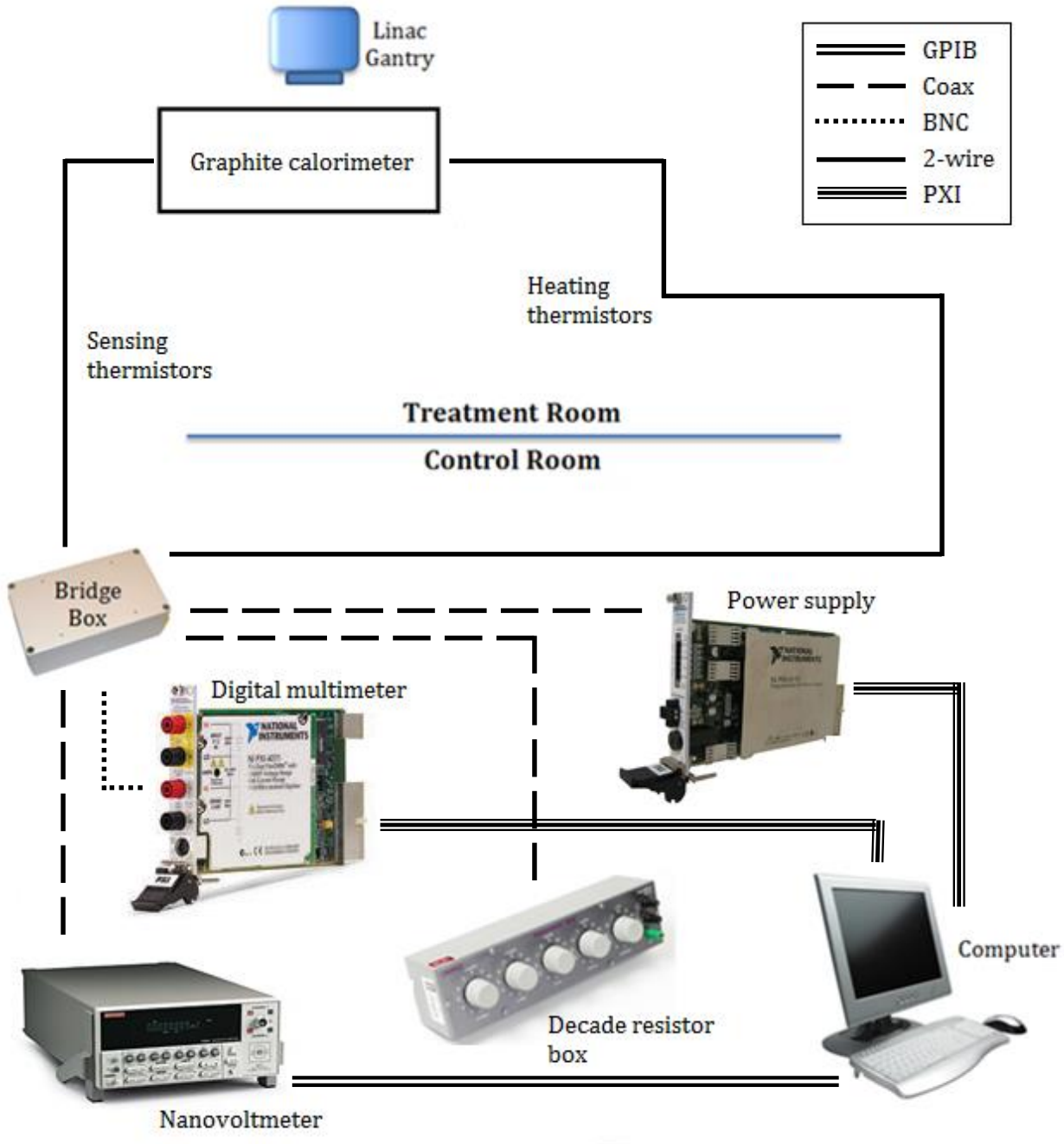

Figure 4.1: A schematic diagram of the graphite calorimetry system setup. All components, their location (inside treatment room or control room), as well as the electrical connections (legend provided) are shown. The true number of connections of the same type between two instruments has been omitted for the sake of clarity. A description of the 'PXI' connection type is provided in *Section* 4.1.

4.2 GRAPHITE PROBE CALORIMETER (GPC)

A detailed description of the in-house built graphite probe calorimeter (GPC) (fourth iteration “MKIV" prototype) is provided in this section. A brief look back at earlier prototypes is also covered to provide context for some of the design choices.

Figure 4.2 shows an isometric view cutaway rendering and a photograph of the fourth (and current) GPC prototype iteration (herein referred to as the GPC-MKIV; also referred to as the Aerrow in *Chapter* 6). The calorimeter consists of three nested graphite cylinders (Grade R 4340, SGL Carbon Group) each of which contain embedded thermistors (USP12837, US Sensor) for temperature sensing and active thermal control. From centre-out, the graphite bodies are referred to as the core, the jacket, and the shield (Figure 4.3). The core is the detector’s sensitive volume and is 6.1 mm in diameter and 10.0 mm long. The jacket and shield are 0.7 mm and 1.0 mm thick, respectively. The graphite bodies are thermally insulated from one another with a layer (0.7 mm and 1.0 mm, respectively) of aerogel-based material (Pyrogel® 2250, Aspen Aerogels Inc.; visible in Figure 4.4). The GPC was designed to be similar in size and shape to a 0.6 cm^3 cylindrical ionization chamber, and used in the radiation therapy clinic in much the same way.

In total, fifteen embedded thermistors with a nominal resistance of 10 kΩ at 25 °C, serve as either temperature sensors or Joule heaters. Each graphite component has one sensing thermistor, and either 3 (core and jacket) or 6 (shield) heating thermistors connected in parallel (referred to as heating networks). Adhesive (Loctite 404, Henkel) is used to fix the thermistors in place. The heating networks have been distributed within their respective graphite bodies to produce an axially-symmetric heating distribution.

The thermistor elements are approximately 0.13 mm thick, 0.28 mm wide, and 0.76 mm long, and are encapsulated in a 3.81 mm long, 0.51 mm diameter polyimide tube. The 38 AWG

(Ø = 0.10 mm), solid conductor, poly-nylon insulated nickel leads are threaded through 0.26 mm diameter holes drilled in the jacket and shield end caps, allowing for electrical connections to be made to a shielded, two-lead 30 AWG (Ø = 0.26 mm) cable outside the graphite assembly. For the jacket and shield, a minimal amount of cyanoacrylate adhesive was used to fasten the end caps to the hollow cylindrical bodies. An acrylic stem was fabricated to envelope and waterproof the calorimeter assembly for submerged dose measurements. It also serves as a rigid shell protecting the electrical connections from the physical strain of handling (Figure 4.4).

Figure 4.2: (Left) An isometric view of a cutaway GPC rendering, with the layers of aerogel-based thermal insulation seen between the three graphite bodies. The graphite assembly is housed in an acrylic stem. (Right) The GPC-MKIV prototype was designed to be similar in size and shape to a 0.6 cm^3 cylindrical ionization chamber, and used in the radiation therapy clinic in much the same way.

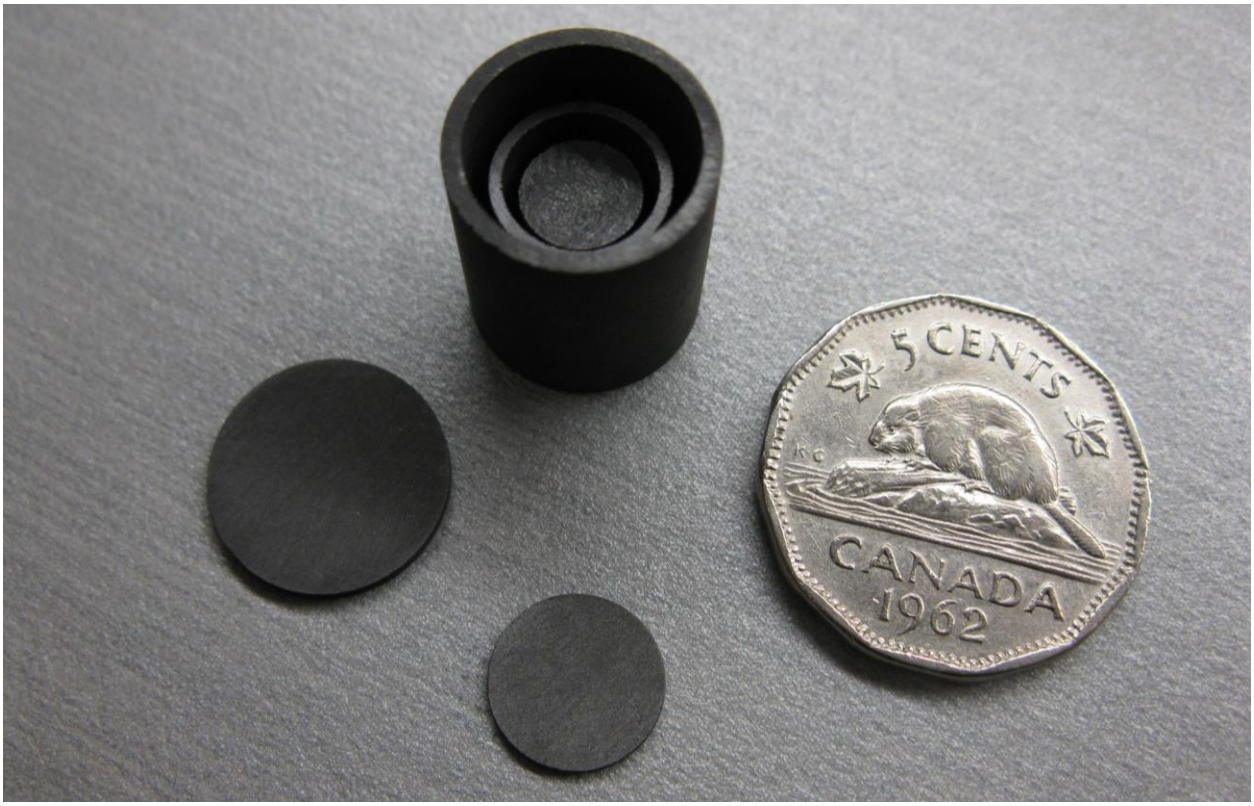

Figure 4.3: The graphite bodies making up the GPC (Grade R 4340, SGL Carbon Group). From centre-out, the graphite bodies are referred to as the core, the jacket, and the shield.

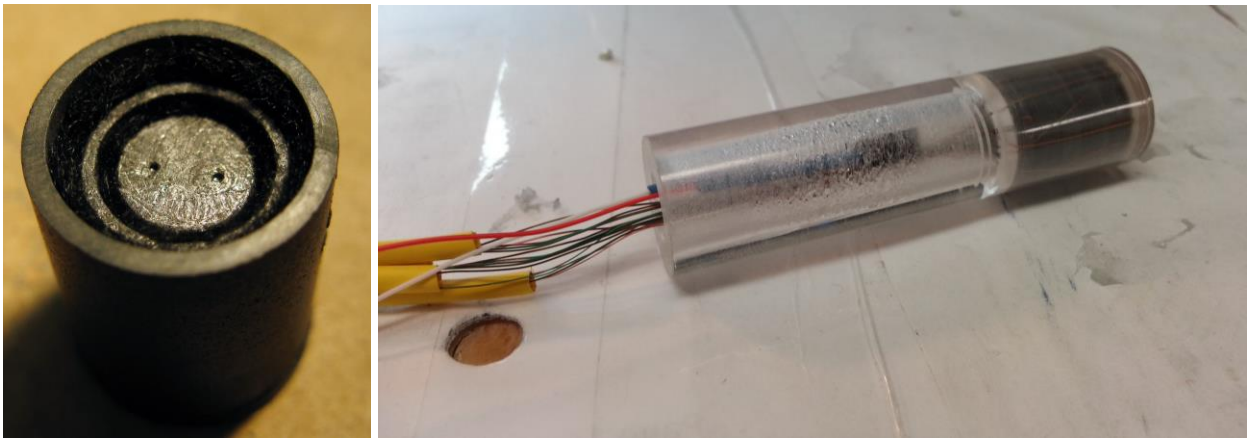

Figure 4.4: (Left) The graphite bodies are thermally insulated from one another with a layer of aerogel-based material (Pyrogel® 2250, Aspen Aerogels Inc.). (Right) An acrylic stem waterproofs the calorimeter assembly and serves as a rigid shell protecting the electrical connections from the physical strain of handling.

4.2.1 Prototype version history

To date, four GPC prototype iterations have been successfully built and tested in-house. To each iteration, improvements in design and construction were applied based on the knowledge acquired from the previous version. In this section, a short description of the history of GPC development is provided.

1) GPC-MKI (2011): The first prototype was built with the help of David Marchington of the National Research Council of Canada's (NRC) Ionizing Radiation Standards group. The probe was assembled at the NRC in Ottawa over a period of two weeks. During this time, experience working with and handling the small thermistors was gained. The MKI contained two thermistors in the core (Thermometrics BR-series; only one functional upon completion), and was intended to be a passive device with no thermal control (Figure 4.5). While an initial set of measurements was acquired suggesting the feasibility of the design, the lone functioning thermistor failed within weeks of construction.

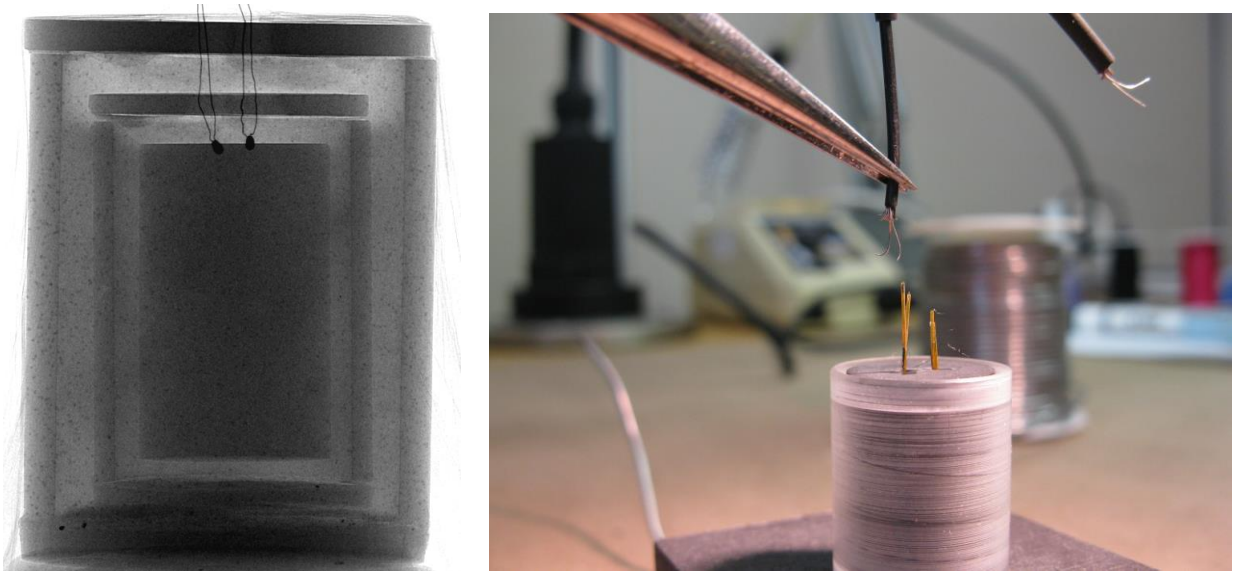

Figure 4.5: (Left) Micro-CT of the GPC-MKI showing a cross-sectional view of the internal structure including the two thermistors embedded in the core. (Right) Construction of the MKI was carried out at the NRC Ionizing Radiation Standards group laboratory.

2) GPC-MKII (2011): Construction of a second prototype was initiated upon failure of the MKI. The MKII design was left unchanged in that the number and arrangement of thermistors was the same as in the MKI. More emphasis was placed upon cable management and strain relief, and as a result, both thermistors survived the assembly process and many months of use afterwards. Data acquired with the MKII established the feasibility of performing absolute dosimetry with such a detector design, the results of which are provided in *Chapter* 5. The MKII is still functional as of late 2016, however its lack of thermal control severely limits its usefulness.

3) GPC-MKIII (2013): The third prototype was the first attempt to incorporate active thermal control into the design. Development began with a relatively inexpensive analogue proportional-integral (PI) temperature controller (Wavelength Electronics, WTC3293-14001). While the number of thermistors in the core was kept at two, the GPC design was modified to include an additional sensing thermistors in the shield and a resistive heating element (Constantan resistance alloy Cu55/Ni45). Figure 4.6 depicts the 90 μm wide resistive wire wrapped around the shield.

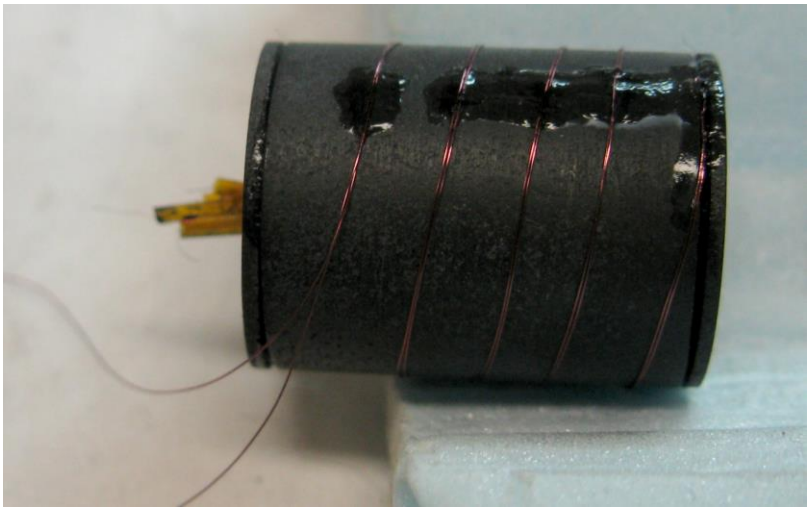

Figure 4.6: GPC-MKIII during the construction phase. A thin Constantan resistive wire is wrapped around the shield in a helical fashion. Holding it in place are drops of adhesive (Loctite 404, Henkel).

The controller was setup to modulate the electrical current flowing the through resistive wire, and thus the electrical power dissipation heating up the graphite assembly. Feedback was provided by the shield thermistor. The hypothesis was that the controller would be able to maintain a stable temperature within the shield, establishing a thermal equilibrium throughout the detector. Unfortunately, adequate stability was never achieved with this setup. In particular, the best short term (~10 min scale) stability was limited to about 1 mK. Development ceased when water infiltrated the acrylic stem, flooding the probe.

4) GPC-MKIV (2014): The vastly different fourth prototype is described in *Section* 4.2. Improved knowledge of thermistor handling and waterproofing has made this iteration particularly robust. Over the last two years, the MKIV has been frequently used in experiments (including overseas). *Chapter* 6 summarizes the most important results acquired in conventional high-energy photon and electron beams.

4.3 FRONT END ELECTRONICS

Thermistor resistances are measured as out-of-balance Wheatstone bridge voltages. On one bridge arm, fixed precision resistors (10 kΩ ± 0.01 %; 71-VSR-B-10K), on the other, the sensing thermistors and an adjustable precision decade resistor box. When both arms are balanced, the voltages across the bridge, as measured by the nanovoltmeter, is zero. Three such bridges are assembled in parallel inside a grounded electronics box (Figure 4.7), one for each body of graphite in the GPC. The box serves as an interface box between the GPC and the instrumentation. Besides the bridge, the box contains inputs from the power supplies for the DC bridge excitation (1 V) and the current flowing to the heating thermistor networks.

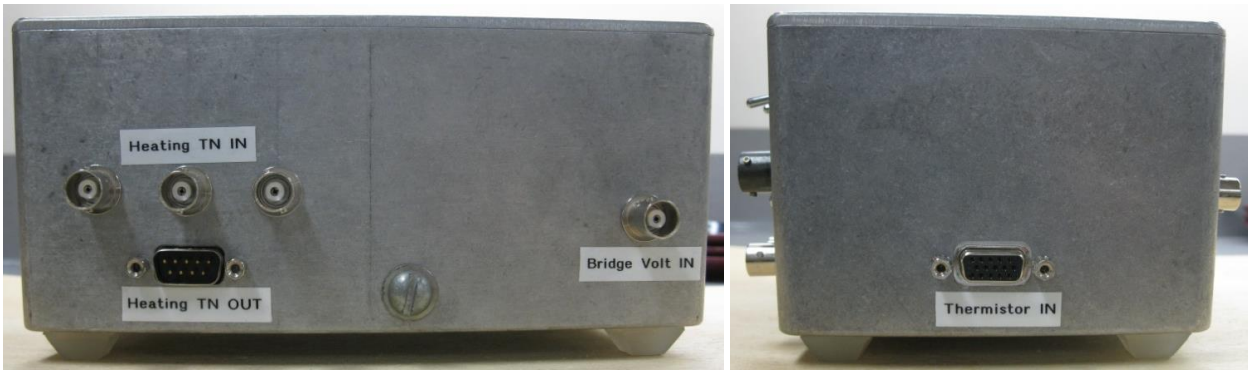

(a) (b)

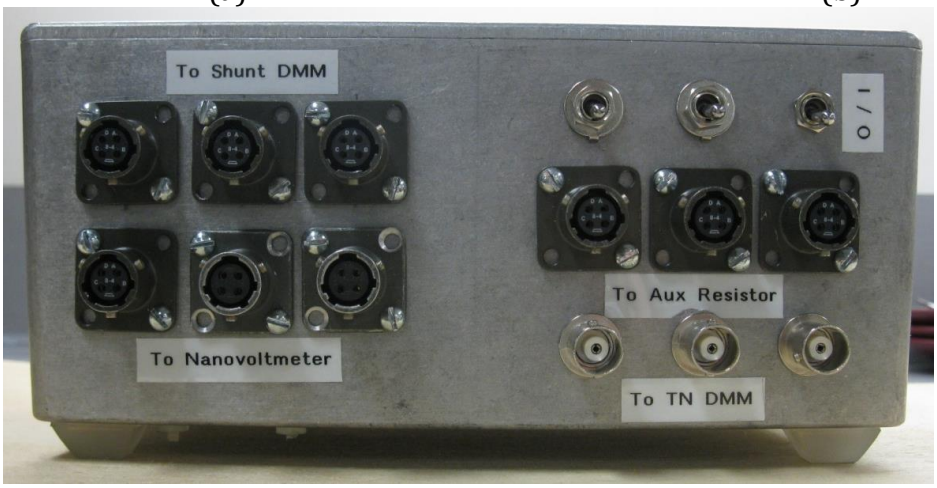

(c)

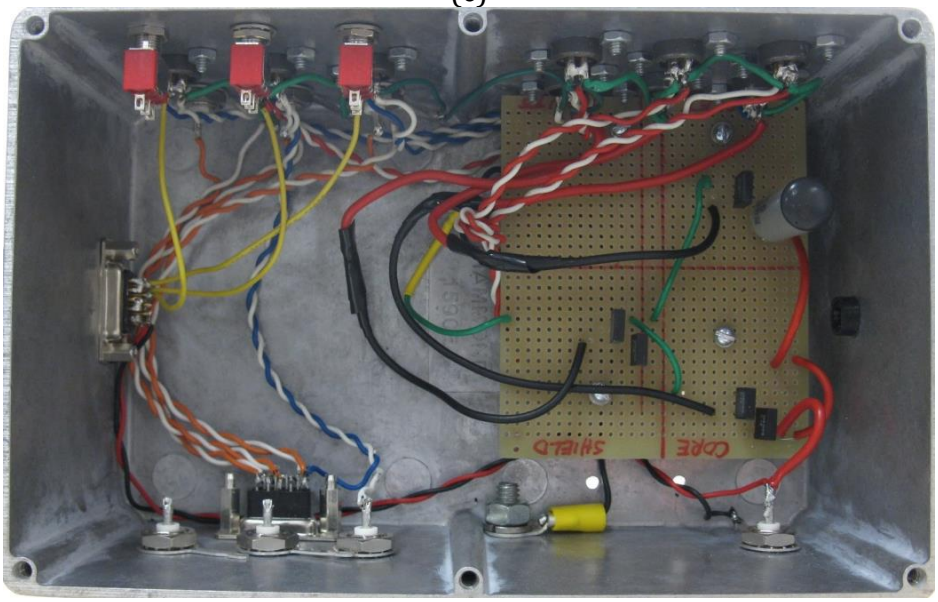

(d)

Figure 4.7: Interfacing electronics box containing three Wheatstone bridge in parallel, as well as inputs and outputs between the instrumentation and the GPC, as seen from the (a) back, (b) side, (c) front, and (d) top.

Round 4-pin military-grade connectors are used to connect the nanovoltmeters, the multimeters measuring the shunt and heating network voltages, and the decade resistor boxes. BNC connectors are used for all other interfacing connections. A two-row DE-9 (serial cable) and a three-row DE-15 (VGA cable) connector are used to connect to the GPC.

4.4 SOFTWARE

Three in-house developed programs were used throughout this work to operate and acquire data from the GPC, analyze the results, and calibrate the sensors. The calibration software, PROBECAL, is also used with the McGill water calorimeter system (see *Section* 7.8). The two other programs were developed in the LabVIEW (NI) and Matlab (MathWorks) environments.

A LabVIEW program was developed to operate the calorimeter and acquire the data during the measurement period. It is used to remotely control the instruments that are connected to the computer via PXI and GPIB controllers. The software has three operation modes: (i) Idle mode is used in between successive runs and continuously displays the readouts from the nanovoltmeters (bridge voltages), multimeters (shunt and heating network voltages), electrical power dissipation in the device (isothermal quantity of interest), as well as the output of the numerical proportional-integral-derivative (PID) controllers. (ii) Run mode is user-initiated and is used to acquire the abovementioned datasets during the measurement cycle. (iii) Simulation mode is used to test the GPC's isothermal performance in a desired irradiation scenario (specified by dose rate and duration). In doing so, the response of the PID to the 'impulse' of energy can be measured (Figure 4.8). The heating effect of radiation is emulated through the manipulation of equivalent electrical parameters, though these two energy deliveries differ in their spatial distribution (localized vs. quasi-uniform). This mode also relies on knowledge of the masses of the graphite bodies (see *Section* 4.5.3).

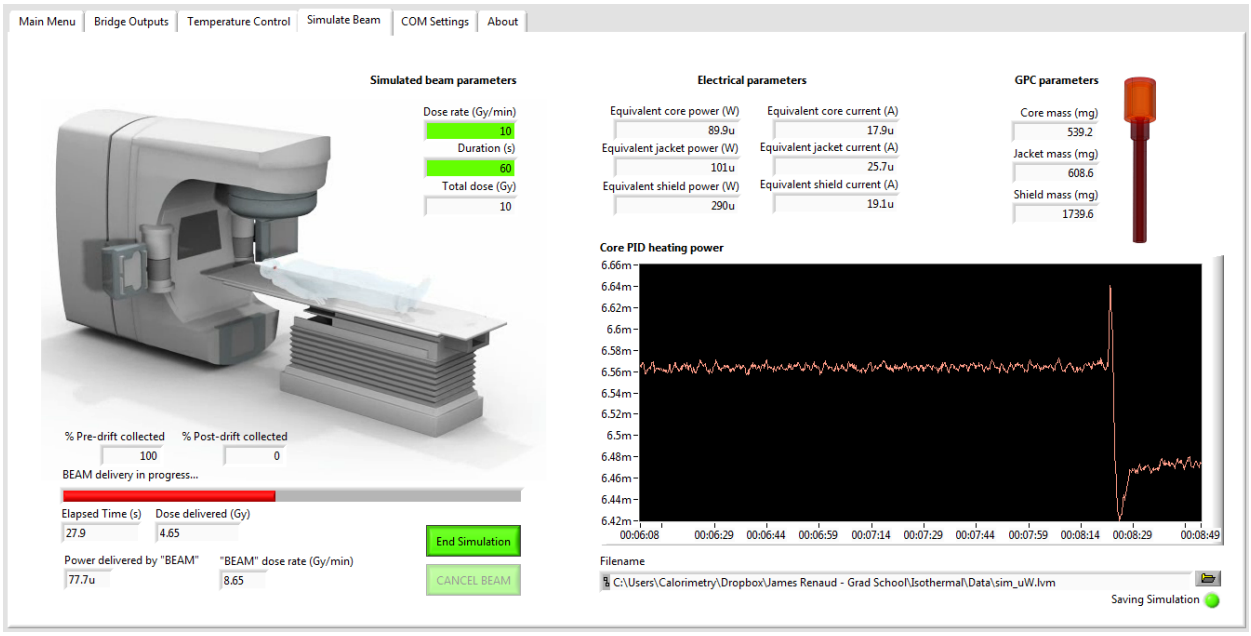

Figure 4.8: Screenshot of the GPC's LabVIEW software 'Simulate Beam' tab half way through the delivery of a simulated 10 Gy/min radiation beam. The large graphical indicator (right; black background) is displaying the output of the numerical proportional-integral-derivative (PID) controller in response to the impulse of the simulated beam.

A Matlab routine was written to automate the analysis of isothermal mode measurements. It does so by fitting the entire run (minus the controller transients when the beam is turned on and off) to either a linear, quadratic, or cubic function. The position and width of the transients are set by the user. The portion of the signal collected during irradiation is then shifted by a small, constant, positive power. The fit is repeated and the quality of the fit (adjusted-R^2) is compared to the previous iteration. This process is looped until a fit of maximum quality is found. The amount of shifting to achieve this optimized fit corresponds to the power deficit, or equivalently, the dose rate of the irradiation. For a given fitting function, a basic sensitivity analysis is carried out by repeating the iterative fitting procedure nine separate times. In each case, the limits over which the fitting are performed (run start, run end, beam on, beam off, and the two transient lengths) are varied by a user-defined value

(5 – 10 seconds). The program outputs the average and standard deviation of all these fits. Combined with the adjusted-R^2, a measure of the quality of the run is provided.

4.4.1 Active thermal control

The LabVIEW acquisition software samples the out-of-balance bridge voltages (process variable) measured by the three nanovoltmeters and feeds the values into independent PID algorithms. Each PID modulates the current output of its respective power supply, driving the electrical power dissipation in the heating elements, and hence the temperature of the core, jacket, and shield to achieve the user-specified setpoints (corresponding to a null bridge output).

The PID algorithms driving the GPC thermal control are adjustable through three tunable gain parameters (K_c, T_i, and T_d). For instance, when operating at 30 °C in room temperature (~22 °C) water, adequate thermal control is achieved in practical timeframe (~5 mins) when the following gain parameter sets are used: core (K_c = 5, T_i = 0.5, T_d = 0.1); jacket (K_c = 5, T_i = 0.5, T_d = 0.1); shield (K_c = 30, T_i = 3, T_d = 0.1).

To understand the tuning process, one must know how these parameters are defined by the error, e:[1]

$$e(k) = (SP - PV(k)) \tag{4.1}$$

where k is the index of the sample signal, SP is the bridge output setpoint (0 V), and PV is the process variable (bridge output voltage). The sampling time of the controller is defined as ΔT.

The controller output (power supply current), $u(k)$, is driven by three separate actions, u_x, defined below; it is the sum of the proportional, integral, and derivative actions, as shown below:

$$u(k) = u_p(k) + u_i(k) + u_d(k) \tag{4.2}$$

where the proportional action, u_p, is defined in terms of K_c, the controller gain by:

$$u_p(k) = K_c \cdot e(k) \tag{4.2a}$$

The second action is the integral action, u_i, which is calculated using a method known as trapezoidal approximation. It adjusts the output to compensate for the sum of all past errors, with the intention of completely eliminating them in a time, T_i (also referred to as the integral gain, measured in minutes).

$$u_i(k) = u_i(k-1) + \frac{K_c}{T_i} \cdot \left(\frac{e(k) - e(k-1)}{2}\right) \cdot \Delta T \tag{4.2b}$$

The third action is the derivative component, u_d. Along with the proportional component, the purpose of derivative component is to effectively predict the error at a time, T_d (also referred to as the derivative gain, measured in minutes), in the future.

$$u_d(k) = -K_c \cdot \frac{T_d}{\Delta T} \cdot (PV(k) - PV(k-1)) \tag{4.2c}$$

4.5 CALIBRATION

In general, graphite calorimeters can be operated in two independent dose-measuring modes (see *Section* 3.1.2): quasi-adiabatic and isothermal. A technical description of these modes, as they pertain to the GPC can be found in *Chapter* 6. As a primary dose standard, graphite calorimeters can measure absorbed dose from radiation without having to be cross-calibrated against another dosimeter. Similar to water calorimetry, a graphite calorimeter can measure dose quasi-adiabatically provided that temperature can be defined and measured. The temperature is not directly measured, but rather from a measurement of the voltage output of the bridge in response to a chance in the thermistor resistance. For

isothermal, dose can be quantified based on the core mass and electrical power, which in turn is defined in terms of voltage and resistance measurements. The subsections below describe the calibrations necessary to operate the McGill graphite calorimetry system.

4.5.1 Quasi-adiabatic mode

The calibration procedure for the GPC's quasi-adiabatic mode is essentially the same as the methodology used for the McGill water calorimetry system. For a detailed description of the thermistor and bridge calibrations, see *Section* 7.9. In brief, the change in bridge voltage, $\Delta V_{1\Omega}$, is related to a relative change in thermistor resistance, $\frac{\Delta R_{1\Omega}}{R_{\text{burster}}}$, through so-called bridge calibrations (user-induced bridge resistance change of 1 Ω), which are carried out periodically throughout the measurement session.

Collectively, these results provide a bridge calibration curve, which relates bridge output per 1 Ω resistance change as a function of temperature. The bridge calibration curve allows for the determination of the radiation-induced thermistor resistance change from the measurement of the bridge response, ΔV_{irrd}.

The change in thermistor resistance is in turn related to a radiation-induced temperature rise, ΔT, using a separately measured thermistor calibration curve (R vs. T; Figure 4.9). A thermistor calibration curve is acquired by submerging a thermistor in a calibrated chiller reservoir and accurately measuring its resistance. It is expressed parametrically through two experimentally-fitted functions, $R_0(T)$ and $\beta(T)$, descriptions of which are provided in *Chapter* 7. Ultimately, the temperature calibration is traceable to a national standard through the use of a mercury thermometer. Dose to the core, D_{core}, is calculated by multiplying a measured temperature rise by the specific heat capacity of core, $c_{p,\text{core}}$.

$$D_{\text{core}} = \frac{\Delta E_{\text{rad}}}{m_{\text{core}}} \cdot \prod_i k_i = c_{p,\text{core}} \cdot \Delta T \cdot \prod_i k_i$$
$$= c_{p,\text{core}} \cdot S^{-1} \cdot \frac{\Delta V_{\text{irrd}} \cdot \Delta R_{1\Omega}}{\Delta V_{1\Omega} \cdot R_{\text{burster}}} \cdot \prod_i k_i \quad (4.3)$$

where S is the sensing thermistor sensitivity:

$$S = \frac{1}{R} \cdot \frac{\mathrm{d}R}{\mathrm{d}T} = -\frac{\beta}{T^2} \quad (4.4)$$

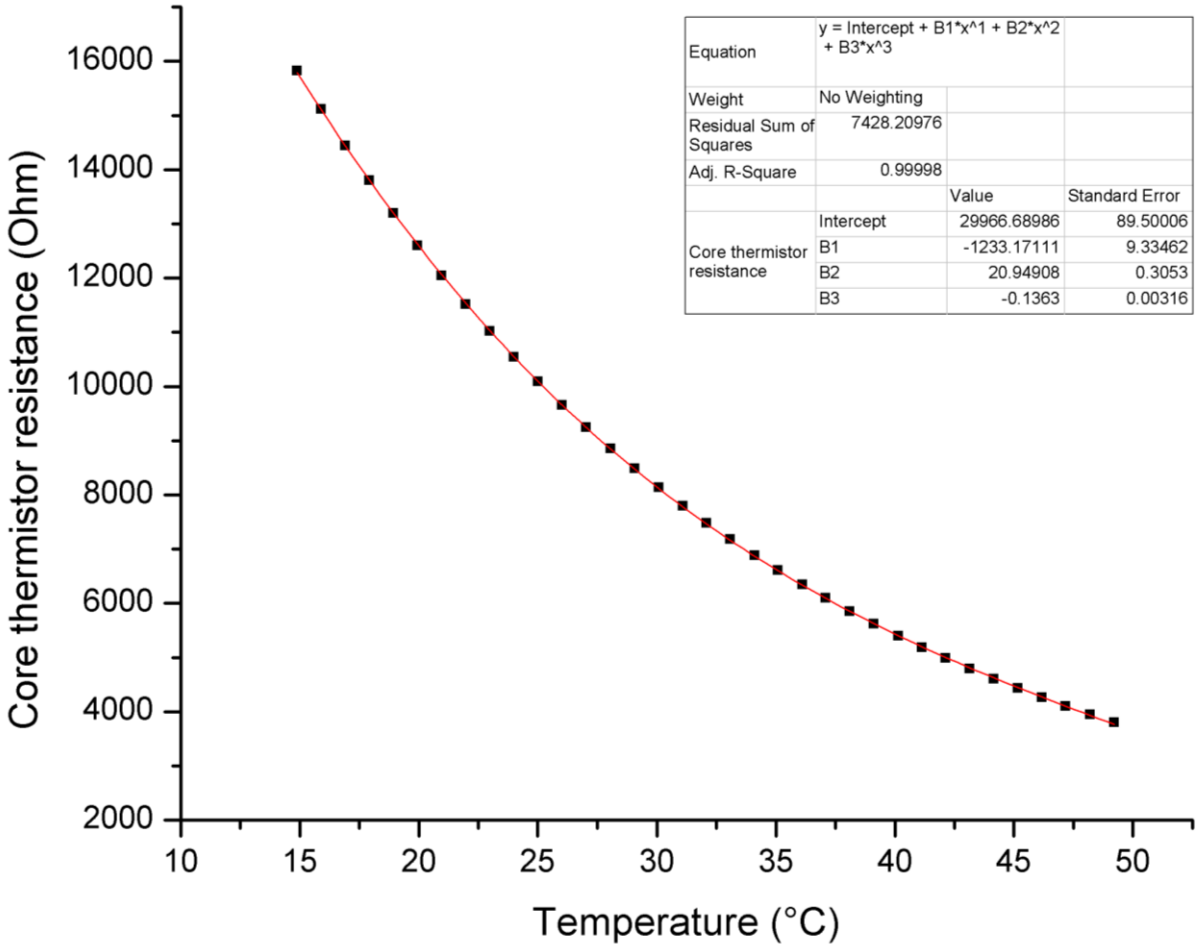

Figure 4.9: Resistance-temperature calibration curve for the core sensing thermistor. Resistance uncertainties are on the order of 0.1 Ω and are too small to view at this scale.

4.5.2 Isothermal mode

In this mode, the raw calorimetric signal is the electrical power dissipated in the core's ohmic heater network, P_{core}. Integrating the deficit in this curve during the period of irradiation and dividing by the mass of the core, m_{core}, yields the absorbed dose to the core, D_{core}. As mentioned in *Section* 4.1, the core power dissipation is determined from the voltage across the heater network, V_{heat}, combined with the voltage across a precision shunt with resistance R_{shunt}, connected serially with the heater network, V_{shunt} (yields the heater current). Hence, besides the core mass, the determination of absorbed dose in isothermal mode relies on the accuracy of the electrical calibration of the instruments used to measure the abovementioned voltages.

Ideally, D_{core} would correspond exactly to the dose to graphite. However, like all graphite calorimeters, the core of the GPC consists of a certain amount of non-graphite materials (*e.g.*, thermistors, epoxy, thermal insulation, etc.), herein referred to as impurities. The presence of impurities contribute to the effective mass, m_{core}, and specific heat capacity of the core, $c_{p,\text{core}}$.[2] For reference, the mass of graphite in the core is approximately 539 mg. *Chapter* 6 provides a listing of the relevant material properties of the impurities present in the GPC-MKIV core, along with a description of how these were determined. The effective mass of the core, m_{core}, is evaluated as the sum of the graphite, m_{gr}, and the impurities, m_i, the latter being weighted by the respective impurity dose contribution, D_i, relative to graphite, D_{gr}:[3]

$$m_{\text{core}} = m_{gr} + \sum_i m_i \cdot \left(\frac{D_i}{D_{gr}}\right) \tag{4.5}$$

Incorporating Eq. 4.3 into the isothermal expression for core dose:

$$\begin{aligned} D_{\text{core}} = \frac{\Delta E_{\text{rad}}}{m_{\text{core}}} \cdot \prod_i k_i &= \frac{\int P_{\text{core}}(t) \cdot dt}{m_{\text{core}}} \cdot \prod_i k_i \\ &= \frac{R_{\text{shunt}}^{-1} \cdot \int V_{\text{heat}}(t) \cdot V_{\text{shunt}}(t) \cdot dt}{m_{gr} + \sum_i m_i \cdot \left(\frac{D_i}{D_{gr}}\right)} \cdot \prod_i k_i \end{aligned} \tag{4.6}$$

The dependence of the effective mass upon the dose ratio introduces a slight energy dependence to the response of the calorimeter. In some cases, an alternative notation is used in which the effective mass of the core is evaluated at a simple sum (*i.e.*, Eq. 4.5 without the dose ratio), and an impurity correction, k_{imp}, is defined:[3]

$$k_{\text{imp}} = \frac{m_{gr} + \sum_i m_i}{m_{gr} + \sum_i m_i \cdot \left(\frac{D_i}{D_{gr}}\right)} \tag{4.7}$$

Typical values of k_{imp} are on the order of 0.996 for graphite calorimeters in the primary dose standards lab setting. While Monte Carlo radiation transport simulations can be used to accurately evaluate $\left(\frac{D_i}{D_{gr}}\right)$, a first order estimate can be obtained for photon beams if by taking the ratio of the mean mass energy-absorption coefficients, $\left(\frac{\mu_{en}}{\rho}\right)_{gr}^{i}$, evaluated at the mean secondary electron energy. For instance, for a conventional 6 MV photon beam, when considering only the nickel, which constitutes about 70 % of the total impurity mass (the only impurity with readily available $\left(\frac{\mu_{en}}{\rho}\right)_{gr}^{i}$ data), k_{imp} is approximately 0.5 %. This approach assumes that the photon energy fluence is constant in both the graphite and the impurities, and that the range of the secondary electrons is small compared to the dimensions of the impurities. For reference, the continuous slowing down approximation (CSDA) range of 0.5 MeV electrons in graphite and nickel is 1.2 mm and 0.3 mm, respectively.

The presence of impurities also contribute to an effective core specific heat capacity, $c_{p,\text{core}}$, which is evaluated similarly to the effective core mass. The presence of impurities unavoidably introduces a slight energy dependence in both the quasi-adiabatic and isothermal modes of operation. For the quasi-adiabatic mode, assuming that the measured core temperature rise, ΔT, is a weighted average of the graphite and impurity temperature rises:

$$\Delta E = \sum_i m_i \cdot c_{p,i} \cdot \Delta T = (m_{gr} \cdot c_{p,gr} + \sum_i m_i \cdot c_{p,i}) \cdot \Delta T$$
$$= m_{gr} \cdot (c_{p,gr} + \sum_i \frac{m_i \cdot c_{p,i}}{m_{gr}}) \cdot \Delta T \quad (4.8)$$

Substituting Eq. 4.5 and 4.8 into Eq. 4.3, the core dose as measured in the quasi-adiabatic mode, yields:

$$D_{\text{core}} = \frac{\Delta E_{\text{rad}}}{m_{\text{core}}} \cdot \prod_i k_i = \frac{m_{gr} \cdot \left(c_{p,gr} + \sum_i \frac{m_i \cdot c_{p,i}}{m_{gr}}\right)}{m_{gr} + \sum_i m_i \cdot \left(\frac{D_i}{D_{gr}}\right)} \cdot \Delta T \cdot \prod_i k_i$$
$$= c_{p,\text{core}} \cdot \Delta T \cdot \prod_i k_i \quad (4.9)$$

Alternatively, the effective core specific heat capacity could simply be taken as the specific heat capacity of graphite (*i.e.,* $c_{p,\text{core}} \equiv c_{p,\text{gr}}$), and an impurity correction, k_{imp}, specific to the quasi-adiabatic mode could be defined as:

$$k_{\text{imp}} = \frac{m_{gr} + \sum_i m_i \cdot \left(\frac{c_{p,i}}{c_{p,gr}}\right)}{m_{gr} + \sum_i m_i \cdot \left(\frac{D_i}{D_{gr}}\right)} \quad (4.11)$$

By comparing the two expressions for k_{imp} (Eq. 4.7 and Eq. 4.11), it is clear that the impurity effect is more important when operating in the quasi-adiabatic mode, as the ratio of specific heat capacities can easily range from 0.5 - 2. Regardless of operating mode, one of the objectives when designing a graphite calorimeter is to minimize the presence of impurities in proximity to the core.

4.6 REFERENCES

[1]D.E. Sebord, T.F. Edgar, and D.A. Mellichamp, "Feedback Controllers," in *Process Dynamics and Control Second Edition*, ed. B. Zobrist (Wiley, Hoboken NJ, USA, 2004).

[2]J. Witzani, K.E. Duftschmid, Ch. Strachotinsky, and A. Leitner, "A graphite absorbed-dose calorimeter in the quasi-isothermal mode of operation," Metrologia 20, 73-79 (1984).

[3]Y. Morishita, M. Kato, N Takata, T Kurosawa, T. Tanaka, and N. Saito, "A standard for absorbed dose rate to water in a ^{60}Co field using a graphite calorimeter at the national metrology institute of Japan," Radiat. Prot. Dosim. 1–9 (2012).

Chapter 5

DEVELOPMENT OF A GRAPHITE PROBE CALORIMETER FOR ABSOLUTE CLINICAL DOSIMETRY

In this chapter, the numerical design, construction, and initial validation of a probe-format graphite calorimeter conceived for clinical dose measurement is presented. The results of this work include dose measurements performed directly in water using the graphite calorimeter and a reference class cylindrical ionization chamber following the AAPM TG-51 protocol. The dose is measured in a clinical accelerator-based 6 MV photon beam. The absolute measures of dose as determined using the calorimeter and the ionization chamber are directly compared, and an estimated breakdown of the overall uncertainty on the calorimeter dose is provided. This work establishes the feasibility of using such a design in the clinical environment as a practical means of measuring absolute dose to water in therapeutic photon beams.

Authors: James Renaud[1], David Marchington[2], Jan Seuntjens[1], and Arman Sarfehnia[1]

[1]Medical Physics Unit, McGill University, Montréal, Québec, H3G 1A4, Canada
[2]Ionizing Radiation Standards, National Research Council of Canada, Ottawa, Ontario, K1A 0R6, Canada

ABSTRACT

Purpose: The aim of this work is to present the numerical design optimization, construction and experimental proof of concept of a graphite probe calorimeter (GPC) conceived for dose measurement in the clinical environment (U.S. provisional patent 61/652,540).

Methods: A finite element method (FEM) based numerical heat transfer study was conducted using a commercial software package to explore the feasibility of the GPC and to optimize the shape, dimensions and materials used in its design. A functioning prototype was constructed in-house and used to perform dose to water measurements under a 6 MV photon beam at 400 MU/min and 1000 MU/min, in a thermally insulated water phantom. Heat loss correction factors were determined using FEM analysis while the radiation field perturbation and the graphite to water absorbed dose conversion factors were calculated using Monte Carlo simulations.

Results: The difference in the average measured dose to water for the 400 and 1000 MU/min runs using the TG-51 protocol and the GPC was 0.2 % and 1.2 %, respectively. Heat loss correction factors ranged from 1.001 to 1.002, while the product of the perturbation and dose conversion factors was calculated to be 1.130. The combined relative uncertainty was estimated to be 1.4 %, with the largest contributors being the specific heat capacity of the graphite (type B, 0.8 %) and the reproducibility, defined as the standard deviation of the mean measured dose (type A, 0.6 %).

Conclusions: By establishing the feasibility of using the GPC as a practical clinical absolute photon dosimeter, this work lays the foundation for further device enhancements, including the development of an isothermal mode of operation and an overall miniaturization, making it potentially suitable for use in small and composite radiation fields. It is anticipated that,

through the incorporation of isothermal stabilization provided by temperature controllers, a sub-percent overall uncertainty will be achieved.

5.1 INTRODUCTION

Calorimetry is a unique primary absorbed dose to water standard in that device calibration can be achieved entirely in terms of quantities with traceable standards (electrical energy and temperature) independent of radiation.[1] Unfortunately, due to their general bulkiness and fragility, calorimeters are currently impractical to use as routine clinical dosimeters, and as such, they have been limited to standards laboratories.

Ionization chambers have long been relied upon for reference clinical dosimetry in conventional radiation fields.[2,3] However, with the emergence of linear accelerators and other specialized treatment units (GammaKnife®, CyberKnife®, TomoTherapy®, etc.) designed for intensity modulated radiation therapy and/or stereotactic radiosurgery, comes the need for new protocols that address calibration in nonstandard radiation fields[4], a practice currently lacking an international standard. As shown by Duane *et al.*[5], a sufficiently miniaturized calorimeter can offer a more direct and accurate way of measuring absorbed dose to water in small and composite radiation fields by doing away with the need to transfer calibration factors according to the radiation beam quality of interest and serve as an independent check for other dosimeters.

In the late 1970's, Sundara Rao and Naik[6] demonstrated the feasibility of calibrating ionization chambers and other dosimeters in terms of absorbed dose to water in a ^{60}Co beam

using a graphite calorimeter similar in dimension and shape to a Farmer-type ionization chamber. Despite achieving an overall estimated calibration accuracy of ± 1.2 %, dosimetry of clinical megavoltage beams using a small-scale graphite calorimeter has not yet been explored; but, if successful, it could potentially open the door to a self-calibrating clinical reference dosimeter.

The aim of this paper is to present the numerical design optimization, construction and experimental proof of concept of a graphite probe calorimeter (GPC) for absolute dosimetry in the clinical environment (U.S. provisional patent 61/652,540). The enabling idea was the incorporation of an aerogel-based material as thermal insulation, rather than the traditional vacuum[7-9], which makes the portability and robustness of the GPC design suitable for routine clinical use.

5.2 METHODS

5.2.1 Design Considerations

A numerical design optimization study was conducted over the past two years with the intent to fabricate a clinically-suitable graphite calorimeter capable of operation in both high-energy photon and electron beams (^{60}Co to 18 MV x-rays and 4 to 25 MeV electrons) and at dose rates in the range of normal clinical linear accelerator operation and higher. With an emphasis placed on portability and ease-of-use, the format of the calorimeter was chosen to be probe-like, similar in size to an air-filled 0.6 cm^3 ionization chamber, giving it a comparable spatial resolution. The design was also kept robust enough to allow for repeated handling. The overarching goal of the GPC is to develop an absolute clinical dosimeter

capable of providing a direct measurement of absorbed dose to water to within a sub-percent uncertainty in a practical time frame.

5.2.2 Heat Transfer Modeling

In the absence of electrical heating, a graphite calorimeter measures the dose averaged over a graphite core volume based on its fundamental relation to temperature rise and the heat transfer[1], as shown below:

$$\bar{D}_{gr} = c_{gr,p} \cdot \Delta T_{gr} \cdot k_{ht} \cdot \prod k_i \qquad (5.1)$$

where ΔT_{gr} is the temperature rise averaged over the core due to radiation, and $c_{gr,p}$ is the specific heat capacity of graphite at constant pressure. The temperature rise is traditionally determined by linearly fitting the pre- and post-irradiation temperature traces, extrapolating them to the midpoint of the irradiation period and measuring the relative difference in temperature.[10]

Since heat loss, k_{ht}, is the most significant effect perturbing an accurate dose measurement, the GPC design optimization was primarily driven by a finite element method-based numerical heat transfer study conducted using COMSOL Multiphysics® v.4.2 software (Fig. 5.1(a) and (b)). The product, $\prod k_i$, corrects for lesser effects which are not included in this proof of principle, including the presence of impurities in the graphite, which is assumed to be small for a probe of this size, and the volume averaging effect of the core. These effects are assumed to be relatively minor and will be the subject of future investigation.

Throughout the optimization process, a 2D axially-symmetric modeling of the GPC was conducted, dramatically reducing the number of mesh elements (degrees of freedom) required to describe the detector geometry. Thermal properties of the involved materials,

boundary conditions, and distribution of heat sources and sinks in space and time were included as input parameters.

5.2.3 Design Optimization

Heat transfer simulations were conducted to determine the optimal number and shape of nested graphite components (core, jackets, and shield) to minimize the heat transfer experienced in the core. A number of constraints were imposed on the optimization to narrow the design solution space: i) The minimum thickness of any component was set to 0.5 mm to limit the difficulty of prototype fabrication and assembly. ii) The maximum thermal insulation layer thickness was set to 1.0 mm to avoid overly large radiation field perturbation effects. iii) The mass of each jacket was kept equal to that of the core to minimize the magnitude of the radiation-induced thermal gradients across these bodies when they absorb the same average dose.

Both the cylinder and the sphere were considered as base geometries. The choice of shape affects the surface area to volume ratio of the core and the amount of heat transfer experienced in a given volume. Air, expanded polystyrene and a flexible aerogel-based material (Pyrogel® 2250, Aspen Aerogels, Inc.) were investigated as possible thermal insulations. The relevant thermal properties of these materials are listed in Table 5.1. Vacuum gaps were not considered because the associated pumping system would have undermined our desire for a lightweight, portable calorimeter system.

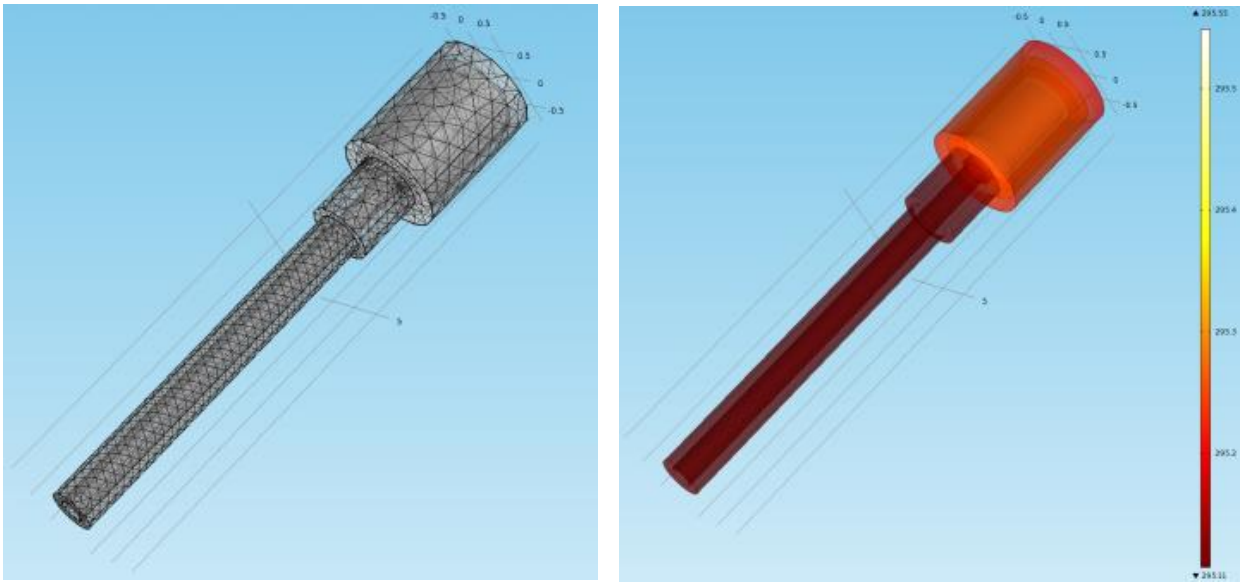

(a) (b)

Figure 5.1: (a) Finite element analysis of the GPC using COMSOL Multiphysics®. Thermal properties of the involved materials, boundary conditions, and distribution of heat sources and sinks in space and time are included as input parameters. (b) Resulting radiation-induced temperature distribution (295.11 K < T < 295.55 K) in the GPC at a time point, t, post-irradiation.

Table 5.1. Material properties used in simulating heat transport with COMSOL Multiphysics® at 22 °C.

Material	Mass density ($kg \cdot m^{-3}$)	Specific heat capacity ($J \cdot kg^{-1} \cdot K^{-1}$)	Thermal conductivity ($W \cdot m^{-1} \cdot K^{-1}$)
Pyrogel® 2250	170[a]	1046[a]	0.0155[a]
Expanded Polystyrene	997.8[b]	4.1823[b]	0.6009[b]
Air	1.194[b]	1005[b]	0.0259[b]

[a] Taken from Ref. 11

[b] Taken from Ref. 12

Optimization was initially carried out using an axially-symmetric heat conduction model in which the initial temperature of the GPC was set above ambient and was left to reach thermal equilibrium with a surrounding environment of 22 °C. For each design variation, the average temperature of the core was traced as it decreased exponentially, and the degree of thermal isolation was quantified by measuring the associated time constants. Later, a Monte Carlo (MC) calculated heat source defined in space and time to mimic the effects of the dose distribution deposited by a 6 MV photon beam was added to the heat transport model. Heat transfer correction factors, k_{ht}, were determined by measuring the ratio of the temperature rise in the core in the absence of heat transfer to that of the realistic case. The model was further refined through the addition of thermistors with electrical power dissipation, platinum alloy leads and a Lucite stem.

5.2.4 Monte Carlo Simulations

A 2D axially-symmetric model of the GPC inside a water phantom was simulated with the DOSRZnrc user code of the EGSnrcMP[13] MC code system. An in-house developed 6 MV photon spectrum and an electron energy cutoff of 521 keV were used. The radiation field perturbation correction[14,15] due to the presence of the Pyrogel®, and the graphite to water absorbed dose conversion factor[16] were calculated together as the ratio of the MC-scored dose in the GPC core volume to that of an equivalent volume of water at the same depth in a water-only model. Since both of these quantities are beam quality-dependent, knowledge of the incident radiation spectrum is required to accurately calculate them. The dose averaged over the volume can also be converted to absorbed dose to a point.

5.2.5 Graphite Probe Calorimeter

Figures 5.2(a) and (b) show a schematic diagram and microCT scan of the resulting optimized GPC design used in this work. Pyrogel® was selected as the insulator due to its

relatively low thermal conductivity and because of its ease of manipulation. Made up of concentric cylinders, the 6.0 mm diameter, 10.0 mm long graphite core is separated from a 0.7 mm thick jacket by a 0.7 mm isotropic layer of insulation. Likewise, a 1.0 mm layer of insulation thermally isolates the jacket from a 1.0 mm thick graphite shield.

5.2.6 Construction

The GPC prototype consists of cylindrically nested components of graphite (Grade R 4340, SGL Carbon Group) with a density of 1.72 g/cm^3 and Pyrogel® thermal insulation. Two negative temperature coefficient thermistors with a nominal resistance of 10 kΩ at 25 °C and a bead diameter of 0.36 mm were fixed to the core (111-103EAJ-H01, Honeywell) (Fig. 5.3(a)). The 9.6 mm long platinum alloy thermistor leads were covered by polyimide tubing with an inner diameter of 0.18 mm and were threaded through 0.5 mm diameter holes in the jacket (Fig. 3(b)) and shield caps, allowing for electrical connections to be made to a shielded, two-lead cable outside the body. For the jacket and shield, a high-purity (99 %) graphite adhesive (931, Cotronics Corp.) was used to fasten the end caps to the hollow cylinder bodies. A Lucite stem was fabricated to encapsulate and waterproof the GPC for submerged dose measurements (Fig. 5.3(c)). It also serves as a rigid shell protecting the electrical connections from the physical strain of handling.

5.2.7 Absorbed Dose Measurements

Twenty-five absorbed dose to water measurements were made using the GPC prototype in a 6 MV photon beam using a Novalis Tx (Varian Medical Systems) radiosurgery system. The GPC was positioned vertically and coincident with the central beam axis at a depth of 5.0 cm inside of a 30 x 30 x 30 cm^3 temperature-controlled water phantom at an SSD of 107.3 cm. The water set point temperature was set to 24 °C and left to stabilize overnight. Temperature control was shut off before performing absorbed dose measurements at dose rates of

400 MU/min and 1000 MU/min. A collimator setting of 10 x 10 cm^2 was used throughout the experiment. Raw calorimetric signals acquired were the voltage output of an active bridge type circuit (Fig. 5.4). Bridge voltage was related to a relative change in thermistor resistance through Ohm-calibrations (see inlay of Fig. 5.4) conducted during the experimental session. Change in thermistor resistance was in turn related to a temperature rise using a prior-measured thermistor calibration curve. The corresponding dose to graphite measurements were then corrected for heat transfer and radiation field perturbation effects and converted to water dose using MC-calculated data. GPC-acquired dose to water values were compared against dose to water measurements made with an Exradin A12 ionization chamber (Standard Imaging, Inc.) with a calibration traceable to a primary standards laboratory (National Research Council of Canada), following the AAPM TG-51 protocol[17].

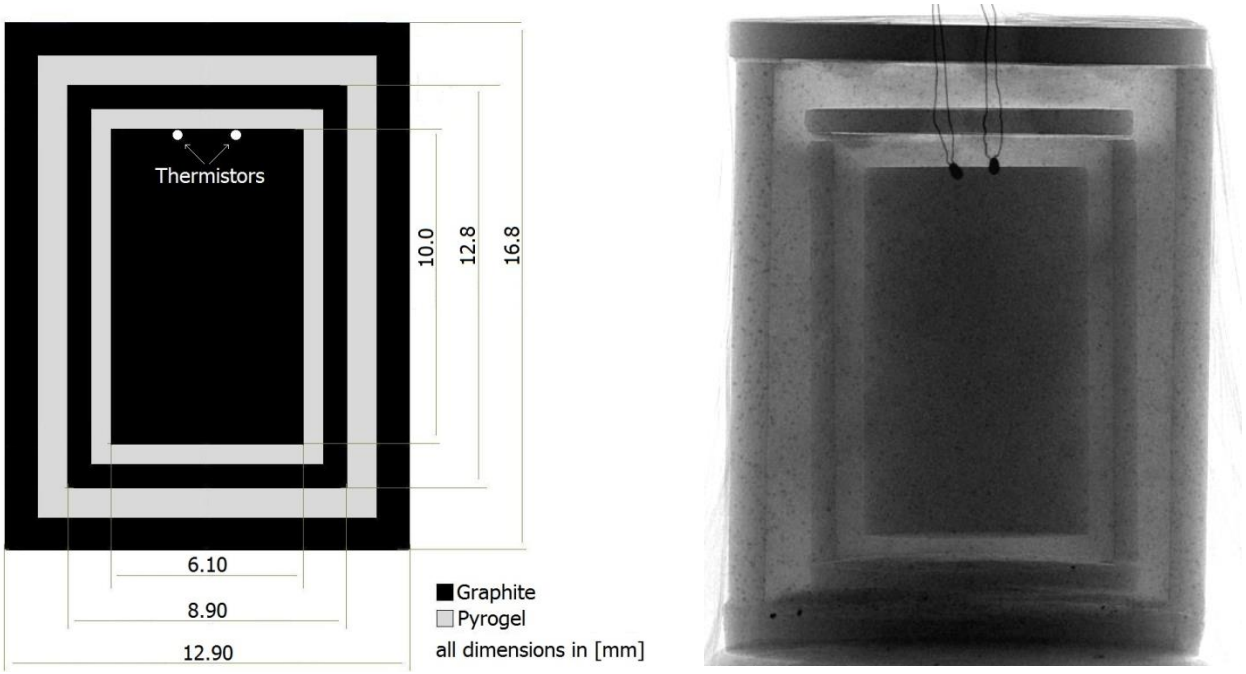

(a) (b)

Figure 5.2: (a) A schematic diagram of the optimized GPC design. (b) A microCT scan of the constructed GPC prototype showing the thermistors fixed to the core.

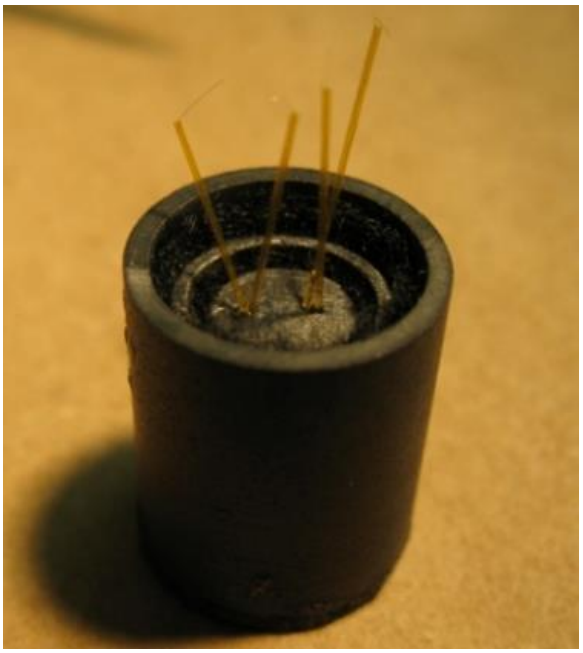

(a)

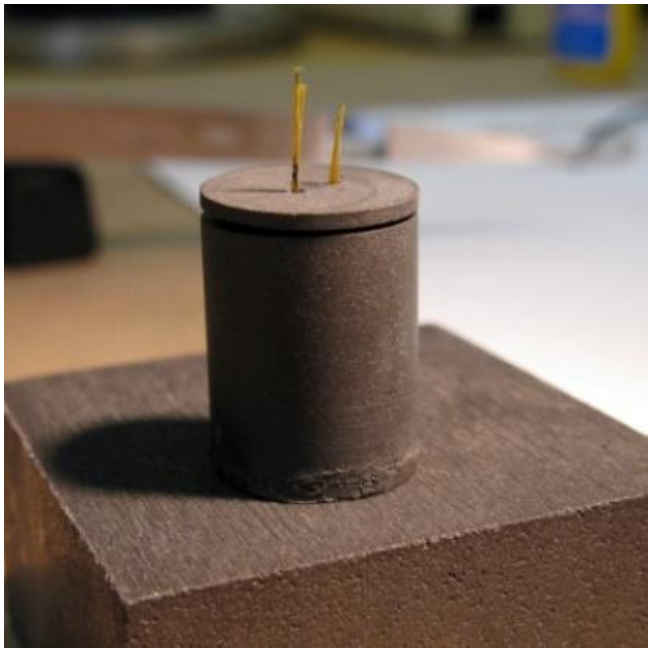

(b)

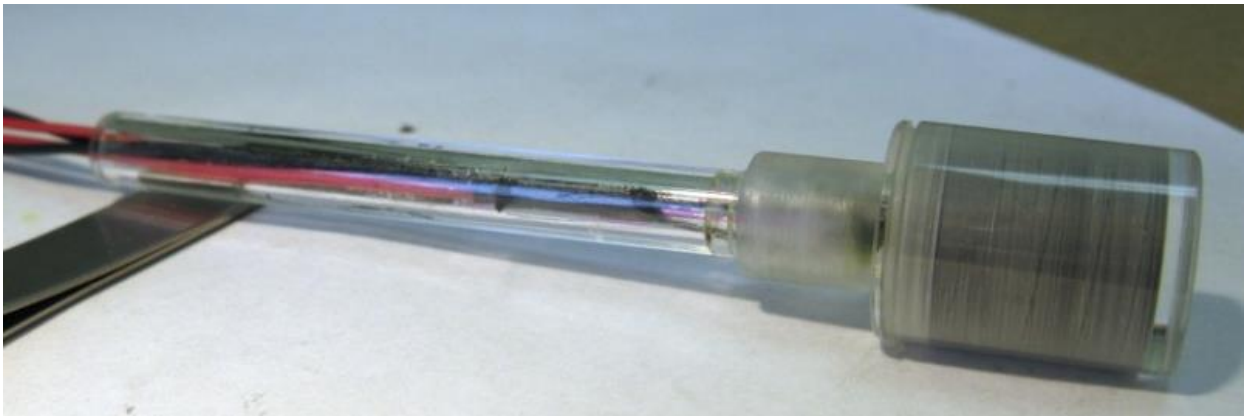

(c)

Figure 5.3: (a) The GPC prototype consists of cylindrically nested components of graphite. Two thermistors with a bead diameter of 0.36 mm were embedded in the core. (b) The platinum alloy thermistor leads were covered by polyimide tubing and were threaded through holes in the jacket and shield caps. (c) A Lucite stem was fabricated to protect the electrical connections from physical strain and to waterproof the GPC.

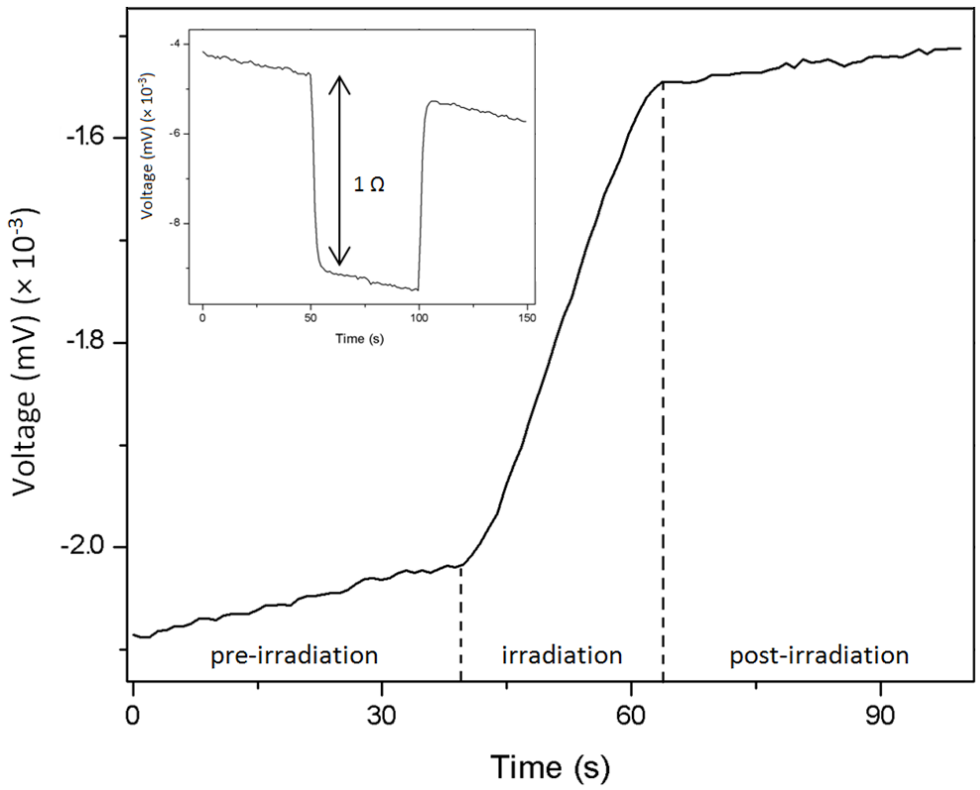

Figure 5.4: A sample calorimetric run acquired during a 30 sec irradiation (200 MU delivered). The raw data is in units of active bridge voltage, which is proportional to temperature. The inlay depicts an ohm calibration, in which the bridge voltage response to a change in resistance of 1 Ω is recorded.

5.3 RESULTS

5.3.1 Measurements

A summary of the results of the experiments performed by delivering 200 MU and 333 MU, at a rate of 400 MU/min and 1000 MU/min, respectively, are shown in Table 5.2. The uncertainty in each column represents one standard deviation on those measurements. The table also lists the averages of all quantities measured normalized to a delivery of 100 MU.

The maximum percent difference between a dose to water measured using the GPC and the corresponding TG-51 derived value was 2.2 %. A clear trend was observed between the accuracy of dose measurement and the stability of the water bath temperature: During the first hour of measurement, the water temperature was stable to within 2 mK and the average discrepancy between the GPC and the ion chamber was 0.6 %. During the last hour of measurement, the water was cooling at a rate of about 15 mK/hour and the average discrepancy increased to 1.5 %.

Table 5.2. Summary of dose measurements performed using the GPC for the different MU deliveries. The number of calorimetric runs performed in each case is also noted. Percent difference noted in the last column is defined as [(TG-51 calculated dose) - (measured dose)] / (TG-51 calculated dose) · 100 %.

Delivered MU	Runs	Temperature rise (mK)	Dose to graphite (cGy)	Dose to water (cGy)	TG-51 dose (cGy)	Δ %
333	20	2.99 ± 0.02	213.9 ± 1.2	241.8 ± 1.4	244.4	+1.2
200	5	1.79 ± 0.01	128.1 ± 0.6	144.8 ± 0.6	145.1	+0.2
Average per 100 MU	25	0.90 ± 0.01	64.2 ± 0.4	72.6 ± 0.4	73.2	+0.9

5.3.2 Dose to Water Measurement Uncertainties

In an effort to identify the areas most in need of improvement, a breakdown of the estimated uncertainty budget, listing the largest contributing type A and B uncertainties used in the data analysis was assembled. It is important to note that the uncertainty budget shown in Table 5.3 is meant to provide a high-level perspective and should not be considered complete. Although the heat transfer corrections are likely to be near unity for this setup, their dependencies have not yet been fully evaluated and require a detailed sensitivity analysis. As such, this quantity has been assigned a standard uncertainty of 0.5 % in

accordance with the methodology of Sander *et al.*[18] The reproducibility represents one standard deviation of the raw mean. The Ohm and thermistor calibrations reflect the uncertainty in the fits of their respective curves. Since the specific heat capacity of the graphite used in the GPC's construction is unknown, a standard value with a rectangular distribution of 715 ± 10 J kg^{-1} K^{-1} at 24 °C was used based on the experimentally determined values using pure graphite in the literature.[12,19] The positioning refers to the effect of the uncertainty in the GPC depth measurements. Finally, the perturbation-dose conversion refers to the statistical uncertainty in the MC simulations used to calculate this quantity. On the other hand, the relative uncertainty associated with the TG-51 measurements is estimated to be 0.9 % (k = 1). This value was determined from the 0.7 % uncertainty on the value of $N_{D,w}$ provided by the standards lab, 0.5 % uncertainty on the beam quality conversion factor k_Q[20] and 0.4 % total uncertainty associated with P_{pol}, P_{ion}, P_{TP}, humidity, depth setting and leakage current.

5.3.3 Corrections and Dose Conversion

Conductive heat transfer corrections, k_{ht}, calculated using a three-dimensional model of the GPC submerged in a constant temperature water phantom were determined to be 1.001 and 1.002 for the 20 sec and 30 sec irradiations, respectively. The effects of convection in the water phantom are assumed to be negligible. A MC-calculated dose distribution for this experimental setup was used as a heat source input parameter in the heat transport model. The product of the radiation field perturbation factor and the graphite to water dose conversion factor was determined using MC to be 1.130 ± 0.005.

Table 5.3. Estimated uncertainty budget for GPC in high-energy photon beam water dose measurements.

Quantity	Type A % uncertainty	Type B % uncertainty
Heat transfer correction	--	0.5
Reproducibility	0.6	--
Ohm calibration	--	0.5
Thermistor calibration	--	0.2
Specific heat capacity	--	0.8
Positioning	0.2	--
Perturbation-dose conversion	--	0.4
Other uncertainties not considered in this work	--	0.4
Quadratic summation	0.6	1.2
Combined relative standard uncertainty in dose to water	1.4	

5.4 DISCUSSION

The results shown in Table 5.2 suggest the feasibility of performing absolute clinical photon dose measurements using the GPC. The reproducibility achieved in this work is similar to the 0.6 % estimated by Duane *et al.*[5] in their work with a small-scale IMRT calorimeter. There are areas, however, that will require improvement if the device is to ever become a viable clinical dosimeter. As expected, the observed relation between temperature stability and measurement accuracy suggests that clinical use of the GPC will require it to be able to provide its own stable background temperature against which a temperature rise can be measured. The discrepancies observed between the GPC and TG-51 are partly due to the fact that the heat loss correction applied to the measured dose to graphite has been calculated assuming a stable surround temperature. In reality, the water in the tank is slowly drifting towards room temperature. As these thermal gradients increase in magnitude, the less

adequate the heat transfer correction becomes. Developing a PID temperature controller algorithm and associated electronic circuitry necessary to operate in the isothermal mode[21], in which the measured quantity is the power dissipated in the core to maintain a set point temperature, will now be the focus of further enhancement of the GPC. The benefits of the isothermal mode are an increased reproducibility, vastly decreased initialization time and delay time between measurements, and the ability to operate at higher dose rates than achievable when operating in the quasi-adiabatic radiation mode. Furthermore, the calibration procedure carried in this work (voltage to resistance, resistance to temperature) will become unnecessary in this mode with *a priori* knowledge of the core mass. As a result, the ohm-calibration (0.5 %), thermistor calibration (0.2 %) and specific heat capacity (0.8 %) sources of type B uncertainty are replaced by the uncertainty of a mass measurement, which is expected to be no more than a few tenths of a percent. While an overall uncertainty of 1.4 % was estimated for the dose measurements in this work, it is hypothesized that this can be reduced to well below 1.0 % if operating in isothermal mode. With the potential for automated data analysis, the GPC could be made to be a battery-powered, absolute clinical dosimeter that could store and wirelessly transmit the measured dose values and automatically notify the user of an out-of-specification reading without anyone having to manually measure and recognize faulty values.

5.5 CONCLUSIONS

This proof of concept demonstrates the feasibility of using the GPC as a practical clinical absolute photon dosimeter and justifies further effort to enhance its operation and design. It is expected that the implementation of an isothermal mode of operation, driven by a PID temperature controller, will shield the GPC from thermal fluctuations in the surrounding environment and establish the stable background necessary for accurate dose

measurements in a matter of minutes. By incorporating this mode of operation, a sub-percent overall uncertainty on absorbed dose to water measurements is expected. Plans to develop a further miniaturized GPC prototype suitable for small and composite field dosimetry are underway.

ACKNOWLEDGEMENTS

This work has been supported in part by Grant RGPIN 298191 of the Natural Sciences and Engineering Research Council of Canada (NSERC). J.R. is a recipient of a NSERC M.Sc. scholarship.

5.6 REFERENCES

[1]J. Seuntjens, and S. Duane, "Photon absorbed dose standards," Metrologia **46**, S39-S58 (2009).

[2]P. Almond, P. Biggs, B. Coursey, *et al.*, "AAPM's TG-51 protocol for clinical reference dosimetry of high-energy photon and electron beams," Med. Phys. **26**, 1847-1870 (1999).

[3]International Atomic Energy Agency, "Absorbed dose determination in external beam radiotherapy based on absorbed-dose-to-water standards: An international code of practice for dosimetry," IAEA TecDoc TRS 398.

[4]R. Alfonso, P. Andreo, R. Capote, *et al.*, "A new formalism for reference dosimetry of small and nonstandard fields," Med. Phys. **35**, 5179-5186 (2008).

[5]S. Duane, M. Aldehaybes, M. Bailey, *et al.*, "An absorbed dose calorimeter for IMRT dosimetry," Metrologia **49**, S168-S173 (2012).

[6]I.S. Sundara Rao, and S.B. Naik, "Graphite calorimeter in water phantom and calibration of ionization chambers in dose to water for ^{60}Co gamma radiation," Med. Phys. **7**, 196-201 (1980).

[7]V.A. Berlyand, and Yu.I. Bregadze, "Portable calorimeter for measuring absorbed doses of x-rays and electrons from accelerators," Measurement Techniques **34**, 1179-1184 (1991) (Translated from Izmeritel'nava Teknika, No. 11, pp. 56-58, 1991).

[8]H. Palmans, R. Thomas, M. Simon, *et al.*, "A small-body portable graphite calorimeter for dosimetry in low-energy clinical proton beams," Phys. Med. Biol. **49**, 3737-3749 (2004).

[9]Y. Morishita, M. Kato, N. Takata, *et al.*, "A standard for absorbed dose rate to water in a ^{60}Co field using a graphite calorimeter at the national metrology institute of Japan," Radiation Protection Dosimetry, pp. 1-9 (2012).

[10]J.P. Seuntjens, and A.R. DuSautoy, "Review of calorimeter-based absorbed dose to water standards," IAEA Int. Symp. on Standards and Codes of Practice in Med. Rad. Dosimetry, IAEA-CN-96-3 (2002).

[11]Aspen Aerogels, "Pyrogel® 2250 Datasheet", (Aspen Aerogels, Inc., Northborough, USA, 2010).

[12] Alberts, L., *et al.*, "CRC handbook of Chemistry and Physics, 87th edition", edited by R. C. Weast, (CRC Press, Cleveland, USA, 1976).

[13]I. Kawrakow, and D.W.O. Rogers, "The EGSnrc code system: Monte Carlo simulation of electron and photon transport," NRC Reports, PIRS-701 (2006).

[14]M. Boutillon, "Gap correction for the calorimetric measurement of absorbed dose in graphite with a ^{60}Co beam," Phys. Med. Biol. **34**, 1809-21 (1989).

[15]B. Owen, and A.R. DuSautoy, "Correction for the effect of the gaps around the core of an absorbed dose graphite calorimeter in high energy photon radiation," Phys. Med. Biol. **36**, 1699-1704 (1991).

[16]R.F. Nutbrown, S. Duane, D.R. Shipley, and R.A. Thomas, "Evaluation of factors to convert absorbed dose calibrations in graphite to water for mega-voltage photon beams," NPL Rep. CIRM 37 (2000).

[17] P. Almond, P. Biggs, B. Coursey, *et al*., "AAPM's TG-51 protocol for clinical reference dosimetry of high-energy photon and electron beams", Med. Phys. **26**, 1847-1870 (1999).

[18]T. Sander, S. Duane, N.D. Lee, *et al*., "NPL's new absorbed dose standard for the calibration of HDR ^{192}Ir brachytherapy sources", Metrologia **49**, S184-S188 (2012).

[19]S. Picard, D.T. Burns, and P. Roger, "Determination of the specific heat capacity of a graphite sample using absolute and differential methods," Metrologia **44**, 294-302 (2007).

[20]D.W.O. Rogers, “The Physics of AAPM’s TG-51 Protocol”, in Clinical Dosimetry Measurements in Radiotherapy, Medical Physics Monograph No. 34, edited by D.W.O. Rogers and J.E. Cygler (Medical Physics Publishing, 2009), pp. 239-298.

[21]J. Daures, and A. Ostrowsky, “New constant-temperature operation mode for graphite calorimeter at LNE-LNHB”, Phys. Med. Biol. **50**, 4035-4052 (2005).

Chapter 6

AERROW: A PROBE-FORMAT GRAPHITE CALORIMETER FOR USE AS A LOCAL ABSORBED DOSE STANDARD FOR CLINICAL HIGH-ENERGY PHOTON AND ELECTRON BEAMS

In this chapter, the design, operation, initial validation, and characterization of a small scale graphite calorimeter probe -- herein referred to as the Aerrow -- developed for routine use in the clinical environment, is described. The results of this work include validation dose measurements, which were performed using both Aerrow operation modes in a 6 MV photon beam and were directly compared to results derived using a calibrated reference-class ionization chamber. The dose is measured in clinical accelerator-based 6 MV, 10 MV, 10 FFF, 15 MV, and 15 FFF photon beams, as well as 6 MeV, 9 MeV, 12 MeV, 16 MeV, and 20 MeV electron beams. An evaluation of linearity, dose rate, orientation, and beam quality dependences is also provided. This work demonstrates the feasibility of using an ion chamber-sized calorimeter as a practical means of measuring absolute dose to water in the radiotherapy clinic.

Authors: James Renaud[1,2], Arman Sarfehnia[1,3], Julien Bancheri[2], and Jan Seuntjens[1,2]

[1]Medical Physics Unit, McGill University, Montréal, Québec, H3G 1A4, Canada
[2]Department of Physics, McGill University, Montréal, Québec, H3A 2T8, Canada
[3]Department of Radiation Oncology, University of Toronto, Toronto, Ontario, M5S 3E2, Canada

ABSTRACT

Purpose: In this work, the design, operation, initial validation, and characterization of a small-scale graphite calorimeter probe -- herein referred to as the Aerrow -- developed for routine use in the clinical environment, is described. Similar in size and shape to a Farmer-type cylindrical ionization chamber, the Aerrow represents the first translation of calorimetry from the primary standards dosimetry laboratory to the radiotherapy clinic.

Methods: Based on a numerically-optimized design obtained in previous work, a functioning Aerrow prototype capable of two independent modes of operation (quasi-adiabatic and isothermal) was constructed in-house. Reference dose measurements were performed using both Aerrow operation modes in a 6 MV photon beam and were directly compared to results derived using a calibrated reference-class ionization chamber. The Aerrow was then used to quantify the absolute output of five high-energy photon (6 MV, 6 MV FFF, 10 MV, 10 MV FFF, and 15 MV), and five electron beams (6 MeV, 9 MeV, 12 MeV, 16 MeV, and 20 MeV). Linearity, dose rate, orientation, and beam quality dependences were also evaluated.

Results: Compared to the chamber-derived dose to water of 0.763 ± 0.007 cGy/MU, the average Aerrow-measured doses were 0.762 ± 0.007 (n = 25) and 0.753 ± 0.007 (n = 32) cGy/MU for the quasi-adiabatic and isothermal modes, respectively. Furthermore, all photon and electron beam outputs measured using the Aerrow were in statistical agreement with clinical reference dosimetry data. The linearity of the Aerrow's response (n = 30) was characterized by an adjusted R^2 value of 0.9998 in the region of 80 cGy to 470 cGy. For the dose rate dependence, no statistically significant effects were observed in the range of 0.5 Gy/min to 5.4 Gy/min. For photon and electron beam qualities in the range of 58.4 % < $\%dd(10)_X$ < 86.8 % and 2.33 cm < R_{50} < 8.27 cm, respectively, no statistically significant trend is exhibited and a maximum deviation of about ±1 % from the average response across all beams qualities is observed. Finally, the angular dependence (gantry

stationary and detector rotated) of the Aerrow's response is insignificant to within ±0.5 % of the average taken across all angles.

Conclusions: This work demonstrates the feasibility of using an ion chamber-sized calorimeter as a practical means of measuring absolute dose to water in the radiotherapy clinic. The potential introduction of calorimetry as a mainstream device into the clinical setting is significant as this fundamental technique has formed the basis of absorbed dose standards in many countries for decades and could one day form the basis of a new local absorbed dose standard for clinics.

6.1 INTRODUCTION

For more than sixty years, calorimeters of various designs have been applied to radiation dosimetry. Owing to a myriad of technical refinements achieved over this time, calorimeters now form the basis of primary absorbed dose standards in many countries around the world. These operate on the principle that radiation interacting with matter will result in a measurable temperature rise in the absorbing medium. Even amongst primary standards, calorimetry is considered the most direct and absolute method of measuring absorbed radiation dose since device calibration can be achieved in terms of quantities with traceable standards (*i.e.,* electrical and temperature), entirely independent of radiation.[1-3] This avoids the need to rely on dosimetric quantities such as $(W/e)_{air}$ (the average energy required to produce an ion pair in dry air) and $(\epsilon G)_{Fe^{3+}}$ (the product of the molar extinction coefficient and the radiation chemical yield of ferric ions), the knowledge of which are relatively more uncertain than current electrical and temperature-based standards.[1,4] To date, calorimeter designs have primarily been driven by national metrology institutes, whose principle motivation is to achieve the lowest possible measurement uncertainty.[5] Utility and usability of the devices are secondary considerations, and as a result, most calorimeters today are

generally both bulky and fragile, and are operated by only handful of individuals possessing the required specialized equipment and tacit knowledge.[6-11]

In radiotherapy, clinical reference dosimetry of high-energy photon and electron beams is based on absorbed dose to water standards (most commonly calorimetry). Generally based on calibrating ionization chambers in a standard ^{60}Co field, protocols such as AAPM TG-51 and IAEA TRS-398 detail recommended practices in regard to reference dosimetry.[12-14] The emergence of specialized and non-conformal radiation delivery modalities (MR-linacs, Gammaknife®, Cyberknife®, etc.) incapable of producing a standard reference field (10×10 cm^2) have prompted the development of methodologies to adapt current reference dosimetry traceability to smaller fields.[15] In this approach, a suitable ionization chamber with a conventional calibration traceable to a primary standard is used under non-standard conditions. Correction factors must then be applied to the chamber readings to account for all the effects (*e.g.*, volume averaging, fluence perturbation, etc.) which cause the detector response to vary between reference and non-reference conditions. Most recently, this correction-based technique has been extended to include the effects due to the presence of a magnetic field.[16]

As a more direct alternative method to realize absorbed dose in non-standard fields, new graphite and water calorimeters specifically designed to measure dose based on first principles are being developed.[17-19] Often times these calorimetry systems are also made to be transportable to permit operation at the user's facility.[20-23] Thus, calorimetry-based dose measurements can form the basis of a direct dose calibration of an ionization chamber in the clinically-relevant field, or a derivation of the abovementioned correction factors for those beams. The minimal beam quality and field size dependence of calorimeters also make them useful transfer instruments. Despite their advantages over other dosimetry systems, calorimeters have yet to be incorporated into regular clinical use. Any widespread adoption of calorimetry by physicists in the radiotherapy clinic will necessitate a high degree of

dependability, robustness, and a relative ease of use (*i.e.*, practicality) on the part of the detector.

One aim of this paper is to present the development of a probe-format graphite calorimetry system specifically designed for routine use as a local dose standard in the clinical environment (filing no. PCT/CA2013/000523). Originally constructed at McGill University by Renaud *et al*. (2013),[24] the calorimeter, referred to herein as the Aerrow, shares design aspects with graphite calorimeters developed at the Bhabha Atomic Research Centre during the late 1970's[25], and more recently at the National Physical Laboratory (NPL)[17] and the Laboratoire National Henri Bequerel (LNE-LNHB)[18]. In contrast to nearly all other graphite calorimeters, the Aerrow design incorporates aerogel-based material as opposed to a vacuum to achieve thermal isolation from the surrounding environment.[10,11,17-19,25-30] This design choice was made to simplify the assembly process, to maximize the compactness, and to improve the structural robustness of the device. Furthermore, it allows for use of the dosimeter in a standard water phantom; a feature not shared by most graphite calorimeters.

The purpose of this work is to present the design and operating principles of the Aerrow system, an ionization chamber-sized probe format calorimeter designed specifically for routine absolute dosimetry in the radiotherapy clinic. A validation study in which the Aerrow's two independent operating modes are directly compared to a reference class ionization chamber in a high-energy photon beam is described. The corrections and dose conversion factors necessary to determine absorbed dose to water for photon and electron beam dosimetry are also discussed. Furthermore, a detailing of the Aerrow's relative characterization (linearity, dose rate dependence, energy dependence, and angular dependence) is provided. This work represents the first successful translation of radiation calorimetry from the dose calibration laboratory to the clinical setting.

6.2 METHODS

6.2.1 Graphite Calorimeter

A cross-sectional view and micro-CT scan of the Aerrow (fourth prototype iteration) is shown in Figure 6.1. Similar in size to a 0.6 cm^3 cylindrical ionization chamber, the Aerrow was designed to determine the absorbed dose to a small sensitive volume, either in a water or solid phantom, in clinical accelerator-based photon (^{60}Co to >24 MV x-rays) or electron (4 MeV to >20 MeV) beams down to field sizes of 2 × 2 cm^2. Unlike an ionization chamber however, the Aerrow was built with the aim of providing an absolute measure of the absorbed dose without the need for a beam quality-specific calibration factor, nor setup-, nor environment-dependent correction factors (*e.g.*, polarity, ion recombination, variations in ambient conditions, etc.). The incorporation of an aerogel-based thermal insulator (Pyrogel® 2250, Aspen Aerogels Inc.) has enabled this effective translation of calorimetry from the primary standards dosimetry laboratory to the clinical environment.

The graphite components of the calorimeter (Grade R 4340, SGL Carbon Group, density: 1.72 g cm^{-3}) are arranged in a nested cylindrical geometry. The 6.1 mm diameter, 10.0 mm long graphite core (the sensitive volume) is separated from a 0.7 mm thick jacket by a 0.7 mm isotropic layer of Pyrogel insulation. Likewise, a 1.0 mm layer of Pyrogel thermally isolates the jacket from a 1.0 mm thick graphite shield. The mechanical support provided by the solid insulation maintains the constant relative positioning of the graphite components, and allows for normal handling by the user.

Each of the core, jacket and shield are fitted with negative temperature coefficient thermistors (USP12837, US Sensor) with a nominal resistance of 10 kΩ at 25 °C, which serve as either temperature sensors or Joule heaters. Each graphite component has one sensing thermistor, and 3 (core and jacket) or 6 (shield) thermistors connected in parallel for thermal regulation.

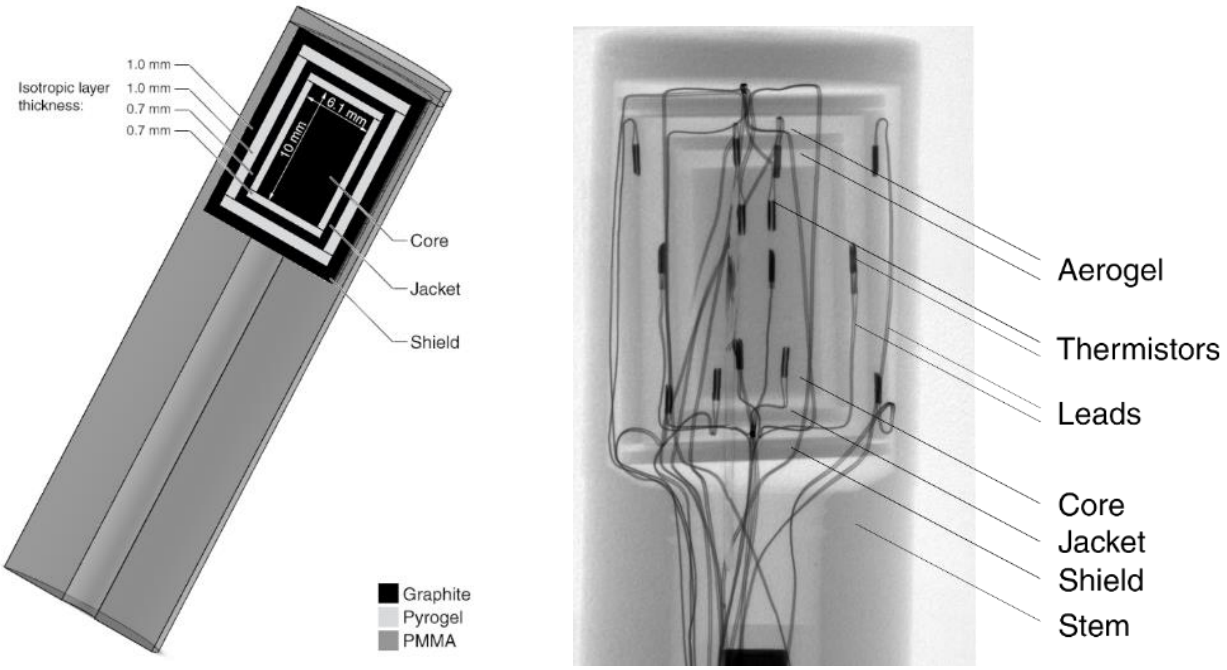

(a) (b)

(c)

Figure 6.1: (a) A cross-sectional schematic diagram of the Aerrow design, and (b) a digitally reconstructed radiograph of a micro-CT scan of the prototype calorimeter showing multiple embedded thermistors and leads. (c) The comparable size of the Aerrow to that of a Farmer-type ionization chamber is illustrated by the Exradin A12 positioned alongside the probe calorimeter (in red) and a nickel for scale.

They have been positioned in their respective graphite bodies to produce an axially-symmetric heating distribution. While fifteen thermistors far exceed the minimum required to operate the instrument, this number was selected for the prototype to provide sufficient redundancy in the event of multiple connection failures. The thermistor elements are approximately 0.13 mm thick, 0.28 mm wide, and 0.76 mm long, and are encapsulated in a 3.81 mm long, 0.51 mm diameter polyimide tube. The 38 AWG (Ø = 0.10 mm), solid conductor, poly-nylon insulated nickel leads were threaded through 0.26 mm diameter holes drilled in the jacket and shield end caps, allowing for electrical connections to be made to a shielded, two-lead 30 AWG (Ø = 0.26 mm) cable outside the graphite assembly. For the jacket and shield, a minimal amount of cyanoacrylate adhesive was used to fasten the end caps to the hollow cylindrical bodies. An acrylic (PMMA) stem was fabricated to envelope and waterproof the calorimeter assembly for submerged dose measurements. It also serves as a rigid shell protecting the electrical connections from the physical strain of handling.

Like all graphite calorimeters, the core of the Aerrow consists of a certain amount of non-graphite materials (thermistors, epoxy, thermal insulation), herein referred to as impurities. The presence of impurities contributes to the perturbation of the absorbed dose in the graphite component of the core and must be taken into account. Table 6.1 lists the relevant material properties present in the prototype used in this work. Masses were repeatedly measured using a high-precision balance (Type AJ100L, Mettler) at every stage of the assembly, whereas specific heat capacities were taken from literature.[31,32] A thermistor was dissected in order to separate and measure the individual component masses (nickel, polyimide, polyurethane nylon, transition metal oxide), which were found to be in agreement with manufacturer-provided data to within about 0.2 mg.

Table 6.1. Graphite and impurity contributions to the effective core mass and specific heat capacity of the Aerrow. The mass (m), absolute uncertainty (u) and specific heat capacity (c_p) are given for each constituent material.

Core material	m_i (mg)	$u(m_i)$ (mg)	$c_{p,i}$ (J kg^{-1} K^{-1})	$u(c_{p,i})$ (J kg^{-1} K^{-1})	$(c_{p,i} \cdot m_i)$ (J K^{-1})	$u(c_{p,i} \cdot m_i)$ (J K^{-1})
Graphite	539.2	0.1	715	10	3.9E-01	5.4E-03
Nickel leads	174.0	0.2	445	5	7.7E-02	8.7E-04
Polyimide tubing	0.8	0.2	1110	20	8.9E-04	2.2E-04
Polyurethane nylon	11.5	0.2	1650	50	1.9E-02	6.6E-04
Transition metal oxide	1.6	0.2	600	200	9.6E-04	3.4E-04
Cyanoacrylate	5.5	0.5	1420	50	7.8E-03	7.6E-04
Pyrogel® (50-70 % silica gel, 30-50% polyacrylonitrile	35.9	0.5	1080	20	3.9E-02	9.0E-04

6.2.2 Quasi-adiabatic operation

In general, graphite calorimeters can be operated in one of two independent modes to measure absorbed radiation dose: quasi-adiabatic and isothermal (also referred to as constant-temperature mode). In this work, the Aerrow was operated in both of these modes, the results of which were compared to one another as an initial form of validation. The quasi-adiabatic mode, as it has been implemented in this work, cannot however be considered practical for routine clinical application for reasons of time efficiency. Isothermal mode (see *Section* 6.2.3) is expected to be the practical means of everyday clinical use.

In this mode, no active thermal regulation is directly applied to the graphite; rather, the Aerrow is submerged in a temperature-controlled water phantom with a setpoint of

297.45 K. Originally designed for use with McGill University's electron sealed water calorimeter (ESWcal)[33,34], the water phantom used in this work has been designed to stabilize the water temperature to within a few 10's of μK. In this setup, the core, jacket, and shield temperatures rise under irradiation, causing a fractional resistance change of approximately 0.45 Ω/mK in the embedded thermistors. Changes in temperature are indirectly determined by measuring the response of a DC Wheatstone bridge circuit to resistance changes in the sensing thermistor. Two precision 10 kΩ resistors (model 1152, Burster) make up one arm of the bridge, while the sensing thermistor and an adjustable decade resistor box (Type 1408, Burster) make up the other. The bridge response voltage is measured (2182A, Keithey) and related back to temperature through separate calibrations of the thermistors (against a calibrated mercury thermometer traceable to national standards), and the bridge response.[35]

The bridge response is calibrated by adjusting the decade resistor box setting by a known amount, typically 1 Ω, when the bridge is nominally balanced (*i.e.,* the sensing thermistor resistance is equal to the decade resistor box setting). This bridge calibration procedure is performed in the absence of large drifts, regularly throughout the experiment. Collectively, these calibration results represent the change in bridge voltage per unit resistance change, $\Delta V_{1\,\Omega}$, as a function of balanced decade resistor box setting.

In the quasi-adiabatic mode, the Aerrow measures the mean absorbed dose in the core, D_{core}, based on its fundamental relation to the temperature rise, ΔT, and the specific heat capacity at constant pressure, $c_{p,\text{core}}$, as shown in Eq. 6.1:

$$D_{\text{core}} = \frac{\Delta E_{\text{rad}}}{m_{\text{core}}} = c_{p,\text{core}} \cdot \Delta T \cdot \prod k_i \tag{6.1}$$

For the purpose of the inter-comparison of operating modes, the product, $\prod k_i$, of the correction factors is simply the conductive heat transfer, k_c. Other corrections, such as the radiation field perturbation (k_p), and the radiation dose profile non-uniformity (k_{dd}) are accounted for when determining the absorbed dose to water from a realistic Monte Carlo (MC) model (see *Section* 6.2.5).

The acquired signal during a single quasi-adiabatic run consists of three distinct parts: the pre-drift, the irradiation period, and the post-drift. Prior to irradiation, a pre-drift signal is recorded to provide an initial state condition. During irradiation, the bridge signal resulting from the temperature rise at the core sensing thermistor is acquired. Following the irradiation, a post-drift signal is collected to compared against the initial slope of the pre-drift and provide a measure of the temperature rise (Figure 6.2). Due to the thermal insulation of the calorimeter box and the low thermal diffusivity of water, the pre- and post-drift signals are quasi-linear over the time scale of the measurement. The correction for heat loss due to conduction, k_c, is defined as the ratio of the temperature rise in the absence of conduction to the actual temperature rise, and is numerically simulated using a finite element method software package (COMSOL Multiphysics® v.4.2). Temperature gradients arise for two main reasons: i) dose gradients induced by the non-uniform radiation field, and ii) the lower specific heat capacity of the graphite relative to the surrounding water (in principle, all non-water materials contribute to this effect). The software is able to calculate time dependent thermal distributions in a 3D model of the Aerrow (Figure 6.3) by solving, in both time and space, the partial differential equation governing thermal conduction. The solving algorithm requires several input parameters including the physical and thermal properties of the involved materials, geometric boundary conditions, and the distribution of heat sources and sinks in space and time.

6.2.3 Isothermal operation

First experimented on by Witzani *et al*. (1986) and later further developed by Daures and Ostrowsky (2005) at the French dose standards laboratory, LNE-LNHB, to overcome the thermally-dynamic nature of the quasi-adiabatic mode, the isothermal mode has since been shown to be generally more reproducible, accurate, and flexible than Domen's original technique.[36-38] In this mode, each graphite component is subject to active thermal control such that a constant setpoint temperature is precisely maintained throughout operation at a sampling frequency of 6 Hz.

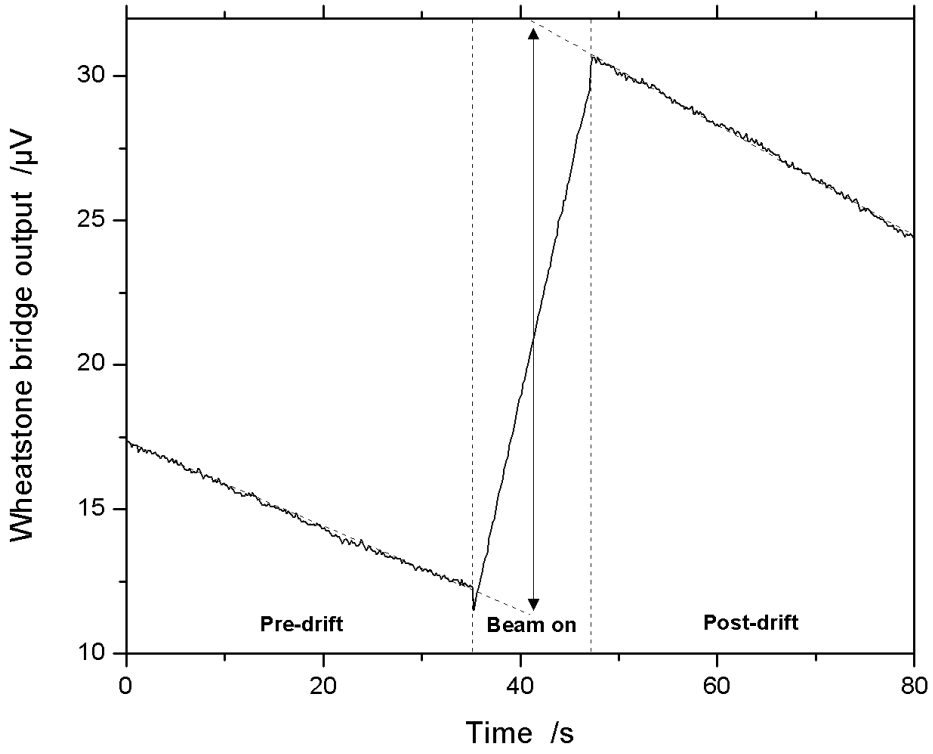

Figure 6.2: Example of a 12 s quasi-adiabatic mode measurement acquired using the Aerrow in a 6 MV photon beam at a dose rate of approximately 7.5 Gy/min. During the beam on period, the increasing bridge signal resulting from the temperature rise at the core sensing thermistor is acquired. This voltage offset (indicated by the vertical arrow) is directly proportional to the absorbed dose. The transients exhibited at beam on and off are electrical in nature, and are likely due to an unresolved ground loop.

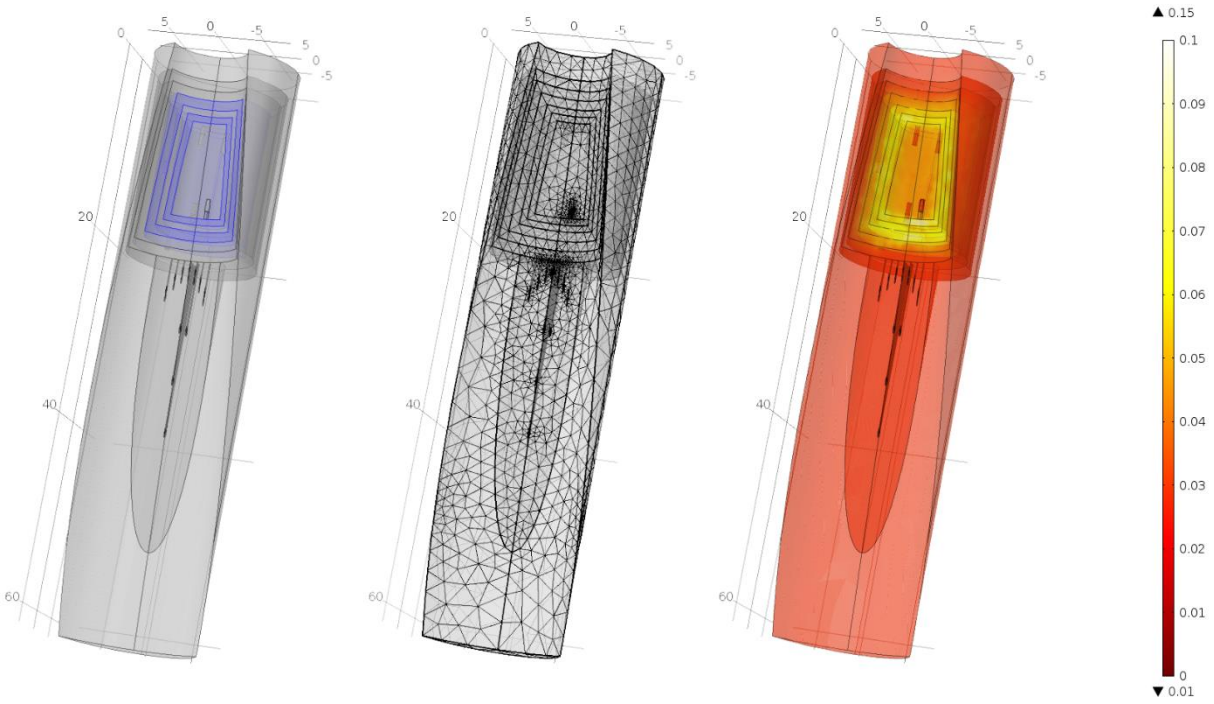

Figure 6.3: Finite element analysis of the Aerrow using COMSOL Multiphysics®. (Left) Geometric 3D model with thermal property assignment of the involved materials, boundary conditions, and distribution of heat sources and sinks in space and in time are included as input parameters. (Centre) Discretization, or 'meshing', of the model into element domains over which the differential equations for heat conduction are solved. (Right) Resulting radiation-induced time dependent temperature distribution (baseline of 295.15 K subtracted; 0.01 K < T < 0.15 K) in the Aerrow at a time point, t, post-irradiation.

Active control in the jacket and shield is done in order to prevent core signal perturbation due to thermal fluctuations in the surrounding environment, and removes the need for a thermally-controlled water phantom. Absorbed dose determination is based on an electrical substitution method. Conceptually, a constant temperature is maintained independently in each graphite body during the irradiation period by reducing the amount of electrical energy dissipated in the heating thermistors, P_i, by an amount equal to the energy deposited by the radiation. By subtracting the baseline power, P_0, and integrating over the timespan, the total deposited energy, and hence the dose, can be derived. In this mode, *a priori* knowledge of the

core mass, m_{core}, is required. In Equation 6.2, the product of the correction factors, $\prod k_i$, is the same as for the quasi-adiabatic mode, with the exception that conductive heat transfer is assumed to be unity to within 0.05 %.

$$D_{\text{core}} = \frac{\Delta E_{\text{rad}}}{m_{\text{core}}} = \frac{\int_0^t (P_0 - P_i) \cdot dt}{m_{\text{core}}} \cdot \prod k_i \tag{6.2}$$

As before, the variations in sensing thermistor resistance are measured by means of a precision DC Wheatstone bridge circuit. The voltage drop across each bridge is used as an input process variation, fed into a software-implemented PID controller (LabVIEW v.11.0, National Instruments) whose setpoint is zero (*i.e.* a null and balanced bridge output). The controller achieving thermal regulation in a given graphite body by modulating the current output of a programmable DC power supply (PXI-4110, National Instruments) connected directly to the heating thermistor network embedded in that particular component. An accurate measure of the electrical power dissipated in the heating elements is continuously determined by measuring the voltage drops (PXI-4070, National Instruments) across the heating thermistor network, and a precision resistor shunt (type 1152, Burster).[39]

As alluded to earlier, the advantage of isothermal operation is that it is significantly more time-efficient than quasi-adiabatic, due to the fact that temperatures are nearly static (*i.e.*, the final physical state of the system is virtually the same as the initial state). Also, no distinct electrical response calibration is required to derive the absorbed dose, since electrical power is continuously measured, with and without the presence of radiation.[38] That said, the response of the Aerrow to electrical power dissipation has been characterized in this work, not only to periodically verify the consistent operation of the isothermal mode, but also to study the effects of varying the rate and duration of energy dissipation (analogous to the dose rate dependence and response linearity). Emulating the energy deposition of a

radiation field can be carried out electrically by manipulating the output parameters of the power supplies.

Similar to the quasi-adiabatic mode, the signal acquired during an isothermal run consists of a pre-drift, irradiation period, and post-drift. The principle difference is that instead of voltage across the bridge, the measurand is the electrical power dissipation in the core (Figure 6.4). Prior to, and following irradiation, a pre- and post-drift signal is recorded, respectively, to provide a baseline electrical power dissipation. During irradiation, the decrease in the electrical power resulting from the addition of a radiation-induced energy contribution is acquired. The power deficit, ($P_0 - P_i$), equivalently the dose rate, is then determined by iteratively offsetting the irradiation portion of the acquired signal by a small, constant, positive power, and repeatedly fitting the entire run with a linear function. The power offset leading to a globally optimized fit (minimized adjusted R^2) is recorded as the radiation dose rate. Timing information is measured based on the sharp transients observed in the signal that corresponds to when the beam is turned on and off. With the exception of the transients, the signal is normally quasi-linear over the time scale of the run.

6.2.4 Reference Dosimetry

The representation of uncertainties in this work follows that of the BIPM JCGM 100:2008 guide, and that TG-51 notation will be used throughout.[12,13,40] As a first-stage validation of the Aerrow system, absorbed dose measurements were performed in a medical accelerator-based high-energy photon beam using the two independent calorimeter modes and compared against those acquired with a reference-class ionization chamber (Exradin A12, Standard Imaging Inc.) with a calibration traceable to the NRC primary standard water calorimeter. This test was chosen based on the history of agreement that has been shown between other calorimeters and calibrated chambers of this type.[5] Calibrated in a reference

^{60}Co field, the uncertainty associated with the absorbed dose calibration coefficient for the Exradin A12 was 0.5 %.[41]

Graphite calorimetry was performed in a 6 MV photon beam at a repetition rate setting of 1000 monitor unit (MU) per minute, a collimator field size setting of 10 x 10 cm^2, a source to surface distance (SSD) of 107.6 cm, and at depth in water of 5 cm. The shallower reference depth and the extended SSD (normally 10 cm and 100 cm, respectively) represent distances practically achievable with the thermally-regulated water phantom setup.

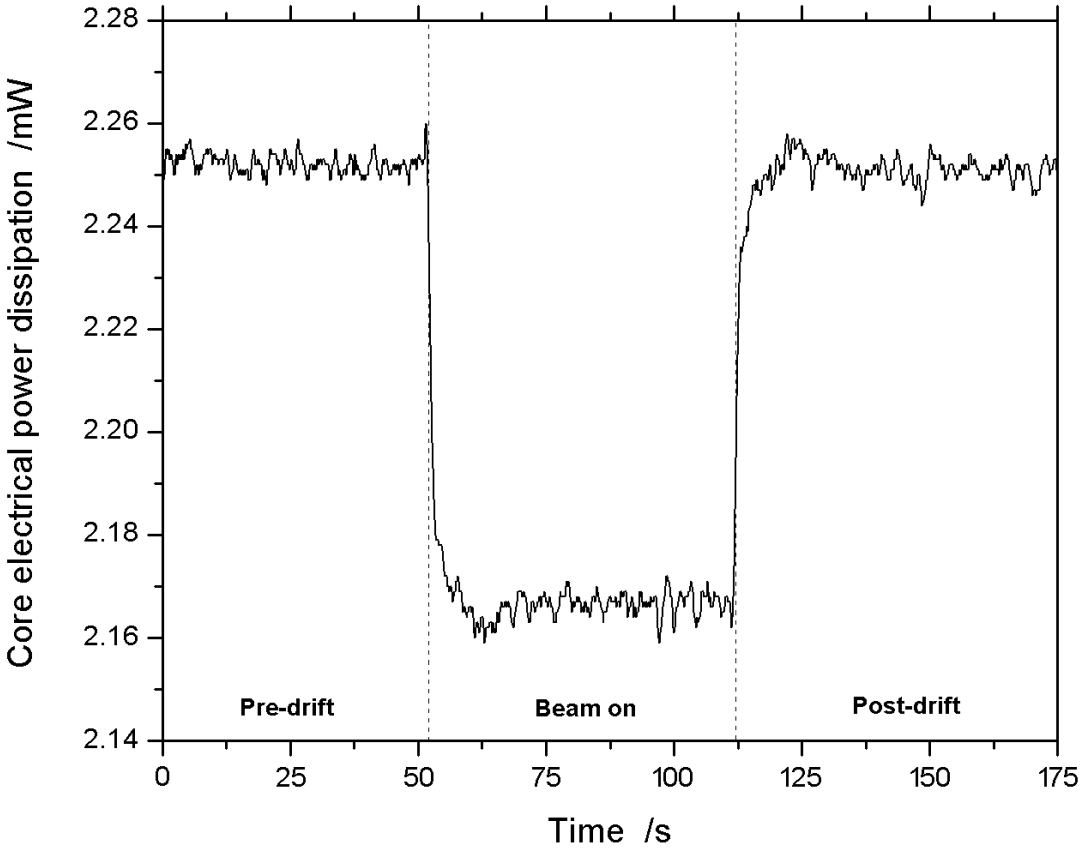

Figure 6.4: Example of a 60 s isothermal mode measurement acquired using the Aerrow in a 6 MV photon beam at a dose rate of approximately 7.5 Gy/min. During the beam on period, a decrease in the electrical power dissipated in the sensitive volume resulting from the addition of a radiation-induced energy contribution is recorded. This power deficit is directly proportional to the absorbed dose rate.

A total of 25 quasi-adiabatic calorimetry measurements were performed by delivering irradiations of 200 MU (12 s nominally), delivering a dose of about 1.5 Gy at the position of the core. The beam on time was kept relatively short to minimize the correction due to conductive heat loss. In each case, 30 s of pre-drift and 30 s of post-drift data were collected for extrapolation and analysis.[42] Throughout the measurement set, 20 bridge calibrations were performed to quantify the voltage response to a 1 Ω change in resistance. Similarly, a total of 32 isothermal calorimetry measurements were performed by delivering irradiations of 1000 MU (60 s nominally), delivering a dose of about 7.6 Gy at the position of the core. In this operation mode, the beam on time was kept relatively long, since preliminary electrical-based characterization of the Aerrow has suggested that the detector's accuracy is maximized at this timescale. In each case, 60 s of pre- and post-drift data were collected for the purpose of analysis.

All chamber measurements were performed under the same conditions as the calorimeter measurements, including water temperature. A calibrated 6517A electrometer (Keithley) was used to read out the collected charge. The centre of the chamber was positioned at the same depth that the calorimeter core had been positioned for the photon beam measurements. For the electrons, the position of the A12 was shifted to account for the effective point of measurement (EPoM), which was taken as $0.5 \cdot r_{cav}$.[12] Water phantom temperature and air pressure were monitored using a mercury thermometer and mercury barometer (both traceable to national standards) in order to correct for environmental effects. Throughout the experiment, humidity remained in a range such that no correction was required. Correction for ion recombination and polarity effects were also applied according to the AAPM's TG-51 protocol.[12]

6.2.5 Dose Conversion

From the Aerrow's raw signal, a measure of the dose to graphite averaged over the core volume, D_g, is obtained. The quantity of interest is the absorbed dose to water, D_w, in the water phantom in the absence of the calorimeter:

$$D_{\mathrm{w}} = (\frac{D_w}{D_g})_{MC} \cdot D_g \tag{6.3}$$

Where the dose ratio, $(\frac{D_w}{D_g})_{MC}$, is calculated using MC simulation, and includes the perturbative effects of the aerogel gaps and the impurities. In Eq. 6.3, D_w may be either evaluated at a point or volume averaged. In this work, a 3D model of the Aerrow (Figure 6.3) inside a water phantom was modelled with the egs_chamber user code of the EGSnrcMP MC code system.[43] ^{60}Co and Mohan photon spectra (4 MV, 6 MV, 10 MV, 15 MV, and 24 MV; 58.4 % < %dd(10)$_X$ < 86.8 %), as well as a set of validated in-house electron spectra (6 MeV, 9 MeV, 12 MeV, 16 MeV, and 20 MeV; 2.33 cm < R_{50} < 8.27 cm) were used as simulation sources.[44,45] $(\frac{D_w}{D_g})_{MC}$ were calculated as the ratio of doses scored in the core volume at the reference depth, as per TG-51, and were plotted as a function of photon and electron beam quality. Dose conversions used in the experimental portion of this work were interpolated from these curves. A statistical uncertainty of 0.1 % was sought out for a given simulation.

6.2.6 Isothermal Characterization

A dosimetric characterization of the Aerrow's isothermal mode was carried out in medical accelerator-based high-energy photon beams (TrueBeam, Varian Medical Systems), at a depth of 2.5 cm, in a 5 cm thick, 30 × 30 cm^2 water-equivalent phantom (Solid Water®, Gammex RMI), under otherwise reference conditions. An Exradin A12 was used as an external monitoring chamber for the calorimetry measurements, which spanned the course of several evenings. To this end, a separate, 12 cm thick, 30 x 30 cm^2 water-equivalent phantom of the same material was used to reproducibly position the ion chamber at a depth

of 2.1 cm. This block was positioned beneath the phantom block containing the Aerrow, such that the ion chamber depth of measurement was 7.1 cm and the total thickness of the phantom was 17 cm. Charge readings were corrected for deviations from the reference air density, as well as for polarity and ion recombination effects in accordance with TG-51. The relative ion chamber readings were applied to the calorimeter datasets to account for the variation in accelerator output. Clinical reference dosimetry was performed in a water-equivalent phantom for all beams using an Exradin A19 (SN/XAQ141084, Standard Imaging Inc.) and a SuperMAX electrometer (SN/P141014, Standard Imaging Inc.) with a calibration traceable to national standards. The photon qualities of interest in this study were a 6 MV, 6 MV FFF, 10 MV, 10 MV FFF, and 15 MV (66.3 % < %$dd(10)_X$ < 76.3 %) beam. Similarly, the electron qualities of interest were a 6 MeV, 9 MeV, 12 MeV, 16 MeV, and 20 MeV (2.33 cm < R_{50} < 8.27 cm) beam.

The isothermal mode was evaluated for response linearity, dose rate dependence, energy dependence, field size dependence, and rotational dependence. In each case, 60 s of pre- and post-drift data were collected for the purpose of analysis. Linearity of the detector reading was evaluated in the 6 MV beam (%$dd(10)_X$ = 66.3 %) in the range of 0.8 Gy to 4.7 Gy by varying the number of MU (100 to 600; increments of 100) delivered at a repetition rate of 600 MU/min. Dose rate dependence was quantified, again in the 6 MV beam, in the range of 0.5 Gy/min to 5.4 Gy/min by maintaining a constant irradiation time of 60 s and varying the repetition rate from 60 MU/min to 600 MU/min. Energy dependence of the signal to the dose delivered was measured for all five high-energy photon, and all five high-energy electron beam qualities by delivering a 60 s irradiation at the highest available repetition rate (600 to 2400 MU/min^{-1}). Finally, rotational dependence was characterized in the 6 MV beam by rotating the Aerrow about its major axis in increments of 90 ° while maintaining a constant gantry angle (0 °).

6.3 RESULTS

6.3.1 Isothermal Signal Baselines

With the Aerrow embedded in a solid body phantom, the typical level of stability observed in the core electrical power dissipation was on the order of 1.5 μW/min, with an associated 1σ signal variation of 1.2 μW. Given the effective mass of the core volume of this particular prototype, this amount of variation is equivalent to an absorbed dose rate of about 0.1 Gy/min. The two voltage measurements (thermistor heating network and precision shunt resistor voltages) from which this power is derived exhibit 1σ signal variations of about 1 mV each. In terms of control parameters, a negligible drift was observed in the bridge setpoint voltage (on the order of 1 nV/min) in comparison to the 1σ signal variations of about 90 nV. For this particular prototype design and operating conditions, a change in bridge voltage, ΔV, of 1 μV is approximately equivalent to a temperature change, ΔT, of 100 μK. Thus, the setpoint temperature in the core is maintained to within about 10 μK (1σ).

An example of an electrically emulated 8.5 Gy/min, 60 s irradiation is shown in Figure 6.5 alongside an equivalent experimental measurement (labeled as 'actual beam') acquired under standard conditions in a water equivalent phantom. The user-initiated emulation was carried out by entering the desired dose rate and duration into the control software, which then drove the equivalent electrical parameters for each of the core, jacket, and shield based on mass information and the thermistor heating network voltages. In both cases, the signal variation is the same. There are, however, a few qualitative differences between the emulated and actual beam signals. Most notably, the emulated trace exhibits relatively large spikes in response to the "beam" being turned on and off. This feature is absent in the actual beam acquisition and is likely due to the abrupt addition and subsequent removal of the emulated beam current. Another difference is that a smaller relative rise in the post-irradiation transient, as well as a quicker return to stability is observed in the actual beam.

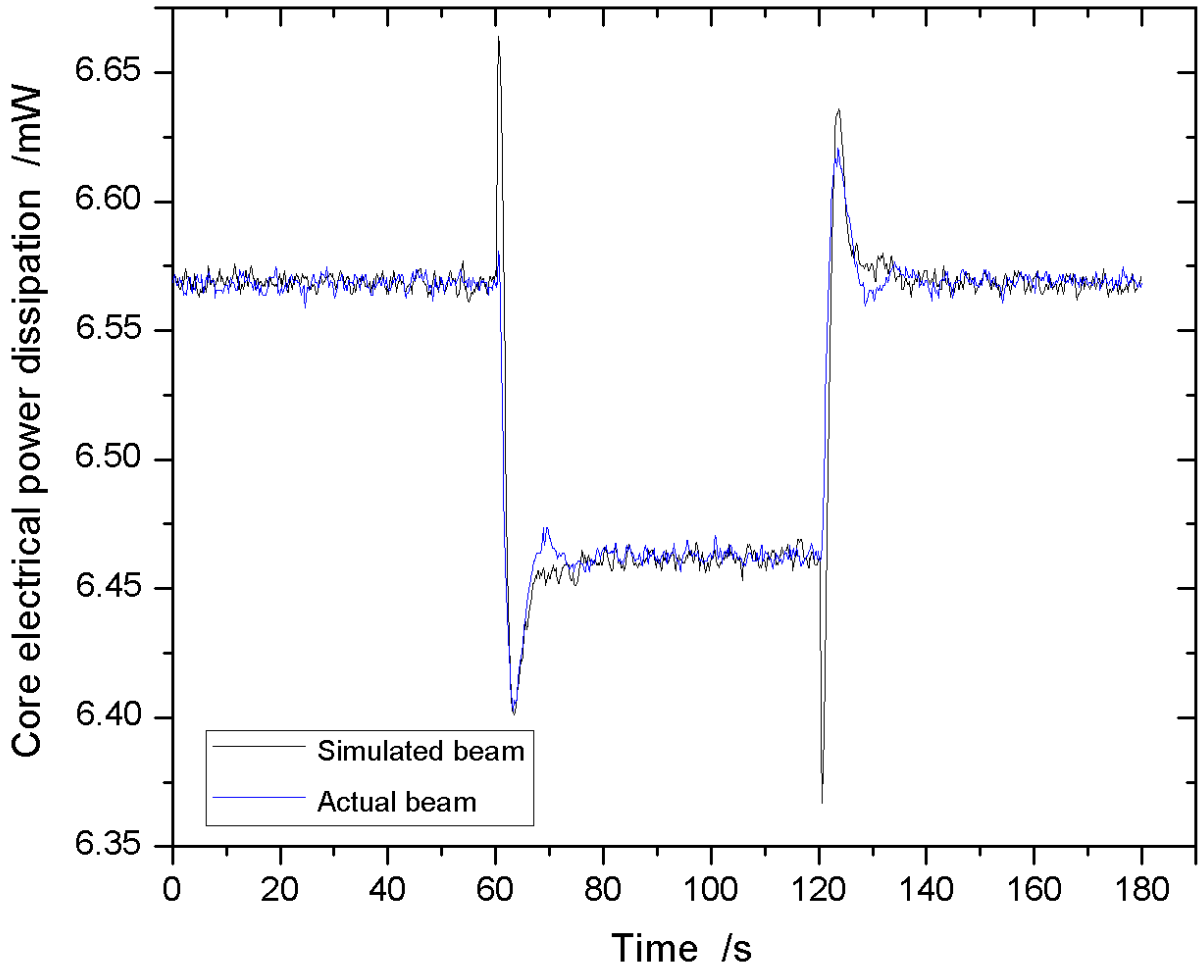

Figure 6.5: Example of a 60 s isothermal mode measurement acquired using the Aerrow in a 6 MV photon beam overlaid on an equivalent electrically-emulated irradiation (labeled 'Actual beam' and 'Emulated beam', respectively). Qualitative differences between the two signals include spikes in the emulated beam at the time of beam on and beam off, as well as a smaller relative rise in the post-irradiation transient and a quicker return to stability in the radiation induced measurement.

6.3.2 Dose Conversion

MC-derived dose ratios, $(\frac{D_w}{D_g})_{MC}$, were found to vary linearly as a function of beam quality for both photons and electrons in the therapeutic range. For the photon beams, $(\frac{D_w}{D_g})_{MC}$ ranged between 1.129 ± 0.001 for ^{60}Co ($\%dd(10)_X$ = 58.4) and 1.140 ± 0.001 for the 24 MV Mohan spectrum ($\%dd(10)_X$ = 86.8). Figure 6.6 depicts $(\frac{D_w}{D_g})_{MC}$, normalized to ^{60}Co, as a function of beam quality. For comparison, the beam quality conversion factor, k_Q, for an Exradin A12 ionization chamber is also shown in Figure 6.6 as an example of a typical reference class chamber. In contrast to the ionization chamber's ~3.5 % beam quality dependence across the range 58.4 > $\%dd(10)_X$ > 81.0 , the Aerrow shows less than a 1 % variation.

For the electron beam qualities studied in this work, $(\frac{D_w}{D_g})_{MC}$ was found to vary in the range of 1.174 ± 0.001 for a 6 MeV beam (R_{50} = 2.33 cm) to 1.147 ± 0.001 for a 20 MeV beam (R_{50} = 8.27 cm). In keeping consistent with TG-51, Figure 6.7 shows the variation of $(\frac{D_w}{D_g})_{MC}$ as a function of electron beam quality when normalized to R_{50} = 7.5 cm. Once again, a cylindrical ionization chamber dataset is included for the sake of comparison. The two types of detectors exhibit similar beam quality dependences (~2.5 % for the Aerrow, and ~3 % for the ionization chambers). Similar to TG-51, a photon-electron conversion factor, k_{ecal}, of 0.984 ± 0.001 was determined for the Aerrow by evaluating the ratio of $(\frac{D_w}{D_g})_{MC}$ for ^{60}Co and an electron beam with an R_{50} = 7.5 cm. This is significantly closer to unity than typical k_{ecal} values for cylindrical chambers (~0.900).

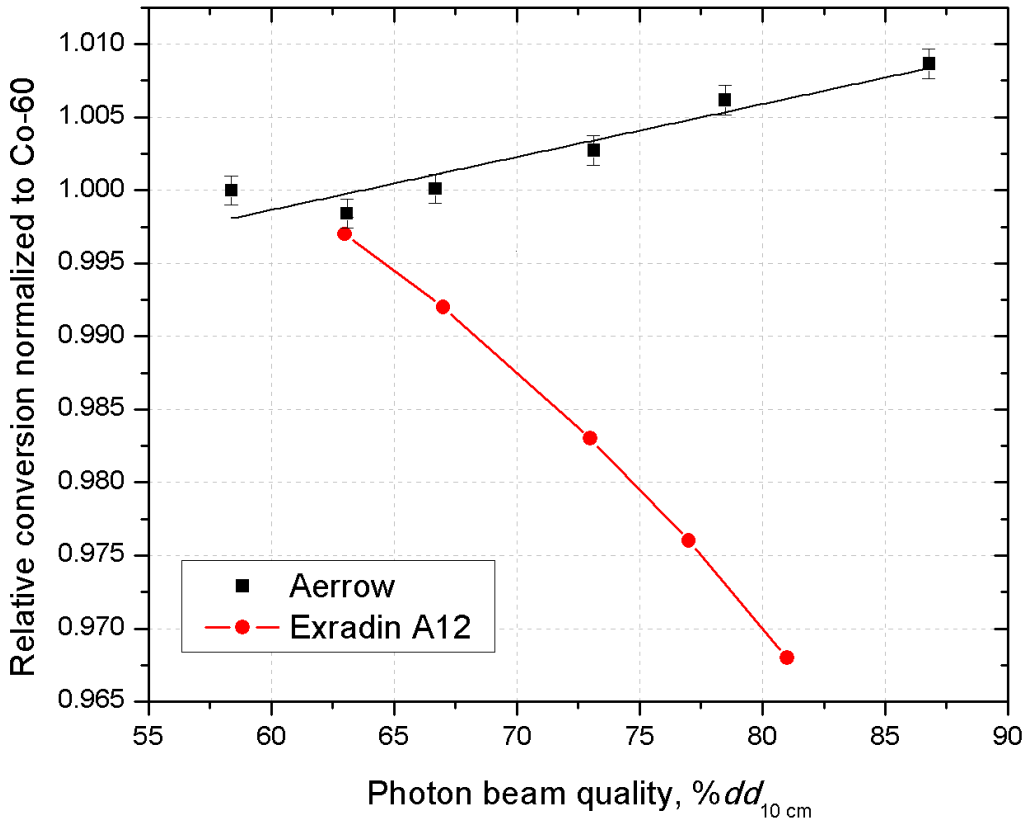

Figure 6.6: The relative photon beam quality dependence for both the Aerrow (black squares) and the Exradin A12 (red circles; McEwen *et al*. 2014) in the therapeutic range. The Exradin A12 is representative of a typical reference class ionization chamber. Both datasets are normalized to the beam quality of ^{60}Co (%*dd*(10)$_X$ = 58.4).

6.3.3 Reference Dosimetry Comparison

As a first stage validation of the Aerrow, absorbed dose measurements were performed under reference condition using the Aerrow's two independent modes (quasi-adiabatic and isothermal) and were directly compared to the dose derived from a calibrated reference class ionization chamber (Exradin A12) in a 6 MV photon beam. A total of 25 quasi-adiabatic (200 MU; 12 s) and 32 isothermal measurements (1000 MU; 60 s) were acquired, a summary of which is provided in Table 6.2.

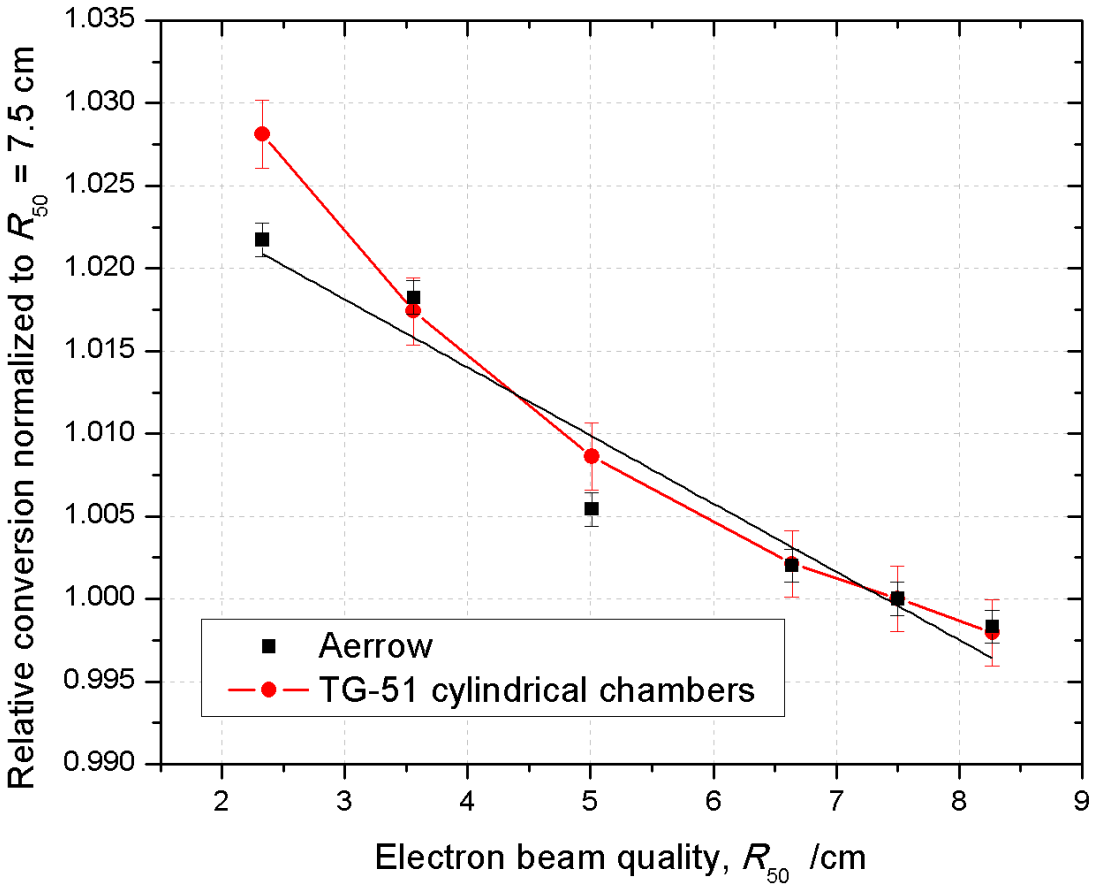

Figure 6.7: The relative electron beam quality dependence for both the Aerrow (black squares) and the cylindrical ionization chambers (red circles; Almond *et al.* 1999) in the therapeutic range. Both datasets are normalized to the beam quality, k_{ecal}, corresponding to R_{50} = 7.5 cm).

The repeatability (defined as 1σ) for both modes of operation in this particular experimental setup was 0.6 %. For this beam quality, a $(\frac{D_w}{D_g})_{MC}$ of 1.131 ± 0.001 was applied to the Aerrow measurements. For the quasi-adiabatic readings, a Comsol-derived conductive heat transfer correction, k_c, of 1.002 ± 0.002 was additionally applied. The expressed uncertainty in the average temperature and energy columns represents 1σ for that particular measurement. The uncertainty in the absorbed dose to water columns reflect the combined standard uncertainty (k = 1) for that particular technique (see section 6.3.5). A combined standard

uncertainty of 0.9 % was assumed for the ionization chamber measurements, based on the "best case" scenario as described in the TG-51 addendum.[13] The results of this study suggest not only self-consistency between the two Aerrow modes of operation, they also demonstrate statistically significant agreement between the doses measured using the Aerrow and that derived from the calibrated reference class chamber.

Table 6.2. Summary of dose measurements performed using the two independent operating modes of the Aerrow. Please note the differing number of MU's delivered in each case. The expressed uncertainty in the average temperature and energy columns represents 1σ for that particular measurement. The uncertainty in the absorbed dose to water columns reflect the combined standard uncertainty (k = 1) for that particular technique (see section 6.3.5). Percent difference noted in the last column is defined as [(Aerrow dose)-(TG-51 dose)] /(TG-51 dose) × 100%.

Aerrow mode of operation	Runs (#)	MU (#)	Avg. ΔT (mK)	Avg. ΔE (mJ)	Avg. D_w (cGy)	TG-51 D_w (cGy)[a]	Δ (%)
Quasi-adiabatic	25	200	1.88 ± 0.01	--	152.5 ± 1.5	152.5 ± 1.4	+0.01
Isothermal	32	1000	--	5.02 ± 0.03	753.2 ± 6.8	762.6 ± 6.8	-1.23

[a]The uncertainty expressed in this column (0.9 %) is taken as a "best case" from McEwen *et al*. 2014.

In a follow-up study, the Aerrow's isothermal mode was used to measure the absolute output of five high-energy photon and five electron beams under reference conditions in a water-equivalent phantom. These results, which are summarized in Figures 6.8 and 6.9, were directly compared to the output measured using a calibrated reference class chamber (Exradin A19). Overall, statistically significant agreement was observed for all output measurements. As in Table 6.2, the uncertainty in Figure 6.8 and 6.9 reflect the combined standard uncertainty (0.9 %; k = 1) for both measurement techniques. A minimum of five

repeated measurements were performed for each beam quality. The repeatability of the isothermal measurements ranged between 0.4 % (10 MV FFF; ~17 Gy/min) to 1.1 % (6 MV; ~4 Gy/min). On average, the Aerrow's measured photon outputs were 0.4 % greater than those obtained with the chamber (range: -0.5 % to 0.9 %), though based on the distribution of data points, there doesn't appear to be any obvious systematic effect. The statistically insignificant difference in the slopes of best fit in Figure 6.8 could be indicative of a slight intrinsic energy dependence not being considered. For the electrons, the Aerrow measured outputs that were, on average, 0.7 % less that those derived from the chamber readings (range: -1.4 % to -0.3%), and while not statistically significant (*i.e.*, no definitive conclusions can be drawn), there does appear to be a systematic difference between the two dosimeters.

6.3.4 Experimental Characterization of the Isothermal Mode

Figures 6.10 and 6.11 show plots of the Aerrow's response linearity and dose rate dependence, respectively. In the case of the former, a strong linear response with an adjusted R^2 value of 0.9998 (n = 30) is observed in the range of 80 cGy to 470 cGy. The five repeated measurements performed per data point exhibited a statistical variation (1σ) of 0.6 % to 0.8 % for all deliveries, with the exception of the 100 MU (0.8 Gy) run, which varied by 1.4 %. This relatively sharp increase in the spread of the data is due to the finite amount of time (~10 s) required for the temperature controllers to re-establish equilibrium during and after irradiation. In the case of the dose rate dependence, no statistically significant effects are observed in the range of 0.5 Gy/min to 5.4 Gy/min. As seen in Figure 6.11, the relative responses in this range all lie within ±0.8 % of the average. Similar to the linearity measurement sets, the statistical variation (1σ) for the dose rate data points down to 1.8 Gy/min ranged between 0.6 % and 1.0 %. A sharp increase was seen at dose rates of 0.9 Gy/min (σ ~ 1.7 %) and 0.5 Gy/min (σ ~ 3.3 %). This behavior is attributed to a relative

decrease in the signal to noise, which at 0.5 Gy/min, is equivalent to a dissipated power of about 6.5 μW in the core (normal 1σ signal variations are on the order of 1 μW).

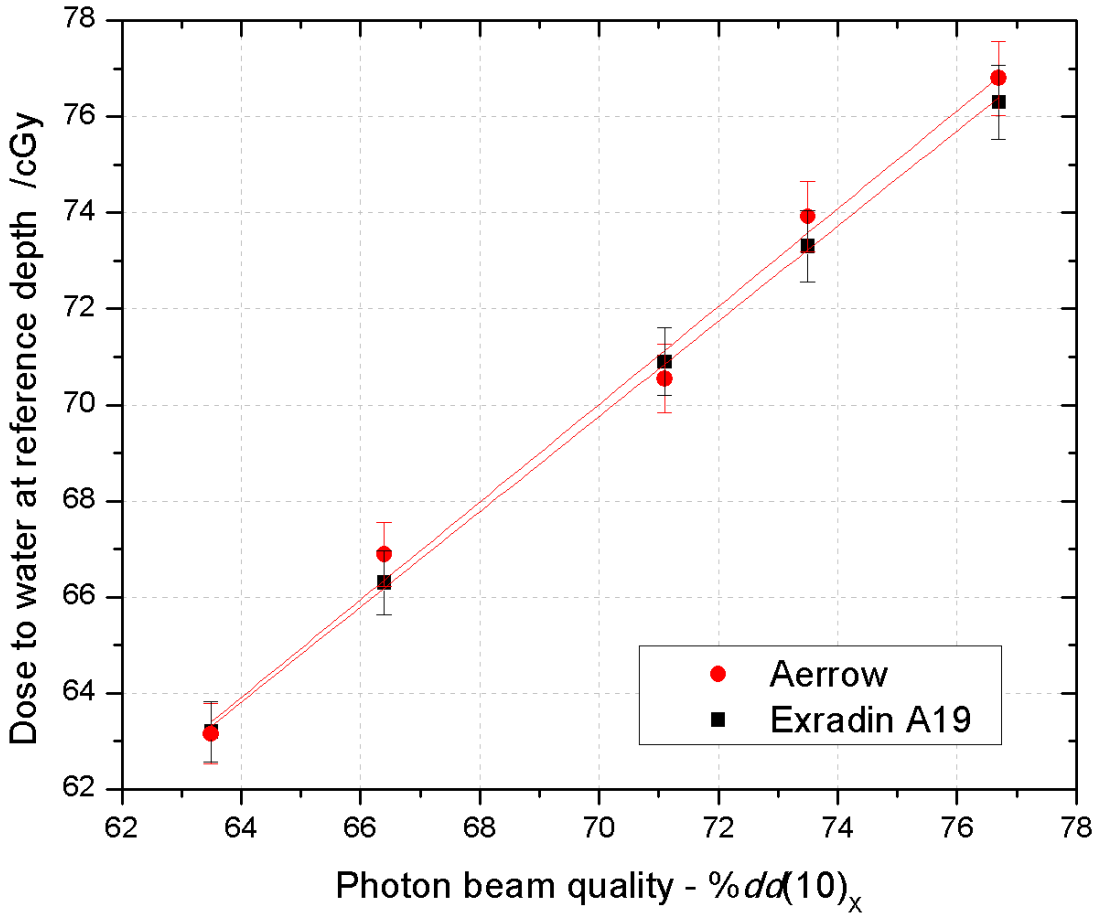

Figure 6.8: A comparison of output measurements for five high-energy photon beam qualities (6 MV, 6 MV FFF, 10 MV, 10 MV FFF, and 15 MV) as determined with the Aerrow operating in isothermal mode and a reference class ionization chamber (Exradin A19). Statistically significant agreement is seen for all included beams. On average, the Aerrow measured an output 0.4 % greater than that derived from the chamber readings.

Figure 6.12 depicts the relative dependence of the Aerrow's response to photon and electron beam quality in the range of 58.4 % < %$dd(10)_X$ < 86.8 % and 2.33 cm < R_{50} < 8.27 cm, respectively. In both cases, no statistically significant trend is exhibited as a function of energy, and a maximum deviation of about ±1 % from the average response across all beams qualities is observed.

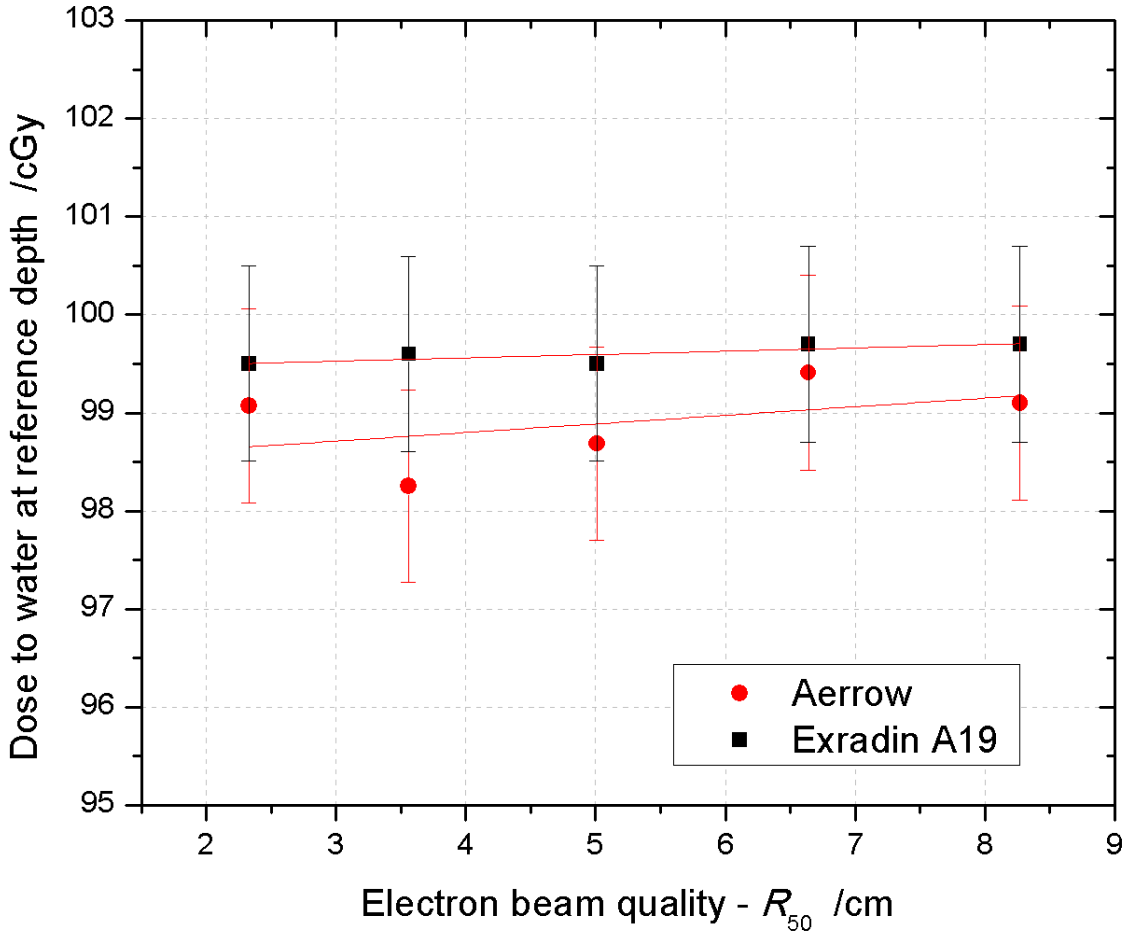

Figure 6.9: A comparison of output measurements for five high-energy electron beam qualities (6 MeV, 9 MeV, 12 MeV, 16 MeV, and 20 MeV) as determined with the Aerrow operating in isothermal mode and a reference class ionization chamber (Exradin A19). Statistically significant agreement is seen for all included beams. On average, the Aerrow measured an output 0.7 % lesser than that derived from the chamber readings.

The error bars shown in in Figure 6.12 represent the standard error on the mean measured signal for a given beam quality. Finally, the angular dependence (gantry stationary and detector rotated) of the Aerrow's response is shown in Figure 6.13 in increments of 90°. No statistically significant dependence is observed to within ±0.5 % of the average taken across all angles. The error bars represent the standard error on the mean measured signal for a given angle.

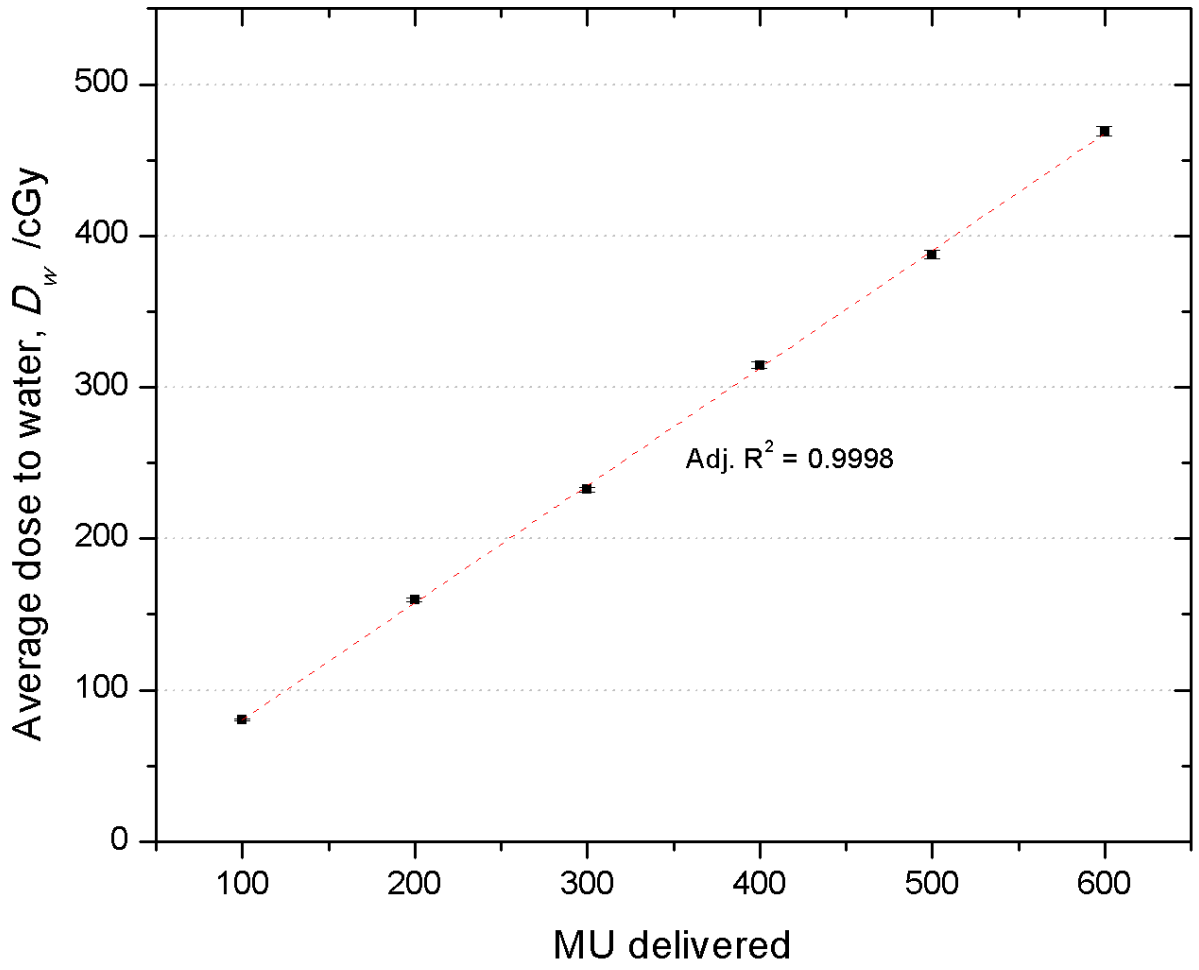

Figure 6.10: The Aerrow's response linearity as experimentally determined in a 6 MV beam (%*dd*(10)X = 66.3 %) in the range of 80 cGy to 470 cGy. Linearity of the detector reading was evaluated by varying the number of MU (100 to 600; increments of 100) delivered at a fixed accelerator repetition rate of 600 MU/min.

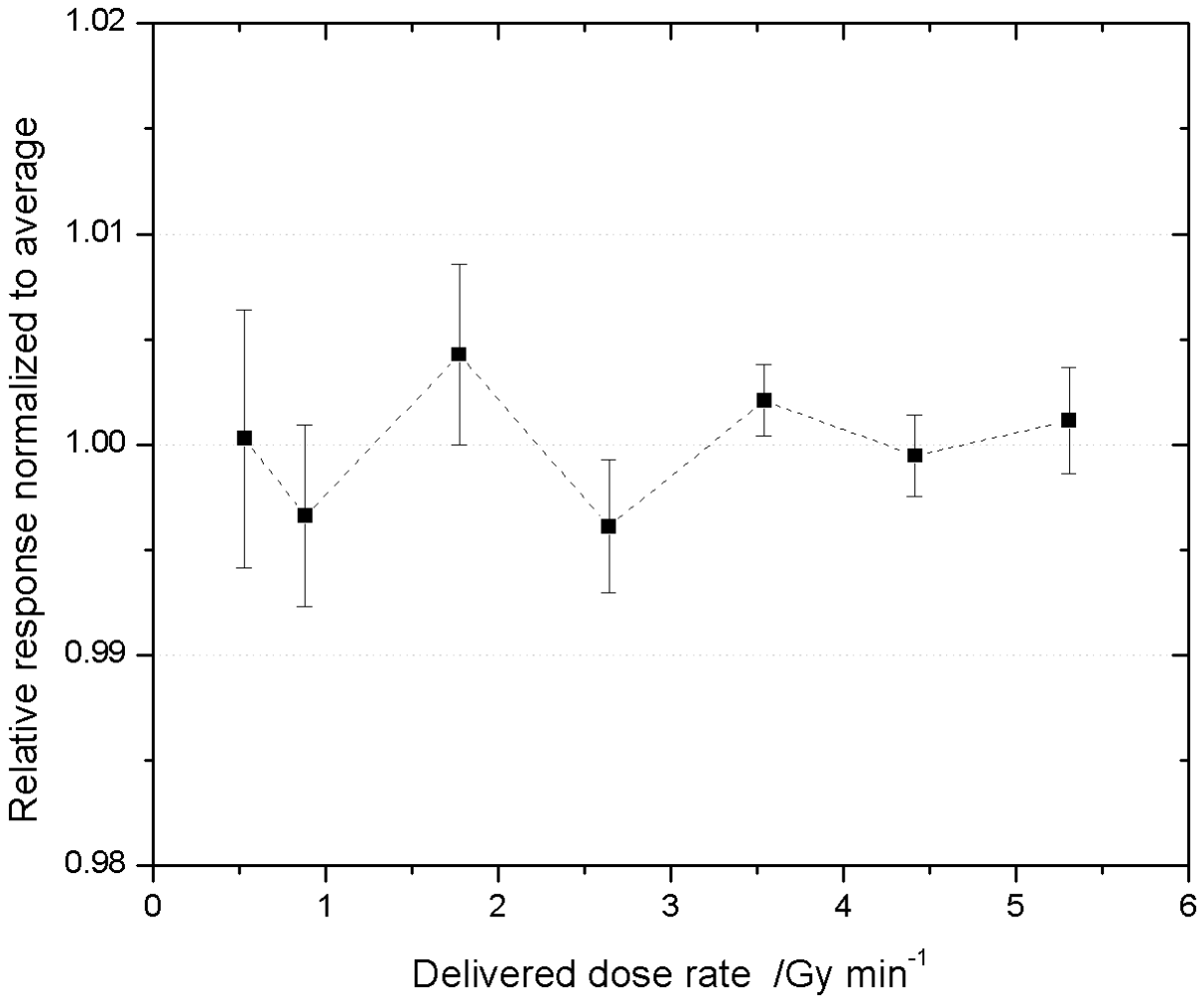

Figure 6.11: The dose rate dependence of the Aerrow was quantified in a 6 MV beam in the range of 0.5 Gy/min to 5.4 Gy/min by maintaining a constant irradiation time of 60 s and varying the repetition rate from 60 MU/min to 600 MU/min. No statistically significant effects are observed, although a sharp deterioration in the device repeatability is seen at dose rates of less than 1.8 Gy/min. The error bars in this plot are the standard errors on the mean measured dose, normalized to the average response across all dose rates.

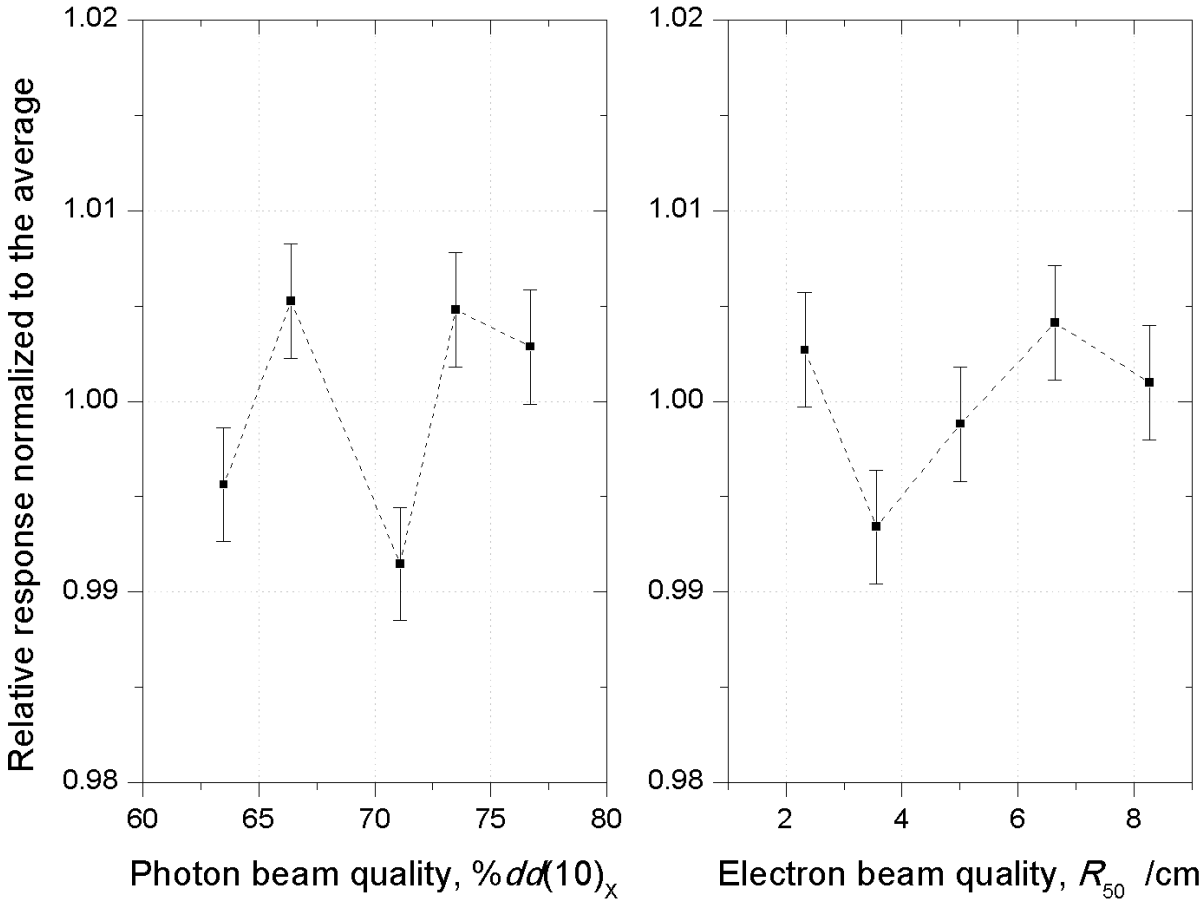

Figure 6.12: Energy dependence of the raw Aerrow signal to the dose delivered to the sensitive volume was measured for (left) five high-energy photon, and (right) five high-energy electron beam qualities by delivering a 60 s irradiation at the highest available repetition rate (600 to 2400 MU/min^{-1}). In both cases, no statistically significant trend is exhibited as a function of energy. The error bars shown represent the standard error on the mean measured signal for a given beam quality.

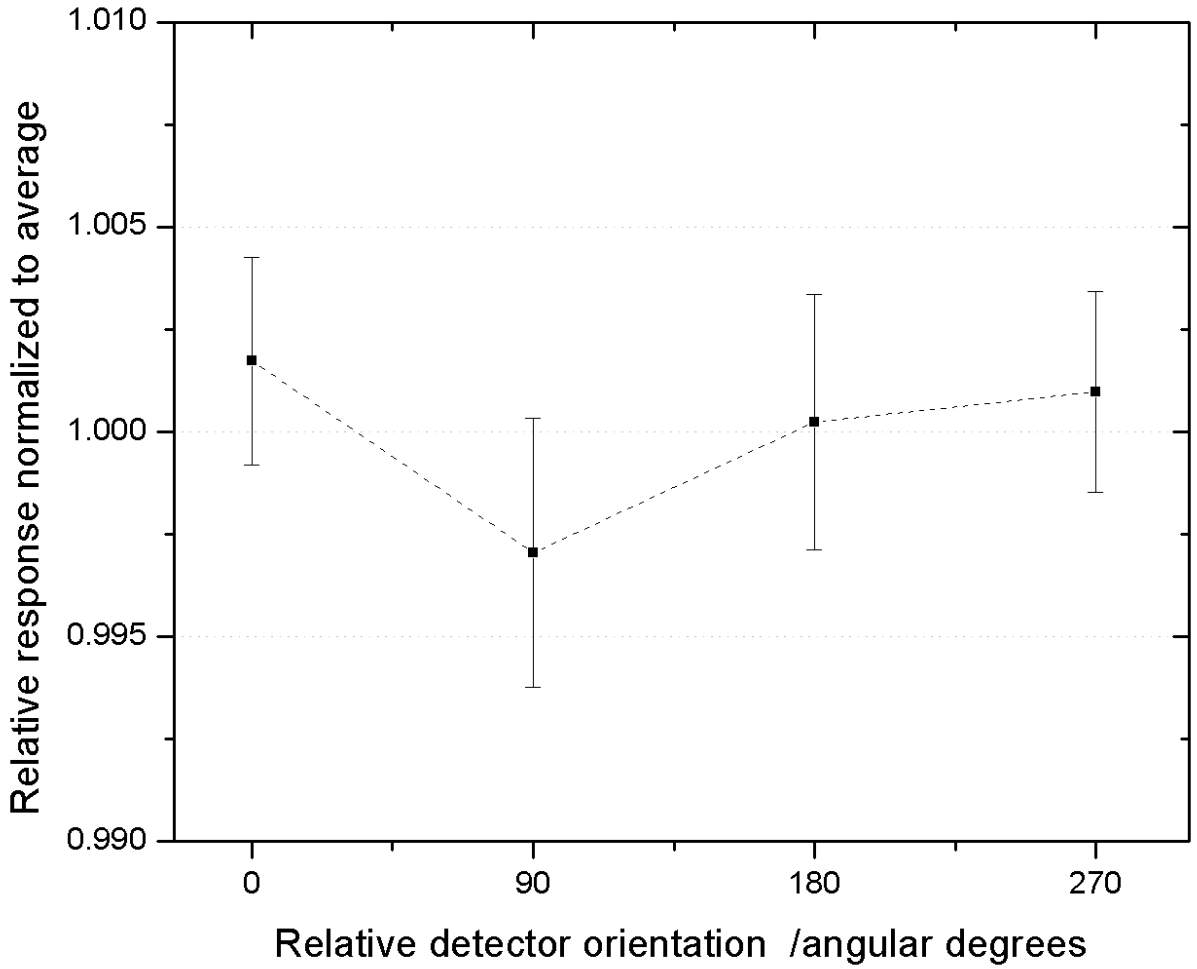

Figure 6.13: The angular dependence of the Aerrow as measured in a 6 MV beam by rotating the detector about its major axis in increments of 90 °. In this experiment, the gantry angle setting remained constant. No statistically significant dependence is observed to within ±0.5 % of the average taken across all angles. The error bars represent the standard error on the mean measured signal for a given angle.

6.3.5 Uncertainties

In an effort to identify the areas most in need of improvement, a breakdown of the estimated uncertainty budgets (in %), listing the largest contributing type A and B uncertainties associated with the determination of absorbed dose water, is provided in Table 6.3. It is

important to note that these uncertainty estimates are meant to provide a high-level perspective and should not be considered complete.

For instance, the heat transfer correction used in the adiabatic mode measurements (assumed to be unity for isothermal), while likely near unity for this type of setup, has not been extensively studied with a proper sensitivity analysis. As such, this quantity has been assigned a standard uncertainty of 0.1 – 0.2 %. The reproducibility represents a typical measurement uncertainty (the standard deviation of the raw mean acquired signal), however this can be reduced by performing repeated measurements ($u \propto (\sqrt{N})^{-1}$).

Applicable to the quasi-adiabatic mode only, the bridge and thermistor calibrations reflect the uncertainty in the fits of their respective curves. Since the specific heat capacity of the graphite used in the GPC's construction is unknown, a standard value with a rectangular uncertainty distribution of 715 ± 10 J kg^{-1} K^{-1} at 297.45 K was assigned based on experimentally determined values of pure samples found in the literature.[31,32] The positioning refers to the effect of the uncertainty in the GPC depth measurements. Finally, the perturbation/dose conversion refers to the statistical uncertainty (k = 1) in the MC simulations used to calculate this quantity.

Please note that some of the type B uncertainties lists in Table 6.3 can be significantly improved in future prototypes. In particular, the specific heat capacity and mass uncertainties could be reduced through a combination of manufacturer-provided values and appropriate measurements systems for independent validation. With these improvements, the combined relative standard uncertainty on the determination of D_w could sit around 0.8 %, assuming the current value for the reproducibility (0.6 %). On the other hand, the equivalent combined standard uncertainty associated with the reference ion chamber

measurements is estimated to be 0.9 % (k = 1).[13] A figure dominated by the uncertainties associated with $N_{D,w}^{Co_{60}}$ (0.75 %) and k_Q (0.4 %).

Table 6.3. Estimated uncertainty budgets (in %) for the Aerrow's isothermal and quasi-adiabatic modes of operation in high-energy photon beams.

Source of uncertainty	Isothermal		Quasi-adiabatic	
	Type A [%]	Type B [%]	Type A [%]	Type B [%]
Heat transfer correction	—	0.1	—	0.2
Reproducibility	0.6	—	0.6	—
Bridge calibration	—	—	—	0.1
Thermistor calibration	—	—	—	0.2
Electrical power	—	0.2	—	—
Specific heat capacity	—	—	—	0.8
Mass	—	0.5	—	—
Positioning	0.2	—	0.2	—
Dose perturbation / conversion	—	0.3	—	0.3
Other sources	—	0.2	—	0.2
Quadratic summation	0.6	0.6	0.6	0.9
Combined relative standard uncertainty on D_w	0.9		1.1	

6.4 DISCUSSION

Within combined uncertainties, the absorbed doses to water obtained with the Aerrow in the high-energy photon and electron beams are in good agreement with those derived from TG-51 using a calibrated reference class ionization chamber. Collectively, these reference dosimetry results demonstrate the feasibility of measuring absolute clinical photon and electron doses to within 1 % accuracy using this type of probe-format calorimeter. This is an

important finding, as currently, there is no other means of realizing absolute dose to water outside of the established primary dose standard calibration chain. Furthermore, no other calorimetry-based technology suitable for mainstream use has ever been shown to be a potential independent alternative to ionization chambers for clinical reference dosimetry. Other similarly-small calorimeters, such as the IMRT calorimeters developed by Duane *et al*. and Daures *et al.*, rely on elaborate vacuum pump systems to achieve pressures of typically less than 10^{-3} Pa in order to minimize the conductive and convective heat transfer inside the calorimeter.[17,18] While incredibly effective at thermally isolating the various constituent bodies of the calorimeter, the physical size of the pumps combined with the fragility of the plumbing connections make these cumbersome systems unsuitable for frequent transport, much less regular clinical use. Furthermore, the Aerrow's aerogel-based thermal insulation evidently provides a level of isolation adequate to achieve a repeatability similar to the 0.6 % achieved by Duane *et al*.[17]

The Aerrow's two independent modes were, to first-order, validated by demonstrating self-consistency between quasi-adiabatic and isothermal operation, and by showing agreement between them and the NRC-calibrated Exradin A12 chamber in a standard 6 MV photon beam. While the absolute accuracy of any primary technique (graphite calorimetry and water calorimetry-calibrated chamber) cannot be directly measured, showing agreement among independent methods helps validate the involved techniques.[3,41] Since the Exradin A12 was calibrated against a standard water calorimeter, this type of test can be considered an independent verification, since both calorimetry systems consist of different absorbing media and employ different approaches in determining correction factors. Any correlations which may potentially bias the comparison are considered outside of the scope of this study. The level of agreement shown by the quasi-adiabatic mode results suggest that there are no identifiable discrepancies in the absolute determination of dose. The isothermal mode results, however, suggest that one or more discrepancies may be contributing to a

systematic underestimation of the dose by about 0.5 % - 1.0 %. The most probable cause for this would be an equivalent overestimation of the effective mass of the core, which is likely to also be minimally energy dependent over the therapeutic range.[37] A reduction in the relative portion of non-graphite masses in the core (*e.g.*, smaller and fewer thermistors, thinner leads, etc.) is expected to improve the accuracy in the determination of the core mass effective during irradiation. Another potential contributing factor to this systematic difference is heat transfer between the core and the surrounding bodies (jacket, Pyrogel®, thermistor leads, etc.).

The successful implementation of the isothermal mode represents an important step towards the goal of developing a clinical-version of the Aerrow suitable for routine use. Compared to the quasi-adiabatic mode, the benefits of isothermal include a vastly decreased initial stabilization time (~10 mins) and the virtual elimination of inter-measurement delay. Further effort, however, is required to improve the repeatability, particularly for measurements involving dose rates of less than 2 Gy/min. This may be achieved through means of hardware (*e.g.*, eliminating ground loops and crosstalk, improving the resolution of the current source, digitizing nearer to the detector), software (*e.g.*, signal averaging, alternative analysis technique) or both (*e.g.*, analog or digital filtering). The same active thermal control systems developed to operate the Aerrow isothermally could also be used to intrinsically verify the response of the detector to electrical energy.[1,38] Where dosimetry is concerned, this is a very powerful feature; aside from the benefit of not requiring radiation, electrically calibrating the Aerrow eliminates the need to know the specific heat capacity of the constituent graphite and thermistor assemblies, heat transfer correction, and thermistor temperature calibration. Such a feature could also be programmed to be fully automated and performed at regular intervals when not in use. The practical impact of this functionality would be a dosimeter that could measure and take into account any potential drifts in its own response.

6.5 CONCLUSIONS

This work demonstrates the feasibility of using an ionization chamber-sized calorimeter as a practical means of measuring absolute dose to water in the radiotherapy clinic. In this study, the Aerrow was successfully used to quantify the absolute output of five high-energy photon (6 MV, 6 MV FFF, 10 MV, 10 MV FFF, and 15 MV), and five electron beams (6 MeV, 9 MeV, 12 MeV, 16 MeV, and 20 MeV). Overall, doses to water were determined with a combined $k = 1$ uncertainty of 0.9 % for the isothermal mode measurements, and 1.1 % when operated quasi-adiabatically. In terms of relative characterization, the Aerrow exhibited a strong linear response, which was characterized by an adjusted R^2 value of 0.9998 in the region of 80 cGy to 470 cGy. No statistically significant dose rate effects were observed in the range of 0.5 Gy/min to 5.4 Gy/min. For photon and electron beam qualities in the range of 58.4 % < $\%dd(10)_X$ < 86.8 % and 2.33 cm < R_{50} < 8.27 cm, respectively, no statistically significant trend is exhibited and a maximum deviation of about ±1 % from the average response across all beams qualities was observed. Finally, the angular dependence (gantry stationary and detector rotated) of the Aerrow's response is insignificant to within ±0.5 % of the average taken across all angles. While statistically insignificant, the isothermal mode results suggest that one or more discrepancies may be contributing to a systematic underestimation of the dose by about 0.5 % - 1.0 %. The most probable cause for this would be an equivalent overestimation of the effective mass of the core. In general, the potential introduction of calorimetry as a mainstream device into the clinical setting is significant as this fundamental technique has formed the basis of absorbed dose standards in many countries for decades. Considered as the most direct means of measuring dose, a calorimetry-based local dose standard could play an important role in solving some of the major challenges of contemporary dosimetry. In particular, investigations into the use of the Aerrow for MRgRT dosimetry, as well as plans to develop a further miniaturized Aerrow prototype suitable for small and composite field dosimetry are underway.

ACKNOWLEDGEMENTS

The efforts of Joe Larkin and Pavlos Papaconstadopoulos of the McGill University Health Centre, Greg Stanisz, Lynsie Thomason, and Ayelet Atkins of the Sunnybrook Research Institute, as well as David Marchington and Malcolm McEwen of the NRC are greatly appreciated. This work has been supported in part by the CREATE Medical Physics Research Training Network grant of the Natural Sciences and Engineering Research Council (NSERC) (grant no. 432290), as well as NSERC grant RGPIN 298191 and 435608. J. Renaud is a recipient of a Canadian Institutes of Health Research doctoral scholarship.

6.6 REFERENCES

[1]J. Seuntjens, and S. Duane, "Photon absorbed dose standards," Metrologia **46**, S39-S58 (2009).

[2]J.P. Seuntjens, and A.R. DuSautoy, "Review of calorimeter-based absorbed dose to water standards," in *Standards and Codes of Practice in Medical Radiation Dosimetry: Proc of an International Symposium* IAEA-CN-96-3 (International Atomic Energy Agency, Vienna, Austria, 2003).

[3]M.R. McEwen, and A.R. DuSautoy, "Primary standards of absorbed dose for electron beams," Metrologia **46**, S59-S79 (2009).

[4]D. Burns, "An analysis of existing data for W_{air}, I_c and the product of $W_{air}s_{c,air}$," Metrologia **49**, 507-512 (2012).

[5]BIPM (Bureau International des Poids et Mesures), "Measurement of absorbed dose to water for Cobalt 60 - Key and supplementary comparisons, Ionizing Radiation, Section I (x and gamma rays, electrons)," BIPM.RI(I)-K4 (BIPM, Paris, France, 2015).

[6]A. Krauss, "The PTB water calorimeter for the absolute determination of absorbed dose to water in ^{60}Co radiation," Metrologia **43**, 259-272 (2006).

[7]C.K. Ross, M. McEwen, and N.V. Klassen, "Vessel designs and correction factors for water calorimetry," *Workshop on Absorbed Dose and Air Kerma Primary Standards* (*Paris, France, 9-11 May 2007*) (LNE, CEA-LIST-LNHB & BIPM).

[8]A. Sarfehnia, K. Stewart, and J. Seuntjens, "An absorbed dose to water standard for HDR ^{192}Ir brachytherapy sources based on water calorimetry: numerical and experimental proof-of-principle," Med. Phys. **34**, 4957-4961 (2007).

[9]L.A. de Prez, and J.A. de Pooter, "The new NMi orthovoltage x-rays absorbed dose to water primary standard based on water calorimetry," Phys. Med. Biol. **53**, 3531-3542 (2008).

[10]M. Pinto, M. Pimpinella, M. Quini, M. D'Arienzo, I. Astefanoaei, S. Loreti, and A.S. Guerra, "A graphite calorimetry for absolute measurements of absorbed dose to water: application in medium-energy x-ray filtered beams," Phys. Med. Biol. **61**, 1738-1764 (2016).

[11]P.D. Harty, J.E. Lye, G. Ramanathan, D.J. Butler, C.J. Hall, A.W. Stevenson, and P.N. Johnston, "Absolute x-ray dosimetry on a synchroton medical beam line with a graphite calorimeter," Med. Phys. **41**(5), 052101 (2014).

[12]R. Almond, P.J. Biggs, B.M. Coursey, W.F. Hanson, M. Saiful Huq, R. Nath, and D.W.O. Rogers, "AAPM's TG-51 protocol for clinical reference dosimetry of high-energy photon and electron beams," Med. Phys. **26**, 1847-1870 (1999).

[13]M. McEwen, L. DeWerd, G. Ibbott, D. Followill, D.W. Rogers, S. Seltzer, and J. Seuntjens, "Addendum to the AAPM's TG-51 protocol for clinical reference dosimetry of high-energy photon beams," Med. Phys. **41**, 041501 (2014).

[14]IAEA (International Atomic Energy Agency), "Absorbed dose determination in external beam radiotherapy based on absorbed-dose-to-water standards: An international code of practice for dosimetry," Technical Report Series 398 (IAEA, Vienna, Austria, 2001).

[15]R. Alfonso, P. Andreo, R. Capote, M. Saiful Huq, W. Kilby, P. Kjäll, T.R. Mackie, H. Palmans, K. Rosser, J. Seuntjens, W. Ullrich, and S. Vatnitsky, "A new formalism for reference dosimetry of small and nonstandard fields," Med. Phys. **35**, 5179-5186 (2008).

[16]D.J. O'Brien, D.A. Roberts, G.S. Ibbott, and G.O. Sawakuchi, "Reference dosimetry in magnetic fields: formalism and ionization chamber correction factors," Med. Phys. **43**(8), 4915-4927 (2016).

[17]S. Duane, M. Aldehaybes, M. Bailey, N.D. Lee, C.G. Thomas, and H. Palmans, "An absorbed dose calorimeter for IMRT dosimetry," Metrologia **49**, S168-S173 (2012).

[18]J. Daures, A. Ostrowsky, and B. Rapp, "Small section graphite calorimeter (GR-10) at LNE-LNHB for measurements in small beams for IMRT," Metrologia **49**, S174-S178 (2012).

[19]S. Dufreneix, A. Ostrowsky, M. Le Roy, L. Sommier, F. Delaunay, B. Rapp, J. Daures, and J.-M. Bordy, "Using a dose-area product for absolute measurements in small fields: A feasibility study," Phys. Med. Biol. **61**, 650-662 (2016).

[20]L. de Prez, J. de Pooter, B. Jansen, and T. Aalbers, "A water calorimeter for on-site absorbed dose to water calibrations in ^{60}Co and MV-photon beams including MRI incorporated treatment equipment," Phys. Med. Biol. **61**, 5051-5076 (2016).

[21]J. Renaud, S. Rossomme, A. Sarfehnia, S. Vynckier, H. Palmans, A. Kacperek, and J. Seuntjens, "Development and application of a water calorimeter for the absolute dosimetry of short-range particle beams," Phys. Med. Biol. **61**, 6602-6619 (2016).

[22]H. Palmans, R. Thomas, M. Simon, S. Duane, A. Kacperek, A. DuSautoy, and F. Verhaegen, "A small-body portable graphite calorimeter for dosimetry in low-energy clinical proton beams," Phys. Med. Biol. **49**, 3737-3749 (2004).

[23]M.R. McEwen, and S. Duane, "A portable calorimeter for measuring absorbed dose in the radiotherapy clinic," Phys. Med. Biol. **45**, 3675-3691 (2000).

[24]J. Renaud, D. Marchington, J. Seuntjens, and A. Sarfehnia, "Development of a graphite probe calorimeter for absolute clinical dosimetry," Med. Phys. **40**(2), 020701 (2013).

[25]I.S. Sundara Rao, and S.B. Naik, "Graphite calorimeter in water phantom and calibration of ionization chambers in dose to water for ^{60}Co gamma radiation," Med. Phys. **7**(3), 196-201 (1980).

[26]V.A. Berlyand, and Yu.I. Bregadze, "Portable calorimeter for measuring absorbed doses of x-rays and electrons from accelerators," Measurement Techniques **34**, 1179-1184 (1991) (Translated from Izmeritel'nava Teknika, No. 11, pp. 56-58, 1991).

[27]Y. Morishita, M. Kato, N. Takata, T. Kurosawa, T. Tanaka, and N. Saito, "A standard for absorbed dose rate to water in a ^{60}Co field using a graphite calorimeter at the national metrology institute of Japan," Radiation Protection Dosimetry, pp. 1-9 (2012).

[28]A.S. Guerra, S. Loreti, M. Pimpinella, M. Quini, M. D'Arienzo, I. Astefanoaei, C. Caporali, C. Bolzan, and M. Pagliari, "A standard graphite calorimeter for dosimetry in brachytherapy with high dose rate ^{192}Ir sources," Metrologia **49**, S179-S183 (2012).

[29]A.R. DuSautoy, "The UK primary standard calorimeter for photon-beam absorbed dose measurements," Phys. Med. Biol. **41**, 137-151 (1996).

[30]B. Owen, and A.R. DuSautoy, "Correction for the effect of the gaps around the core of an absorbed dose graphite calorimeter in high energy photon radiation," Phys. Med. Biol. **36**(12), 1699-1704 (1991).

[31]"Heat capacity of the elements at 25 °C," in *CRC handbook of Chemistry and Physics, 89th edition*, edited by D.R. Lide (CRC Press/Taylor and Francis, Boca Raton, FL, 2009), pp. 4-127.

[32]S. Picard, D.T. Burns, and P. Roger, "Determination of the specific heat capacity of a graphite sample using absolute and differential methods," Metrologia **44**, 294-302 (2007).

[33]K. Stewart, N. Klassen, C. Ross, and J. Seuntjens, "Design and testing of a new sealed water calorimeter for electron beams," Med. Phys. **32**, 2419 (2005).

[34]J. Renaud, A. Sarfehnia, K. Marchant, M. McEwen, C. Ross, and J. Seuntjens, "Direct measurement of electron beam quality conversion factors using water calorimetry," Med. Phys. **42**(11), 6357-6368 (2015).

[35]K.J. Stewart, "The development of new devices for accurate radiation dose measurement: A guarded liquid ionization chamber and an electron sealed water calorimeter," Ph.D. thesis, McGill University, Montreal, 2007.

[36]S.R. Domen, and P.J. Lamperti, "A heat-loss-compensated calorimeter: Theory, design, and performance," J. Res. Natl. Bur. Stand. A Phys. Chem. **78A**, 595-610 (1974).

[37]J. Witzani, K.E. Duftschmid, Ch. Strachotinsky, and A. Leitner, "A graphite absorbed-dose calorimeter in the quasi-isothermal mode of operation," Metrologia **20**, 73-79 (1984).

[38]J. Daures, and A. Ostrowsky, "New constant-temperature operating mode for graphite calorimeter at LNE-LNHB," Phys. Med. Biol. **50**, 4035-4052 (2005).

[39]J. Renaud, A. Sarfehnia, and J. Seuntjens, "On the practical use of calorimetry for routine absolute dosimetry in the radiotherapy clinic," *World Congress on Medical Physics and Biomedical Engineering* (*Toronto, Canada, 7-12 June 2015*) IFMBE Proceedings 51, pp. 667-670.

[40]BIPM (Bureau International des Poids et Mesures), “Evaluation of measurement data – Guide to the expression of uncertainty in measurement,” JCGM 100:2008, First ed. (BIPM, Paris, France, 2008).

[41]K.R. Shortt, “The role of comparisons in confirming the accuracy of dosimetric standards," in *Recent developments in accurate radiation dosimetry* (Medical Physics Publishing, Madison, WI, 2002). Ed. J.P. Seuntjens, and P.N. Mobit.

[42]S. R. Domen, “Advances in Calorimetry for Radiation Dosimetry,” in *The Dosimetry of Ionizing Radiation, Vol. II*, edited by K. R. Kase, B. E. Bjärngard, F. H. Attix (Academic Press, Inc., Orlando, 1987), pp. 245-320.

[43]I. Kawrakow, and D.W.O. Rogers, “The EGSnrc code system: Monte Carlo simulation of electron and photon transport,” NRC Technical Report No. PIRS-701 v4-2-2-5 (National Research Council of Canada, Ottawa, Canada, 2007).

[44]R. Mohan, C. Chui, and L. Lidofsky, “Energy and angular distributions of photons of medical linear accelerators,” Med. Phys. **12**, 592-597 (1985).

[45]T. Connell, A. Alexander, M. Evans, and J. Seuntjens, “An experimental feasibility study on the use of scattering foil free beams for modulated electron radiotherapy,” Phys. Med. Biol. **57**, 3259-3272 (2012).

Chapter 7

THE MCGILL WATER CALORIMETRY SYSTEM

7.1 INSTRUMENTATION

This section provides an overview of the McGill water calorimetry system from a hardware point of view (equipment and circuitry). This section is meant to provide a high level perspective of our experimental setup and to compliment the theory provided in *Chapter* 3. Following this, a section is dedicated to each of the two water calorimeters used during this project. The remainder of this Chapter focuses on the details of the various components of the calorimeter, as well as an explanation of the methodologies employed throughout the experimental portion of this work.

Figure 7.1 shows a schematic diagram of the experimental setup, including the most important components and electrical connections. A water calorimeter is simply a water phantom with a very precise thermal control system. The temperature of the water is cooled to 4 °C (temperature at which the density of water is maximum) to reduce convection, and

actively maintained to provide an adequately stable environment to measure sub-mK radiation-induced temperature rises.[1]

A Keithely 2002 digital multimeter was used to measure the resistance of the three PT-100 resistance temperature detectors (RTDs) (Thermo Kinetics, R21-D100E4) which were used to continuously monitor the temperature of the water phantom. These temperature readings were used as feedback to adjust the temperature of a fridge (coolant circulator) in order to prevent excessive thermal drifts inside the water phantom and to maintain stability to within 5 mK – 10 mK over several hours.

A thermistor is a temperature sensitive resistor that is used as the sensor of choice in water calorimetry.[1-4] Using two such thermistor beads, temperature rises of few hundred μK can be measured in water. For a typical temperature rise of roughly 240 μK/Gy, a thermistor's resistance will decrease by roughly 100 mΩ. These small resistance changes are measured using a Wheatstone bridge type circuit. The acquired signal is thus obtained in terms of bridge output voltage, which for the above example, would correspond to ΔV = 4.8 μV.

In this work, we used a bridge circuit similar to a classic Wheatstone[5], although instead of using passive components only (resistors, capacitors, etc.), this 'active' bridge is also made up of operational amplifiers. The result of which is a more robust voltage output with lower uncertainty (*i.e.*, higher signal to noise ratio, and thus more highly reproducible). An SR850 lock-in amplifier (Standard Research Systems) was used to measure the output voltage from the bridge. The lock-in allows accurate measurements of an AC signal down to a few nV.[1,4] It accomplishes this task through a phase-sensitive detection technique whereby the component of the signal at a specified frequency and phase is singled out; hence, the lock-in feeds the system with an internally generated reference sinusoidal frequency (V_{peak} = 1 V), and isolates the component of the output signal that is at the same reference frequency. As

such, the lock-in amplifier permits for very sensitive measurements, as it acts like a precise bandpass filter.

A Burster 1408 high-precision decade resistor box is used to balance the thermistor resistance in the bridge circuit, and also to perform bridge calibrations (see *Sections* 7.6 and 7.9.3, respectively). The unit consists of a series of high precision Zeranin® resistors with nominal accuracies of 0.01 % - 0.02 %. The case of the resistance decade box is grounded to earth, and is directly connected to the bridge via a well-shielded coax cable. Similarly, a decade capacitor box is used to balance the 90 ° out-of-phase (capacitive) component of the bridge impedance. Together, the resistor and capacity boxes are adjusted to balance the bridge circuit, meaning that a null voltage is recorded as the output signal.

All major devices, including the computer, are interconnected through a General Purpose Interface Bus (GPIB, IEEE-488). Due to radiation safety, the operator must be outside the treatment room during experiments. For this reason, two GPIB extending devices (HP 37204A) are used to transfer the data over a 15 m coax cable to the computer in the control area. To avoid ground loops, all devices and cables are grounded through a single power supply. Please note that the power supply is not shown in Fig. 7.1.

A 2-channel flatbed paper chart plotter (Soltec 1242) is connected to the analog output of the lock-in amplifier and is used to produce a hard copy of the recorded signal. This is a duplicate (backup only) of the signal that is also digitally acquired by the computer. The plots produced by the chart recorder have never been used for analysis; they serve only to facilitate the visualization of the calorimeter's response and to track behaviour of the system as a whole over very long time periods. All of the equipment mentioned in this section are controlled remotely from the operator (control) area via the computer.

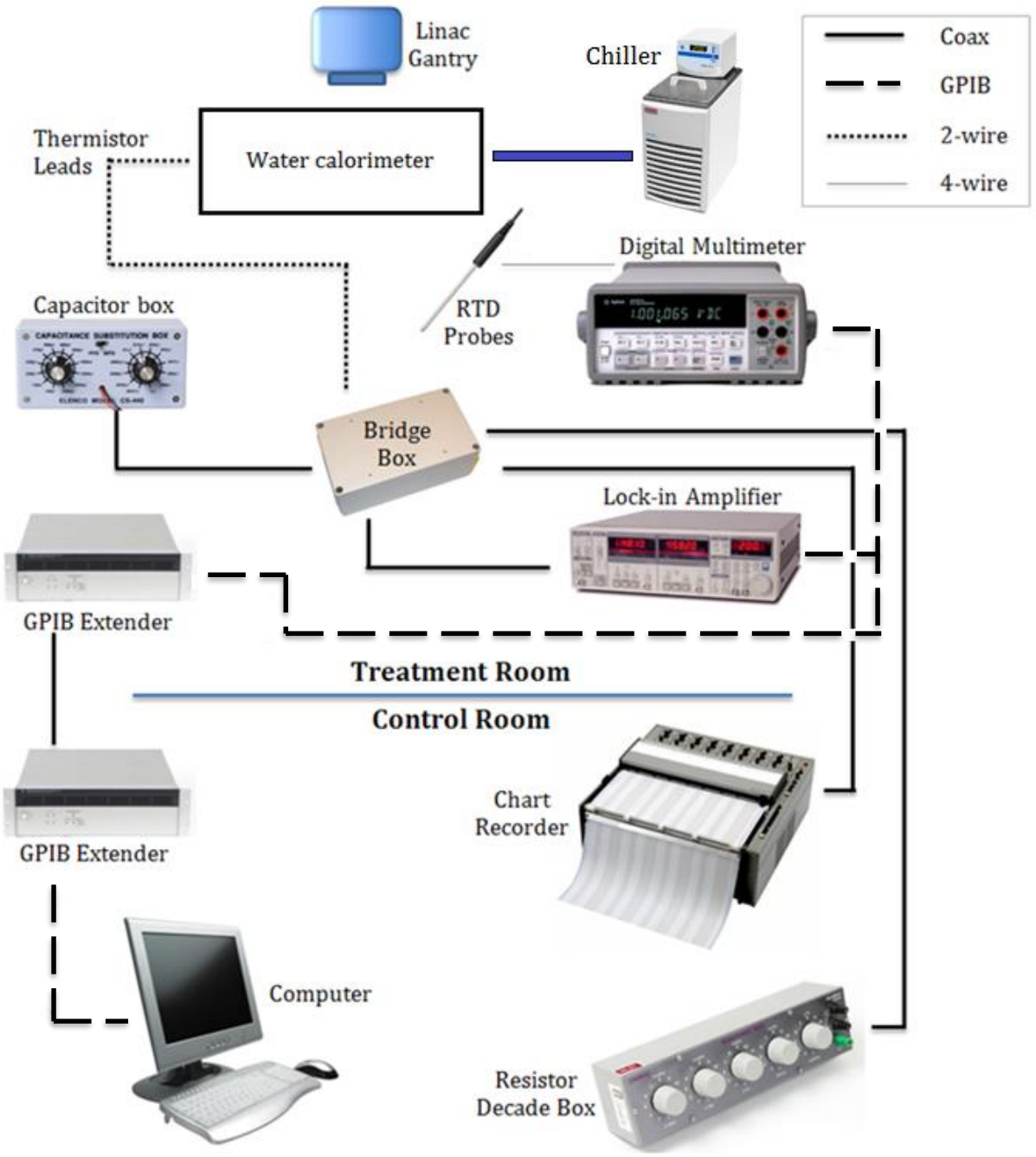

Figure 7.1: A schematic diagram of the water calorimetry system setup. All components, their location (inside treatment room or control room), as well as the electrical connections (legend provided) are shown. The power supplies have been omitted to maintain clarity. The thick blue line between the chiller and water calorimeter represents the circulating fluid. Here, the water calorimeter may either be the electron sealed or short range water calorimeter (ESWcal or SHREWcal; *Sections* 7.2 and 7.3, respectively).

7.2 ELECTRON SEALED WATER CALORIMETER (ESWCAL)

A detailed description of the in-house built electron sealed water calorimeter (ESWcal) is provided in this section. Please note that a short description of the device is also provided in *Section* 8.2.1.

Figures 7.2 and 7.3 show a schematic diagram and pictures of the ESWcal, respectively. The calorimeter consists of a 30 × 30 × 20 cm^3 acrylic water tank (phantom) with an integrated cooling system for active thermal control. The phantom is surrounded by two 5 cm thick polystyrene slabs which are separated by a 5 mm thick copper plate. The copper forms an enclosure that surrounds the tank on all sides. On the top surface (the lid), the copper plate has a 12 × 12 cm^2 cutout which serves as an entrance window. The purpose of the window is to permit the external radiation beam to enter the calorimeter with minimal attenuation and scatter. This opening is covered by a 0.15 mm thick brass foil that is attached to the copper plate with a silver-based thermally-conductive epoxy. The entire assembly is housed inside a 19 mm thick high density polyethylene box. The external dimensions of the box are approximately 55 × 60 × 60 cm^3.

A single plumbing circuit of copper tubing (Ø ≈ 10 mm) has been epoxied to all sides of the copper box in a zig zag pattern (see Figure 8.1). A Neslab RTE-7 refrigerated circulator (Thermo Scientific) is used to actively control the temperature of the copper plate by pumping a cooled fluid through the tubing network. The resolution of temperature control of the fluid if 0.1 °C.

The ESWcal is also equipped with a heat exchanger, a length of copper tubing forming a ring that is in direct contact with the water inside the phantom. The heat exchanger is connected to a manifold which serves as the fluid inlet. The manifold also feeds the larger tubing network attached to the copper box. The exchanger is used for rapid temperature

manipulations of the water phantom (*e.g.*, initial cooling of the water from room temperature to 4 °C) by means of a manual valve connected to the manifold. Measurements are also performed with the heat exchanger valve closed because adequate thermal drifts in the phantom cannot be achieved otherwise.

A magnetically-coupled stirrer at the bottom of the water phantom is used to mix the water in between sets of calorimetric runs and remove any temperature gradients that have built up during consecutive runs. The water temperature is monitored by taking the average reading of two RTDs; a third RTD is used to measure the copper temperature. The probe readings are continuously recorded and are used as feedback to adjust the chiller.

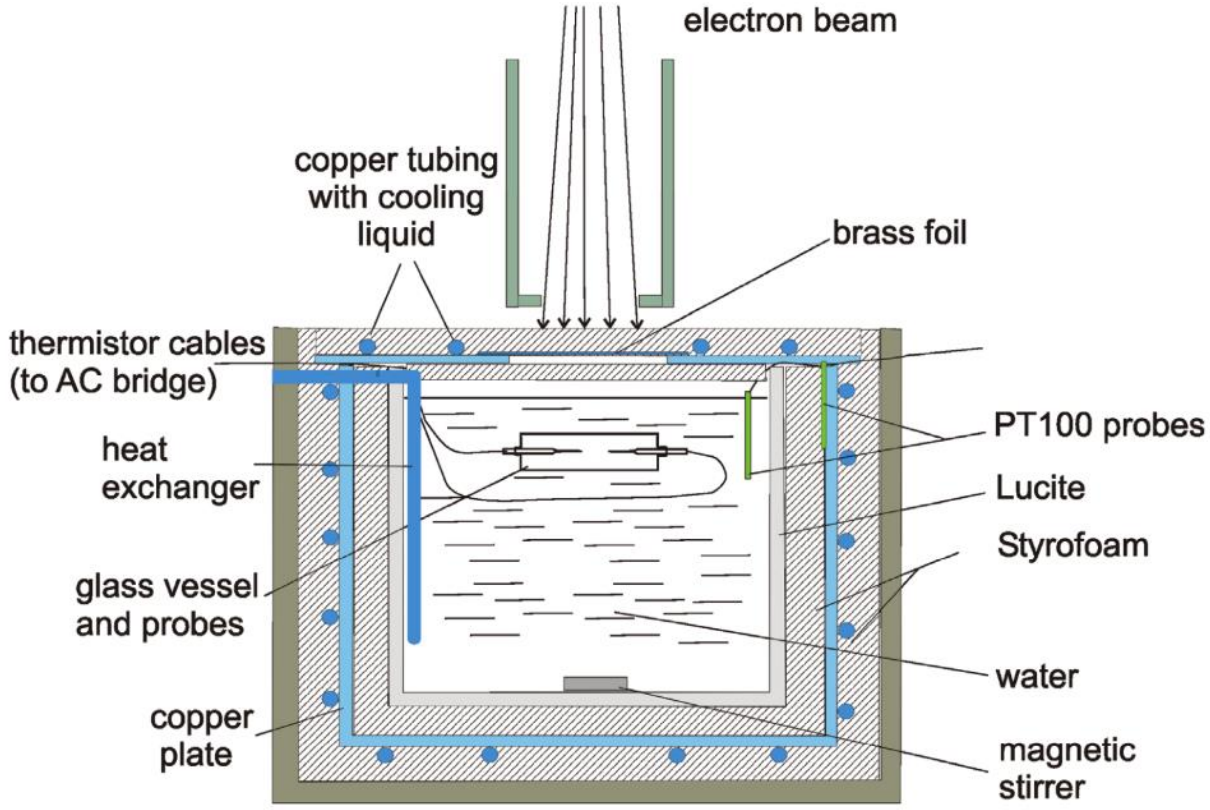

Figure 7.2: A schematic diagram of the electron sealed water calorimeter (ESWcal) positioned under a vertically incident linac-based high-energy electron beam.[1]

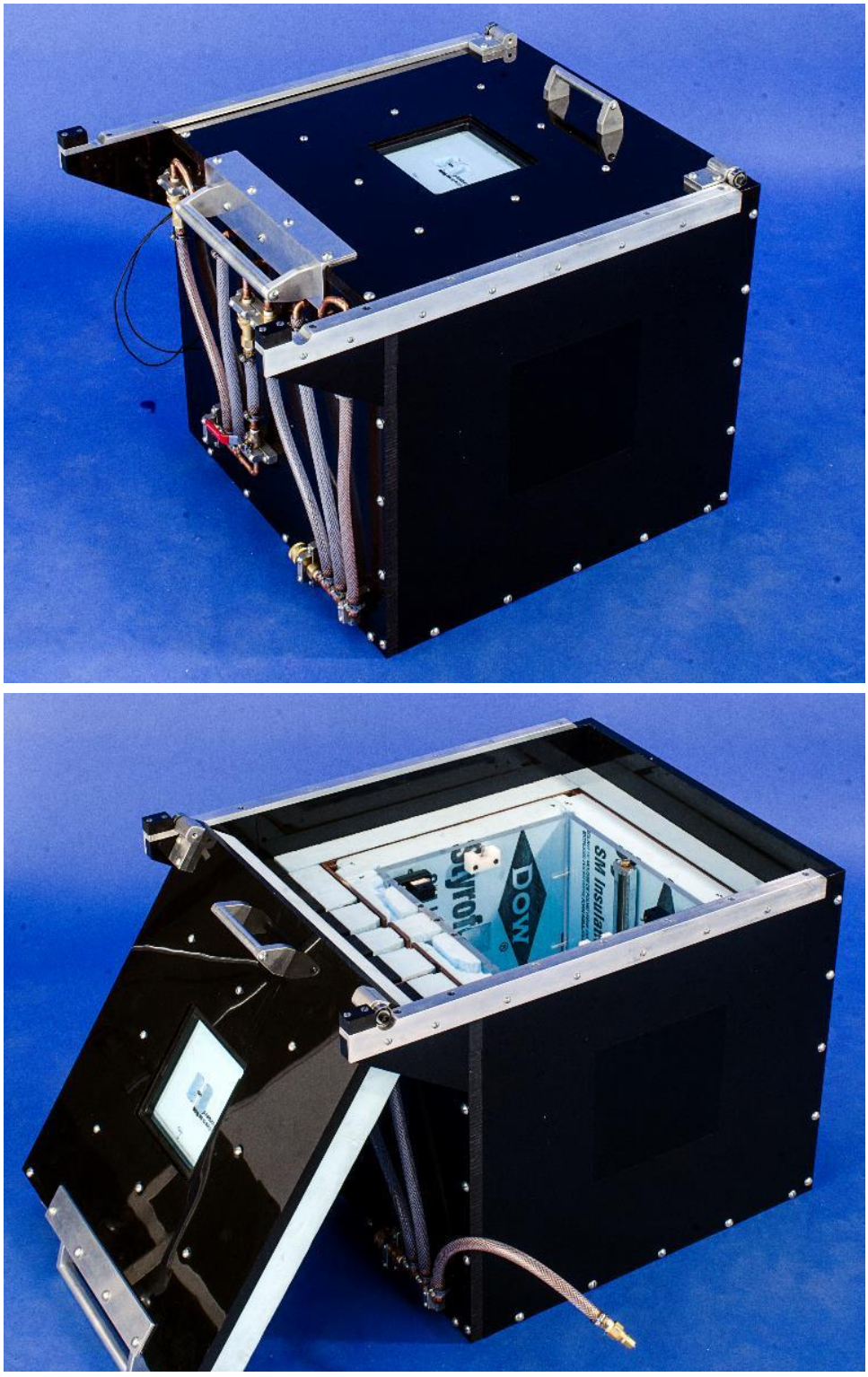

Figure 7.3: Photographs of the ESWcal with the lid (top) securely fastened, and (bottom) removed. Plumbing manifolds (inlet and outlet), layers of expanded polystyrene, copper plate, black polyethylene outer box, and acrylic phantom are all visible.

At the heart of the calorimeter, are the thermistor probes and the vessel which encloses them. To accurately position the vessel, a precise vertical depth positioning device was fixed to one side of the inner acrylic wall of the phantom (see Figure 7.6). The vessel is then mounted onto a holder device which itself is mounted onto the positioning bracket with three plastic screws. A stainless steel ball bearing is used as a pivot point (positioned in between the three screws) such that the screws can be used to make fine adjustments to the tilt of the vessel.

In order to cross calibrate an ionization chamber against the water calorimeter, the chamber is placed inside the water tank (this avoids any uncertainties due to experimental setup differences). In such cases, a modified holder is used to support the chamber as opposed to the vessel. Moreover, during such measurements, the water temperature is maintained at room temperature in accordance with conventional ionization chamber use.

7.3 SHORT RANGE WATER CALORIMETER (SHREWCAL)

A detailed description of the in-house built short range water calorimeter (SHREWcal) is provided in this section. Please note that a short description of the device is also provided in Section 9.2.3.

Figure 7.4 shows pictures the SHREWcal from several angles. The calorimeter consists of block of expanded polystyrene milled to accommodate the glass calorimeter vessel and air cooling system for active thermal control. As the name suggests, the calorimeter is designed to perform dose measurements at shallow depths (in the range of 6 mm to 20 mm). The enabling idea permitting such short range measurements to be made is the elimination of a traditional standard water phantom (*i.e.*, $30 \times 30 \times 30$ cm^3). Sitting atop a three-legged acrylic base, the polystyrene block is enclosed on all side by a 5 cm thick layer of expanded

polystyrene and ~13 mm thick plywood. The airtight box has two 12 × 12 cm^2 cutouts in the front and back providing a line of sight through the calorimeter for alignment. Additionally, the front cutout serves as a beam entrance window. The external dimensions of the box are approximately 50 × 50 × 40 cm^3.

A vertically-mounted radiator and fan assembly (Eco C240 240MM, Coolit Systems) inside the calorimeter box is used to circulate the contained air mass through the heat-exchanging fins. A Neslab RTE-7 refrigerated circulator (Thermo Scientific) is used to actively control the temperature of the circulated air by pumping a cooled fluid through the radiator. The resolution of temperature control of the fluid is 0.1 °C. The air temperature is monitored by taking the average reading of two RTDs; a third RTD is used to measure the temperature of the polystyrene block. The probe readings are continuously recorded and are used as feedback to adjust the chiller.

An aluminum plate designed to accept a 70 cm long mechanical pointer is mounted to the outer front face of the calorimeter. The pointer can be slid inside the calorimeter and be brought into contact with the face of the vessel. Similarly, the pointer can be slid outward and be brought into contact with an external point of reference. A measure of internal distance (vessel to outer box, and outer box to reference point) can thus be measured to within a few tenths of a millimeter, both before and after cooling down of the system.

A small-scale water phantom (referred to as the mock vessel; Figure 7.5) used to directly calibrate ionization chambers against the water calorimeter, was designed to experimentally replicate the radiation field perturbation due to the vessel's front face. The mock vessel is made of an acrylic tube, closed at one end, and covered at the other end by glass of the same thickness (1.12 mm) as the calorimeter vessel. A slot milled on the top side of the tube permits the insertion and accurate positioning of an ionization chamber (see *Section* 9.2.3).

Figure 7.4: Photographs of the SHREWcal as seen from (top) the side with one wall removed, (bottom left) the side with the vessel window outlined by a red dashed line, and (bottom right) from the beam's eye point of view.

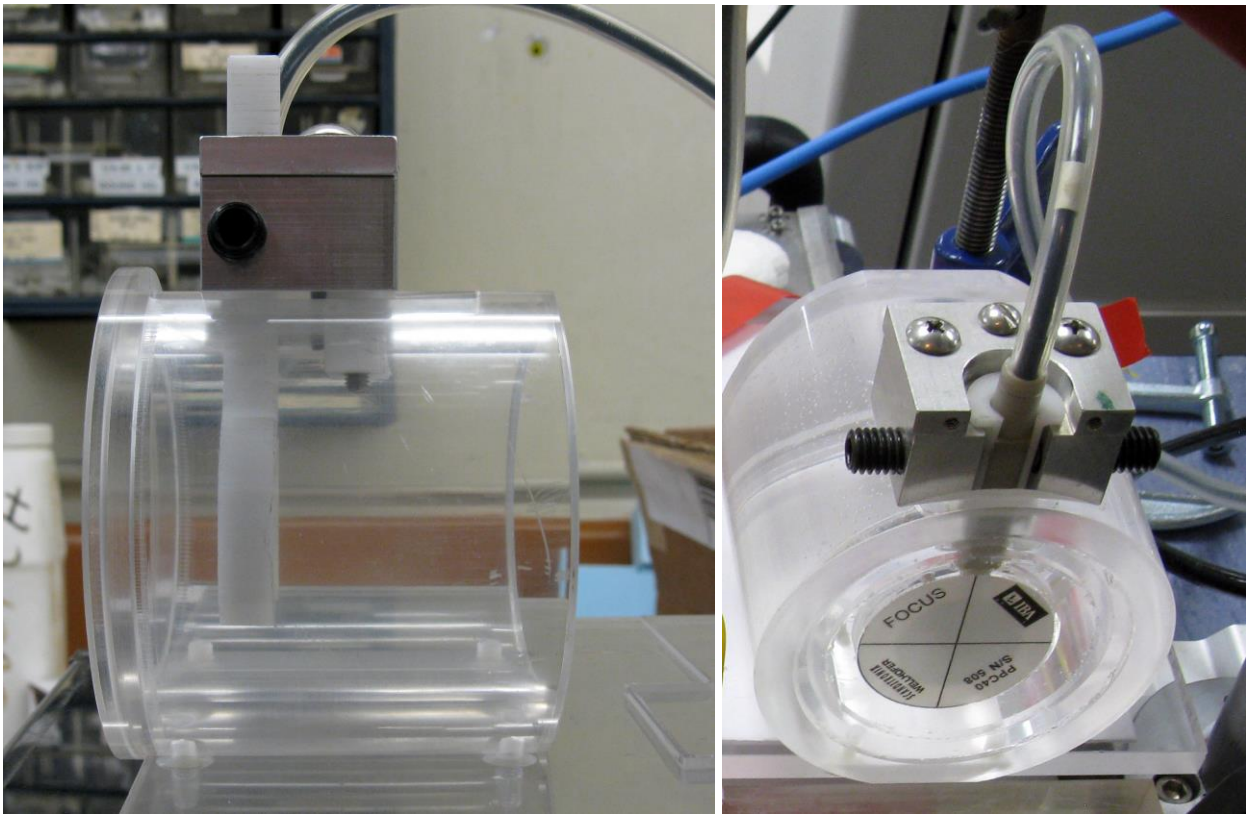

Figure 7.5: The mock vessel, a small-scale water phantom, containing a plane parallel ionization chamber, as seen from the (left) side, and (right) top down view. The purpose of the mock vessel is to reproduce the radiation field perturbation due to the front face of the calorimeter glass vessel.

7.4 CALORIMETER VESSEL

The temperature increase due to irradiation is measured in the centre of a cylindrical glass vessel (National Research Council of Canada (NRC), Ionizing Radiation Standards (IRS) group; Figure 7.6) which is designed to isolate a small volume of high purity water from the water in the rest of the phantom. A schematic diagram of the vessel is also provided in *Section* 8.2.1. It consists of a central cylindrical portion, about 23 mm in height and 80 in diameter, which is attached to conical side ports. Threaded fittings on the side ports hold the thermistor probes in place.

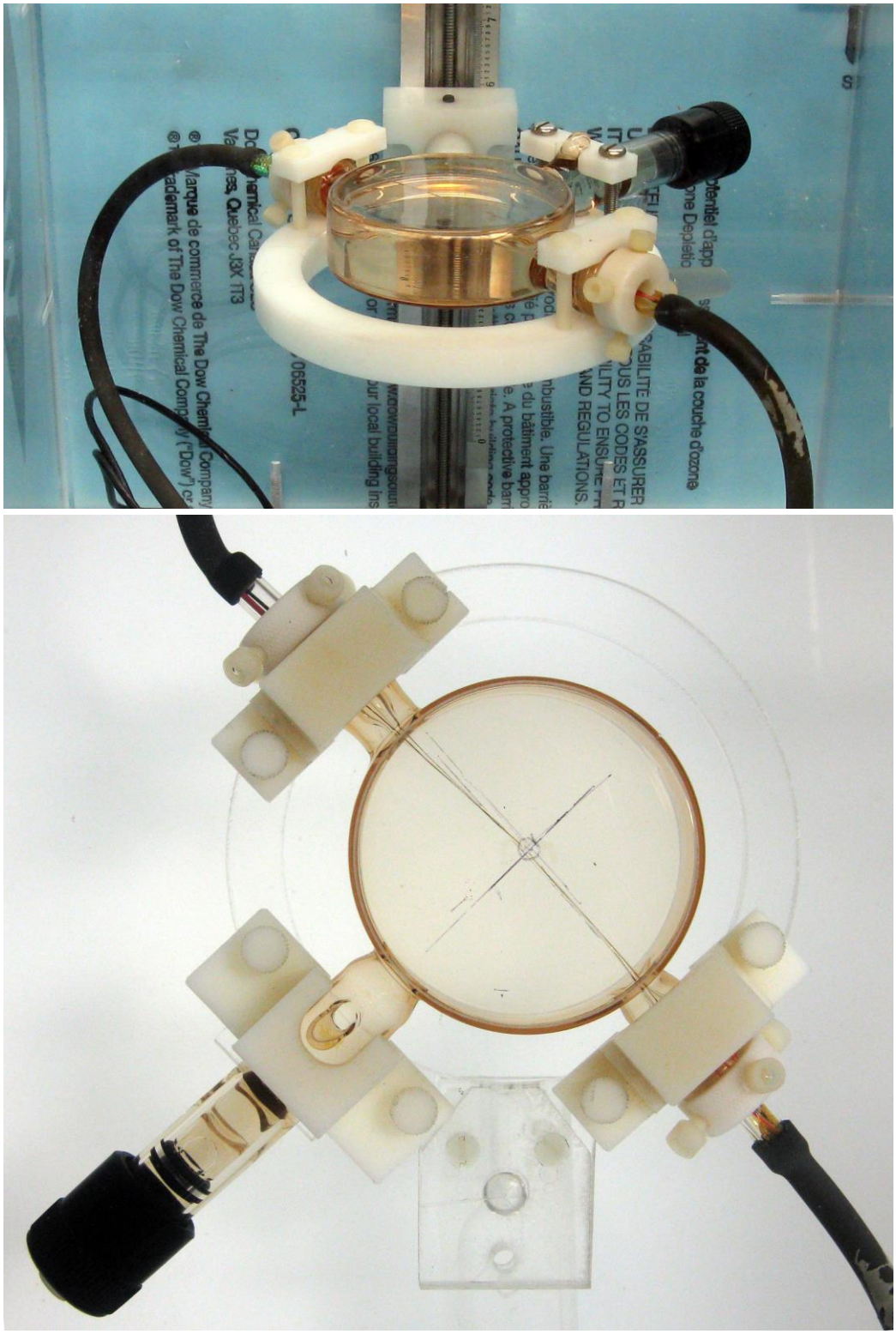

Figure 7.6: Glass detection vessel with the thermistor probes aligned in the centre, as seen from the (top) side, and (bottom) top down view. The vessel is firmly held by a positioning bracket which attaches to a vertical slide inside the water calorimeter phantom.

Water proofing is achieved through the use of Teflon encapsulated O-rings. A third port at the tail-end of the vessel facilitates the filling and bubbling of pure water. This port is sealed using an O-ring and glass stopcock. The vessel design include a small glass bulb on the vessel arm in which a gas bubble can be trapped. This accommodates volume changes in the water due to changes in temperature. The vessel is mounted in the water phantom on an adjustable slide so that its position along the beam axis can be varied.

7.5 THERMISTOR PROBES

The thermistors (Figure 7.7; NRC-IRS) are made of Pyrex tubing that has been pulled down to an outside diameter of 0.5 mm over a length of about 4 cm. Probes are flame sealed on the small end, where the wall thickness is approximately 0.1 mm. Inside the tube, the 0.03 mm diameter wires of the negative temperature coefficient (NTC) thermistors (Ø = 0.25 mm; GE Thermometrics BR-series) are soldered to 0.1 mm diameter copper extension wires, and one wire of the pair is inserted into a 0.2 mm diameter microtubing to avoid electrical shorts. The remaining tube volume is filled with UV-curable adhesive. A Delrin rod fitted into the end of the glass tube acts as a strain relief for the soldered cables. A latex rubber tube serves to waterproof the glass tube. A schematic diagram of a thermistor is provided in *Section* 8.2.1.

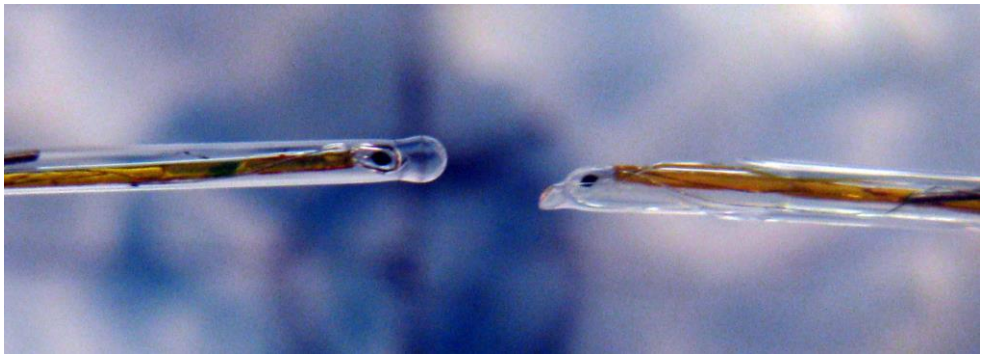

Figure 7.7: The thermistor probes consist of cone-shaped pipettes with 0.25 mm diameter NTC thermistors embedded at the tips.

7.6 BRIDGE CIRCUIT

Figure 7.8 depicts a simplified schematic diagram of the bridge circuit.[2] One arm of the bridge is composed of the two thermistors as well as the decade resistor box, which are connected in series. Two fixed 20 kΩ (±0.01 %) zeranin resistors connected in series make up the opposite arm of the bridge. A reference AC excitation signal from the lock-in amplifier's internal oscillator is connected to one end of the bridge, while the other end is grounded to earth. The lock-in amplifier is used to measure the voltage difference between points A and B. Not shown in the diagram are capacitors (IET Labs, CSH4-10pf-WC), which are used to balance the 90 ° out of phase component of the bridge impedance. A balanced bridge is achieved when the impedance of the decade resistor box is adjusted such that is matched the combined impedance of the two thermistors, resulting in a zero voltage difference between points A and B.

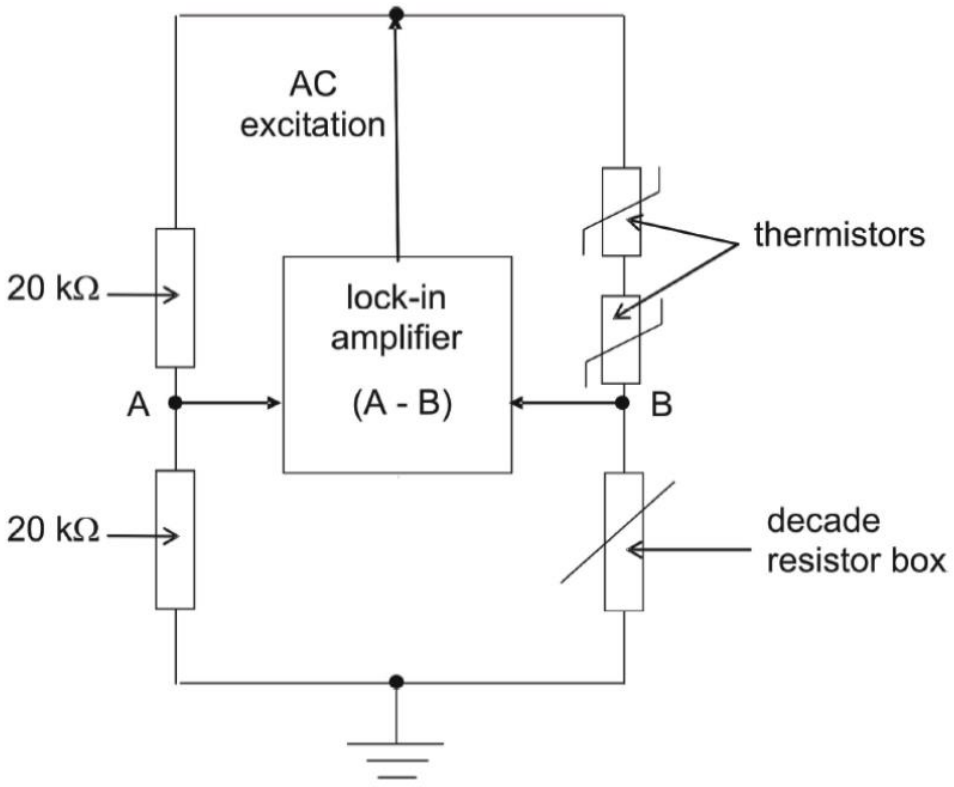

Figure 7.8: A simplified circuit diagram of the Wheatstone bridge type AC circuit.[1]

In addition to the passive components shown in Figure 7.8, two operational amplifiers (OP177, Analog Devices) are used: one acting as a unity gain amplifier, while the other acts as a voltage inverter. These components are powered by a ±15 V external power supply (Systron-Donner TL8-3). Four 10 kΩ (±0.01 %) zeranin resistors (along with several other resistors) also make up part of the circuitry. A more detailed circuit diagram of the bridge circuit can be seen in *Section* 8.2.2.

7.7 RTD PROBES

Three PT-100 RTD probes were used in this work to continuously monitor the average temperature of the water phantom and copper plate. Each probe has a nominal resistance of 100 Ω at the reference temperature of 0 °C, and have a nominal sensitivity of 0.39 Ω K^{-1}. The RTDs are read out by a multimeter in a 4-wire resistance measurement mode.

In a situation in which the resistances to be measured are small relative to the total resistance across the length of the wire, the ohmmeter resistance reading error introduced by the wire's resistance can be substantial. In such instances, a 4-wire resistance measurement mode proves useful. In this configuration, the resistance of a component is measured indirectly by measuring the current flowing through it (with an ammeter) and the voltage drop across it (with a voltmeter). This technique yields the resistance of the RTD detectors, R_{RTD} without the effect of the lead wires.

7.8 SOFTWARE

Three in-house developed programs (H2ORUN, H2OVIEW, and PROBECAL) were used throughout this work to operate and acquire data from the water calorimeter, analyze the

results, and calibrate the sensors. This software was originally developed in C-language by Togane and Seuntjens (1997) for the NRC water calorimeter system. Slight modifications have since been made to adapt the programs for use with the McGill water calorimeter system. The programs share a common parameter file which contains all necessary information pertaining to the device GPIB addresses and default settings, as well as physical parameter (*e.g.*, specific heat capacity of water as a function of temperature).

H2ORUN is the program used operate the calorimeter and acquire the data during the measurement period. It is used to remotely control the instruments that are connected to the computer via GPIB controller. The software has three operation modes: (i) Idle mode is used in between successive runs and simply displays the water temperature (as measured by both the thermistors and RTDs) and copper plate temperature. This data is then used to control the thermal drifts inside the water phantom, ensuring long-term stability. (ii) Bridge calibration (also referred to 'Ohm' calibration) mode is used to calibrate the bridge response to a small change in resistance, the end result of which is a voltage-resistance calibration curve (see *Section* 7.9.3). (iii) Run mode is used to acquire temperature data during the measurement cycle directly from the lock-in amplifier output.

H2OVIEW is the program used to analyze the bridge calibrations as well as the calorimetric runs acquired with H2ORUN (see *Section* 3.2.3 for details).

PROBECAL is the program used to calibrate the RTD probes and thermistors. The sensors to be calibrated are submerged in the software-driven chiller, and at each temperature setpoint, the software acquires the readout as measured by the multimeter (*Section* 7.9).

7.9 CALIBRATION

A water calorimeter is commonly referred to as a primary standard because it can measure absorbed dose from radiation without having to be cross-calibrated against another dosimeter. Indeed, as long as temperature can be defined and measured, a water calorimeter can measure dose. The temperature is not directly measured, but rather from a measurement of the voltage output of the bridge in response to a chance in the thermistor resistance. There are three calibrations which are required to operate the McGill water calorimetry system, each of which are briefly described below.

7.9.1 RTD probe calibration

The RTD probes are calibrated against a mercury thermometer (Kessler) with a calibration traceable to the National Institute of Standards and Technology (NIST). The RTDs are submerged in the reservoir of the chiller as it is stepped through a temperature range of -4 °C to 12 °C. The probes are readout in a 4-wire resistance mode measurement via the Keithley 2002 multimeter. Both the chiller and multimeter are computer-controlled using the PROBECAL software through RS-232 and GPIB connections, respectively. The software steps through the temperature range in increments of 1 °C, allowing for stabilization to within 10 μK min^{-1} after each setpoint adjustment. The user manually provides the chiller temperature as measured using the mercury thermometer (to within 0.02 °C). An average of 15 RTD resistance measurements are taken at each temperature point. As such, a resistance vs. temperature calibration curve is established for each RTD probe.

7.9.2 Thermistor calibration

The thermistors are calibrated against the previously-calibrated RTD probes (typically all three). All involved sensors are submerged in the chiller reservoir. As before, the RTD probe

resistances are measured in 4-wire mode, while the thermistor resistances are measured in 2-wire more. The calibration is again performed over a temperature range of -4 °C to 12 °C in steps of 1 °C. The chiller temperature is measured by taking the average of 15 temperature readings for each of the three RTD probes. In this case, an acceptable stability is 0.4 mK/min, which corresponds to a fractional thermistor resistance change of less than 0.005 %. There are two effects that need to be taken into account: (i) Since thermistor resistance measurements are done in 2-wire mode, the 1 Ω lead wire resistance must be subtracted to obtain an accurate thermistor resistance. (ii) The current (~10 μA) passing through the thermistor (R ~ 10 kΩ) results in a slight power dissipation (~1 μW), which in turn causes a local temperature rise of approximately 2 mK.

The resistance of a thermistor, R, as a function of temperature, T, over the 16 °C calibration range can be accurately described by[3]:

$$\ln(R) = a + \frac{b}{T} + \frac{c}{T^2}; \qquad a, b, c \in \mathbb{R} \tag{7.1}$$

A solution to equation 7.1 is:

$$R = R_0 \cdot e^{\beta \cdot \left(T^{-1} - T_0^{-1}\right)} \tag{7.2}$$

where T_0 is 25 °C (298 K), and R_0 and β are functions of temperature described by:

$$\beta(T) = b + \frac{2 \cdot c}{T} \tag{7.2a}$$

$$R_0(T) = e^{\left(a + \beta(T) \cdot T_0^{-1} - c \cdot T^{-2}\right)} \tag{7.2b}$$

Together $R_0(T)$ and $\beta(T)$ describe the thermistor calibration curve, and are determined for each thermistor. Although the range is relatively large (16 °C), measurements are typically performed within a narrow range (0.2 °C) centered about 4 °C. As such, the slowly varying functions $R_0(T)$ and $\beta(T)$ can be approximated as constant for a given thermistor operating at 4 °C. For the type of thermistors used in this system, a sensitivity of about 4 % is measured at the operating temperature.

7.9.3 Bridge calibration

When unbalanced (*i.e.*, impedance of thermistors and decade resistance box are not equal), the bridge output voltage is non-zero. This can occur when a radiation-induced resistance change occurs in the thermistors, or alternatively, the user can adjust the decade resistor box setting. The former is the signal of interest during measurements, while the latter is carried out to calibrate the bridge.

The bridge calibration procedure involves the temporary adjustment of the decade resistor box setting by 1 Ω and recording the resulting bridge response, as measured by the lock-in amplifier (Figure 7.9). Bridge calibrations are performed periodically throughout an experimental session, each time at a unique temperature. When combined, these results provide a bridge calibration curve (Figure 7.9), relating bridge output per 1 Ω resistance change as a function of temperature.

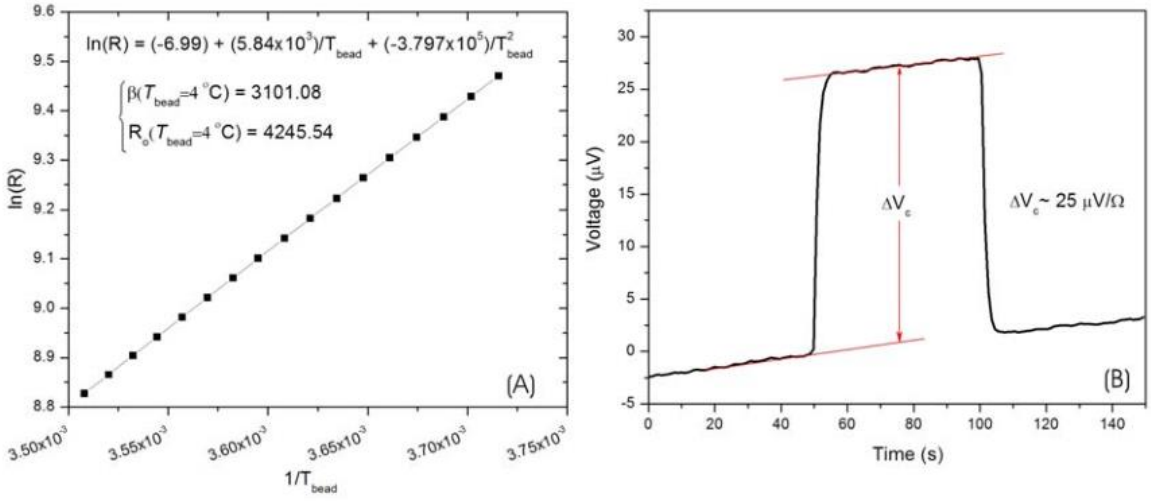

Figure 7.9: (Left) A typical thermistor calibration curve plotted in terms of ln(R) against the T^{-1}. By fitting a quadratic equation to the dataset, the values of constants, and thus the values of $R_0(T)$ and $\beta(T)$ can be determined. (Right) An example of a bridge calibration run in which the user temporarily adjusts the setting of the decade resistor box by 1 Ω.[4]

7.10 MEASUREMENT PREPARATION

Prior to the positioning of the vessel inside the calorimeter phantom and cooling down to 4 °C, a number of vessel preparation steps are carried out:

1) After being thoroughly washed with detergent and deionized water, the two calibrated thermistors are placed inside the vessel such that their tips are separated by only 2-3 mm near the central axis of the vessel. Fine positional adjustment is achieved using four orthogonal nylon screws on each of the bushings (Figure 7.6).

2) The vessel-thermistor assembly is rinsed several times with deionized water, followed by a rinsing with pure water (organic content < 2 ppb). A MilliQ-UV Plus (Millipore) water purification system is used to produce the pure water. The vessel is subsequently filled with pure water, and is bubbled with either pure hydrogen or nitrogen (99.999 % purity, Alphagaz) for a minimum of three hours (Figure 7.10). The bubbling is performed by inserting a 4-French Teflon tube down the bubbling port inside the vessel. At the end of the bubbling procedure, a gas bubble is trapped inside the vessel's small glass bulb, prior to the removal of the tube and complete sealing of the vessel using the glass stopcock.

3) The vessel is subsequently irradiated by a 6 MV photon beam to a dose of 200-400 Gy. Radiation facilitates the onset of radiation-induced chemical reactions that occur in the presence of impurities in water (discussed in detail in *Section* 3.3.3). By irradiating the system to high doses prior to start of the irradiation, a chemical equilibrium state in which no further heat gain or loss occurs is ensured.

4) The position of the thermistors with respect to the front glass window of the vessel is measured with a travelling microscope (OptiTech). The microscope is focused (with 25X magnification) on each of the two surfaces of interest. Their separation is determined by the difference in optical tube position, adjusted for the index of refraction of non-air materials.

The Vernier scale of the measuring microscope can make an individual position measurements to the nearest 0.01 mm. Thermistor depth is determined by taking an average of at least 20 measurements (while repeating the entire measurement setup several times to account for setup uncertainties) both before and after the experimental session.

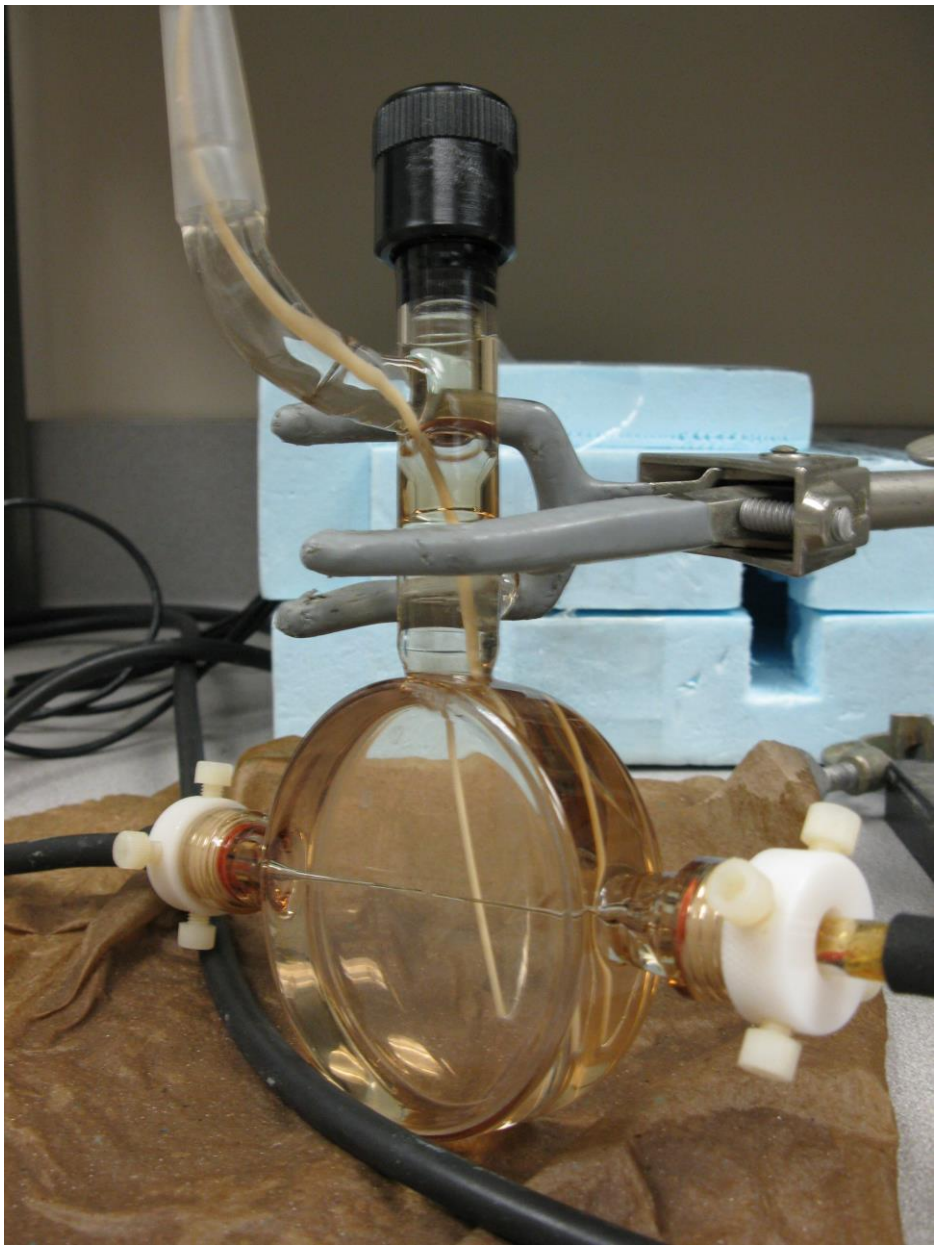

Figure 7.10: A 4-French Teflon tube is inserted in the bubbling port and fed down inside the inverted vessel. Pure hydrogen or nitrogen (99.999 % purity, Alphagaz) is bubbled in the vessel for a minimum of three hours to saturate the aqueous system.

7.11 REFERENCES

[1]K.J. Stewart, “The development of new devices for accurate radiation dose measurement: a guarded liquid ionization chamber and an electron sealed water calorimeter,” *Ph.D. thesis* (Montreal: McGill University 2007).

[2]J. Seuntjens, “Comparative study of ion chamber dosimetry and water calorimetry in medium energy x-ray beams,” *Ph.D. thesis* (Gent: Gent University 1991).

[3]R.B. Barnett, “Water calorimetry for radiation dosimetry,” *Ph.D. thesis* (Calgary, University of Calgary, 1986).

[4]A. Sarfehnia, “Water calorimetry-based radiation dosimetry in iridium-192 brachytherapy and proton therapy,” *Ph.D. thesis* (Montreal: McGill University 2010).

[5]S. Ekelof, “The Genesis of the Wheatstone Bridge," *Eng. Sci. Edu. J.*, 10(1), 2001, 37–40.

Chapter 8

DIRECT MEASUREMENT OF ELECTRON BEAM QUALITY CONVERSION FACTORS USING WATER CALORIMETRY

In this chapter, a water calorimeter designed to directly measure absorbed dose to water in clinical electron beams and its use to derive electron beam quality conversion factors for two ionization chamber types is presented. The results of this work include dose measurements performed directly in water using water calorimetry and both a cylindrical and plane parallel ionization chamber following the AAPM TG-51 protocol. The dose is measured in clinical accelerator-based 6 MeV, 9 MeV, 12 MeV, 16 MeV, and 20 MeV electron beams. To validate the calorimeter, the absolute dose to water measured in a clinical 6 MeV photon beam was directly compared to results derived from the National Research Council of Canada (NRC) photon beam standard water calorimeter. This work forms the foundation for a future absorbed dose to water standard for clinical electron therapy in the range of 9 MeV to 20 MeV.

Authors: James Renaud[1], Arman Sarfehnia[1,2], Kristin Marchant[3,4], Malcolm McEwen[5], Carl Ross[5], and Jan Seuntjens[1]

[1]Medical Physics Unit, McGill University, Montréal, Québec, H3G 1A4, Canada
[2]Department of Radiation Oncology, University of Toronto, Toronto, Ontario, M5S 3E2, Canada

[3]*Allan Blair Cancer Centre, Saskatchewan Cancer Agency, Regina, Saskatchewan, S4T 7T1, Canada*
[4]*Department of Oncology, University of Saskatchewan, Saskatoon, Saskatchewan, S7N 5A1, Canada*
[5]*Ionizing Radiation Standards, National Research Council of Canada, Ottawa, Ontario, K1A 0R6, Canada*

ABSTRACT

Purpose: In this work we describe an electron sealed water calorimeter (ESWcal) designed to directly measure absorbed dose to water in clinical electron beams and its use to derive electron beam quality conversion factors for two ionization chamber types.

Methods: A functioning calorimeter prototype was constructed in-house and used to obtain reproducible measurements in clinical accelerator-based 6 MeV, 9 MeV, 12 MeV, 16 MeV and 20 MeV electron beams. Corrections for the radiation field perturbation due to the presence of the glass calorimeter vessel were calculated using Monte Carlo (MC) simulations. The conductive heat transfer due to dose gradients and non-water materials was also accounted for using a commercial finite element method software package.

Results: The relative combined standard uncertainty on the ESWcal dose was estimated to be 0.50 % for the 9 MeV to 20 MeV beams and 1.00 % for the 6 MeV beam, demonstrating that the development of a water calorimeter-based standard for electron beams over such a wide range of clinically-relevant energies is feasible. The largest contributor to the uncertainty was the positioning (Type A, 0.10 % to 0.40 %) and its influence on the perturbation correction (Type B, 0.10 – 0.60 %). As a preliminary validation, measurements performed with the ESWcal in a 6 MV photon beam were directly compared to results derived from the National Research Council of Canada (NRC) photon beam standard water calorimeter. These two independent devices were shown to agree well

within the 0.43 % combined relative uncertainty of the ESWcal for this beam type and quality. Absorbed dose electron beam quality conversion factors were measured using the ESWcal for the Exradin A12 and PTW Roos ionization chambers. The photon-electron conversion factor, kecal, for the A12 was also experimentally determined. Non-statistically significant differences of up to 0.7 % were found when compared to the calculation-based factors listed in the AAPM's TG-51 protocol. General agreement between the relative electron energy dependence of the PTW Roos data measured in this work and a recent MC-based study is also shown.

Conclusions: This is the first time that water calorimetry has been successfully used to measure electron beam quality conversion factors for energies as low as 6 MeV (R_{50} = 2.25 cm).

8.1 INTRODUCTION

In radiotherapy, clinical reference dosimetry of high-energy photon and electron beams is based on absorbed dose to water standards. Generally based on calibrating ionization chambers in a standard ^{60}Co field, protocols such as AAPM TG-51 and IAEA TRS-398 detail recommended practices in regard to reference dosimetry.[1-3] For more than forty years, the development and maintenance of absorbed dose standards based on ^{60}Co teletherapy sources has been carried out by the primary standards dosimetry laboratories (PSDLs) of the world.[4]

The three major classes of techniques used at PSDLs to determine absorbed dose to water are: (1) ionization chamber-based absorbed dose standards, (2) total absorption

(*i.e.*, Fricke)-based absorbed dose standards, and (3) calorimeter-based absorbed dose standards.[4,5] Generally, the former two techniques rely on a well-characterized radiation field as a reference. Ionometry relies on the knowledge of the average energy required to produce an ion pair in dry air, $(W/e)_{air}$[6], and a restricted graphite-to-air stopping power ratio. Fricke dosimetry relies on an accurate transfer of absorbed dose from a calibration quantity and on the knowledge of the product of the molar extinction coefficient and the radiation chemical yield of ferric ions, $(\epsilon G)_{Fe^{3+}}$. On the other hand, calibration of a calorimeter can be achieved entirely independent of radiation using temperature and electrical standards. For this reason, calorimeters are considered the most fundamental method of determining absorbed dose.[4,5,7] Calorimeters are used to this end by measuring the radiation-induced temperature rise in medium, which in nearly all cases is either approximated as a point in water (water calorimetry), or averaged over a thin graphite volume (graphite calorimetry) under adiabatic conditions. In the case of the latter, it is assumed that all energy deposited in the materials is expressed as heat (*i.e.*, no heat defect).

In spite of the numerous practical challenges (relative to photons) associated with electron beam dosimetry, applications of the above-mentioned techniques to develop primary standards of absorbed dose for electron beams have been well-documented.[7-13] The biggest challenge is the relatively short ranges and high dose gradients involved. For therapeutic energies (4 MeV to 20 MeV), the electron range varies from approximately 2 cm to 10 cm, within which dose gradients can exceed 5 % per mm at the lowest energies. Another challenge of electron dosimetry is the associated depth-dependent charge deposition. Charge build-up is a particular concern for calorimeters with extremely sensitive DC-based measurement systems and can be successfully managed with proper grounding.[5,7] This phenomenon is less of a problem for other types of dosimetry systems, but nonetheless can affect the result of measurement if neglected.[6] Current electron standards include a total absorption-calibrated Fricke-based system operated by The Swiss Federal Office of

Metrology and Accreditation (METAS)[9], and a graphite calorimeter employed by the National Physical Laboratory (NPL) in the UK.[10] McEwen and DuSautoy[7] have reviewed these standards and compared them to the NRC and McGill University water calorimeters.[11] It is noteworthy to mention that although there is only one electron beam standard based on water calorimetry (NRC) in current operation, it is expected that as many as five PSDLs will have established such a standard in the near future. Most recently, McEwen *et al*. (2015) have reported on a trial comparison of national standards for electron beams, including the NRC water calorimeter standard.[12]

One aim of this paper is to present the development of a sealed water calorimetry system specifically designed to operate and directly calibrate ionization chambers across a wide range of clinical electron beams. Originally constructed at McGill University by Stewart (2007), the calorimeter, referred to herein as ESWcal[11,13,14], shares design aspects with water calorimeters developed at the NRC[15] and the Nederlands Meetinstitut (NMi).[16] In contrast to nearly all other water calorimeters, the ESWcal was designed to operate under a vertical beam arrangement. This was done to help contend with the shallow measurement depths required by the lowest energy electrons. Furthermore, a thin-window calorimeter vessel was specially-developed to accommodate electron energies as low as 6 MeV, where the reference point is at a depth of approximately 12 mm. In 2007, Ross *et al.* described a direct comparison of this vessel to alternate NRC designs and the associated correction factors in a 6 MV photon beam.[17]

Traditionally, water calorimetry has been implemented as a standard of absorbed dose to water for ^{60}Co[18-22], although its use has been extended to include absorbed dose standards for higher-energy photon beams[10,21-24,31], as well as the dosimetry of medium-energy x-rays[25-29], protons[21,30-34], heavy-ions[21], and high dose rate (HDR) brachytherapy sources.[35-37] There has also been extensive work done with using water calorimetry to measure the

absorbed dose beam quality conversion factors, k_Q, for ionization chambers in high-energy photon beams.[38-43] These factors are used in the previously-mentioned clinical dosimetry protocols. The same cannot yet be said about high-energy electron beams. That said, the feasibility of using water calorimetry to directly calibrate cylindrical and parallel-plate chambers in high energy (≥12 MeV) electron beams has been demonstrated by McEwen and Ross at the NRC.[42] For lower energies down to 4 MeV, Cojocaru *et al.*[44] have successfully measured electron beam quality conversion factors using a water calorimetry-calibrated Fricke dosimetry system. Their $k'_{R_{50}}$ results for the PTW Roos are included for comparison in *Section* 8.3. Electron beam k_Q factors included in clinical protocols have been based solely on MC calculations. Since the dependence of chamber response upon fine constructional details is relatively important in electron beams[45], particularly at lower energies, experimental corroboration of simulation-based k_Q values will help validate current numerical chamber models.

Recent studies, both experimental[46,47] and simulation-based[48-52], suggest that there may be errors in some of the factors used in calculating k_Q for electron beams in current protocols. For instance, work by Buckley and Rogers (2006) suggests that the wall perturbation factor, p_{wall}, assumed to be unity for cylindrical chambers in electron beams, may take on a value of up to 1.006.[45] In a detailed study of the fluence perturbation in plane parallel chambers, Zink *et al*. (2014) demonstrated that electron transport across the lateral gas-water interface is a non-negligible effect to include in the calculation of cavity corrections.[52] That said, there is a well-defined need for a water calorimetry system capable of directly measuring the value of k_Q for various chambers in electron beams over a wide range of energies. Such a system could be used to verify the accuracy of reference condition values included in current clinical dosimetry protocols. Moreover, since the relative perturbation of ionization chambers has been shown to vary as a function of depth, particularly at low energies, a water calorimetry-based system could be used to measure

relative calibration coefficients, and extract absolute perturbation factors.[53,54] Ultimately, the goal would be to establish absorbed dose to water standards for electrons based on water calorimetry and forego the beam quality conversion from ^{60}Co.

In this work, we present the design and operating principles of the McGill ESWcal system. We also discuss the various correction factors necessary to determine absorbed dose to water. Furthermore, we detail the application of the ESWcal to the evaluation of beam quality conversion factors for the Exradin A12 cylindrical chamber and the PTW Roos plane-parallel chamber for electron beam energies between 6 MeV and 20 MeV.

8.2 METHODS

8.2.1 Water Calorimeter

A cross-sectional and isometric view of the McGill ESWcal is shown in Figure 8.1. Designed to maintain a stable operating temperature of 4 °C, the calorimeter box consists of a 30×30×20 cm^3 Lucite water phantom surrounded on all sides by two 5 cm expanded polystyrene sheets. Separating the polystyrene sheets is a 5 mm layer of copper with soldered copper tubing. Temperature-regulated refrigerant is pumped throughout the tubing network by a refrigerated bath (Thermo Scientific Neslab RTE-7). The copper acts as a quasi-isothermal shield that encompasses the water phantom with the exception of a 12×12 cm^2 beam entrance window on the top surface. An epoxied 0.15 mm brass foil covers the window opening to maintain a continuous temperature over the area with minimal beam perturbation.

Contained within the water phantom are two resistance temperature detectors (RTDs) used to monitor the average water temperature, a magnetically coupled stirring bar used to homogenize the water temperature distribution, and a vertical translation slide used to position either the calorimeter vessel or the ionization chambers. An additional RTD is placed in direct contact with the copper box, outside the phantom.

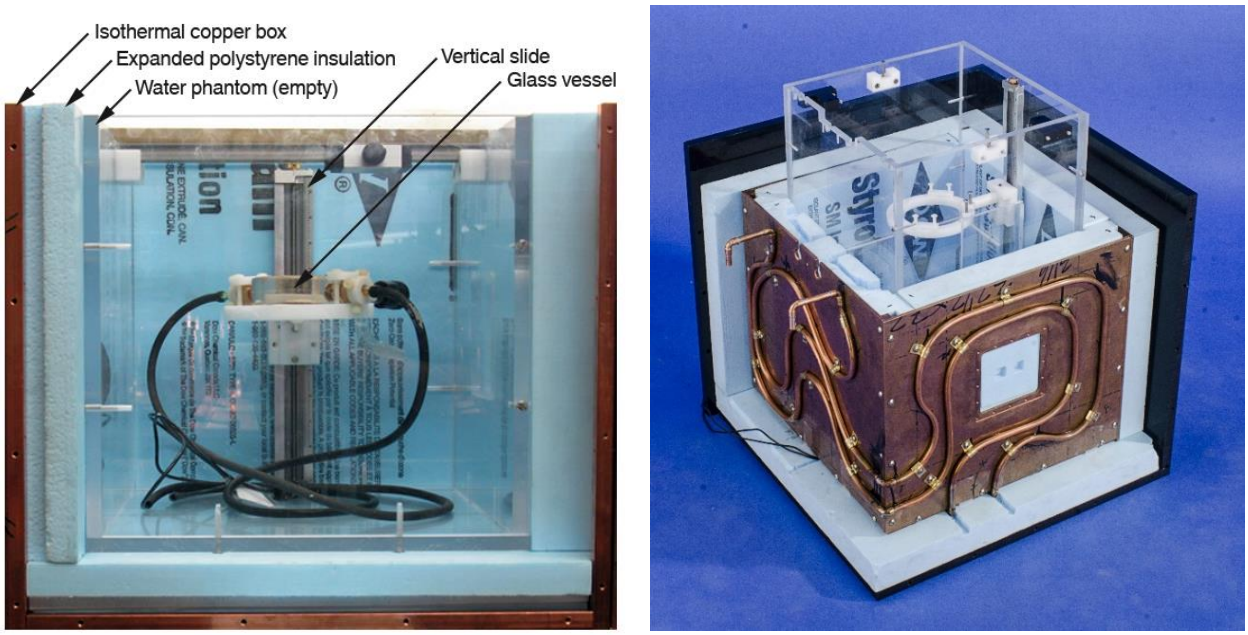

Figure 8.1: Left: Sealed Pyrex vessel containing thermistors placed at depth within Lucite water phantom (outer polystyrene layer omitted for clarity). Right: Water phantom temperature is stabilized by surrounding layers of expanded polystyrene and actively chilled copper box (lid not shown). Please note that the Lucite water phantom has been propped up from inside the copper box to more clearly depict the assembly.

The NRC-constructed calorimeter vessel used in this work (Figure 8.2 (a)) is made of Pyrex and is of a cylindrical design similar in size and shape to a standard ice hockey puck. The front and back circular windows are 79 mm in diameter and 1.12 mm thick, while the hollow space between the windows is 22.66 mm. There are two threaded ports in the side

wall for the insertion of the cone-shaped pipettes with 0.25 mm diameter NTC thermistors embedded at the tips (Figure 8.2 (b)). Positioned proximally to the central axis, the thermistors (General Electric Thermometrics, NTC BR11 series, ~10 kΩ @ 25 °C) define the point of measurement.

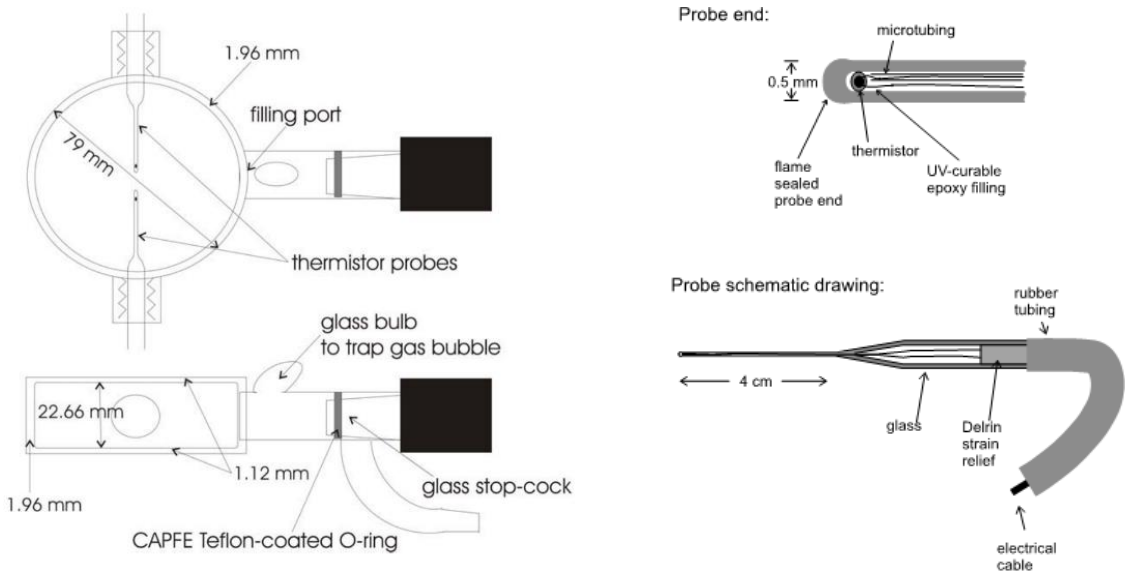

(a) (b)

Figure 8.2: (a) Schematic diagram of the electron sealed water calorimeter vessel, and (b) thermistor probes (reproduced from Seuntjens et al. 1999).

The thickness of the vessel windows, the inner separation of the windows, and the distance from the front window to each thermistor bead was measured using a traveling microscope with a Vernier scale with a resolution of 0.01 mm. This is done by focusing first on the front of the glass, then lowering the microscope until the thermistor bead is in focus and reading the translation off the Vernier scale. Using the method described in Ross *et al.* (2007), a correction of (0.35 ± 0.01) mm is applied to account for the effect of the index of refraction of the glass[17]. Through this method, the k = 1 uncertainty on the position of the thermistor is ± 0.20 mm.

8.2.2 Temperature Measurement

A radiation-induced temperature rise will cause the thermistors used in this work (~10 kΩ @ 25 °C) to experience a fractional resistance change on the order of 400 Ω/K. Changes in temperature are indirectly determined by measuring the response of an active AC Wheatstone bridge circuit to resistance changes in the thermistors (Th1 & Th2 in Figure 8.3).[55] This particular design permits the evaluation of the out of balance bridge voltage (point A in Figure 8.3) relative to earth ground (point B) instead of an elevated AC reference, resulting in a more stable measurement and requiring very little capacitive compensation. Relating this bridge voltage back to temperature requires separate calibrations of the RTDs (against a calibrated mercury thermometer traceable to national standards), the thermistors (against RTDs), and the bridge response[11].

The bridge response is calibrated by adjusting the decade resistor box (X1 in Figure 8.3) setting by a known amount, typically 1 Ω, when the bridge is nominally balanced (*i.e.*, the combined thermistor resistance is equal to the decade resistor box setting). This bridge calibration procedure is performed (in the absence of large drifts) regularly throughout the experiment at different equilibrium temperatures. Together, these results represent the change in bridge voltage per unit resistance change, $\Delta V_{1\,\Omega}$, as a function of balanced decade resistor box setting[11].

The acquired signal during a single calorimetric run consists of three distinct parts: The pre-drift, the irradiation, and the post-drift. Prior to irradiation, a pre-drift signal is recorded to provide an initial state condition. During irradiation, the bridge signal resulting from the average temperature rise at the two thermistor beads is acquired. Following the irradiation, a post-drift signal is collected to compare against the initial slope of the pre-drift and provide a measure of the heat loss. Due to the thermal insulation of the calorimeter box and the low thermal diffusivity of water, the pre- and post-drift signals are

quasi-linear over the time scale of the measurement. To first order, the influence of heat transfer can be corrected by treating the calorimeter as a two-body system with a constant heat transfer. In such a system, it can be shown that the heat transfer-corrected temperature rise is quantified by measuring the difference between the linear extrapolations of the pre-drift and post-drift to the irradiation midpoint.[56] The validity of this procedure is dependent upon the assumption that the time scale of heat loss processes is much larger than the irradiation period. To accurately model the effects of heat transfer in more complex geometries, numerical simulations as described in *Section* 8.2.3 are used.

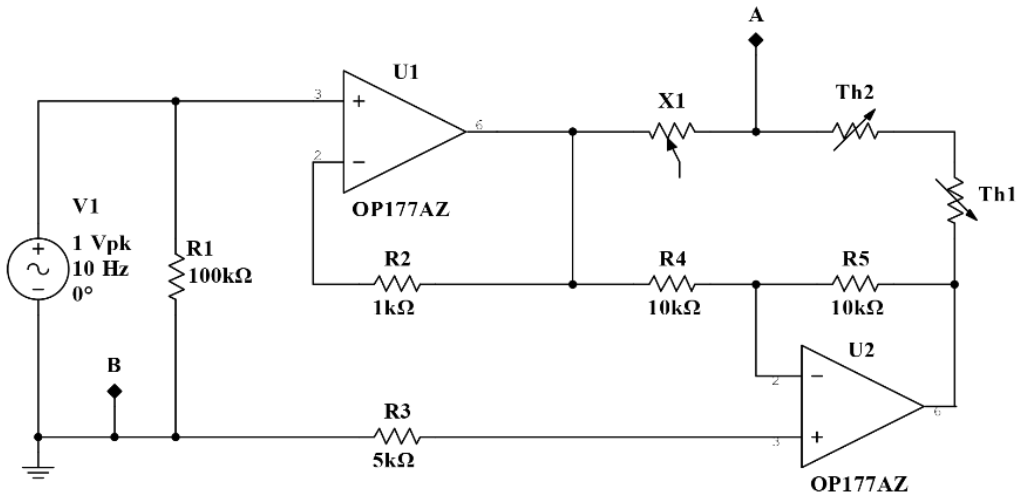

Figure 8.3: A schematic diagram of the active AC bridge circuit used to measure the change in thermistor resistances (Th1 & Th2) resulting from radiation-induced temperature rises.

8.2.3 Determination of Absorbed Dose

The water calorimeter measures dose to water, D_w, at a point based on its fundamental relation to temperature rise, ΔT_w, and the specific heat capacity at constant pressure of water, $c_{w,p}$ ($4.205 \times 10^3 J \cdot kg^{-1} \cdot K^{-1}$ @ 4 °C)[57,58], as shown in Eq. 8.1. For this particular setup, the front face of the calorimeter vessel is aligned to the surface of the water phantom and translated vertically to the desired measurement depth.

$$D_w = c_{w,p} \cdot \Delta T_w \cdot k_c \cdot k_p \cdot k_\rho \cdot k_{dd} \cdot \frac{1}{1 - k_{HD}} \quad (8.1)$$

The various k factors are the corrections taken into consideration in this study. In order of appearance in the equation above, they are the conductive heat transfer (k_c), radiation field perturbation (k_p), water density (k_ρ), radial dose profile non-uniformity (k_{dd}), and heat defect (k_{HD}) corrections, respectively. It is important to note that the design of the vessel and the calorimeter operating temperature have been chosen such that thermal perturbations resulting from convection and radiative processes are negligible and are not considered in this work.

k_c is defined as the ratio of the temperature rise in the absence of conduction to the actual temperature rise, and is numerically simulated using a finite element method software package (COMSOL Multiphysics® v.4.2). Temperature gradients arise for two main reasons: i) dose gradients induced by the non-uniform radiation field, and ii) the lower specific heat capacity of the Pyrex vessel relative to the surrounding water (in principle, all non-water materials contribute to this effect). The software is able to calculate time-dependent thermal distributions in a 3D model of the calorimeter (Figure 8.4) by solving, in both time and space, the partial differential equation governing thermal conduction. The solving algorithm requires several input parameters including the physical and thermal properties of the involved materials, geometric boundary conditions, and the distribution of heat sources and sinks in space and time.

The heat source term representing the dose distribute on was determined from percent depth dose (PDD) acquired using diodes (IBA EFD-3G and PFG-3G) beneath the calorimeter lid and corrected for the effect of non-water materials using the MC simulations described further in this section. For each beam energy studied, a series of ten successive irradiations, including associated pre- and post-drift periods, were simulated. Analysis of the

simulations were carried out in the same way as measurements. By calculating the temperature change assuming no heat loss, heat transfer corrections were derived by dividing the average temperature rise of the ten successive runs by the temperature rise achieved under ideal conditions.

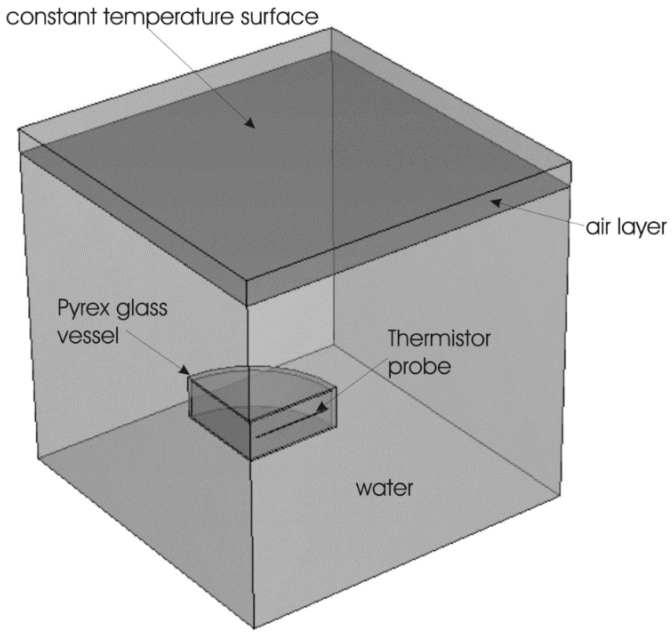

Figure 8.4: Quartered geometric model of the water calorimeter used in COMSOL Multiphysics® to model heat transfer by conduction.

k_p is a result of the effect of non-water materials present in the beam path, particularly the glass vessel and thermistor probes, and is determined using the DOSRZnrc user code of the EGSnrcMP MC code system.[59] The perturbation is taken as the ratio of the dose scored at the thermistor position for two similar MC geometries, one containing non-water materials and one made entirely of water.

k_ρ accounts for the difference in water density, and hence effective depth at 4 °C (calorimeter operating temperature) and at room temperature. While this is a relatively small effect (0.2 mm difference at 8 cm depth), it is taken into account when performing the

cross-calibration of the ionization chambers. Photon and electron PDDs measured using diodes (IBA EFD-3G and PFG-3G) beneath the calorimeter lid provide the data necessary to calculate the effective depth shifts.

k_{dd} corrects for the difference between the dose measured at the thermistors, which are off-axis by 1 mm to 2 mm, and the dose at the central axis of the beam. To this end, the average dose measured by the thermistors is scaled by the average lateral dose profile at the two points of measurement. Similar to the PDDs mentioned above, in-plane and cross-plane profiles were measured at several depths for each beam under the calorimeter lid. For the electrons and 6 MV photons, profiles across the centre of the field at d_{ref} and at 8 cm, respectively, were acquired.

k_{HD} is a measure of the net heat lost and gained due to radiation-induced chemical reactions occurring within the vessel. In this work, hydrogen gas was used to saturate the pure water under conditions that would introduce a minimal amount of organic impurities. For this method of water preparation, the steady-state heat defect has been predicted to be 0.000 ± 0.15 %.[60]

8.2.4 Calorimeter Measurements

Please note that the representation of uncertainties in this work follows that of the BIPM JCGM 100:2008 guide.[61] Water calorimetry was performed on a Varian Clinac 21 EX linear accelerator for electron energies of 6 MeV, 9 MeV, 12 MeV, 16 MeV and 20 MeV, as well as 6 MV photons at a source to surface distance (SSD) of 105.6 cm and otherwise reference conditions. The extended SSD represents the closest distance practically achievable with our setup.

For the electrons, a cut-out in the electron applicator was used to produce a reference 10×10 cm^2 field at 100 cm SSD. The PDDs mentioned in the determination of k_p (see *Section* 8.2.3) were used to measure the values of $R_{50,}$ from which values of the electron beam reference depth, d_{ref}, were derived[1]. Irradiations of 1000 MU/min were set for 40 s, delivering a dose of 5.5 Gy to 6.0 Gy at the position of the thermistors. In each case, 60 s of pre-drift and 90 s of post-drift data were collected for extrapolation and analysis. Throughout each experimental session, a minimum of 20 bridge calibrations were performed, and for each electron beam energy, a set of 23 to 30 measurements were acquired.

Adjustments to the depth and signal acquisition times were made for the photon beam measurements. The depth of measurement was set to 8 cm rather than the usual reference depth of 10 cm due to dimensional limitations within the Lucite phantom. Irradiations of 67 s were repeatedly delivered at 600 MU/min (nominally 4.3 Gy). For each run, 60 s and 90 s of pre- and post-drift were collected for the purpose of analysis.

Measurements were also performed in a T-780 unit ^{60}Co beam at an SSD of 67 cm and a field size of 12×12 cm^2 defined at 80 cm SSD. Under these conditions, the dose rate was approximately 1 Gy/min at a reference depth of 5 cm.

8.2.5 Ionization Chamber Measurements

Please note that TG-51 notation will be used throughout this work. Two Exradin A12 farmer type cylindrical chambers (SN 309 & 310) and one PTW Roos parallel plate chamber (SN 273) were used in this study. A Keithley 6517A electrometer (SN 0790027) was used to read out the collected charge. All chamber measurements were performed under the same conditions as the calorimetry measurements except for the water

temperature, which was nominally at 22 °C. For the electron beams, the effective point of measurement (EPoM) of each chamber was positioned at d_{ref}, while for the photon beam measurements (A12 only), the EPoM was positioned at the same depth that the thermistors had been positioned. In this work, the EPoM for the A12 is taken as $0.6 \cdot r_{cav}$ and $0.5 \cdot r_{cav}$, for photons and electrons, respectively. For the Roos (electron only) the EPoM is taken as the inner surface of the top electrode, or 0.18 mm downstream from the front outer face.

One Exradin A12 (SN 309, paired with the above-mentioned electrometer) was calibrated in terms of absorbed dose to water in a ^{60}Co photon field against the primary standard water calorimeter at the NRC. It was used to cross-calibrate the PTW Roos chamber in the 20 MeV electron beam and obtain the product, $k_{ecal} \cdot N_{D,w}^{Co}$.

Water phantom temperature and air pressure were monitored using a mercury thermometer and mercury barometer (both traceable to national standards) in order to correct for environmental effects. Throughout the experiments, humidity remained in a range such that no correction was required. Corrections for ion recombination and polarity effects were also applied according to the AAPM's TG-51 protocol.

An NE 2571 cylindrical chamber (Bicron-NE) was used as an external reference chamber for the calorimetry and ionization chamber measurements, which spanned the course of several months. A 5 cm thick Delrin block specially designed to accept the monitor chamber was fabricated to fit reproducibly in the 10×10 cm^2 electron applicator. The reference chamber was positioned and irradiated with 200 MU (as measured by the internal linac monitoring system) at least twice daily. All charge readings were corrected to the reference air density and to the reference chamber reading acquired on the first day. The relative readings were applied to the calorimeter and chamber datasets as corrections for the daily variation in linac output.

8.3 RESULTS

8.3.1 Measurements under the Calorimeter Lid

Central axis PDDs and radial profiles acquired under the calorimeter lid are overlaid in Figures 8.5 and 8.6, respectively. From the electron beam PDDs, the depth at which the dose falls to 50 % of the maximum value, R_{50}, was used to calculate the reference depth, d_{ref}. Table 8.1 lists these as the depths of measurement, among other data.

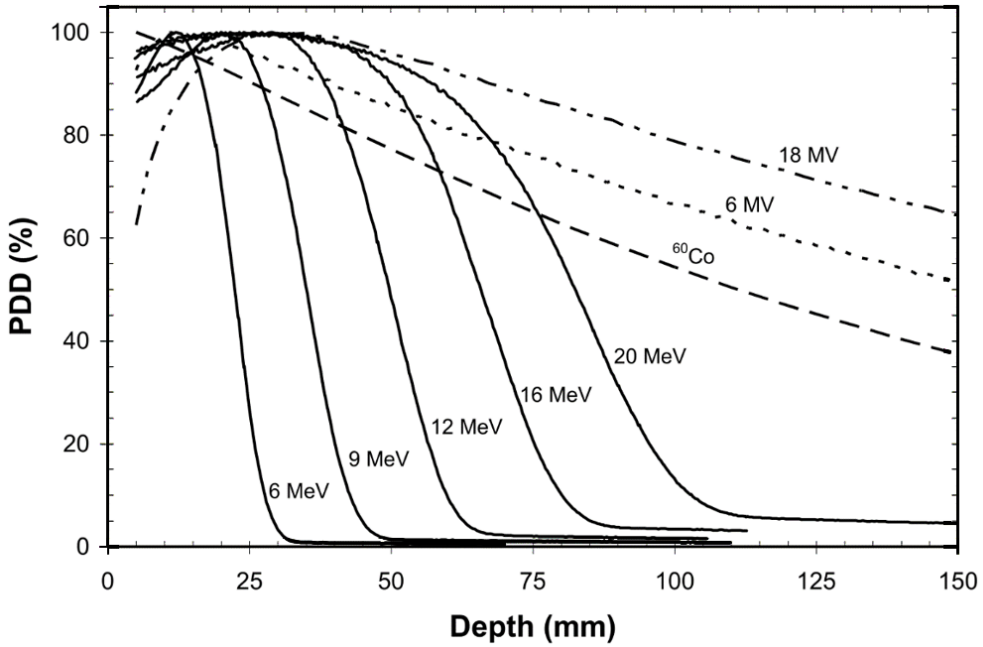

Figure 8.5: Diode-measured PPD curves taken under the ESWcal lid (includes the brass foil) for the photon and electron beams used in this study (18 MV is included to show the trend with increasing energy).

The depicted cross-plane (x-axis) profiles illustrate the gradients present across the width of the calorimeter vessel. For both cross- and in-plane profiles, the 6 MV beam at 8 cm exhibits a ±1 % variation across the vessel, while for the electron beams at d_{ref}, the ±1 % is limited to the central 4 cm before decreasing nearer the edges. This drop off, as measured

3.5 cm from the central axis, varies between 3 % for the 20 MeV beam to 8 % for the 6 MeV beam. Of particular interest is the central 16 mm, the region of measurement for both the thermistors and ionization chambers. Within these limits (see inset of Figure 8.6), all beams are flat to within ±0.2 %. The doses at ±1 mm, the lateral position of the thermistors relative to the central beam axis, differ by at most 0.03 % from the central axis dose. Similarly, the average dose over the central region corresponding to the sensitive volumes of the PTW Roos and Exradin A12 agree to within 0.05 % of the central axis dose. As a result of this agreement, a profile non-uniformity correction of unity was applied and an uncertainty of 0.05 % was associated with this quantity.

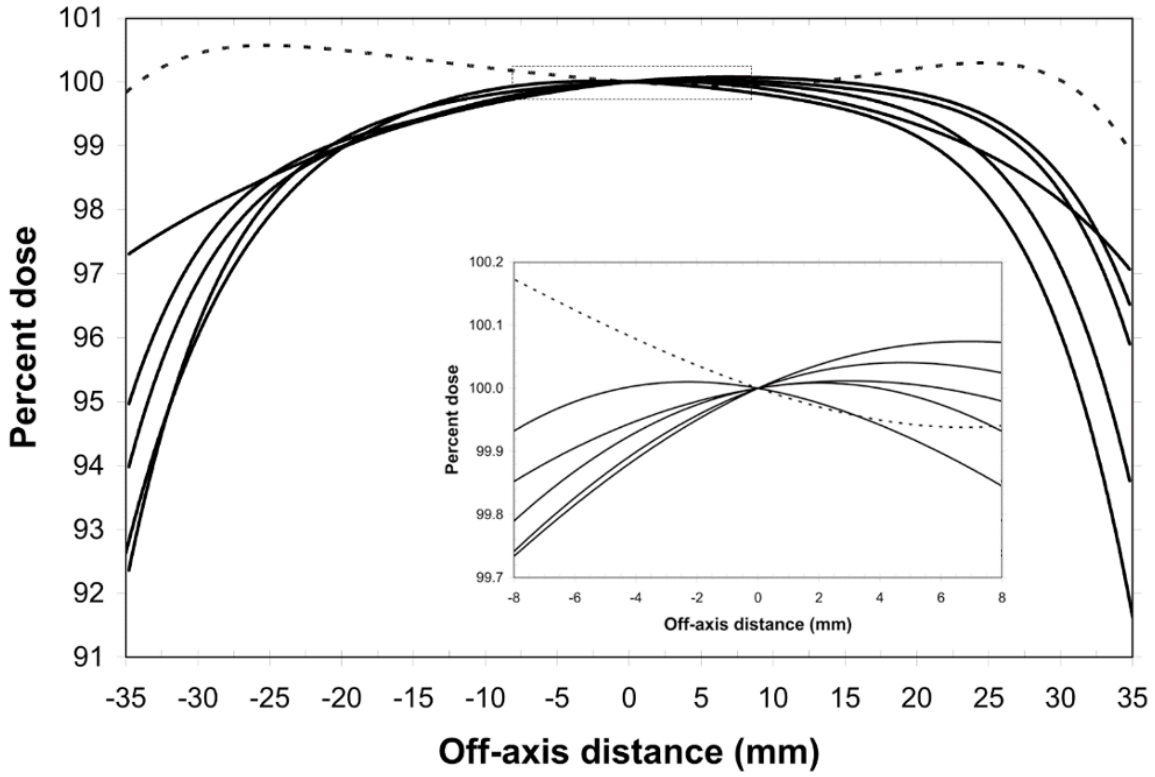

Figure 8.6: Normalized cross-plane (x-axis) profiles across the central 70 mm, and (inset) 16 mm region of each beam at d_{ref} for electrons (solid lines) and 8 cm for the 6 MV photons (dashed line). For the electrons, beam width increases with energy.

8.3.2 Correction Factors

As mentioned earlier, the difference in effective depth between 4 °C and 22 °C due to the temperature-dependent density of water is 0.2 mm at a depth of 8 cm. This equates to a 0.1 % difference in dose for the 6 MV photon beam. For the electron beam measurements, the shift in effective depth is less than 0.1 mm, and hence considered negligible. The uncertainty associated with this quantity was estimated to be 0.05 %.

The values of k_p for each photon and electron beam determined using MC are summarized in Table 8.1. The perturbation includes both attenuation, which decreases the dose, and scatter, which increases the dose. Figure 8.7 shows the variation in k_p as a function of depth in water along the central axis for the 6 MeV and 20 MeV electron beams. In these plots, the simulated vessel is positioned such that the thermistors (vertical grey lines in Figure 8.7) coincide with d_{ref}. The overall uncertainty of k_p includes both positioning uncertainty and MC statistical (Type A) uncertainty (0.10 % to 0.20 %). The positioning component of the uncertainty in the simulations was determined to be 0.60 % for the 6 MeV beam and less than 0.10 % for all others. This corresponds to a thermistor position uncertainty estimate of 0.4 mm.

Also listed in Table 8.1 are the corrections for the conductive heat transfer for each photon and electron beam. Variations of less than 0.20 % are seen among the first ten runs when determining the value of k_c through extrapolation of the normalized post-drift to the mid-irradiation time (Figure 8.8). Uncertainty on this correction is based on the thermistor positional uncertainty and run variation. Any non-linear effect present in the post-irradiation curves should drop out of the analysis as long as the fits are performed over a consistent range.

Finally, the correction for the daily variation in accelerator output (dose/MU) over the measurement period was determined using the NE 2571, and ranged from 0.995 to 1.001 (relative to the first set of measurements). The associated uncertainty on these measurements was estimated to be 0.10 % for all beams based on the standard deviation of 5 consecutive sets of 5 measurements of a 200 MU irradiation. The block and monitor chamber were removed and re-inserted between each set.

Table 8.1. *k_p and k_c* for the different radiation types, energies, depths, and irradiation times investigated in this study. Numbers in parentheses indicate the uncertainty on the final digit.

Beam type	Measurement depth (cm)	Perturbation correction, k_p	Irradiation time (s)	Heat transfer correction, k_c
6 MeV	1.25	1.009(6)	40	1.014(3)
9 MeV	2.02	0.999(2)	40	1.008(2)
12 MeV	2.86	0.999(3)	40	1.006(1)
16 MeV	3.88	1.000(3)	40	1.006(1)
20 MeV	4.86	1.001(3)	40	1.005(1)
^{60}Co	5.00	1.002(1)	180	0.989(1)
6 MV	8.00	1.004(1)	67	1.008(1)

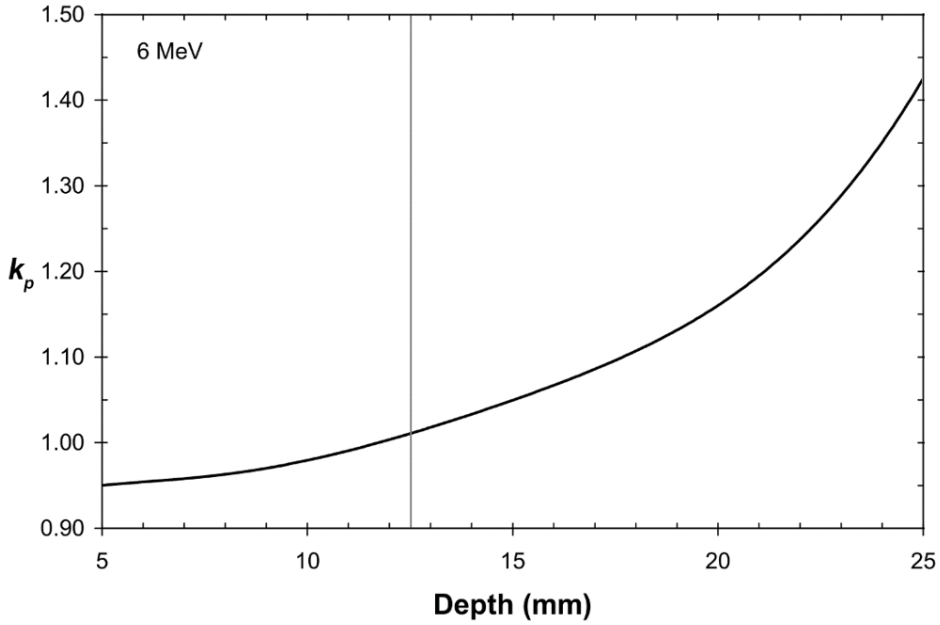

(a)

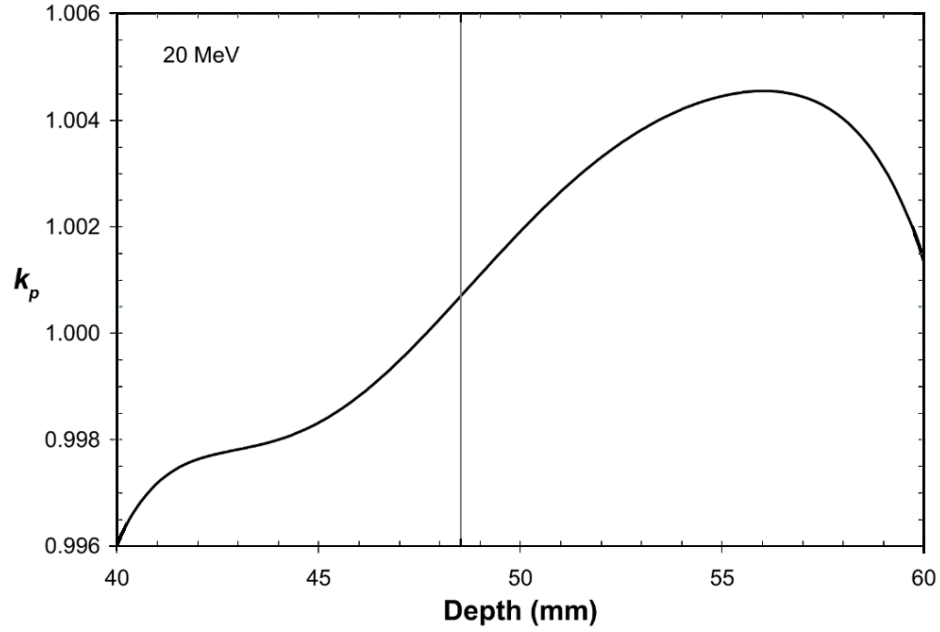

(b)

Figure 8.7: Correction for perturbations to the radiation field due to the glass vessel as a function of depth for the (a) 6 MeV, and (b) 20 MeV electron beams. The position of the thermistor probes is indicated by the vertical grey line. Note the different scales for (a) and (b).

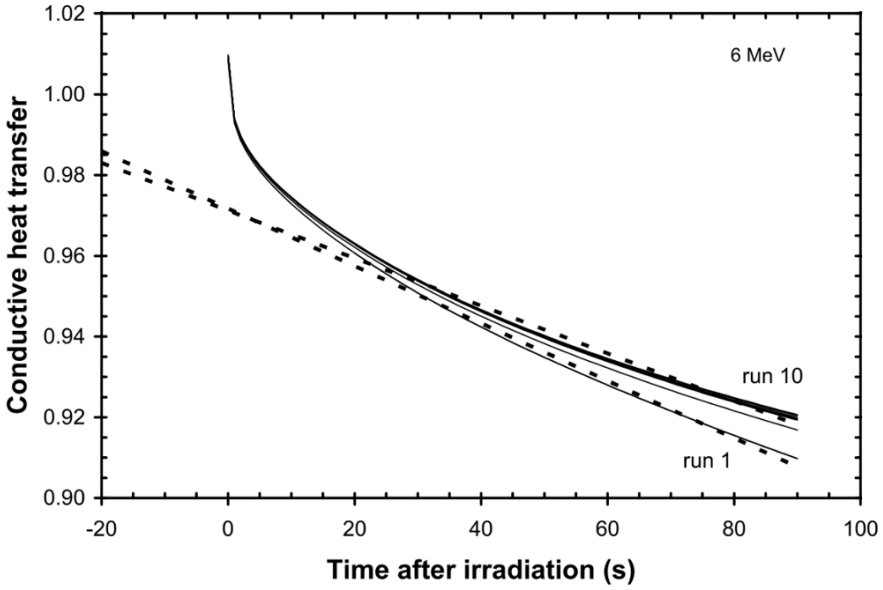

(a)

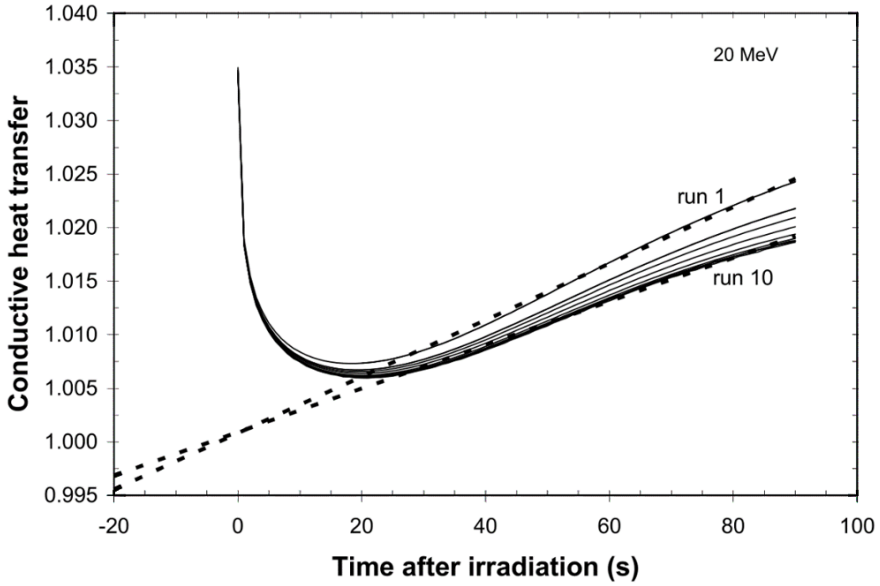

(b)

Figure 8.8: Normalized post-irradiation drifts showing the conductive heat transfer for successive simulated irradiation (runs 1 to 10) for the (a) 6 MeV, and (b) 20 MeV electron beams. The extrapolation to the mid-irradiation time (corresponding to -20 s on the plots) is shown for runs 1 and 10 and is based on a linear fit of the data from 20 s to 90 s. Note that cooling due to the dose gradient is dominant for the 6 MeV beam, while excess heat from the glass vessel can be observed in the case of the 20 MeV beam.

8.3.3 Calorimeter Measurements

An example calorimeter run as acquired in terms of bridge output is provided in Figure 8.9. For each beam, the standard uncertainty on the mean for a set of measurements was calculated. These ranged from 0.15 % to 0.21 % with most sets having an uncertainty of 0.20 %. In addition to statistical uncertainty, the calorimeter data has associated 0.3 mm uncertainty attributed to positioning. This is a combination of the Type A uncertainties associated with measuring the thermistor position within the vessel, and with positioning the vessel within the water phantom. The effect of this uncertainty for the beam types range between 0.10 % for 12 MeV and 16 MeV and 0.40 % for 6 MeV.

8.3.4 Ionization Chamber Measurements

The average of five ionization chamber readings was taken on each measurement occasion and the standard deviation was never greater than 0.04 %. Measurements of the polarity (P_{pol}) and recombination (P_{ion}) corrections were also done for each beam. P_{pol} values ranged from 0.9992 to 1.0007 for both chamber types in all beams with an associated uncertainty of 0.06 %. As expected, P_{ion} values showed more variation with beam and chamber type, with values ranging between 1.0003 for the Exradin A12 in the ^{60}Co beam, and 1.0146 for the Exradin A12 in the 6 MeV beam. The uncertainty on this correction was also estimated to be 0.06 %. Corrections for the effects of pressure and temperature varied from 1.0042 to 1.0227 with an uncertainty of 0.03 %. Finally, the correction associated with the calibration of the electrometer was less than 0.10 %, therefore it was neglected. An uncertainty of 0.05 % was associated to this quantity.

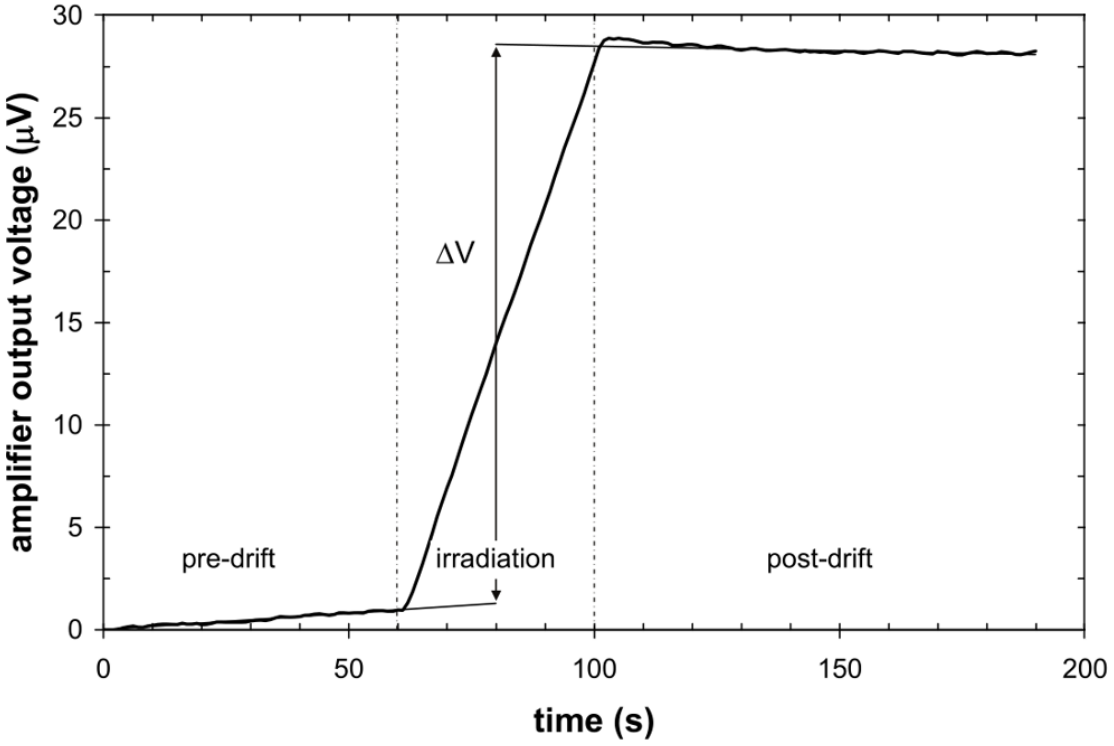

Figure 8.9: Example of an electron beam calorimeter measurement. Straight line fits of the pre- and post-irradiation drifts are extrapolated to the mid-irradiation time to determine ΔV.

8.3.5 Evaluation of Beam Quality Conversion Factors

The ESWcal-measured absorbed dose to water per monitor unit was used to calibrate each chamber in the various electron beams, from which beam quality conversion factors were derived. For each of the chambers, the electron beam k_Q values were normalized to the interpolated value corresponding to R_{50} = 7.5 cm in order to obtain values of $k'_{R_{50}}$ for comparison with TG-51 (Figure 8.10). By doing so, the effects of thermistor calibration, ionization chamber calibration, and chemical heat defect are removed from the analysis, as all are considered independent of electron energy over the investigated range. The results of the comparison are summarized in Table 8.2. The combined uncertainties associated with these evaluations are 1.00 % at 6 MeV, and 0.50 % for all other electron beams.

The photon-electron conversion factor, k_{ecal}, for both Exradin A12 chambers was derived from $N_{D_w}^{60Co}$ and $k'_{R_{50}}$ values determined from the ESWcal measurements. Again, because ratios of measurements are used, the result is independent of thermistor calibration and chemical heat defect. From this we found a k_{ecal} of 0.903 ± 0.004 for both chambers, which is in good agreement with the listed value in TG-51 (0.906).

Table 8.2. Measured values of the relative electron energy dependence, $k'_{R_{50}}$, for two Exradin A12 cylindrical chambers and one PTW Roos plane parallel chamber. Published values from the AAPM TG-51 protocol are listed alongside for comparison. Numbers in parentheses represent uncertainty on the last digit.

Beam	R_{50} (cm)	Exradin A12 (SN 309)			Exradin A12 (SN 310)			PTW Roos		
		$k'_{R_{50}}$	TG-51	Δ (%)	$k'_{R_{50}}$	TG-51	Δ (%)	$k'_{R_{50}}$	TG-51	Δ (%)
6 MeV	2.25	1.03(1)	1.03	0.6	1.04(1)	1.03	0.7	1.05(1)	1.05	0.3
9 MeV	3.54	1.022(5)	1.018	0.4	1.022(5)	1.018	0.4	1.039(5)	1.034	0.5
12 MeV	4.94	1.013(5)	1.009	0.4	1.010(5)	1.009	0.1	1.020(5)	1.020	0.0
16 MeV	6.64	1.003(5)	1.002	0.1	1.003(5)	1.002	0.1	1.004(5)	1.006	-0.3
20 MeV	8.26	0.998(5)	0.998	0.0	0.999(5)	0.998	0.1	0.997(5)	0.996	0.1

8.3.6 Uncertainties

Summaries of the beam-independent and -dependent uncertainties encountered in the determination of absorbed dose using the ESWcal and the ionization chambers are given in Tables 8.3 and 8.4. The combined uncertainties related to the ESWcal and ionization chamber measurements, as well as to the evaluation of k_Q and $k'_{R_{50}}$ are listed in Table 8.5. The combined uncertainties have been calculated assuming independent inputs, however some corrections (*e.g.* perturbation and heat transfer correction) are correlated, and thus are likely overestimated slightly.

Table 8.3. Summary of the relative beam-independent uncertainties in this work[61].

Beam-independent quantity	Type A (%) uncertainty	Type B (%) uncertainty
Ionization chamber reading	0.04	--
Monitor chamber reading	0.10	--
c_w	--	<0.01
Bridge calibration	--	0.13
Absolute temperature	--	0.01
Thermistor calibration	--	0.19
Profile uniformity	--	0.05
k_ρ	--	0.05
k_{HD}	--	0.15
P_{ion}	--	0.06
P_{pol}	--	0.06
P_{TP}	--	0.03
Electrometer calibration	--	0.05
$N_{D_w}^{^{60}Co}$	--	0.44

Table 8.4. Summary of the relative beam-dependent uncertainties in this work.

Beam type	Type A (%) uncertainty			Type B (%) uncertainty	
	ESWcal reading	Depth (chamber)	Depth (thermistors)	k_c	k_p
6 MeV	0.20	0.21	0.42	0.58	0.63
9 MeV	0.21	0.08	0.16	0.16	0.24
12 MeV	0.18	0.02	0.14	0.10	0.26
16 MeV	0.20	0.06	0.11	0.14	0.26
20 MeV	0.19	0.08	0.16	0.13	0.27
^{60}Co	0.13	0.10	0.21	0.13	0.08
6 MV	0.20	0.08	0.15	0.13	0.13

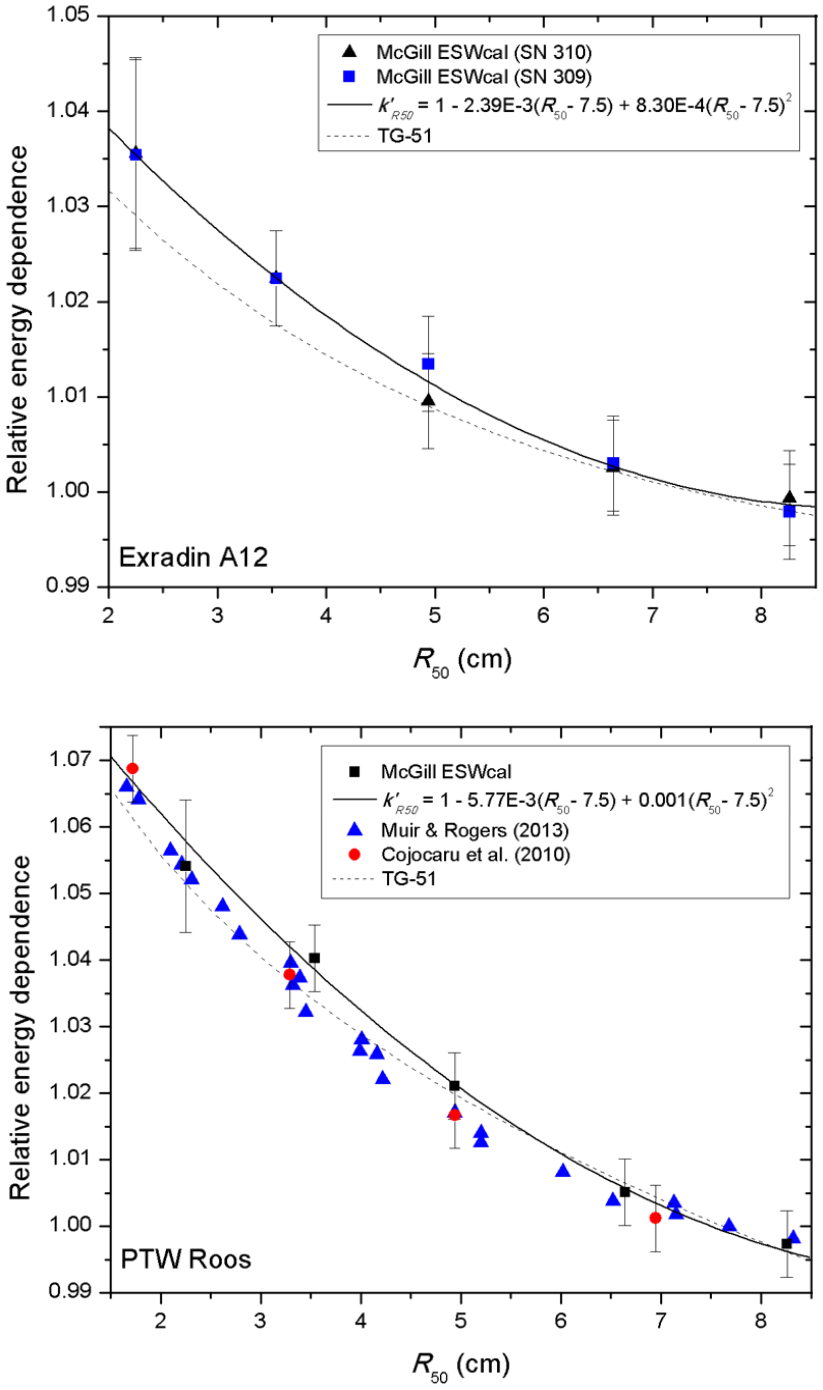

Figure 8.10: Comparison of the energy dependence of calibration factors for the (a) Exradin A12, and (b) the PTW Roos. A second-order polynomial (solid line) was fitted to the measured data. The theoretical energy variations as given by TG-51 (dashed line) are also shown in both plots. For the Roos, a recent simulation-based[67] (triangles), and experiment-based[44] study (circles) are also shown.

Table 8.5. Summary of the combined relative uncertainties, expressed in percent, related to the calorimeter and chamber measurements, as well as to the evaluation of k_Q and $k'_{R_{50}}$.

Beam type	ESWcal	Ionization chamber	k_Q	$k'_{R_{50}}$
6 MeV	1.02	0.51	1.14	1.02
9 MeV	0.50	0.47	0.68	0.46
12 MeV	0.47	0.46	0.66	0.43
16 MeV	0.48	0.47	0.67	0.44
20 MeV	0.49	0.47	0.68	0.46
^{60}Co	0.42	0.48	0.63	--
6 MV	0.43	0.47	0.64	--

8.4 DISCUSSION

Within combined uncertainties, the results obtained with the ESWcal system show general agreement with TG-51 values of $k'_{R_{50}}$ for 6 MeV to 20 MeV electron beams for both the Exradin A12 and PTW Roos chambers. This is an important finding, as previously, direct water calorimeter measurements in low-energy electron beams were considered unfeasible due to the temperature drifts produced by the large dose gradients. In particular, water calorimetry for electron beams with energies between 9 MeV and 20 MeV can be performed with a level of uncertainty similar to that of photon beam water calorimetry. It is also possible to perform reproducible measurements in a 6 MeV beam, however uncertainties become greater due to the steep dose gradient. As is shown in the uncertainty budgets above, positioning uncertainty, which in turn affects the accuracy of the field perturbation correction, is dominant at this relatively low energy. In comparison, Stucki and Vörös (2007) measured electron beam quality correction factors for the NACP02 and PTW34001 plane-parallel chambers for nominal electron energies as low as 5.5 MeV (R_{50} = 1.75 cm) using a total absorption (Fricke) experiment.[66] In the first case, a

~20 MeV (R_{50} = 7.523 cm) electron beam was used as the reference beam quality, Q_0, where in the second case, ^{60}Co was used. This resulted in k_{Q,Q_0} values with relative combined standard uncertainties of 0.5 % and 1 %, respectively.

The overall behavior of the ESWcal system was validated by the agreement shown between it and the NRC-calibrated Exradin A12 chamber in a standard 6 MV photon beam. While the absolute accuracy of any primary standard cannot be directly measured, showing agreement among independent standards helps validate the techniques.[7,63] Despite the fact that the Exradin A12 was calibrated against a water calorimeter, it can still be considered an independent verification, since both calorimetry systems employ different approaches in determining correction factors (*e.g.* NRC measures k_p with a dummy glass vessel). There are correlations which may potentially bias the comparison, however these are considered outside the scope of this study. The level of agreement shown in this work and others suggests that there are no identifiable discrepancies in the absolute determination of dose.[7]

That said, there were a few slight discrepancies observed in this work when comparing to values found in TG-51. For instance, a relatively small, and statistically-insignificant difference (0.3 %) was found between the ESWcal and TG-51 values for k_{ecal} for the Exradin A12 chamber. Muir and Rogers. (2013) found discrepancies of up to 0.8 % in individually calculated correction factors used in the determination of k_{ecal} for the NE2571 chamber (a thimble chamber comparable to the Exradin A12), but because of cancellation, the resulting k_{ecal} factors agreed with TG-51 to within 0.5 %.[67] In that same body of work, electron quality conversion factors for the PTW Roos were derived through MC simulation. These results agree with both the data in this work and those provided by TG-51 (Figure 8.10 b). Although there is much less data available for the Exradin A12, there is some evidence provided in this work to suggest that this type of chamber exhibits a more pronounced

energy dependence, particularly at low energies, than predicted by the protocols (Figure 8.10 a).

The applications of water calorimetry to electron beam dosimetry can be further investigated in two key areas. The first is to carry on using the ESWcal to determine the beam quality conversion factors of different chamber types. This could be an invaluable source of experimental data for future reference dosimetry protocols for electron beams. The second important area in immediate need of attention is the development of improved positioning techniques. The current method of determining the thermistor depth, both in relation to the front face of the vessel and within the calorimeter phantom, must be improved in order to reduce the combined uncertainty on lower energy electron beams (*i.e.*, < 9 MeV). This is of particular interest since newly-developed thin-window (0.7 mm) vessels with angled ports have made it physically possible to perform measurements at the reference depth of beams with energies as low as 4 MeV ($d_{\mathrm{ref}} \approx 0.8$ cm). Until these improvements are made, the feasibility of a water calorimeter-based absorbed dose standard for electrons will be limited to therapeutic energies of about 9 MeV and greater.

8.5 CONCLUSIONS

The ESWcal demonstrates for the first time the feasibility of performing reproducible water calorimetry measurements in electron beam energies as low as 6 MeV. Perturbation effects due to the presence of the glass calorimeter vessel were accounted for using MC simulations. Using finite element modelling, radiation-induced conductive heat transfer was simulated and included in the analysis. A preliminary validation of the ESWcal was carried out by directly comparing the doses measured by the calorimeter and an NRC-calibrated Exradin A12 chamber in a 6 MV photon beam. The two instruments were

shown to agree to within approximately 0.20 %. Overall calorimeter uncertainty was approximately 1.0 % at 6 MeV, a figure dominated by position-related uncertainty, and 0.50 % for higher energies. The combined uncertainties for energies of 9 MeV and above are comparable with the total uncertainty (approximately 0.40 %) associated with photon beam water calorimetry. From the ESWcal-acquired data, values of $k'_{R_{50}}$ were derived for the Exradin A12 and PTW Roos ionization chambers and were shown to agree with TG-51 within combined uncertainties. Furthermore, a value of k_{ecal} for the Exradin A12 chamber was established to be 0.903 ± 0.004, agreeing with the value listed in TG-51. Further investigation into applications of water calorimetry to electron beams will proceed by using the ESWcal to determine $k'_{R_{50}}$ and k_{ecal} for additional chamber types, as well as by improving positioning methods, thereby reducing uncertainties associated with low-energy measurements. Based on the results of this work, it is feasible to construct a water calorimetry-based absorbed dose standard for electron beams in the range of 9 MeV to 20 MeV. This would permit the direct calibration of ionization chambers at several clinically-relevant electron beam energies.

ACKNOWLEDGEMENTS

The efforts of David Marchington and Mike Vandenhoff of the NRC are greatly appreciated. This work has been supported in part by the CREATE Medical Physics Research Training Network grant of the Natural Sciences and Engineering Research Council (NSERC) (grant no. 432290), as well as NSERC grant RGPIN 298191. J. Renaud is a recipient of a Canadian Institutes of Health Research doctoral scholarship.

8.6 REFERENCES

[1]P.R. Almond, P.J. Biggs, B.M. Coursey, W.F. Hanson, M. Saiful Huq, R. Nath, and D.W.O. Rogers, "AAPM's TG-51 protocol for clinical reference dosimetry of high-energy photon and electron beams," Med. Phys. **26**, 1847-1870 (1999).

[2]M. McEwen, L. DeWerd, G. Ibbott, D. Followill, D.W. Rogers, S. Seltzer, and J. Seuntjens, "Addendum to the AAPM's TG-51 protocol for clinical reference dosimetry of high-energy photon beams," Med. Phys. **41**, 041501 (2014).

[3]IAEA (International Atomic Energy Agency), "Absorbed dose determination in external beam radiotherapy based on absorbed-dose-to-water standards: An international code of practice for dosimetry," Technical Report Series 398 (IAEA, Vienna, Austria, 2001).

[4]J. Seuntjens, and S. Duane, "Photon absorbed dose standards," Metrologia **46**, S39-S58 (2009).

[5]J.P. Seuntjens, and A.R. DuSautoy, "Review of calorimeter-based absorbed dose to water standards," in *Standards and Codes of Practice in Medical Radiation Dosimetry: Proc of an International Symposium* IAEA-CN-96-3 (International Atomic Energy Agency, Vienna, Austria, 2003).

[6]D. Burns, "An analysis of existing data for W_{air}, I_c and the product of $W_{air}s_{c,air}$," Metrologia **49**, 507-512 (2012).

[7]M.R. McEwen, and A.R. DuSautoy, "Primary standards of absorbed dose for electron beams," Metrologia **46**, S59-S79 (2009).

[8]D.T. Burns, M.R. McEwen, and A.J. Williams, "An NPL absorbed dose calibration service for electron beam radiotherapy," in *Proc. Int. Symp. On Measurement Assurance in Dosimetry*

IAEA-SM-330/34 (International Atomic Energy Agency, Vienna, Austria, 1994). Ed. S.P. Flitton.

[9]G. Stucki, W. Muench, and H. Quintel, "The METAS absorbed dose to water calibration service for high energy photon and electron beam radiotherapy," in *Standards and Codes of Practice in Medical Radiation Dosimetry: Proc of an International Symposium* IAEA-CN-96-8 (International Atomic Energy Agency, Vienna, Austria, 2003).

[10]M.R. McEwen, A.R. DuSautoy, and A.J. Williams, "The calibration of therapy level electron beam ionization chambers in terms of absorbed dose to water," Phys. Med. Biol. **43**, 2503-2519 (1998).

[11]K.J. Stewart, "The development of new devices for accurate radiation dose measurement: a guarded liquid ionization chamber and an electron sealed water calorimeter," *Ph.D. thesis* (Montreal: McGill University 2007).

[12]M. McEwen, "Evaluation of alanine as a reference dosimeter for therapy level dose comparisons in megavoltage electron beams," Metrologia **52**, 272-279 (2015).

[13]K. Stewart, N. Klassen, C. Ross, and J. Seuntjens, "Design and testing of a new sealed water calorimeter for electron beams," Med. Phys. **32**, 2419 (2005).

[14]A. Sarfehnia, K. Stewart, E. Chung, and J. Seuntjens, "Primary water calorimetry for clinical electron beams, scanned proton beams and ^{192}Ir brachytherapy," in *International Symposium on Standards, Applications and Quality Assurance in Medical Radiation Dosimetry* (International Atomic Energy Agency, Vienna, Austria, 2010).

[15]C.K. Ross, J.P. Seuntjens, N.V. Klassen, and K.R. Shortt, "The NRC sealed water calorimeter: correction factors and performance," in *Proc. Workshop on Recent Advances in Calorimetric*

Absorbed Dose Standards, Report CIRM 42 (National Physical Laboratory, Teddington, UK, 2000).

[16]M. Pieksma, E. van Dijk, and A.H.L. Aalbers, "The NMi absorbed-dose-to-water calorimeter (a status report)," in *Proc. Workshop on Recent Advances in Calorimetric Absorbed Dose Standards*, Report CIRM 42, (National Physical Laboratory, Teddington, UK, 2000).

[17]C.K. Ross, M.R. McEwen, and N.V. Klassen, "Vessel designs and correction factors for water calorimetry," in *Proc. Absorbed Dose and Air Kerma Primary Standards Workshop* (LNE-LNHB, Paris, France, 2007).

[18]J.P. Seuntjens, C.K. Ross, N.V. Klassen, and K.R. Shortt, "A status report on the NRC sealed water calorimeter," NRC Technical Report No. PIRS-0584 (National Research Council of Canada, Ottawa, Canada, 1999).

[19]A. Krauss, "The new PTB primary standard for absorbed dose to water in Co-60 radiation," *Med. Phys. Proc. ICMP2005*, 405-406 (Biomediziniche Technik, Nuremberg, Germany, 2005). Ed. U. Boenick, and A. Bolz.

[20]J. Medin, C.K. Ross, G. Stucki, N.V. Klassen, and J.P. Seuntjens, "Commissioning of an NRC-type sealed water calorimeter at METAS using ^{60}Co gamma-rays," Phys. Med. Biol. **49**, 4073-4086 (2004).

[21]H.J. Brede, K.D. Greif, O. Hecker, P. Heeg, J. Heese, D.T.L. Jones, H. Kluge, and D. Schardt, "Absorbed dose to water determination with ionization chamber dosimetry and calorimetry in restricted neutron, photon, proton and heavy-ion radiation fields," Phys. Med. Biol. **51**, 3667-3682 (2006).

[22]A. Krauss, "The PTB water calorimeter for the absolute determination of absorbed dose to water in ^{60}Co radiation," Metrologia **43**, 259-272 (2006).

[23]M.R. McEwen, and C. Ross, “Direct calibration of ionization chambers in linac photon beams,” Med. Phys. **32**, 2128 (2005).

[24]P. Sharpe, and S. Duane, “Progress Report on Radiation Dosimetry at NPL,” Report CCRI(I)/11-07 (National Physical Laboratory, Teddington, UK, 2011).

[25]J.P. Seuntjens, “Correction factors for a cylindrical ionization chamber used in medium-energy x-ray beams," Phys. Med. Biol. **38**, 805-832 (1993).

[26]A. Krauss, L. Büermann, H.M. Kramer, and H.J. Selbach, “Calorimetric determination of the absorbed dose to water for medium-energy x-rays with generating voltages from 70 to 280 kV,” Phys. Med. Biol. **57**, 6245-6268 (2012).

[27]B. Rapp, N. Perichon, M. Denoziere, J. Daures, A. Ostrowsky, and J.M. Bordy, “The LNE-LNHB water calorimeter for primary measurement of absorbed dose at low depth in water: application to medium-energy x-rays,” Phys. Med. Biol. **58**, 2769-2786 (2013).

[28]R.J. Schulz, L.J. Verhey, M. Saiful Huq, and N. Venkataramanan, “Water calorimeter dosimetry for 160 MeV protons,” Phys. Med. Biol. **37**(4), 947-953 (1992).

[29]L.A. de Prez, and J.A. de Pooter, “The new NMi orthovolt x-rays absorbed dose to water primary standard based on water calorimetry,” Phys. Med. Biol. **53**, 3531-3542 (2008).

[30]H. Palmans, J. Seuntjens, F. Verhaegen, J.M. Denis, S. Vynckier, and H. Thierens, “Water calorimetry and ionization chamber dosimetry in an 85-MeV clinical proton beam," Med. Phys. **23**, 643-650 (1996).

[31]J. Medin, C.K. Ross, N.V. Klassen, H. Palmans, E. Grusell, and J.E. Grindborg, “Experimental determination of beam quality factors *kQ* for two types of Farmer chamber in a 10 MV photon and a 175 MeV proton beam," Phys. Med. Biol. **51**, 1503-1521 (2005).

[32]S. Gagnebin, D. Twerenbold, E. Pedroni, D. Meer, S. Zenklusen, and C. Bula, "Experimental determination of the absorbed dose to water in a scanned proton beam using a water calorimeter and an ionization chamber," Nuc. Instr. Meth. Phys. Res. B **268**, 524-528 (2010).

[33]S. Rossomme, J. Renaud, N. Lee, R. Thomas, A. Sarfehnia, J. Seuntjens, A. Kacperek, D. Bertrand, S. Vynckier, and H. Palmans, "SU-ET-408: Determination of $k_{Q,Q0}$-factors from water and graphite calorimetry in a 60 MeV proton beam," Med. Phys. **41**(6), 319 (2014).

[34]A. Sarfehnia, B. Clasie, E. Chung, H.M. Lu, J. Flanz, E. Cascio, and J. Seuntjens, "Direct absorbed dose to water determination based on water calorimetry in scanning proton beam delivery," Med. Phys. **37**(7), 3541-3552 (2010).

[35]A. Sarfehnia, and J. Seuntjens, "Development of a water calorimetry-based standard for absorbed dose to water in HDR 192Ir brachytherapy," Med. Phys. **37**(4), 1914-1923 (2010).

[36]L.A. De Prez, and J.A. De Pooter, "Development of the VSL water calorimeter as a primary standard for absorbed dose to water measurements for HDR brachytherapy sources," in *Proc. Conf. on Advanced Metrology for Cancer Therapy* (PTB, Braunschweig, Germany, 2011). Ed. R.P. Kapsch.

[37]M. Bambynek, A. Krauss, and H.-J. Selbach, "Calorimetric determination of absorbed dose to water for an ^{192}Ir HDR brachytherapy source in near-field geometry," in *Med. Phys. and Biomed. Eng. WC 2009, IFMBE Proc. 25/XIII* (IUPESM, Munich, Germany, 2009), 89-92, Ed. R. Magjarevic.

[38]H. Palmans, W. Mondelaers, and H. Thierens, “Absorbed dose beam quality correction factors k_Q for the NE2571 chamber in a 5 MV and a 10 MV photon beam," Phys. Med. Biol. **44**, 647-663 (1999).

[39]M. Pieksma, L.A. de Prez, E. van Dijk, and A.H.L. Aalbers, “Measurements of k_Q beam quality correction factors for the NE2611A chamber in high-energy photon beams using the Nederlands Meetinstituut water calorimeter,” in *Standards and Codes of Practice in Medical Radiation Dosimetry: Proc of an International Symposium* IAEA-CN-96-7 (International Atomic Energy Agency, Vienna, Austria, 2003).

[40]J.P. Seuntjens, C.K. Ross, K.R. Shortt, and D.W.O. Rogers, “Absorbed-dose beam quality conversion factors for cylindrical chambers in high energy photon beams," Med. Phys. **27**, 2763-2779 (2000).

[41]S.M. Vatnitsky, J.V. Siebers, and D.W. Miller, “Calorimetric determination of the absorbed dose-to-water beam quality correction factor kQ for high-energy photon beams," Med. Phys. **22**, 1749-1752 (1995).

[42]M.R. McEwen, and C.K. Ross, “Direct calibration of ionization chambers in linac electron beams,” in *Proc. Absorbed Dose and Air Kerma Primary Standards Workshop* (LNE-LNHB, Paris, France, 2007).

[43]M. McEwen, “Measurement of ionization chamber absorbed dose kQ factors in megavoltage photon beams,” Med. Phys. **37**, 2179-2193 (2010).

[44]C.D. Cojocaru, G. Stucki, M.R. McEwen, and C.K. Ross, “Determination of absorbed dose to water in megavoltage electron beams using a calorimeter-Fricke hybrid system,” in *International Symposium on Standards, Applications and Quality Assurance in Medical Radiation Dosimetry*, (International Atomic Energy Agency, Vienna, Austria, 2010).

[45]M.R. McEwen, A.J. Williams, and A.R. DuSautoy, “Determination of absorbed dose calibration factors for therapy level electron beam ionization chambers,” Phys. Med. Biol. **46**, 741-755 (2001).

[46]G.X. Ding, and J.E. Cygler, “Measurement of P_{repl} P_{wall} factors in electron beams and in a ^{60}Co beam for plane-parallel chambers," Med. Phys. **25**, 1453-1457 (1998).

[47]K.J. Stewart, and J.P. Seuntjens, “Comparing calibration methods of electron beams using plane-parallel chambers with absorbed-dose to water based protocols," Med. Phys. **29**, 284-289 (2002).

[48]L.A. Buckley, and D.W.O. Rogers, “Wall correction factors, P_{wall}, for parallel-plate ionization chambers," Med. Phys. **33**, 1788-1796 (2006).

[49]L.A Buckley, and D.W.O. Rogers, “Wall correction factors, P_{wall}, for thimble ionization chambers," Med. Phys. **33**, 455-464 (2006).

[50]K. Zink, and J. Wulff, “On the wall perturbation correction for a parallel-plate NACP-02 chamber in clinical electron beams," Med. Phys. **38**, 1045-1054 (2011).

[51]F. Verhaegen, R. Zakikhani, A. DuSautoy, H. Palmans, G. Bostock, D. Shipley, and J. Seuntjens, “Perturbation correction factors for the NACP-02 plane-parallel ionization chamber in water in high-energy electron beams,” Phys. Med. Biol. **51**, 1221-1235 (2006).

[52]K. Zink, D. Czarnecki, H.K. Looe, P. von Voigts-Rhetz, and D. Harder, “Monte Carlo study of the depth-dependent fluence perturbation in parallel plate ionization chambers in electron beams," Med. Phys. **41**, 111707 (2014).

[53]F. Lacroix, M. Guillot, M. McEwen, C. Cojocaru, L. Gingras, A.S. Beddar, and L. Beaulieu, “Extraction of depth-dependent perturbation factors for parallel-plate chambers in electron beams using a plastic scintillation detector,” Med. Phys. **37**, 4331-4342 (2010).

[54]B.R. Muir, M.R. McEwen, and D.W.O. Rogers, "Determination of relative ion chamber calibration coefficients from depth-ionization measurements in clinical electron beams," Phys. Med. Biol. **59**, 5953-5969 (2014).

[55]J. Seuntjens, "Comparative study of ion chamber dosimetry and water calorimetry in medium energy x-ray beams," *Ph.D. thesis* (Gent: Gent University 1991).

[56]S. R. Domen, "Advances in Calorimetry for Radiation Dosimetry," in *The Dosimetry of Ionizing Radiation, Vol. II*, edited by K. R. Kase, B. E. Bjärngard, F. H. Attix (Academic Press, Inc., Orlando, 1987), pp. 245-320.

[57]J. Seuntjens, and H. Palmans, "Correction factors and performance of a 4 C sealed water calorimeter," Phys. Med. Biol. **44**, 627-646 (1999).

[58]"Properties of water in the range 0-100 °C," in *CRC handbook of Chemistry and Physics, 89th edition*, edited by D.R. Lide (CRC Press/Taylor and Francis, Boca Raton, FL, 2009), pp. 902.

[59]I. Kawrakow, and D.W.O. Rogers, "The EGSnrc code system: Monte Carlo simulation of electron and photon transport," NRC Technical Report No. PIRS-701 v4-2-2-5 (National Research Council of Canada, Ottawa, Canada, 2007).

[60]S. Picard, D.T. Burns, P. Roger, P.J. Allisy-Roberts, M.R. McEwen, C.D. Cojocaru, and C.K. Ross, "Comparison of the standards for absorbed dose to water of the NRC and the BIPM for accelerator photon beams," Metrologia **47**, 06025 (2010).

[61]BIPM (Bureau International des Poids et Mesures), "Evaluation of measurement data – Guide to the expression of uncertainty in measurement," JCGM 100:2008, First ed. (BIPM, Paris, France, 2008).

[62]BIPM (Bureau International des Poids et Mesures), “Measurement of absorbed dose to water for Cobalt 60 - Key and supplementary comparisons, Ionizing Radiation, Section I (x and gamma rays, electrons),” BIPM.RI(I)-K4 (BIPM, Paris, France, 2015).

[63]K.R. Shortt, “The role of comparisons in confirming the accuracy of dosimetric standards," in *Recent developments in accurate radiation dosimetry* (Medical Physics Publishing, Madison, WI, 2002). Ed. J.P. Seuntjens, and P.N. Mobit.

[64]J.P. Seuntjens, C.K. Ross, K.R. Shortt, D.W.O. Rogers, “Absorbed-dose beam quality conversion factors for cylindrical chambers in high energy photon beams,” Med. Phys. **27**, 2763-2779 (2000).

[65]B.R. Muir, and D.W.O. Rogers, “Monte Carlo calculations of k_Q, the beam quality conversion factor,” Med. Phys. **37**(11), 5939-5950 (2010).

[66]G. Stucki, and S. Vörös, “Experimental $k_{Q,Q0}$ electron beam quality correction factors for the types NACP02 and PTW34001 plane-parallel chambers,” in *Proc. Absorbed Dose and Air Kerma Primary Standards Workshop* (LNE-LNHB, Paris, France, 2007).

[67]B.R. Muir, and D.W.O. Rogers, “Monte Carlo calculations for reference dosimetry of electron beams with the PTW Roos and NE2571 ion chambers,” Med. Phys. **40**(12), 121722-1 (2013).

Chapter 9

DEVELOPMENT AND APPLICATION OF A WATER CALORIMETER FOR THE ABSOLUTE DOSIMETRY OF SHORT-RANGE PARTICLE BEAMS

In this chapter, a water calorimeter designed to directly measure absorbed dose to water in non-standard radiation fields with reference depths in the range of 6 - 20 mm, and its initial testing in clinical electron and proton beams.is presented. The results of this work include dose measurements performed directly in water using water calorimetry and the associated simulation and derivation of heat transfer corrections. The dose is measured in clinical accelerator-based 6 MeV and 8 MeV electron beams and cyclotron-based 60 MeV monoenergetic and modulated proton beams. This is the first time that water calorimetry has been used in such a low energy proton beam. This study establishes the feasibility of developing an absorbed dose transfer standard for short-range clinical electrons and protons and forms the basis for a transportable dose standard for direct calibration of ionization chambers in the user's beam.

Authors: James Renaud[1], Séverine Rossomme[2], Arman Sarfehnia[1,3], Stefaan Vynckier[2,4], Hugo Palmans[5,6], Andrzej Kacperek[7], and Jan Seuntjens[1]

[1]Medical Physics Unit, McGill University, Montréal, Canada
[2]Molecular Imaging and Experimental Radiotherapy Department, Université catholique de Louvain, Brussels, Belgium
[3]Department of Radiation Oncology, University of Toronto, Toronto, Canada
[4]Cliniques Universitaires Saint-Luc, Université catholique de Louvain, Brussels, Belgium

[5]*EBG MedAustron GmbH, Medical Physics, Wiener Neustadt, Austria*
[6]*National Physical Laboratory, Acoustics and Ionising Radiation Division, Teddington, United Kingdom*
[7]*The Clatterbridge Cancer Centre NHS Foundation Trust, Bebington, Wirral, United Kingdom*

ABSTRACT

Purpose: In this work, we describe a new design of water calorimeter built to measure absorbed dose in non-standard radiation fields with reference depths in the range of 6 - 20 mm, and its initial testing in clinical electron and proton beams.

Methods: A functioning calorimeter prototype with a total water equivalent thickness of less than 30 mm was constructed in-house and used to obtain measurements in clinical accelerator-based 6 MeV and 8 MeV electron beams and cyclotron-based 60 MeV monoenergetic and modulated proton beams. Corrections for the conductive heat transfer due to dose gradients and non-water materials was also accounted for using a commercial finite element method software package.

Results: Absorbed dose to water was measured with an associated type A standard uncertainty of approximately 0.4 % and 0.2 % for the electron and proton beam experiments, respectively. In terms of thermal stability, drifts were on the order of a couple of hundred μK per minute, with a short-term variation of 5 – 10 μK. Heat transfer correction factors ranged between 1.021 and 1.049. The overall combined standard uncertainty on the absorbed dose to water was estimated to be 0.6 % for the 6 MeV and 8 MeV electron beams, as well as for the 60 MeV monoenergetic protons, and 0.7 % for the modulated 60 MeV proton beam.

Conclusions: This study establishes the feasibility of developing an absorbed dose transfer standard for short-range clinical electrons and protons and forms the basis for a

transportable dose standard for direct calibration of ionization chambers in the user's beam. The largest contributions to the combined standard uncertainty were the positioning (≤ 0.5 %) and the correction due to conductive heat transfer (≤ 0.4 %). This is the first time that water calorimetry has been used in such a low energy proton beam.

9.1 INTRODUCTION

Absorbed dose to water standards form the basis of clinical reference dosimetry of high-energy photon, electron, proton, and heavy-ion beams in radiotherapy. Codes of practice for reference dosimetry such as the IAEA TRS-398[1] and the AAPM TG-51[2,3] generally revolve around the use of ionization chambers calibrated in a reference beam quality (most commonly ^{60}Co gamma radiation). The primary and secondary standards dosimetry laboratories (PSDLs and SSDLs) of the world have often been involved in the drafting of these codes of practice and providing traceable measurement results. PSDLs in particular have been largely responsible for the development and upkeep of absorbed dose standards for the past four decades.[4]

Ionometry, total absorption (*i.e.*, Fricke) -based systems, and calorimetry make up the three major classes of techniques used at PSDLs to measure absorbed dose to water in absolute terms.[5,6] To serve as absorbed dose standards, ionization chambers and Fricke-based methods rely upon a well characterized radiation field as a reference. In the case of ionometry, values for the average energy required to produce an ion pair in dry air, $(W/e)_{air}$, and the restricted graphite-to-air stopping power ratio are necessary.[7] Fricke dosimetry relies on the knowledge of the product of the molar extinction coefficient and the radiation chemical yield of ferric ions, $(\varepsilon G)_{Fe^{3+}}$, and on an accurate transfer standard of

dose from a calibration quantity. In contrast, a calorimeter can be calibrated in terms of temperature and electrical-based quantities, entirely independent of radiation. As a result, calorimetry is considered the most direct means of measuring absorbed radiation dose.[8] They are used to do so by measuring the temperature rise induced by the interaction of radiation with matter at either a point in water (water calorimetry) or averaged over a relatively small volume of graphite (graphite calorimetry), under quasi-adiabatic conditions.

In contrast to high-energy photon beams, the application of the above-mentioned techniques to develop primary absorbed dose standards for charged particles (electrons, protons, heavy-ions) has, to-date, been hampered by the relatively large dose gradients and the short ranges involved, particularly at lower energies. For hadron therapies, the relative lack of widespread availability compounds these challenges. The practical range of the lowest therapeutic electron energies (4 MeV and 6 MeV) can vary from 20 mm to 30 mm, and dose gradients can exceed 5 % per millimeter in the build-up and fall-off regions. Similarly, the practical range of hadron beams used to treat superficial lesions, such as iris melanomas (*e.g.*, 60 MeV proton beam at the Clatterbridge Cancer Centre, CCC), can be as little as 4 – 6 mm.[9] Another, more subtle challenge to charged particle dosimetry is the associated depth-dependent charge deposition. For calorimeters with extremely sensitive DC based measurement circuitry, the effects of charge buildup are a particular concern that can be managed with proper grounding.[6] Primary electron beam dose standards currently in operation include a total absorption-calibrated Fricke-based system employed by The Swiss Federal Office of Metrology and Accreditation (METAS)[10], a graphite calorimeter operated by the National Physical Laboratory (NPL) in the UK[11], and a water calorimetry-based system used at the National Research Council of Canada (NRC)[12]. Much of the recent work on primary electron dose standards has been focused on water calorimetry, with as many as five PSDLs expected to establish such standards in the near

future. For hadron therapy, no primary absorbed dose standard currently exists. Many proton therapy centres rely upon the guidelines provided in ICRU Report 78[13], which recommends the adoption of the IAEA TRS-398 code of practice as the standard proton dosimetry protocol. Implementation of this protocol leads to a dosimetry system in which the dose applied to a patient is ultimately traceable to a primary dose standard through an indirect measurement of dose with an ionization chamber. In this formalism, a chamber-specific, beam-quality dependent conversion factor, k_{Q,Q_0}, is used to relate the chamber calibration obtained in the reference beam quality (Q_0), to the hadron beam quality used during treatment (Q). As a more direct alternative, ICRU 78 recommends that, where possible, the chamber be calibrated with a calorimeter in the user's proton beam.

One aim of this paper is to present the development of a transportable water calorimetry system specifically designed to operate at the user's facility and to calibrate ionization chambers in situ in terms of absorbed dose to water in non-standard particle beams with reference depths in the range of 6 - 20 mm. Originally constructed at McGill University by Renaud et al. (2014)[14], the calorimeter, herein referred to as the SHort RangE Water calorimeter (SHREWcal), shares design aspects with water calorimeters developed in the late 1990s by both the NRC[15] and by Physikalisch-Technische Bundesanstalt (PTB)[16]. In contrast to nearly all other water calorimeters in current use, the SHREWcal was designed to operate without a large (typically on the order of 30 × 30 × 30 cm^3) water phantom. This was done to help optimize the minimum measurable reference depth, as well as to maintain a practical size and weight for ease of setup and transport. It is expected that this design choice will have an insignificant impact on the achievable combined standard uncertainty associated with dose determination as compared to other PSDL-level water calorimeters, provided that the heat transfer and radiation field perturbation corrections are adequately modeled. A thin-windowed Pyrex vessel filled with pure water serves as the calorimeter's core absorbing medium. As a result, the calorimeter requires collimated

radiation fields with diameters no greater than 70 mm. Designed and constructed at the NRC, the vessel was originally developed to accommodate electron energies as low as 6 MeV, where the reference point is at a depth of approximately 12 mm. A detailed comparison study of this vessel design and the associated correction factors are provided by Ross et al (2007).[17]

Water calorimeters are mainly operated as primary absorbed dose standards for ^{60}Co[18,19], however the application of this technique has been extended in the past to include therapy range photon and electron beams[20,21], medium energy x-rays[22-24], protons[25,26], heavy-ions[27], and high dose rate brachytherapy sources[28-30]. Water calorimeters have also been extensively used to measure k_{Q,Q_0} factors for ionization chambers in high-energy photon beams.[31-34] Save for a handful of experimental studies, the same cannot be said about electrons, protons or heavy-ion beams. Values of k_{Q,Q_0} provided in reference dosimetry protocols for these types of radiation have been based solely on Monte Carlo (MC) calculations. That said, the feasibility of using water calorimetry to directly calibrate cylindrical and parallel-plate chambers in high-energy (≥ 6 MeV) electron beams has been demonstrated by McEwen and Ross (2007)[35] and by Renaud et al (2015)[36]. Similar applications of a water calorimeter in scattered proton beams have been reported by Medin et al (2005)[37] and Rossomme et al (2014)[38], as well as in scanned beams by Gagnebin et al (2010)[39], Sarfehnia et al. (2010)[40], and Medin (2010)[41]. Further development of absolute dosimetry systems and experimental corroboration of simulation-based k_{Q,Q_0} values are needed to validate current numerical chamber models.

Recent work at the Laboratoire National Henri Becquerel (LNE-LNHB) reported by Rapp et al. (2013) details the design and application of a specially-developed water calorimeter for primary absorbed dose measurements at low depth (down to 5 mm) in medium-energy x-rays.[42] In this study, calorimetry measurements in beams of 80 keV to 300 keV, at a depth

of 20 mm in water, led to absorbed doses to water with a combined relative standard uncertainty ranging between 0.49 % and 0.72 %. To our knowledge, these types of very shallow water calorimetry measurements have not been performed in other types of ionizing radiation. There is a well-defined need for a water calorimetry system capable of directly measuring k_{Q,Q_0} values for various ionization chambers at reference depths of less than 20 mm, particularly for beams of smaller diameters (< 70 mm diameter). Such a system could be used to verify the accuracy and to reduce the overall uncertainty of reference values provided in clinical dosimetry protocols. Ultimately, this could lead to the establishment of an absorbed dose to water standard for these types of beams based on water calorimetry, foregoing the need for a beam quality conversion procedure altogether.

In this work, we present the design and operating principles of the McGill SHREWcal system, including an overview of the numerical modelling considerations, highlighted aspects of the construction, and a detailing of the experimental proof-of-concepts. Specifically, the feasibility of applying this type of water calorimeter design is established for electrons in the range of 6 MeV to 8 MeV, and for a 60 MeV proton beam (both monoenergetic and modulated) by experimentally evaluating the thermal stability, the radiation-induced heat transfer, baseline signal variations, as well as the reproducibility. While graphite calorimetry has been previously used at the CCC[43], this is the first time a water calorimeter has been successfully used in such a low energy proton beam. Please note that the representation of uncertainties in this work follows that of the BIPM JCGM 100:2008 guide[44], and that a coverage factor of k = 1 is used to remain consistent with other uncertainty budgets found in the literature[5].

9.2 MATERIALS AND METHODS

9.2.1 Design Considerations

A numerical design study was conducted with the intent to fabricate a water calorimeter capable of dose measurement at depths of less than 10 mm in clinically operated electron, proton and carbon-ion fields, with a targeted overall standard uncertainty of 0.5 %. With an emphasis placed on minimizing the material in the path of the beam, a design sans traditional water phantom (*i.e.*, 30 × 30 × 30 cm^3) was chosen. Instead, a sealed glass vessel (designed and constructed at the NRC), serves as a miniature water phantom. This particular vessel was originally designed for use within a high-energy electron water calorimeter constructed at McGill University.[17,36] As this calorimeter was to be used experimentally on-site at various locations in Europe, the design was kept compact enough to allow for easy transport and handling. For this reason, an air-based cooling system was opted over a liquid-based system to regulate the calorimeter operating temperature (4 °C), not unlike in the design of Seuntjens and Palmans (1999)[45].

9.2.2 Water Calorimetry, Heat Transfer and Heat Defect

A water calorimeter measures the dose at a point in water, D_w, based on its fundamental relation to the radiation-induced temperature rise, ΔT_w, and the specific heat capacity at constant pressure of water, $c_{w,p}$ ($4205\ \mathrm{J \cdot kg^{-1} \cdot K^{-1}}$ @ 4 °C)[46] as shown in Eq. 9.1. This technique is possible because the thermal diffusivity of water is sufficiently low that radiation-induced thermal distributions remain in place long enough to permit the accurate measurement of temperature, and hence dose, at a point.

$$D_w = c_{w,p} \cdot \Delta T_w \cdot k_c \cdot \frac{1}{1 - k_{HD}} \cdot \prod_i k_i \qquad (9.1)$$

Corrections for the conductive heat transfer, k_c, and chemical heat defect, k_{HD}, are taken into consideration in this particular study. The remaining corrections common to water calorimetry account for the radiation field perturbation, k_p, radial dose profile non-uniformity, k_{dd}, and water density effect, k_ρ. These will be the subject of a companion paper detailing an inter-comparison between the SHREWcal and a standard graphite calorimeter. It is important to note that the design of the vessel and the calorimeter operating temperature have been chosen such that thermal perturbations resulting from convection and radiative processes are negligible and are not considered in this work.

k_c is defined as the ratio of the temperature rise in the absence of conduction to the actual temperature rise, and is numerically simulated using a finite element method based software package (COMSOL Multiphysics® v.4.2).[47,48] In general, it is one of the most significant correction factors in water calorimetry. Temperature gradients arise from dose gradients induced by the non-uniform radiation field and the presence of non-water materials. The software is used to calculate the time-dependent thermal distributions in a three-dimensional model of the calorimeter (Figure 9.1) by solving the partial differential equation governing heat conduction in both time and space. The solving algorithm requires several input parameters including the physical and thermal properties of the involved materials, boundary conditions, and the geometric and temporal distribution of heat sources and sinks.

For a particular beam type and energy, a heat source term representing the dose distribution was approximated by the clinically-available percent depth dose (PDD) curve and experimentally-used field size, corrected for the effects of non-water materials *m* present in the beam path. The magnitude of the shift in the dose distribution downstream due to the expanded polystyrene and the glass window of the vessel was approximated as the difference between the physical thickness, x, and the water-equivalent thickness, x_{eq}. As

recommended in TRS 398, the water-equivalent thickness of a material in high-energy electron beams can be approximated by scaling x by the mass density of the non-water material, ρ_{m}. For protons, the ratios of the mass densities, $(\rho_{\mathrm{m}}/\rho_{\mathrm{w}})$, and the continuous slowing down approximation (CSDA) ranges, $(R_{\mathrm{w}}/R_{\mathrm{m}})$, are the scaling factors of x. Although $(R_{\mathrm{w}}/R_{\mathrm{m}})$ is a function of proton energy, it is relatively constant over the clinical proton energies of interest. To calculate the approximate dose inside the vessel walls, the ratio of the restricted stopping powers of Pyrex and water were used. For each beam studied, a series of ten successive irradiations, including associated pre- and post-drift periods, were simulated. Analysis of the simulations were carried out over the same time ranges as measurements.

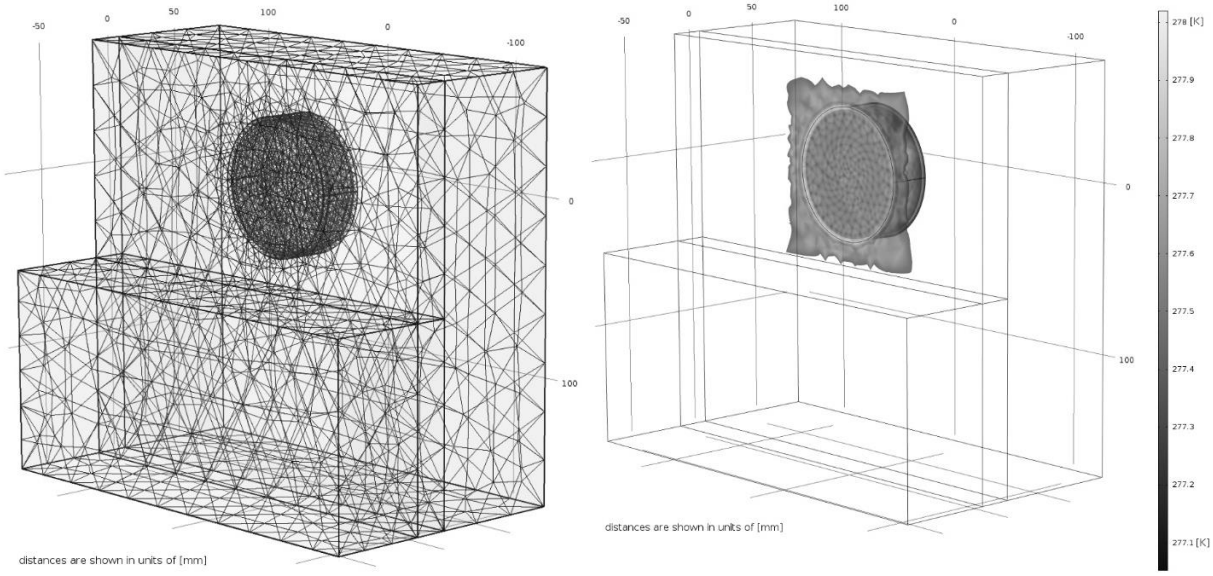

Figure 9.1: (Left) The meshing, or discretization, of the three-dimensional model geometry in the finite element analysis of the SHREWcal using COMSOL Multiphysics®. Physical and thermal properties of the involved materials, boundary conditions, and geometric and temporal distribution of heat sources and sinks are included as input parameters. (Right) Example of a radiation-induced temperature distribution in the wireframe-rendered SHREWcal vessel at an arbitrary time point, *t*, post-irradiation. This is the result of solving of the partial differential equation governing heat conduction in the model in both time and space.

k_{HD} is a measure of the net heat lost and gained due to radiation-induced chemical reactions (chemical heat defect) occurring in the water as a result of impurities and unknown dissolved gases. In general, water calorimeters minimize the heat defect by carefully controlling the purity of the water (organic content < 3 ppb) contained in a sealed glass vessel, which is saturated with a known gas. Hydrogen and nitrogen gas saturated systems are commonly used, and the heat defect of such systems have been well studied.[49,50] In this work, hydrogen gas was used to saturate the pure water under conditions that would introduce a minimal amount of organic impurities, a set-up which has been numerically shown to result in a zero heat defect, even for high-LET radiation. When irradiating a hydrogen gas system, a characteristic exothermic peak is observed initially, corresponding to the depletion of oxygen gas, after which an equilibrium state is achieved. Following sufficient pre irradiation, the steady state heat defect has been predicted to be null within 0.15 % for high-energy photon beams.[51] In this work, it is assumed that this value of uncertainty can be extended to higher LET radiation.

9.2.3 Construction

The SHREWcal design (Figure 9.2) consists of a sealed vessel made of Pyrex glass encased tightly in a milled block of expanded polystyrene. The pancake-style cylindrical vessel, which was constructed by the Ionizing Radiation Standards (IRS) division at the NRC, has been well described elsewhere in the literature.[17,47] The front and back circular windows are 79 mm in diameter and 1.1 mm thick, while the space between the windows is 22.7 mm. There are the two diametrically opposed ports in the sidewall which permit the insertion of NRC-assembled thermistor probes. The probes consist of a 40 mm long, 0.5 mm diameter, glass pipette with a 0.25 mm diameter thermistor (NTC type, BR11 series, Thermometrics) embedded at the tip. Positioned proximally to the vessel central axis such that a ~2 mm gap exists tip to tip, the thermistors, which have a nominal resistance of 10 kΩ at 4 °C, define the point of measurement. A radiation-induced temperature rise will cause the thermistors to experience a fractional resistance change on

the order of 400 Ω/K. When inserted in the vessel, the position of each thermistor bead is measured using a traveling microscope with a Vernier scale with a resolution of 0.01 mm. This is done by focusing first on the front of the glass, then lowering the microscope until the thermistor bead is in focus and reading the translation off the Vernier scale. Using the method described in Ross et al. (2007), a correction of (0.35 ± 0.01) mm is applied to account for the effect of the index of refraction of the glass.[17] Through this method, the k = 1 uncertainty on the position of the thermistors is 0.20 mm.

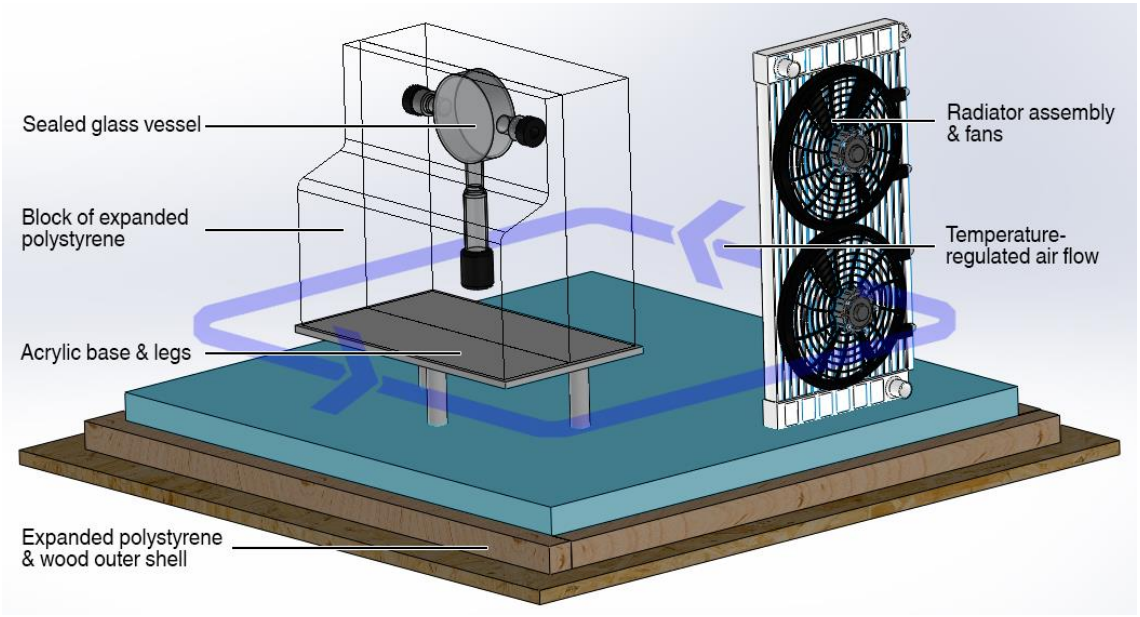

Figure 9.2: Isometric view of the SHREWcal water calorimeter schematic. The sealed glass vessel containing the pure water and two thermistor probes is encased within a milled block of expanded polystyrene (rendered as transparent with outlines). Coolant-fed radiator and fans circulate air (thick lines and arrows) chilled to a stable 4 °C. The walls and lid of the calorimeter, which when assembled form an air-tight seal, are omitted for the sake of clarity. The three resistance temperate detectors (RTDs) have also been omitted.

For the purpose of directly calibrating ionization chambers, a small-scale water phantom, herein referred to as the mock vessel (Figure 9.3), was conceived to experimentally replicate the radiation field perturbation due to the vessel's front face. With an interior

diameter of 100 mm and a circular front face made of the same 1.1 mm thick Pyrex as the calorimeter vessel, the mock vessel was designed to accommodate most common plane parallel ionization chambers. The chamber's depth of measurement is adjustable by longitudinally sliding the aluminum clamping assembly along a milled slot. With this setup, the range of depth adjustment, as measured between the inside surface of the Pyrex and the outside surface of an ionization chamber, is approximately 0 mm to 100 mm.

The vessel-block assembly is registered atop an acrylic base mounted on three acrylic legs. This design helps thermally insulate the vessel from the expanded polystyrene walls and the ambient environment, and also allows temperature-regulated air to circulate beneath it. Square lengths of hardwood and sheets of plywood make up the box frame and protective outer shell, respectively. The box is designed to provide a near air-tight seal when assembled. 12 × 12 cm^2 cut-outs in the front and back of the box and vessel-containing block provide a line of sight through the entire calorimeter for alignment. A vertically mounted radiator (Eco C240 240MM, Coolit Systems) is used to circulate 4 °C coolant pumped from a thermally controlled chiller bath (RTE-7, Thermo Scientific). Attached to the radiator are two fans that force the air mass within the box to circulate through the heat-exchanging fins. Placed inside the air mass are two resistance temperature detectors (RTDs) used to monitor the variation in average air temperature. An additional RTD is embedded in the expanded polystyrene block containing the vessel. The mass of the calorimeter is just under 10 kg, and the overall dimensions are approximately 50 × 50 × 40 cm^3. When the SHREWcal is being setup for an experiment, a milled aluminum plate is mounted to the outer front face of the calorimeter's wood box just beneath the entrance window cut-out. A horizontal slot in the mounted plate is designed to accept a 70 cm long aluminum mechanical pointer, which can then be slid inside the box and be brought into contact with the outer front face of the vessel. Similarly, the pointer can be slid outward and be brought into contact with an external point of reference (*e.g.*, end of a

particle beam line). By doing so, a measure of internal distance (vessel to outer box, and outer box to reference point) can be accurately measured to within a few tenths of a millimeter, both before and after cooling down of the system.

For the purpose of directly calibrating ionization chambers, a small-scale water phantom, herein referred to as the mock vessel (Figure 9.3), was conceived to experimentally replicate the radiation field perturbation due to the vessel's front face. With an interior diameter of 100 mm and a circular front face made of the same 1.1 mm thick Pyrex as the calorimeter vessel, the mock vessel was designed to accommodate most common plane parallel ionization chambers. The chamber's depth of measurement is adjustable by longitudinally sliding the aluminum clamping assembly along a milled slot. With this setup, the range of depth adjustment, as measured between the inside surface of the Pyrex and the outside surface of an ionization chamber, is approximately 0 mm to 100 mm.

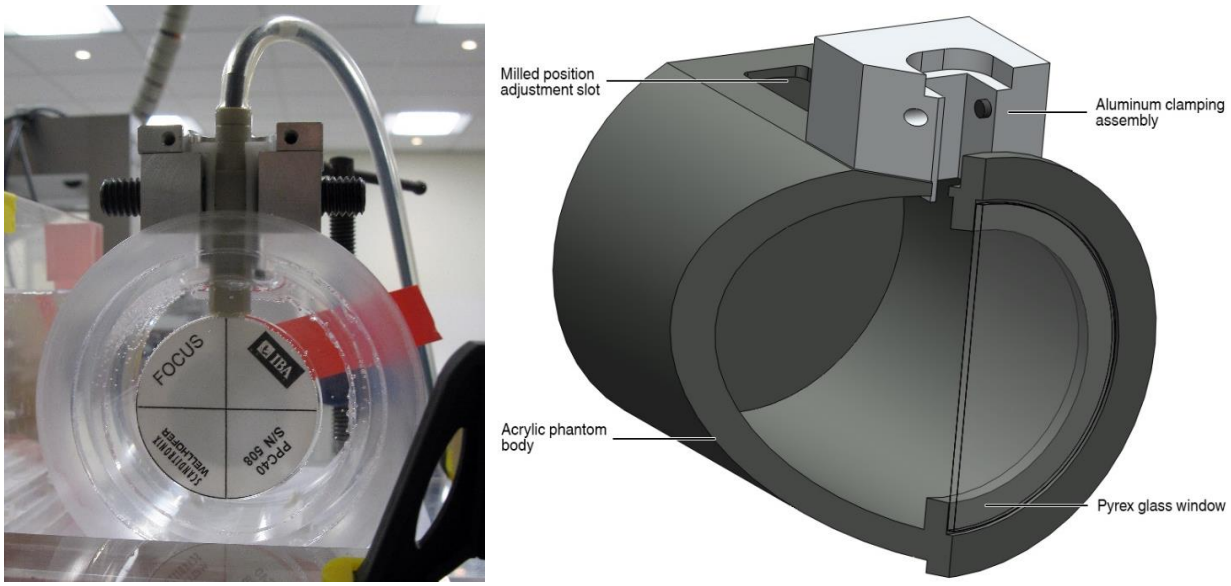

Figure 9.3: (Left) The mock vessel, a small-scale water phantom, was designed to experimentally reproduce the radiation field perturbation due to the front face of the calorimeter glass vessel. (Right) Cutaway rendering: The ionization chamber's depth of measurement is set by sliding the aluminum clamping assembly along a milled slot that runs along the top of the phantom.

9.2.4 Signal Acquisition

Temperature rises were indirectly determined by measuring the response of an active AC Wheatstone bridge circuit to thermistor resistance changes.[52] An example of a raw calorimetric signal is shown in Figure 9.4. Relating this bridge voltage back to temperature requires separate calibrations of the RTDs (against a calibrated mercury thermometer traceable to national standards), the thermistors (against RTDs), and the bridge response.[47] Bridge calibration (also referred to as ohmic calibration) was repeatedly performed throughout the experiment, in the absence of large thermal drifts, by manually adjusting the setting of a precision decade resistor box by 1 Ω when the bridge output was nominally balanced (*i.e.*, the combined thermistor resistance was equal to the decade resistor box setting) (see inlay of Figure 9.5). The results of which represent the change in bridge response per unit resistance change, $\Delta V_{1\ \Omega}$, as a function of temperature. A measured thermistor calibration curve (resistance as a function of temperature) was then used to relate bridge response to radiation-induced temperature rise.

The signal acquired during a single calorimetric run consists of three distinct portions: the pre-drift, the irradiation, and the post-drift. Prior to irradiation, an amount of pre-drift signal (typically 40 s) is collected to provide a measure of the initial thermal background. During irradiation, the bridge signal resulting from the combined temperature rise at the positions of the thermistors is acquired. Following the irradiation, a post-drift signal is recorded to compare against the initial (pre-drift) thermal drift and provide a measure of the radiation-induced heat transfer by means of linear extrapolation.[53] Due to the thermal insulation of the calorimeter box and the low thermal diffusivity of water, the pre- and post-drift signals are quasi-linear over the time scale of the measurement. In practice, the effects of heat transfer are accurately modelled in realistic geometries, as described in *Section* 9.2.2.

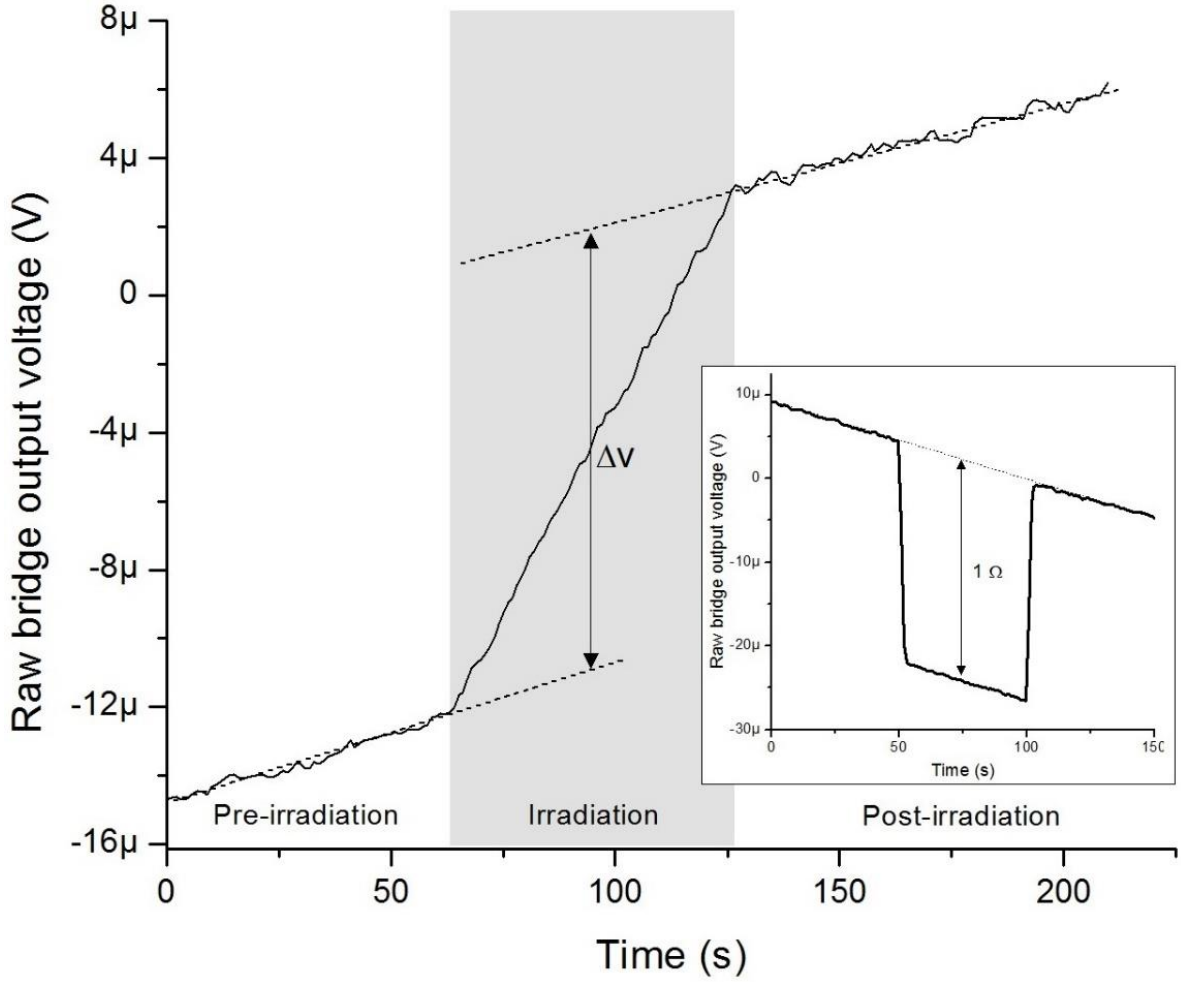

Figure 9.4: A sample calorimetric run acquired during a 60 s irradiation (400 MU delivered) of a 6 MeV clinical electron beam acquired using the SHREWcal. The raw data are in units of active bridge voltage, which, to first order is proportional to temperature rise and dose over a small temperature range. (Inlay): A typical bridge (ohmic) calibration, in which the bridge voltage response to a user induced change in bridge resistance of 1 Ω is recorded.

9.2.5 Electron Absorbed Dose Measurements

To evaluate signal variation, thermal drifts, repeatability and the heat transfer model, absorbed dose to water measurements using the prototype calorimeter were performed in clinical accelerator-based (Elekta Precise SL25) 6 MeV and 8 MeV electron beams with the

linac gantry set to 90° (Figure 9.5). A 10 × 10 cm^2 electron applicator was used to define the field size. The calorimeter entrance window was positioned at a source to surface distance (SSD) of 1000 mm and left to cool down overnight. At this distance, the SSD to the vessel within the calorimeter phantom was 1202 mm. The thermistors were aligned to the radiation field using the clinical laser system available in the room. Relative to the outer front face of the vessel, the thermistors were positioned at a depth of 10.8 mm, resulting in an extended source to axis distance (SAD) of 1213 mm.

In addition to the overnight cooling period, an additional stabilization period of 3 hours was provided following the alignment verification. 400 monitor units (MU) (60 seconds nominally) irradiations were repeatedly delivered in sets of 3 to 6. Between measurement sets, thermal gradients were allowed to dissipate for 30 to 60 minutes. An FC65-P Farmer-type ionization chamber (Wellhöfer) was positioned on the electron applicator, with the sensitive volume placed within the edge of the radiation field, to serve as an external reference chamber throughout the two day experiment. Air temperature and pressure were monitored using a mercury thermometer and barometer with calibrations traceable to national standards in order to correct the monitor chamber readings to the reference air density. Throughout the experiments, humidity remained within a range such that no correction was required. Each calorimetry measurement was normalized by a corrected monitor chamber reading to account for the variation in the beam stability over the course of several days.

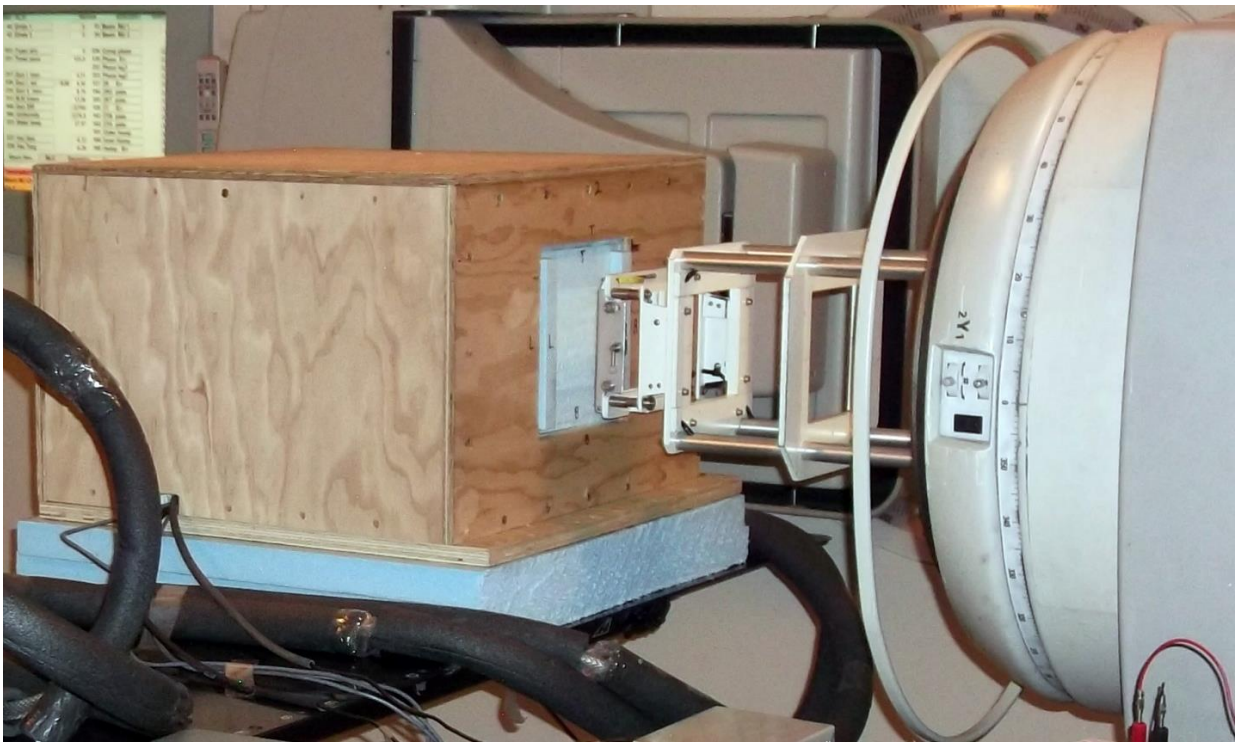

Figure 9.5: The experimental setup of the SHREWcal in a clinical accelerator-based electron beam. A cut-out in the wooden outer shell serves as the beam entrance window. The thermally-insulated tubing and wires visible in the image are the coolant and electrical power connections leading to the calorimeter's radiator assembly.

9.2.6 Proton Absorbed Dose Measurements

A second series of dose measurements were acquired in a 60 MeV proton beam with a nominal penetration depth of 31 mm in water at the Clatterbridge Cancer Centre (CCC) in the UK. From the end of the fixed horizontal beam line, the calorimeter entrance window was positioned at a distance of 56 mm from the final collimator. Given the thermistor depth setting of 7.5 mm within the vessel, the 1.1 mm thickness of Pyrex, the 47 mm of expanded polystyrene, and 159.5 mm of air within the calorimeter box, the geometric distance from the end of the beam line to the point of measurement was 271 mm. At this particular proton energy, the combined thickness of expanded polystyrene, Pyrex, and water in the path of the beam was equivalent to 11.2 mm of water. Alignment of the thermistors was

achieved using a projection radiography system used in clinical treatments. Measurements were performed in both a monoenergetic and a range-modulated proton beam. In both cases, a 30 mm diameter brass collimator was placed on the end of the beam line to shape the field. The calorimeter was repeatedly exposed to irradiations nominally lasting 20 s in sets of 2 to 5. Thermal re-stabilization was achieved between sets within 1 to 2 hours. A PTW TB7862 plane parallel transmission chamber positioned in the 56 mm space between the collimator and calorimeter served as an external reference chamber throughout the experiments, which spanned the course of several days. An acrylic block specially machined to accept the transmission chamber was used to reproducibly position the monitor placed within a few centimeters of the end of the beam line. Removal and replacement of the transmission chamber was necessary to measure the distance from the end of the beam line to a given setup (alternating between SHREWcal measurement sets was a graphite calorimeter operated by NPL as well as various ionization chambers). The relative monitor readings were applied to the calorimeter datasets to correct for variations in beam output. Analysis of the acquired calorimetric data was performed in the same way as described earlier for the electrons measurement sets.

9.3 RESULTS

9.3.1 Absorbed Dose Measurements

A summary of the results of the calorimetry experiments performed in electron beams of 6 MeV and 8 MeV, and a 60 MeV monoenergetic and modulated proton beam is shown in Table 9.1. The expressed uncertainty in the 3rd and 4th column represents the type A standard uncertainty for that particular measured quantity. The uncertainty in the final column, the average absorbed dose to water, is an indication of the calorimeter's

repeatability. For an average of 25 repeated measurements, the standard uncertainty on the mean measured dose ranged between 0.2 % for the proton beams, and 0.4 % for the electron beams. In terms of the raw bridge voltage, the typical collected pre-drifts were on the order of a few μV per minute, with an observed signal variation of approximately 100 - 200 nV (standard deviation, σ). Given that, for this particular calorimeter setup and under these particular operating conditions, a change in voltage, ΔV, of 1 μV is approximately equivalent to a temperature change, ΔT, of 50 μK, the variation (*i.e.*, sample standard deviation) in the observed signal translates to $\sigma \approx 5 - 10$ μK. In terms of dose to water, this corresponds to approximately 2 - 5 cGy.

Table 9.1. Summary of the dose measurements performed using the water calorimeter in clinical accelerator-based 6 MeV and 8 MeV electron and cyclotron-based 60 MeV protons (monoenergetic and modulated) beams. The stated uncertainty in the 3rd and 4th column represents the type A standard uncertainty, defined as $[\sigma / \sqrt{N}]$. In the average dose to water column, the uncertainty represents the calorimeter's repeatability.

Beam type and energy	Number of runs, N	Avg. raw bridge signal, ΔV (μV)	Avg. temperature rise, ΔT (mK)	Average dose to water, D_w (cGy)
6 MeV electrons	28	12.58 ± 0.06	0.625 ± 0.003	262.9 ± 0.4 %
8 MeV electrons	24	13.07 ± 0.05	0.651 ± 0.003	273.9 ± 0.4 %
60 MeV monoenergetic protons	23	29.35 ± 0.26	1.44 ± 0.01	606.4 ± 0.2 %
Modulated protons (60 MeV max.)	24	19.30 ± 0.11	0.950 ± 0.006	399.5 ± 0.2 %

9.3.2 Heat Transfer Corrections

The corrections for the conductive heat transfer, k_c, for each electron and proton beam were calculated as a function of thermistor depth setting (Figure 9.6) using a

three-dimensional model of the water calorimeter vessel embedded in an expanded polystyrene block and surrounded by a constant temperature boundary condition. The effects of air motion, including convection, were assumed to be negligible. For the 60 s electron irradiations, values of k_c at the point of measurement were determined to be 1.042 and 1.049 for the 6 MeV and 8 MeV beams, respectively. Similarly, for the 20 s proton irradiations, k_c was found to be 1.021 for the monoenergetic beam, and 1.024 for the modulated beam. For both electron and proton beams, variations of less than 0.2 % are seen among the first ten runs when determining the heat transfer correction through extrapolation of the normalized post-drift to the mid-irradiation time. Uncertainty on this correction is based on the thermistor positional uncertainty and the run variation.

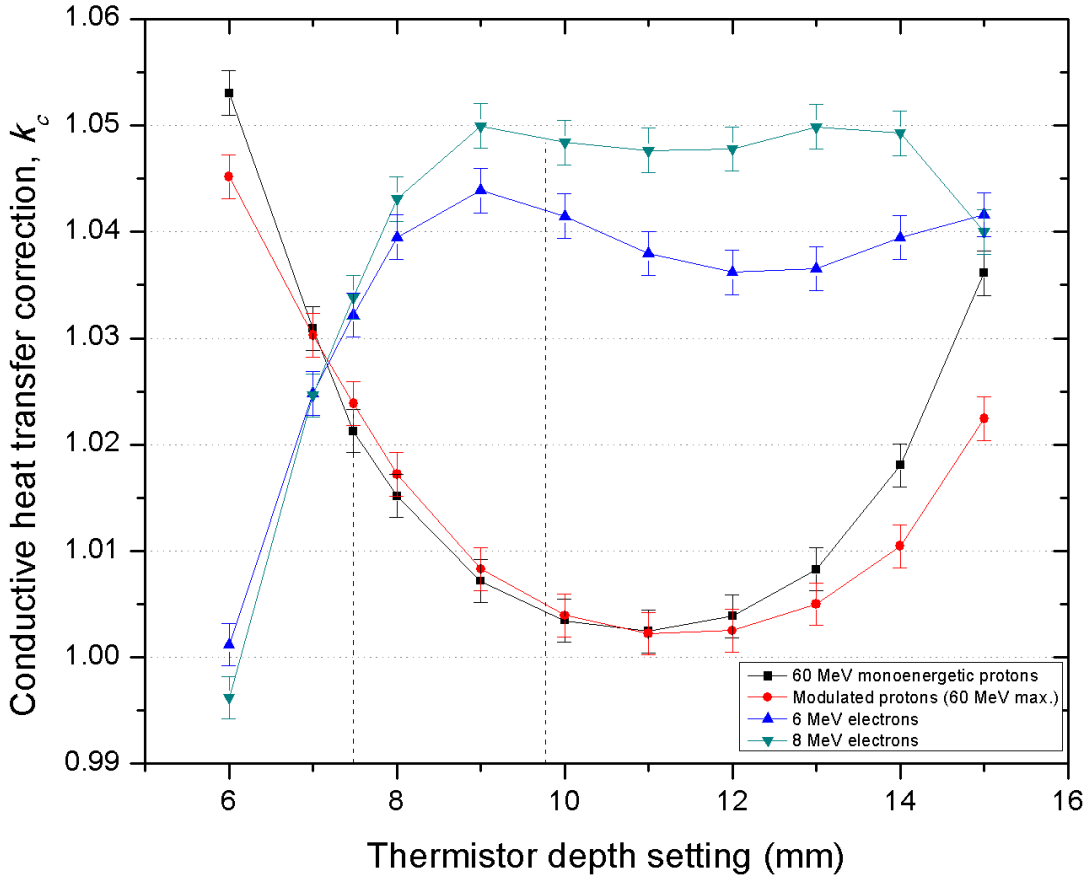

Figure 9.6: Numerically-determined values of k_c, the conductive heat transfer correction, as a function of thermistor depth setting for the four beam types studied in this work:

(squares) 60 MeV monoenergetic protons, (circles) 60 MeV modulated protons, (triangles) 6 MeV electrons, and (inverted triangles) 8 MeV electrons. The investigated depth range corresponds to the extent of adjustment inside the vessel. The vertical dashed lines indicate the points of measurement and the values of k_c applied to the electron (9.68 mm) and proton (7.48 mm) measurement sets. Error bars represent both the uncertainties inherent to the modelling process (meshing, tolerance levels, heat source terms, etc.) and the variation observed among the ten simulated irradiations.

9.3.3 Dose Measurement Uncertainties

Summaries of the beam-independent and -dependent uncertainties associated with quantities involved in the determination of absorbed dose using the water calorimeter are provided in Table 9.2 and 9.3. All values correspond to a k = 1 uncertainty, and have been classified as either Type A or B for clarity. The combined uncertainties related to the calorimetry dose measurements is approximately 0.6 % for the 6 MeV and 8 MeV electron beams, as well as for the monoenergetic proton beam, and 0.7 % for the modulated 60 MeV proton beam. These values have been calculated assuming independent inputs, in other words, contributions have been summed up in quadrature. A reproducibility of 0.2 % and 0.4 % (type A standard uncertainty) was achieved for the proton and electron beams, respectively. The uncertainties on the specific heat capacity of water, $c_{p,w}$, absolute temperature measurement of the calorimeter, as well as the bridge and thermistors calibration factors are taken into consideration. In addition to statistical uncertainty, the type B uncertainties associated with thermistor positioning with respect to the vessel window are also noted. The effect of this uncertainty is greatest (0.5 %) for the modulated proton beam, which is attributed to the level of variation in the spread out Bragg peak.[43] A total uncertainty ranging from 0.2 % to 0.4 % was assigned to the calculation of k_c. These values include the positioning uncertainty, the inherent uncertainties in the COMSOL

modeling of heat transport (due to meshing, tolerance levels, etc., which are assumed to have been set sufficiently high to have a negligible effect on the uncertainty), the variation observed among the ten simulated irradiations, and to a lesser extent, the input heat source (*i.e.*, dose) distributions and the various physical parameters assigned to the materials involved.

Table 9.2. Summary of the relative beam-independent uncertainties in the absolute determination of absorbed dose to water. All values correspond to the $k = 1$ uncertainty.

Beam-independent quantity	Type A (%) uncertainty	Type B (%) uncertainty
Monitor chamber reading	0.1	--
$c_{p,w}$	--	0.05
Bridge (ohmic) calibration	--	0.1
Absolute temperature	--	0.01
Thermistor calibration	--	0.2
k_{HD}	--	0.15

Table 9.3. Summary of the relative beam-dependent uncertainties in the absolute determination of absorbed dose to water. The reproducibility of the SHREWcal reading is based on ~25 measurements. All values correspond to the $k = 1$ uncertainty.

Beam type and energy	Type A (%) uncertainty	Type B (%) uncertainty	
	SHREWcal reading	Depth (thermistors)	k_c
6 MeV electrons	0.4	0.2	0.2
8 MeV electrons	0.4	0.2	0.2
60 MeV monoenergetic protons	0.2	0.2	0.4
Modulated protons (60 MeV max.)	0.2	0.5	0.3

9.4 DISCUSSION

Aside from the delivered dose distribution itself, the largest influencing effects on the value of k_c are the thermal gradient contributions arising in the front and back windows of the vessel. Sarfehnia et al. (2010) studied the influence of the window thicknesses on k_c for this particular vessel design in a spot scanning delivery of protons of nominal energy ranging between 128 MeV and 151 MeV and found variations on the order of a few percent depending on the extent of post-drift extrapolation.[40] In general, a thinner window will result in a smaller influence on the value of k_c. In the same study, a similar modulated proton experiment was carried out for which a k_c of 0.996 was assigned. There are two main reasons why their value is significantly less than the 1.021 to 1.024 effect determined in this work. First, the 30 mm diameter field delivered in this study produced a very sharp lateral thermal gradients inside the vessel. In comparison, Sarfehnia et al. (2010) used a 12 × 12 cm^2 field; more than sufficient to cover the extent of the vessel and a relatively large volume of water proximal to it with a quasi-uniform dose (and thus thermal) distribution.[40] Secondly, their use of a larger water phantom meant that the heat buildup in the vessel material could dissipate, particularly in the transverse direction, away from the thermistors. Efforts to minimize the magnitude of k_c can be made by maximizing the field size (up to ~70 mm diameter) to minimize lateral gradients, and/or by maximizing the dose rate, and thereby the signal detected at the position of the thermistors for a given irradiation period. Moreover, as shown in Figure 9.6, thermistor positioning with respect to the windows can also be optimized in terms of the uncertainty associated with k_c if heat transfer is simulated for a specific beam *a priori*. For the proton beams in this study, the relatively flat dose distributions in the region of the vessel results in an optimal thermistor position of about 11 mm, roughly corresponding to the geometric centre of the vessel (please note that the thermistors were positioned at 7.48 mm in this work). In this case, both the magnitude and uncertainty of k_c are minimized concurrently. In contrast, for the 6 MeV and 8 MeV electrons, the dose gradients inside the vessel are more severe, and as a

result k_c is minimized at a shallower depth (~6 mm). This is likely due to the balancing effect occurring due to the warmer front vessel window and the cooler region inside the vessel beyond the depth of maximum dose. In such a case, the uncertainty associated with k_c is minimized in the depth range of 9 – 14 mm (see Figure 9.6), where the correction is least sensitive to the positioning of the thermistors.

With an appropriate choice of measurement depth, it is expected that the uncertainties associated with the thermistor positioning and the correction due to heat conduction can kept to a minimum (~0.2 % each), resulting in a combined standard uncertainty on the order of 0.4 % - 0.5 % on the absorbed dose to water determination in beams of sufficiently high dose rate. In comparison, absorbed dose to water can be established with a combined relative standard uncertainty of 0.2 % - 0.3 % in high-energy photon beams using primary standard water calorimeters.[12,54] The two remaining sources of uncertainty dominating the SHREWcal system is measurement (reproducibility) and chemical heat defect. The former can be reduced by a larger set of measurements, but may be limited by how the reproducibility is affected by the heat defect.[5] The latter is strongly determined by the operation procedures followed by the user during a particular measurement set. The uncertainty estimate on the heat defect is decreasing as more extensive work is performed. For instance, in an international comparison of high-energy photon absorbed dose standards, Picard et al (2010)[51] reported a heat defect uncertainty of 0.15 % based on the evaluation of Ross et al (2007)[17], which was shown to be consistent with the analysis made by Krauss (2006)[54]. Establishing an absorbed dose standard for short-range particle beams based on the SHREWcal design that can be implemented at the local level could substantially reduce the uncertainties associated with the ^{60}Co-traceable chamber-based reference dosimetry. Such a device could be used to directly calibrate chambers in the user's beam without a need for k_{Q,Q_0} factors. This would represent a significant improvement over the currently recommended practices provided in reference dosimetry

protocols which have combined standard uncertainties of 2 % - 2.3 % for protons, and 3 % - 3.4 % for clinical heavy ion beams.

9.5 CONCLUSIONS

The McGill SHREWcal water calorimeter system was successfully used to measure the absolute dose to water in clinical 6 MeV and 8 MeV electron beams, as well as the 60 MeV monoenergetic and modulated proton beams of the National Centre for Eye Proton Therapy at CCC in the UK. Overall, doses to water were determined with a combined k = 1 uncertainty of 0.6 % for the 6 MeV and 8 MeV electron beams, as well as for the monoenergetic 60 MeV proton beam, and 0.7 % for the modulated proton beam. For the experimental setups in this study, the heat transfer correction due to conduction was determined to vary in the range of 1.042 ± 0.002 to 1.049 ± 0.002 for the large field electron beams, while for the 30 mm diameter proton beams, this quantity was found to be between 1.021 ± 0.004 and 1.024 ± 0.003. By simulating the heat transfer *a priori*, thermistor positioning within the calorimeter vessel can be optimized in terms of the uncertainty associated with k_c, the value of which is strongly dependent upon the dose gradients. In general, this work demonstrate the feasibility of performing water calorimetry in these types of clinical beams using only a relatively small (~78 mm diameter, ~23 mm deep) water-filled vessel as the absorbing medium, and forms the basis for a transportable dose standard for direct calibration of ionization chambers in the user's short-range radiation beam. By using direct water calorimetric measurement techniques like the SHREWcal, it is possible to reduce the uncertainties associated with TRS-398 reference dose measurements in which a numerically-derived k_{Q,Q_0} is used to transfer a chamber calibration to the beam quality of interest.

ACKNOWLEDGEMENTS

The efforts of Russell Thomas and Nigel Lee of the National Physical Laboratory, and Antoine Delor of the Université catholique de Louvain are greatly appreciated. The thermistor probes were built and provided by David Marchington of the IRS division of the NRC. This work has been supported in part by the CREATE Medical Physics Research Training Network grant of the Natural Sciences and Engineering Research Council (NSERC) (Grant: number 432290), as well as NSERC grants RGPIN 298191 and 435608. J. Renaud is a recipient of a Canadian Institutes of Health Research (CIHR) doctoral scholarship.

9.6 REFERENCES

[1]Andreo P, Burns D T, Hohlfeld K, Huq M S, Kanai T, Laitano F, Smyth V and Vynckier S 2000 Absorbed dose determination in external beam radiotherapy: an international code of practice for dosimetry based on standards of absorbed dose to water IAEA Technical Report Series No. 398 (Vienna: IAEA)

[2]Almond P R, Biggs P J, Coursey B M, Hanson W F, Saiful Huq M, Nath R and Rogers D W O 1999 AAPM's TG-51 protocol for clinical reference dosimetry of high-energy photon and electron beams *Med. Phys.* **26** 1847–70

[3]McEwen M, DeWerd L, Ibbott G, Followill D, Rogers D W, Seltzer S and Seuntjens J 2014 Addendum to the AAPM's TG-51 protocol for clinical reference dosimetry of high-energy photon beams *Med. Phys.* **41**, 041501

[4]Domen S R and Lamperti P J 1974 A heat-loss-compensated calorimeter: Theory, design, and performance *J. Res. Natl. Bur. Stand. A Phys. Chem*. **78A**(5), 595-610

[5]Seuntjens J and Duane S 2009 Photon absorbed dose standards *Metrologia* 46, S39-S58

[6]McEwen M R and DuSautoy A R 2009 Primary standards of absorbed dose for electron beams *Metrologia* **46**, S59-S79

[7]Burns D 2012 An analysis of existing data for W_{air}, I_c and the product of $W_{\text{air}}S_{c,\text{air}}$ *Metrologia* **49**, 507-512

[8]Seuntjens J P and DuSautoy A R 2003 Review of calorimeter-based absorbed dose to water standards Standards and Codes of Practice in Medical Radiation Dosimetry: Proceedings of an International Symposium IAEA-CN-96-3 (Vienna: IAEA)

[9]Kacperek A 2009 Protontherapy of eye tumours in the UK: A review of treatment at Clatterbridge *Appl. Radiat. Isot*. **67**, 378-386

[10]Stucki G, Muench W and Quintel H 2003 The METAS absorbed dose to water calibration service for high energy photon and electron beam radiotherapy Standards and Codes of Practice in Medical Radiation Dosimetry: Proceedings of an International Symposium IAEA-CN-96-8 (Vienna: IAEA)[11]McEwen M R, DuSautoy A R and Williams A J 1998 The calibration of therapy level electron beam ionization chambers in terms of absorbed dose to water *Phys. Med. Biol*. **43**, 2503-2519

[12]Ross C K, Seuntjens J P, Klassen N V and Shortt K R 1999 The NRC sealed water calorimeter: Correction factors and performance Proceedings of Workshop on Recent Advances in Calorimetric Absorbed Dose Standards, Report CIRM 42 (Teddington, UK: NPL)

[13]ICRU 2007 Prescribing, Recording, and Reporting Proton-Beam Therapy ICRU Report No 78 (Bethesda, MD: ICRU)

[14]Renaud J, Rossomme S, Sarfehnia A, Vynckier S and Seuntjens J 2014 Poster – Thur Eve – 22: A water calorimeter for low-energy particle beams *Med. Phys*. **41**, 11

[15]Seuntjens J P, Ross C K, Klassen N V and Shortt K R 1999 A status report on the NRC sealed water calorimeter NRC Tech Report No. PIRS-0584 (Ottawa:NRCC)

[16]Brede H J, Hecker O and Hollnagel R 2000 An absorbed dose to water calorimeter for collimated radiation fields *Nucl Instrum Meth A* **455**, 721-732

[17]Ross C K, McEwen M R and Klassen N V 2007 Vessel designs and correction factors for water calorimetry Proceedings of Absorbed Dose and Air Kerma Primary Standards Workshop (Paris: LNE-LNHB)

[18]Medin J, Ross C K, Stucki G, Klassen N V and Seuntjens J P 2004 Commissioning of an NRC-type sealed water calorimeter at METAS using ^{60}Co gamma-rays *Phys. Med. Biol*. 4073-4086

[19]Krauss A 2005 The new PTB primary standard for absorbed dose to water in Co-60 radiation Proceedings of ICMP on Medical Physics ed U Boenick and A Bolz (Nuremburg: Biomediziniche Technik), pp 405-406

[20]McEwen M R and Ross C 2005 Direct calibration of ionization chambers in linac photon beams *Med. Phys*. **32**, 2128

[21]Sharpe P and Duane S 2011 Progress report on radiation dosimetry at NPL Report CCRI(I)/11-07 (Teddington, UK: NPL)

[22]Seuntjens J P 1993 Correction factors for a cylindrical ionization chamber used in medium-energy x-ray beams *Phys. Med. Biol*. **38**, 805-832

[23]de Prez L A and de Pooter J A 2008 The new NMi orthovoltage x-rays absorbed dose to water primary standard based on water calorimetry *Phys. Med. Biol*. **53**, 3531-3542

[24]Krauss A, Büermann L, Kramer H M and Selbach H J 2012 Calorimetric determination of the absorbed dose to water for medium-energy x-rays with generating voltages from 70 to 280 kV *Phys. Med. Biol*. **57**, 6245-6268

[25]Schultz R J, Verhey L J, Saiful Huq M and Venkataramanan 1992 Water calorimeter dosimetry for 160 MeV protons *Phys. Med. Biol*. **37**(4), 947-953

[26]Palmans H, Seuntjens J, Verhaegen F, Denis J M, Vynckier S and Thierens H 1996 Water calorimetry and ionization chamber dosimetry in an 85-MeV clinical proton beam *Med. Phys.* **23**, 643-650

[27]Brede H J, Greif K D, Hecker O, Heeg P, Heese J, Jones D T L, Kluge H and Schardt D 2006 Absorbed dose to water determination with ionization chamber dosimetry and calorimetry in restricted neutron, photon, proton, and heavy-ion radiation fields *Phys. Med. Biol*. **51**, 3667-3682

[28]Sarfehnia A and Seuntjens J 2010 Development of a water calorimeter-based standard for absorbed dose to water in HDR ^{192}Ir brachytherapy *Med. Phys*. **37**(4), 1914-1923

[29]de Prez L A and de Pooter J A 2011 Development of the VSL water calorimeter as a primary standard for absorbed dose to water measurements for HDR brachytherapy sources Proceedings of Conference on Advanced Metrology for Cancer Therapy ed R P Kapsch (Braunschweig, Germany: PTB)

[30]Bambynek M, Krauss A and Selbach H J 2009 Calorimetric determination of absorbed dose to water for an ^{192}Ir HDR brachytherapy source in near-field geometry IFMBE Proceeding 25/XIII on Medical Physics and Biomedical Engineering ed R Magjarevic (Munich, IUPESM) pp 89-92

[31]Vatnitsky S M, Siebers J V and Miller D W 1995 Calorimetric determination of the absorbed dose-to-water beam quality correction factor k_Q for high-energy photon beams *Med. Phys*. **22**, 1749-1752

[32]Palmans H, Mondelaers W, and Thierens H 1999 Absorbed dose beam quality correction factors k_Q for the NE2571 chamber in a 5 MV and a 10 MV photon beam *Phys. Med. Biol*. **44**, 647

[33]Seuntjens J P, Ross C K, Shortt K R and Rogers D W O 2000 Absorbed-dose beam quality conversion factors for cylindrical chambers in high energy photon beams *Med. Phys*. **27**, 2763-2779

[34]McEwen M 2010 Measurement of ionization chamber absorbed dose k_Q factors in megavoltage photon beams *Med. Phys*. **37**, 2179-2193

[35]McEwen M R and Ross C K 2007 Direct calibration of ionization chambers in linac electron beams Proceedings of Absorbed Dose and Air Kerma Primary Standards Workshop (Paris: LNE-LNHB)

[36]Renaud J, Sarfehnia A, Marchant K, McEwen M, Ross C and Seuntjens J 2015 Direct measurement of electron beam quality conversion factors using water calorimetry *Med. Phys.* **42**, 6357-6368

[37]Medin J, Ross C K, Klassen N V, Palmans H, Grusell E and Grindborg J E 2005 Experimental determination of beam quality factors k_Q for two types of Farmer chamber in a 10 MV photon and a 175 MeV proton beam *Phys. Med. Biol*. **51**, 1503-1521

[38]Rossomme S, Renaud J, Lee N, Thomas R, Sarfehnia A, Seuntjens J, Kacperek A, Bertrand D, Vynckier S and Palmans H 2014 SU-ET-408: Determination of $k_{Q,Q0}$-factors from water and graphite calorimetry in a 60 MeV proton beam *Med. Phys*. **41**(6), 319

[39]Gagnebin S, Twerenbold D, Pedroni E, Meer D, Zenklusen S and Bula C 2010 Experimental determination of the absorbed dose to water in a scanned proton beam using a water calorimeter and an ionization chamber *Nucl. Instrum. Meth. Phys. Res., Sect. B* **268**, 524-528

[40]Sarfehnia A, Clasie B, Chung E, Lu H M, Flanz J, Cascio E and Seuntjens J 2010 Direct absorbed dose to water determination based on water calorimetry in scanning proton beam delivery *Med. Phys*. **37**(7), 3541-3552

[41]Medin J 2010 Implementation of water calorimetry in a 180 MeV scanned pulsed proton beam including an experimental determination of kQ for a Farmer chamber *Phys. Med. Biol.* **55**, 3287-3298

[42]Rapp B, Perichon N, Denoziere M, Daures J, Ostrowsky A and Bordy J M 2013 The LNE-LNHB water calorimeter for primary measurement of absorbed dose at low depth in water: Application to medium-energy x-rays *Phys. Med. Biol*. **58**, 2769-2786

[43]Palmans H, Thomas R, Simon M, Duane S, Kacperek A, DuSautoy A and Verhaegen F 2004 A small-body portable graphite calorimeter for dosimetry in low-energy clinical proton beams, *Phys. Med. Biol*. **49**, 3737-3749

[44]BIPM 2008 Evaluation of measurement data – Guide to the expression of uncertainty in measurement JCGM 100 (Paris: BIPM)

[45]Seuntjens J and Palmans H 1999 Correction factors and performance of a 4 C sealed water calorimeter *Phys. Med. Biol*. **44**, 627-646

[46]Lide D R 2009 Properties of Water in the Range 0-100 °C CRC Handbook of Chemistry and Physics, 89th Edition, ed D R Lide (Boca Raton, FL, CRC Press/Taylor and Francis)

[47]Stewart K J 2007 The development of new devices for accurate radiation dose measurement: A guarded liquid ionization chamber and an electron sealed water calorimeter *Ph.D. thesis* (Montreal: McGill University)

[48]Sarfehnia A 2010 Water calorimetry-based radiation dosimetry in iridium-192 brachytherapy and proton therapy *Ph.D. thesis* (Montreal: McGill University)

[49]Sassowsky M and Pedroni E 2005 On the feasibility of water calorimeter with scanner proton radiation *Phys. Med. Biol*. **50**, 5381-5400

[50]Klassen N V and Ross C K 1997 Water calorimetry: the heat defect *J. Res. Natl. Inst. Stand. Technol.* **102**, 63-74

[51]Picard S, Burns D T, Roger P, Allisy-Roberts P J, McEwen M R, Cojocaru C D and Ross C K 2010 Comparison of the standards for absorbed dose to water of the NRC and the BIPM for accelerator photon beams *Metrologia* **47**, 06025

[52]Seuntjens J 1991 Comparative study of ion chamber dosimetry and water calorimetry in medium energy x-ray beams *Ph.D. thesis* (Gent: Gent University)

[53]Domen S R 1987 Advances in calorimetry for radiation dosimetry The Dosimetry of Ionizing Radiation ed K R Kase, B E Bjärngard and F H Attix (Orlando: Academic, Inc.) Vol 2, pp 245-320

[54]Krauss A 2006 The PTB water calorimeter for the absolute determination of absorbed dose to water in ^{60}Co radiation *Metrologia* **43**, 259-272

Chapter 10

CONCLUSIONS

10.1 SUMMARY

The aim of this work has been to develop absorbed dose calorimeter systems for the purpose of accurate radiation dosimetry in the clinical environment. Currently, calorimeter-based absolute dosimetry at the clinical level is the exception, and not the rule. Absorbed dose measurement protocols based around the use of calibrated ionization chambers are presently relied upon to determine the dose rate to water, which is subsequently used in treatment planning to calculate the necessary dose to be delivered to a patient during treatment.[1,2]

Through this work, we have shown the feasibility of measuring the absolute absorbed dose directly in water for clinical high-energy photon, electron, and proton therapy. Through a reduction of the total uncertainty on the determination of dose relative to that achieved by currently accepted dosimetry protocols, we hope to improve the quality of care that patients may receive from these treatment modalities in the future. A summary of the final results of this work and the remaining work to be done towards improving and establishing primary and local dosimetry standards for these modalities at a clinical, national and/or international level are discussed in this chapter.

1) *Development of a clinical absorbed dose standard based on graphite calorimetry*

A finite element method (FEM) based numerical heat transfer study was conducted using Comsol MULTIPHYSICS® to explore the feasibility of a graphite probe calorimeter (GPC) conceived for dose measurement in the clinical environment. Comsol was used to optimize the shape, dimensions and materials incorporated into its design. A functioning prototype (GPC-MKII) was constructed in-house and used to perform dose to water measurements under a 6 MV photon beam at 400 MU/min and 1000 MU/min, in a thermally insulated water phantom. Heat loss correction factors were determined using FEM analysis while the radiation field perturbation and the graphite to water absorbed dose conversion factors were calculated using Monte Carlo (MC) simulations.

The difference in the average measured dose to water for the 400 and 1000 MU/min runs using the American Association of Physicists in Medicine (AAPM) TG-51 protocol and the GPC-MKII was 0.2 % and 1.2 %, respectively.[2] Heat loss correction factors ranged from 1.001 to 1.002, while the product of the perturbation and dose conversion factors was calculated to be 1.130. The combined relative uncertainty was estimated to be 1.4 %, with the largest contributors being the specific heat capacity of the graphite (type B, 0.8 %) and the reproducibility, defined as the standard deviation of the mean measured dose (type A, 0.6 %).

Based on the GPC-MKII design, a functioning prototype capable of two independent modes of operation (quasi-adiabatic and isothermal) was constructed in-house (GPC-MKIV; a.k.a Aerrow). Reference dose measurements were performed using both Aerrow operation modes in a 6 MV photon beam and were directly compared to results derived using a calibrated reference-class ionization chamber. The Aerrow was then used to quantify the absolute output of five high-energy photon (6 MV, 6 MV FFF, 10 MV, 10 MV FFF, and 15 MV),

and five electron beams (6 MeV, 9 MeV, 12 MeV, 16 MeV, and 20 MeV). Linearity, dose rate, orientation, and beam quality dependences were also evaluated.

Compared to the chamber-derived dose to water of 0.763 ± 0.007 cGy/MU, the average Aerrow-measured doses were 0.762 ± 0.007 (n = 25) and 0.753 ± 0.007 (n = 32) cGy/MU for the quasi-adiabatic and isothermal modes, respectively. Furthermore, all photon and electron beam outputs measured using the Aerrow were in statistical agreement with clinical reference dosimetry data. The linearity of the Aerrow's response (n = 30) was characterized by an adjusted R^2 value of 0.9998 in the region of 80 cGy to 470 cGy. For the dose rate dependence, no statistically significant effects were observed in the range of 0.5 Gy/min to 5.4 Gy/min. For photon and electron beam qualities in the range of 58.4 % < %$dd(10)_X$ < 86.8 % and 2.33 cm < R_{50} < 8.27 cm, respectively, no statistically significant trend was exhibited and a maximum deviation of about ±1 % from the average response across all beams qualities was observed. Finally, the angular dependence (gantry stationary and detector rotated) of the Aerrow's response was insignificant to within ±0.5 % of the average taken across all angles.

This work has demonstrated the feasibility of using an ion chamber-sized calorimeter as a practical means of measuring absolute dose to water in the radiotherapy clinic. The potential introduction of calorimetry as a mainstream device into the clinical setting is significant as this fundamental technique has formed the basis of absorbed dose standards in many countries for decades and could one day form the basis of a new local absorbed dose standard for clinics.[3]

2) *Development of a water calorimetry based dose standard for clinical electron therapy*

A functioning water calorimeter prototype (ESWcal) was constructed in-house and used to obtain reproducible measurements in clinical accelerator-based 6 MeV, 9 MeV, 12 MeV, 16 MeV and 20 MeV electron beams. Corrections for the radiation field perturbation due to the presence of the glass calorimeter vessel were calculated using MC simulations. The conductive heat transfer due to dose gradients and non-water materials was also accounted for using Comsol MULTIPHYSICS®.

As a preliminary validation, measurements performed with the ESWcal in a 6 MV photon beam were directly compared to results derived from the National Research Council of Canada (NRC) photon beam standard water calorimeter. These two independent devices were shown to agree well within the 0.43 % combined relative uncertainty of the ESWcal for this beam type and quality. Absorbed dose electron beam quality conversion factors were measured using the ESWcal for the Exradin A12 and PTW Roos ionization chambers. The photon-electron conversion factor, kecal, for the A12 was also experimentally determined. Non-statistically significant differences of up to 0.7 % were found when compared to the calculation-based factors listed in the AAPM's TG-51 protocol.

The relative combined standard uncertainty on the ESWcal dose was estimated to be 0.50 % for the 9 MeV to 20 MeV beams and 1.00 % for the 6 MeV beam, demonstrating that the development of a water calorimeter-based standard for electron beams over such a wide range of clinically-relevant energies is feasible. The largest contributor to the uncertainty was the positioning (Type A, 0.10 % to 0.40 %) and its influence on the perturbation correction (Type B, 0.10 – 0.60 %). This is the first time that water calorimetry has been successfully used to measure electron beam quality conversion factors for energies as low as 6 MeV (R_{50} = 2.25 cm).

3) *Development of a water calorimetry based dose standard for short range particle beams*

A functioning calorimeter prototype (SHREWcal) with a total water equivalent thickness of less than 30 mm was constructed in-house and used to obtain measurements in clinical accelerator-based 6 MeV and 8 MeV electron beams and cyclotron-based 60 MeV monoenergetic and modulated proton beams. Corrections for the conductive heat transfer due to dose gradients and non-water materials was also accounted for using Comsol MULTIPHYSICS®.

Absorbed dose to water was measured with an associated type A standard uncertainty of approximately 0.4 % and 0.2 % for the electron and proton beam experiments, respectively. In terms of thermal stability, drifts were on the order of a couple of hundred μK per minute, with a short-term variation of 5 – 10 μK. Heat transfer correction factors ranged between 1.021 and 1.049. The overall combined standard uncertainty on the absorbed dose to water was estimated to be 0.6 % for the 6 MeV and 8 MeV electron beams, as well as for the 60 MeV monoenergetic protons, and 0.7 % for the modulated 60 MeV proton beam.

This work has established the feasibility of developing an absorbed dose transfer standard for short-range clinical electrons and protons and forms the basis for a transportable dose standard for direct calibration of ionization chambers in the user's beam. The largest contributions to the combined standard uncertainty were the positioning (≤ 0.5 %) and the correction due to conductive heat transfer (≤ 0.4 %). This is the first time that water calorimetry has been used in such a low energy proton beam.

10.2 FUTURE WORK

1) *GPC (Aerrow)*:

The manuscripts presented in Chapters 5 and 6 presented some potential ways in which the repeatability and calibration of the Aerrow could be improved. In addition to what has already been mentioned in *Sections* 5.4 and 6.4, potential future work done towards improving the design and operation of the Aerrow may include: (i) the replacement of the current aerogel-based thermal insulator with a rigid, machinable formulation, such as Airloy™; Not only will this improve the reproducibility of the construction, but also ensure that the graphite bodies remain perfectly concentric during assembly. (ii) the reduction of the size and number of embedded thermistors from fifteen to as few as six; By using as few thermistors as necessary, the amount of non-graphite material in the device will be minimized, and by extension, the energy-dependence contributed by impurities. (iii) the miniaturization of the scale of the design by about 50 %; At half of its current scale, the Aerrow could potentially be used to measure absolute dose in even the smallest radiation fields used clinically (~5 mm) provided that the increased core surface area to volume ratio does not result in an unmanageable amount of heat transfer.

2) *ESWcal:*

As discussed in Chapter 8, clinical electron beam water calorimetry can be improved by implementing more accurate positioning methodologies. The current method of determining the thermistor depth, both in relation to the front face of the vessel and within the calorimeter phantom, must be improved in order to reduce the combined uncertainty (~1 %) for lower energy electron beams (*i.e.*, < 9 MeV). Positioning uncertainties become

greater at low energies due to the steep dose gradients, which in turn affect the accuracy of the field perturbation correction. Rather than positing the vessel or ionization chamber within the water phantom by hand, one of several types of linear encoders could be used to reduce the positioning uncertainty from a few tenths of a mm to a few 10s of μm. This improvement would permit the suitability of this technique to include 4 MeV and 6 MeV electrons. This is of particular interest since newly-developed thin-window (0.7 mm) vessels with angled ports have made it physically possible to perform measurements at the reference depth of beams with energies as low as 4 MeV.

3) *SHREWcal*:

While the manuscript of Chapter 9 covers the construction and initial testing of the SHREWcal in great detail, it does not include a comparison against a ground truth to establish the accuracy of the absorbed dose measurements. While the absolute accuracy of any primary standard cannot be directly measured, showing agreement among independent standards helps validate the technique. To this end, we are currently completing a comparison study in which SHREWcal and a graphite calorimeter (built and operated by the National Physics Laboratory of the UK) were operated side-by-side to measure the dose from the same 60 MeV proton beam as described in Chapter 9.

10.3 REFERENCES

[1]Andreo P, Burns D T, Hohlfeld K, Huq M S, Kanai T, Laitano F, Smyth V and Vynckier S 2000 Absorbed dose determination in external beam radiotherapy: an international code of practice for dosimetry based on standards of absorbed dose to water IAEA Technical Report Series No. 398 (Vienna: IAEA)

[2]Almond P R, Biggs P J, Coursey B M, Hanson W F, Saiful Huq M, Nath R and Rogers D W O 1999 AAPM's TG-51 protocol for clinical reference dosimetry of high-energy photon and electron beams *Med. Phys.* **26** 1847–70

[3]Seuntjens J and Duane S 2009 Photon absorbed dose standards *Metrologia* 46, S39-S58

List of Acronyms and Abbreviations

2D	Two dimensional
3D	Three dimensional
CPU	Central processing unit
^{60}Co	Cobalt-60 radioisotope
AAPM	American Association of Physicists in Medicine
AC	Alternating current
ADCL	Accredited dosimetry calibration laboratory
AWG	American wire gauge
BIPM	International Bureau of Weights and Measures
BNC	Bayonet Neill-Concelman
CCC	Clatterbridge Cancer Centre
CIHR	Canadian Institutes of Health Research
CPE	Charged particle equilibrium
CREATE	Collaborative Research and Training Experience Program
CSDA	Continuously slowing down approximation
CT	Computed tomography
CVD	Chemical vapour deposition
DC	Direct current
DNA	Deoxyribonucleic acid
EPoM, PoM	Effective point of measurement
ESWcal	Electron sealed water calorimeter
FEM	Finite element method
FFF	Flattening filter free
GPC	Graphite probe calorimeter
GPIB	General purpose interface bus
Gy	Gray
HDR	High dose rate

IAEA	International Atomic Energy Agency
ICRU	International Commission on Radiation Units and Measurements
IEEE	Institute of Electrical and Electronics Engineers
IMRT	Intensity modulated radiation therapy
IRS	Ionizing Radiation Standards
JCGM	Joint Committee for Guides in Metrology
KERMA	Kinetic energy released per unit mass
kV, keV	Kilo-electron volt
LET	Linear energy transfer
LNE-LNHB	Laboratoire National Henri Becquerel
MC	Monte Carlo
METAS	Swiss Federal Office of Metrology and Accreditation
MK	Mark (designation)
MOSFET	Metal-oxide semiconductor field effect transistor
MR	Magnetic resonance
MRgRT	Magnetic resonance guided radiation therapy
MSR	Machine-specific reference
MU	Monitor unit
MV, MeV	Mega-electron volt
NI	National Instruments
NIST	National Institute of Standards and Technology
NMI	National metrology institute
NPL	National Physical Laboratory
NRC	National Research Council of Canada
NSERC	Natural Sciences and Engineering Research Council of Canada
NTC	Negative temperature coefficient
OD	Optical density
OSLD	Optically-stimulated luminescent dosimeter
PCI	Peripheral component interconnect
PCSR	Plan class-specific reference
PCT	Patent cooperation treaty

PDD	Percent depth dose
PDE	Partial differential equation
PI, PID	Proportional integral derivative
PMMA	Polymethyl methacrylate
PSL, PSDL	Primary standards dosimetry laboratory
PTB	Physikalisch-Technische Bundesanstalt
PXI	Extensions for instrumentation
RAM	Random-access memory
RF	Radio frequency
RT	Radiation therapy
RTD	Resistance temperature detector
SAD	Source-axis distance
SATP	Standard ambient temperature and pressure
SHREWcal	Short range water calorimeter
SI	International system of units
SOBP	Spread-out Bragg peak
SRS	Stereotactic radiation surgery
SSD	Source to surface distance
SSDL	Secondary standard dosimetry laboratory
TCP, TCPE	Transient charged particle equilibrium
TG	Task group
TLD	Thermoluminescent dosimeter
TPR	Tissue-phantom ratio
TRS	Technical report series
USB	Universal serial bus
UV	Ultraviolet
VGA	Video graphics array
VSL	Van Swinden Laboratory (Dutch Metrology Institute)
WHO	World Health Organization